Group 13 Metal Oxide and Pnictide Thin Films:

Developing Novel Single-Source Precursors for the Deposition of Functional Materials

This thesis is submitted in partial fulfilment of the requirements for the Degree of Doctor of Philosophy (Chemistry)

Peter James Marchand

Supervised by Professor Claire J. Carmalt

Department of Chemistry

University College London

Christopher Ingold Laboratories

20 Gordon Street

London

WC1H 0AJ

2013

I, Peter James Marchand, confirm that the work presented in this thesis is my own. Where information has been derived from other sources, I confirm that this has been indicated in the thesis.

Abstract

This thesis describes the development of a range of novel single-source precursors based on group 13 metals aluminium, gallium and indium and an investigation into their applicability for the deposition of group 13 oxide and pnictide thin films by chemical vapour deposition (CVD).

The search for tuneable ligand systems has led to the investigation of *β*-ketoimines as ligands for the isolation of monomeric group 13 metal complexes and the development of a range of bis-*β*-ketoimine compounds of the form L^nH_2, where n denotes the length of the carbon chain bridging the two *β*-ketoimine moieties. The reactivity of these compounds towards group 13 metals has been investigated, resulting in the formation and structural characterisation of a number of novel complexes. A range of monomeric, 5-coordinate chloride complexes of the form $[M(L^n)Cl]$ (M = Al, Ga, In) have been synthesised through salt metathesis of the metal trichlorides with the corresponding sodium salts of the ligands, displaying geometries varying between square-based pyramidal and trigonal bipyramidal. In addition, the isolation of a number of 6-coordinate species were isolated from the reactions of L^2H_2 with $InCl_3$ on account of the larger size of the In^{3+} cation.

Alkyl complexes were synthesised *via* alkane elimination, with a mixture of mono- and bi-metallic products being isolated. Finally, the ligands were successfully used for the stabilisation of rare gallium monohydride species, $[Ga(L^n)H]$ (n = 2, 3), which exhibited considerable thermal stability.

The thermal decomposition of the group 13 *β*-ketoiminate complexes was investigated by thermogravimetric analysis and subsequently the deposition of Ga_2O_3 was carried out on glass substrates in an aerosol assisted (AA)CVD process. The resulting films were amorphous as-deposited, however crystalline Ga_2O_3 was obtained in some cases through the addition of a post-deposition annealing step.

The single-source deposition of InAs by AACVD has been investigated, including an investigation of the alkane elimination reaction between $InMe_3$ and $^tBuAsH_2$ in the formation of InAs cluster complexes. InAs was successfully deposited,

representing the first report of the deposition of this material by AACVD. Thin films were analysed and characterised by multiple common techniques, including glancing angle powder X-ray diffraction, energy-dispersive X-ray analysis, X-ray photoelectron spectroscopy and scanning electron microscopy, confirming the formation of InAs, though film quality was hampered by varying degrees of In_2O_3 formation within the films, in particular at the surface. Hall effect measurements provided an initial investigation of the electrical properties of the films, showing the formation of conductive, n-type InAs. However, electron mobility was poor by comparison to literature suggesting that optimisation of the deposition conditions is required in order to yield device-quality materials.

Acknowledgements

There are a number of people to whom I would like to offer my gratitude for their support on both academic and personal levels.

Firstly, I would like to thank my supervisor, Prof. Claire Carmalt, for her continued investment, encouragement, guidance, support and leadership as I have carried out my PhD. I am also hugely grateful to Prof. Andrea Sella as my secondary supervisor, for some very useful discussions along the way. Furthermore, I would like to offer my thanks to Dr. Andy Johnson, under whom I studied for my MChem at the University of Bath, without whose enthusiasm and teaching I would not be where I am today.

I am grateful to a large number of people who have helped me in my research. In particular I would like to thank Dr. David Pugh for breaking me in and showing me the ropes, as well as for helping with the majority of the X-ray crystallographic analysis and the synthesis of gallium hydride complexes. I am also greatly indebted to Dr. Sanjay Sathasivam for all his help with the thin film deposition and characterisation, in particular for the collection of all XPS data.

There are a large number of staff to whom I am grateful for their technical assistance in carrying out much of the analysis within this thesis, namely Lisa Haigh and John Hill (mass spectrometry); Abil Aliev (NMR); Jill Maxwell (elemental analysis); Martin Vickers (XRD); Kevin Reeves (SEM); and Steve Firth (TGA/DSC). I would also like to thank the National Crystallography Service for the collection of crystallographic data for a number of the complexes within this work.

Thanks also go to all the past and present members of the Carmalt, Parkin and Hogarth research groups on the third floor, who have made my PhD such an enjoyable experience. In no particular order, thanks to Ralph Leech, Jared Crane, Allie Cross, Anna Roffey, Nuru Noor, Nathan Hollingsworth, Colin Crick, Davinder Bachu, Andreas Kafizas, Joe Bear, Shishir Ghosh, Joe Manzi, Caroline Knapp, Kris Page, Leanne Bloor, Savio Moniz, Charlie Hunston, Iman Hassan, Raul Quesada, Clair Chew, Pragna Kiri, Penny Carmichael, Veronica Diesen, Mike Powell, Will Peveler and Nick Chadwick.

Finally I would like to thank my whole family for their emotional and financial support throughout my life and in particular over the past three years. My parents, Peter and Gill, and my brothers George and William have been continued inspirations to me and have provided me endless encouragement.

Finally, and above all else, I would like to dedicate this thesis to my amazing wife, Corinne. Thank you for standing with me over the last five years through the highs and lows. I could not have done this without your support and belief in me.

"Now to Him who is able to do immeasurably more than all we ask or imagine, according to His power that is at work within us, to Him be glory in the church and in Christ Jesus throughout all generations, for ever and ever! Amen."

Ephesians 3 v 20 – 21

Table of Contents

List of Figures

List of Schemes

List of Tables

List of Abbreviations

Å	Angstrom
AACVD	Aerosol-assisted chemical vapour deposition
acac	Acetylacetonate
ALD	Atomic Layer Deposition
Anal.	Analysis
APCVD	Atmospheric pressure chemical vapour deposition
Ar	Aryl
bdk	*β*-diketonate
br	Broad
^{n}Bu	*normal*-butyl
^{t}Bu	*tertiary*-butyl
Calc.	Calculated
CI	Chemical Ionisation
cm	Centimetre
CVD	Chemical Vapour Deposition
Cy	Cyclohexyl
d	Doublet
δ	Chemical shift / ppm
Dipp	Diisopropylphenyl
Dmp	Dimethylphenyl
DMSO	Dimethylsulphoxide
DSC	Differential scanning calorimetry
Et	Ethyl
EDXA	Energy dispersive X-ray analysis
eV	Electron volts
FTO	Fluorine-doped tin oxide
g	Gram
hfac	hexafluoroacetylacetonate
HSQC	Heteronuclear single quantum coherence
IR	Infra-red
ITO	Tin-doped indium oxide (indium-tin oxide)
J	Coupling constant
L^2H_2	N,N'-ethylenebis(4-aminopent-3-en-2-one)
L^3H_2	N,N'-propylenebis(4-aminopent-3-en-2-one)
L^4H_2	N,N'-tetramethylenebis(4-aminopent-3-en-2-one)
LACVD	Laser-assisted chemical vapour deposition
LPCVD	Low pressure chemical vapour deposition
LSMOCVD	Liquid source metal-organic chemical vapour deposition
M	multiplet
MBE	Molecular beam epitaxy

Me	Methyl
Mes	Mesityl
mL	Millilitre
mmol	Millimole
mol	Mole
MOCVD	Metal-organic chemical vapour deposition
MS	Mass spectrometry
NMR	Nuclear Magnetic Resonance
PECVE	Plasma enhanced chemical vapour deposition
Ph	Phenyl
ppm	Parts per million
^{i}Pr	*iso*-propyl
PVD	Physical vapour deposition
pXRD	Powder X-ray diffraction
Py	Pyridine
q	Quartet
QD	Quantum dot
quin	Quintet
R	Organic substituent
r.t.	Room temperature
SEM	Scanning electron microscopy
s	Singlet
sept	Septet
t	Triplet
TCO	Transparent conducting oxide
thd	2,2,3,3,-tetramethylheptane-3,5-dionate
THF	Tetrahydrofuran
TGA	Thermogravimetric analysis
TMEDA	Tetramethyl ethylenediamine
UV	Ultraviolet
Vis	Visible
XRD	X-ray diffraction
XPS	X-ray photoelectron spectroscopy
YSZ	Yttria-stabilized zirconia

Chapter 1

Introduction

This chapter introduces the topic of discussion for the thesis, namely the use of single-source precursors in the chemical vapour deposition (CVD) of group 13 oxide and pnictide thin film materials. Initial focus will be given to the materials themselves, their properties and their applications. The range of deposition methods available for the fabrication of these materials will then be discussed, with special attention paid towards CVD, in particular a variant called aerosol-assisted (AA) CVD, and why this has been selected as the deposition method of choice for the experimental studies discussed later in the thesis. Finally, the topic of precursor chemistry is reviewed, as well as the relative merits and weaknesses of dual-source and single-source approaches and considerations relating to the design of molecular precursors. The introduction will provide a rationale for the direction of the research which is to be discussed in the remainder of the thesis.

1 Introduction

1.1 Properties and Applications Group 13 Oxides and Pnictides

1.1.1 Semiconductors – A Brief Introduction

Within inorganic materials, the combination of an almost infinite number of molecular bonding and antibonding orbitals gives rise to continuous 'bands' of energy levels, referred to as the 'valence' and 'conduction' bands. It is the nature of these bands that give rise to the electronic properties of the inorganic solid (Figure 1.1).

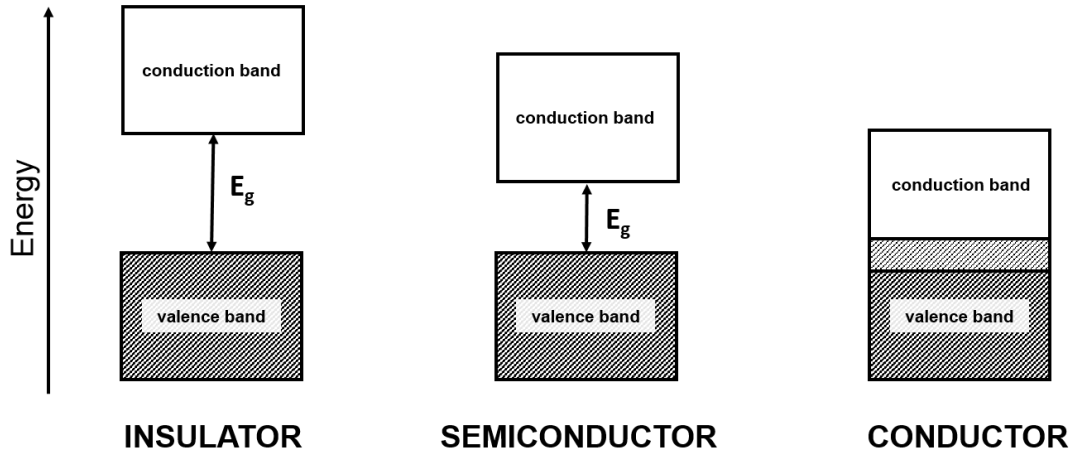

Figure 1.1 - Illustration of the band gaps possessed by insulators, semiconductors and conductors.

The highest occupied orbital at 0 K is known as the Fermi level, and its corresponding energy is the Fermi Energy, E_f. If there are available energy levels close to E_f, electrons can be easily promoted to these nearby levels, allowing a free flow of electrons through the material, making the material a conductor. This can arise if either the valence band is not completely full or if there is an overlap between the valence and conduction bands. Insulators are materials which have enough electrons to completely fill the valence band, but where a substantial energy gap (> 4 eV) exists between the valence and conduction bands (the band gap). Semiconductors, on the other hand, are materials which display relatively small band gaps (< 4 eV). This band separation is sufficiently small that, at room temperature, enough thermal energy is available to promote electrons across this band gap from the valence band to the conduction band. The promoted electrons, as well as the electron holes left behind in the valence band, therefore act as charge carriers and

give rise to an electrical conductivity, which increases with temperature (i.e. with increasing thermal energy).

Intrinsic semiconductors are pure materials which have a sufficiently small band gap to display some conductivity at room temperature. This conductivity, however, is generally small since only a small number of electrons are promoted to the conduction band and, concurrently, only a small number of positive holes are created in the valence band.

Since the carrier densities displayed by most intrinsic semiconductors are low, semiconductivity can be induced or enhanced through doping with precise amounts of impurities, forming extrinsic semiconductor materials. The presence of dopants either increases or decreases the number of electrons in the system and this increase in the number of charge carriers, or charge carrier density, leads to an increase in electrical conductivity (Figure 1.2).

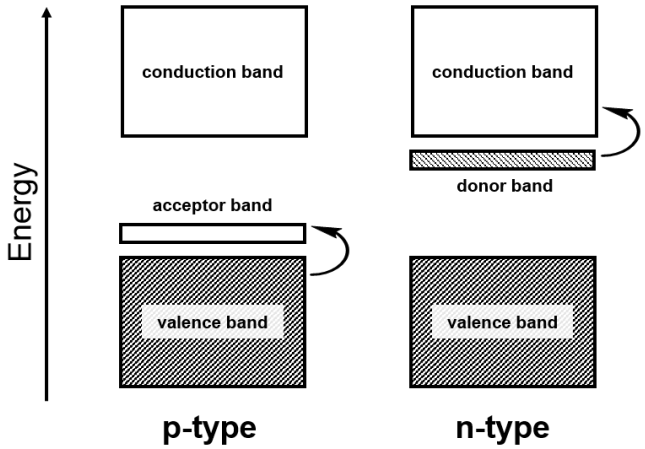

Figure 1.2 – Band structures showing p- and n-type doping in extrinsic semiconductors.

P-type doping (positive charge carriers), through the introduction of impurity atoms with fewer valence electrons than the parent material, leads to an effective increase in the number of electron holes in the valence band. This occurs through formation of an empty acceptor band that lies above the valence band, energetically speaking. This acceptor band is able to accept electrons promoted from the valence band. In contrast, n-type doping (negative charge carriers) involves the substitution of dopants with more electrons than the parent material. The dopant atom levels lie in a donor band closer in energy to the conduction band, thus facilitating the promotion of electrons to the conduction band.

The transition of electrons between valence and conduction bands within semiconductors can be either direct or indirect. The energy levels within a band are characterised by their wave vector, k, which is related to the momentum of the electron. Conservation of momentum produces a selection rule for transitions between bands, such that an electron cannot change its wave vector when it absorbs or emits radiation.[1] Direct band gap materials are those in which the minima of the conduction band and the maxima of the valence band have the same wave vector, thus an allowed transition occurs at the band gap energy (Figure 1.3).[1] Within indirect band gap materials, the maxima and minima of the valence and conduction bands, respectively, do not have the same wave vector. In order for the excitation of an electron to occur, phonon absorption or emission is required in addition to photon absorption to conserve momentum. Optical transitions in indirect band gap materials are, therefore, less efficient making them less suitable for optoelectronic applications.[2]

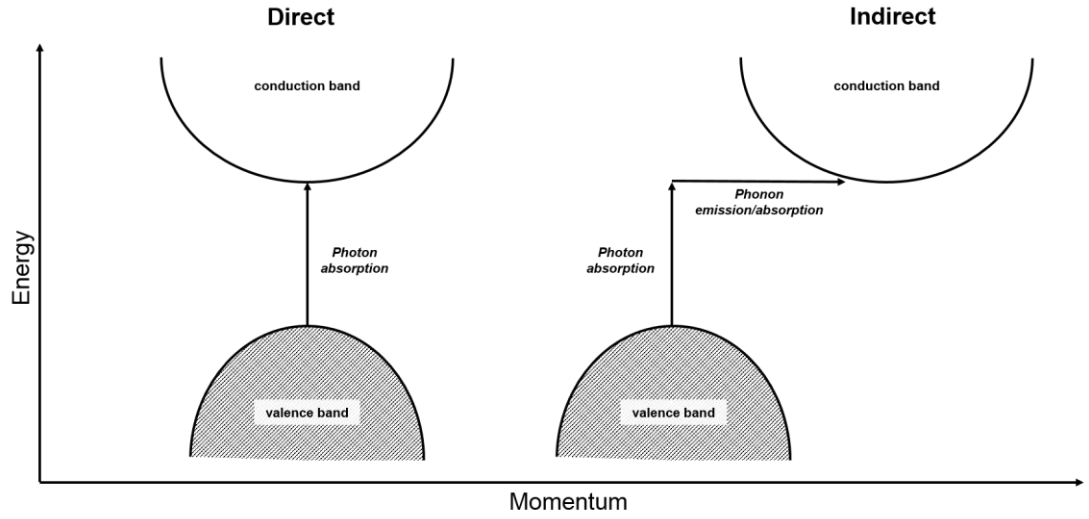

Figure 1.3 - Diagram showing mechanisms of electron promotion in direct and indirect band gap semiconductors.

1.1.2 Aluminium Oxide

The most stable form of aluminium oxide is the trigonal α-Al_2O_3, widely known as corundum,[3] which is an electrical insulator with an optical band gap of *ca.* 8.8 eV.[4]

Over the last few decades, thin films of aluminium oxide have found a diverse range of applications. For example, porous Al_2O_3 coatings on glass surfaces, with a porosity of 63 – 65% and a mode pore radius of ~40 Å, can significantly reduce the reflectivity of the surface, leading to an increase in transmission of 4 – 8% and improved performance of devices where energy is transmitted by radiation.[5] Coatings of Al_2O_3 have also been used in anti-corrosion protective layers for high precision applications such as automotive, aerospace or speciality gas handling.[6, 7]

Al_2O_3 has also been investigated as a replacement for SiO_2 as a high-κ gate dielectric materials for use within complementary metal oxide semiconductor (CMOS) transistors.[8, 9] The dielectric constant, κ, of Al_2O_3 is 9, compared to the industry standard material SiO_2 (κ = 3.9) and thus thicker materials can be used to achieve equivalent capacitance, since the capacitance of a material is inversely proportional to its thickness. This reduces the loss in performance due to tunnelling, which is associated with material thicknesses less than 2 nm.

1.1.3 Gallium Oxide

Like other group 13 oxide materials, gallium oxide has found use in a diverse range of industrially and technologically important applications. There are five known crystallographic phases of Ga_2O_3, with the most stable being α-Ga_2O_3 (trigonal) and β-Ga_2O_3 (monoclinic). Whilst α-Ga_2O_3 is only metastable, β-Ga_2O_3 is the thermodynamically stable phase on account of its low density.[10, 11] β-Ga_2O_3 is a wide band gap material (4.2 – 4.9 eV),[12, 13] which is electrically insulating at room temperature, however, displays n-type semiconductivity at elevated temperatures.[14]

At temperatures above 500 °C, β-Ga_2O_3 acts as a sensor for reducing gases such as CO and H_2,[15, 16] whilst at temperatures above 900 °C it can be used as a catalytically inactive oxygen sensor,[14] being used as a temperature dependant gas sensor. More recently, Ga_2O_3 nanowires have been found to show reversible response to O_2 and CO at much lower working temperatures in the range of 100 – 500 °C.[17] Lanthanum gallate ($LaGaO_3$) doped with various metals shows superior oxygen-ion-conductivities in comparison to other materials such as yttria-stabilised zirconia (YSZ), making these materials highly desirable for use as solid electrolytes in solid oxide fuel cells (SOFCs).[18]

In addition, gallium oxide thin films have been used as white-light emitting phosphors for use in light-emitting devices (LEDs),[19] as well as a potential deep UV transparent conducting oxide.[20] Further applications include use within catalytic zeolite systems to enhance the conversion of lower alkanes into aromatics.[21]

1.1.4 Indium Oxide

Similarly to Ga_2O_3, In_2O_3 displays a metastable rhombohedral phase and a thermodynamically stable cubic phase.[22, 23] Whilst it is widely quoted as having a direct optical band gap of 3.75 eV,[24] recent experimental and theoretical investigations have shown In_2O_3 to have a direct band gap of *ca.* 3 eV, being dependent upon the crystallographic phase.[23, 25, 26]

In_2O_3 has significant utility within the field of gas sensing. In_2O_3 nanorods have been found to give strong responses to formaldehyde, even at low concentrations,[27] whilst at high temperatures In_2O_3-modified Ga_2O_3 thin films show a sensitivity to ozone much greater than in either of the pure materials.[28] Perhaps the most noteworthy application of indium oxide thin films is as transparent conducting oxides (TCOs). TCOs are materials which exhibit both conductivity and optical transparency in the visible range and are useful in optoelectronic devices such as flat-panel displays and solar cells. $GaInO_3$ is reported to have a resistivity comparable to the widely employed indium tin oxide (ITO), while exhibiting superior light transmission properties.[29, 30]

1.1.5 Doped Materials

While the range of applications of the group 13 oxides (particularly of gallium and indium) is wide, the properties of the materials can be altered and enhanced by doping with other elements, thus broadening their potential use still further. As mentioned previously, one of the most widely used TCO materials currently is tin-doped indium oxide (ITO) which has utility in a large number of applications, including within electrochromic devices used in ‘smart windows’, which can improve energy efficiency.[31] Doping with tin improves the conductivity of the film without affecting its transparency and whilst ITO is the most commonly used material, increased conductivity can also be achieved by doping with other elements including fluorine,[32] sulphur[33] and gallium.[34] A research area of significant current interest is the production of photocatalysts for use in water-splitting, producing

hydrogen, an environmentally friendly fuel source. Both In_2O_3 and Ga_2O_3 have been found to be effective photocatalysts for this purpose through doping with nitrogen[35] and zinc[36] respectively.

1.1.6 Gallium-Indium Oxide

Further to these applications, the mixed-metal material gallium-indium-oxide is a promising material for use in transparent conducting oxide (TCO) devices.[37] Whilst tin-doped (ITO) indium oxide is one of the most widely used materials in TCO applications,[38, 39] gallium-indium oxide has been found to exhibit improved transmittance in the blue-green regions over these materials.[29]

1.1.7 III/V Semiconductors - Indium Arsenide

The band structure of a semiconducting material, and hence its electrical properties, is determined by the nature of the bonding.[2] For III/V materials, strong bonding results in a large energy band gap and low electron mobilities and *vice versa*. The strength of the bonding in III/V compounds decreases with increasing atomic radii and thus across the series AlAs, GaAs and InAs the band gaps are seen to decrease with increasing atomic number of the group 13 metal, whilst the electron mobilities are seen to increase (Figure 1.4).

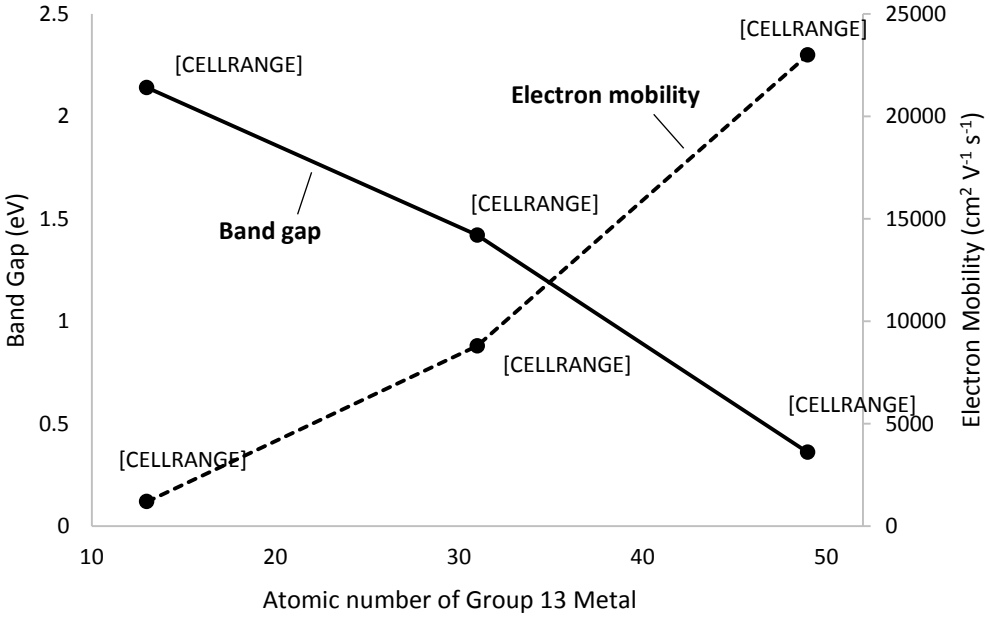

Figure 1.4 - Band gaps (eV) and Electron Mobilities ($cm^2\ V^{-1}\ s^{-1}$) of group 13 arsenides as a function of atomic number of the group 13 metal. Data obtained from Ref. 2.

The III/V compounds of group 13 metals aluminium, gallium and indium are a very important class of semiconductor materials for technological applications. In comparison to the isoelectronic elemental group 14 materials (silicon, germanium), III/V semiconductors offer typically high electron mobilities and direct band gaps (excluding GaP and AlP), giving them particular usefulness in optoelectronic devices such as light emitting diodes (LEDs).[40] Of the III/V materials, GaAs is the most widely used for integrated optoelectronics due to the ease of fabrication, its reliability and low cost.[41] InAs has a direct band gap of 0.35 eV and has been known to display high electron mobility greater than 20,000 $cm^2\ V^{-1}\ s^{-1}$ at room temperature, compared to those of the more commonly used semiconductors silicon and GaAs (1,500 and 8,500 $cm^2\ V^{-1}\ s^{-1}$, respectively).[42, 43] This gives InAs a particular application within high frequency field effect transistors and magnetoresistive sensors, which make use of the change of resistance of the active material in the presence of a magnetic field, since electron mobility is a key parameter which determines the sensitivity of a device to a magnetic field.[43]

1.2 Techniques for the Deposition of Group 13 Oxides and Pnictides

1.2.1 Overview

A wide range of techniques have been designed and developed for the fabrication of such materials. The following section briefly describes a number of commonly used techniques and references their use in the deposition of group 13 oxides and III/V materials.

- **Sputtering:** a process which involves the high-energy vapourisation of a target material, followed by condensation onto a substrate and film growth.[44] Particle energies between the target and the substrate can be controlled by a variety of methods, allowing control over the deposition process and the fabrication of materials with good optical and electronic properties at low temperatures.[45] Variations have been employed in the deposition of Al_2O_3,[46] Ga_2O_3,[47] and In_2O_3.[48]
- **Sol-gel:** a solution-based process involving the use of a concentrated solution/colloidal suspension, which is heat-treated to form a gel. Immersion of the substrate within the gel is followed by calcination to form a solid film.[1] The

widely used method has been used in the synthesis of group 13 oxides,[49, 50] as well as III/V materials.[51]

- **Spray Pyrolysis:** thin films are deposited by spraying a precursor solution onto a heated substrate, where solvent evaporation and pyrolysis occur.[52] Spray pyrolysis benefits from a simple, low-cost experimental setup, whilst offering the versatility for the deposition of a wide range of materials.[53-55]
- **Screen Printing:** a paste is made up from precursor powders with an organic 'vehicle', which is forced through the open meshes of a screen onto a substrate.[56] The films are then dried and sintered at high temperatures to afford the desired material. A number of parameters must be optimised, such as grain size, grain form, surface properties and packing density of the powders, as well as sintering time, temperature and deposition.[57] The technique has been reported for the production of metal oxide gas sensors.[58]
- **Atomic Layer Deposition (ALD):** a variant of chemical vapour deposition (CVD, which is to be discussed in detail shortly), where film growth is carried out by sequential introduction of gas phase precursors to a heated substrate. Self-terminating gas-solid reactions occur before the reaction chamber is purged and the cycle repeated with different precursors.[59] The process offers excellent control over film thickness and composition and can be carried out on industrial scales with good uniformity and conformality.[60] ALD has become widely used and has been reported for the deposition of group 13 oxide films[61-63] and III/V materials.[64]

1.2.2 Chemical Vapour Deposition (CVD)

Amongst the available techniques for the deposition of thin films of functional materials, CVD is one of the most widely employed for the production of thin films for industrial and technological applications. Conventional CVD is a gas phase deposition technique, which occurs by a series of stages illustrated in Figure 1.5. Precursors (either dual or single-source) are introduced into a reaction chamber in the gas phase by a carrier gas, which undergo diffusion to a heated substrate surface. When using dual-source precursors, it is possible that gas-phase reactions occur prior to this diffusion, a point which will be discussed further when comparing the relative benefits and shortcomings of dual and single-source approaches. Adsorbed precursors undergo surface reaction, after which any reaction by-products are

desorbed, diffuse away from the substrate surface and are carried to exhaust by the carrier gas. Under the elevated temperatures involved, surface-adsorbed adatoms migrate to the lowest energy substrate sites, after which nucleation and film growth can occur.[60]

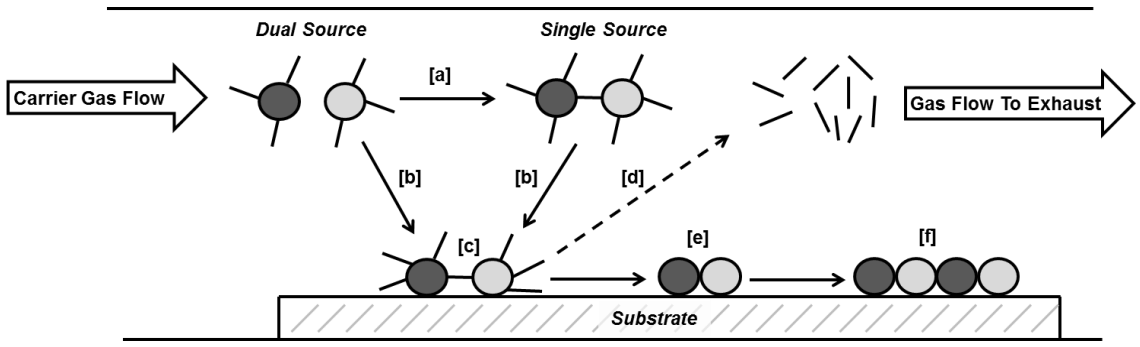

Figure 1.5 - Schematic diagram showing the physical process involved during chemical vapour deposition (CVD): [a] gas phase reaction of precursors; [b] diffusion of precursors to substrate surface; [c] surface reaction of adsorbed precursors; [d] desorption and diffusion of by-products; [e] diffusion of adatoms to lowest energy substrate sites; [f] nucleation and film growth. Reprinted with permission from Ref. 70. Copyright 2013 Royal Society of Chemistry.

CVD is an attractive technique for the production of functional materials due to the versatility it offers towards a variety of materials spanning the periodic table and its ability to produce thin films on industrial scales with excellent control over composition and uniformity. A number of variations on the technique have been developed to meet the needs of specific materials and applications and the method selected will depend largely on the target material, desired characteristics and available precursors. Commonly used variations include metal-organic (MO)CVD,[65] plasma enhanced (PE)CVD,[66] low pressure (LP)CVD,[67] atmospheric pressure (AP)CVD,[68, 69] laser-assisted (LA)CVD,[66] liquid injection CVD[66] and molecular beam epitaxy (MBE).[66]

1.2.3 Aerosol-Assisted Chemical Vapour Deposition (AACVD)

Aerosol-assisted (AA)CVD is one particular variant of interest.[70] Whilst the deposition mechanism is much the same as for conventional CVD processes, it is in the delivery of the precursor that AACVD is unique (Figure 1.6). A precursor solution is made up in a suitable organic solvent, which is then nebulised using an ultrasonic humidifier to create a precursor aerosol mist, which is transported to the reaction chamber by a carrier gas. As the mist passes into the heated reaction chamber, evaporation of the solvent occurs and the precursor molecules undergo

diffusion to the substrate surface where surface reaction, migration and nucleation can occur.

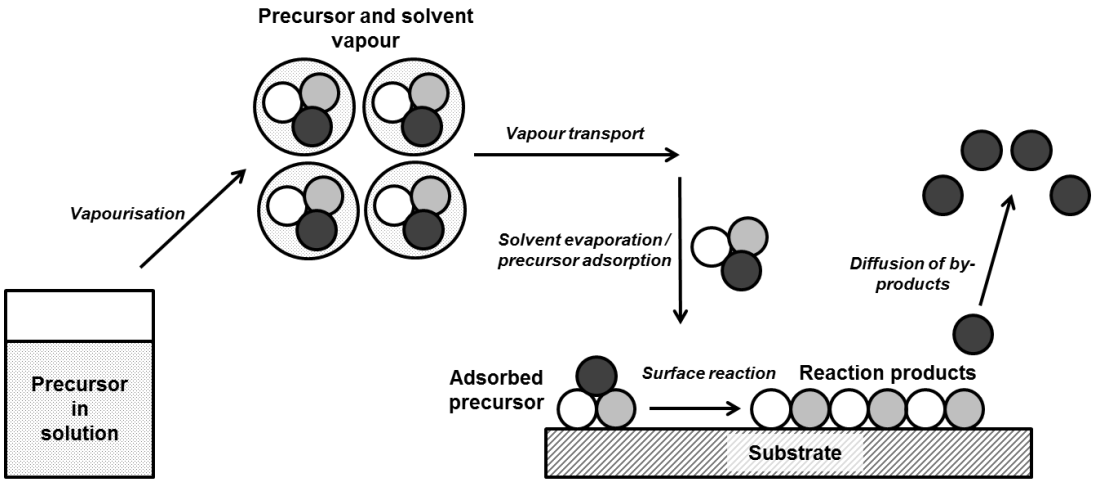

Figure 1.6 – Schematic illustration of the processes involved in AACVD. Reproduced with permission from Ref. 70. Copyright 2013 Royal Society of Chemistry.

AACVD has been comprehensively reviewed, including in depth discussion of the physical processes involved and the advantages of using the technique in the fabrication of materials for a range of applications.[60, 71, 72] The following section will give a general overview of the advantages of the technique and the reader is directed to these reviews for a more in depth discussion.

As outlined by Hou *et al.*,[71] AACVD offers some key advantages over the conventional CVD method:

i) simplification of the precursor vapourisation and delivery process through aerosol generation;
ii) high mass-transport rate of the precursor, leading to high deposition rates;
iii) a flexible reaction environment, offering the potential to operate at low pressure, atmospheric pressure and open atmospheres;
iv) precise stoichiometric control over the formation of multicomponent materials;
v) a broadening of the range of available precursors.

The final point of increasing the choice of available precursors is critical for mass production and opens avenues to the deposition of novel composite materials. Rather than relying on the volatility of the precursor, as in conventional CVD, AACVD

depends on the solubility within suitable organic solvents. This dramatically increases the range of potential precursors and gives greater scope for optimisation of the precursor in order to yield the desired deposition.

An example of the exploitation of this advantage is in the deposition of thin films of gold. CVD is a desirable technique for industrial production, however deposition by this method relies on volatile precursors. Whilst organo-gold complexes (e.g. $[F_3CAu(CNMe)]$, $[AuMe_3PMe_3]$) and gold carboxylate complexes are known to be effective precursors, their poor thermal, photochemical, air and/or moisture sensitivity presents difficulties in their synthesis and handling.[73-76] Instead, a methanol solution of the involatile precursor, hydrogen tetrachloroaurate $[HAuCl_4]$, has been used as a source of gold in an AACVD process.[77] Deposition of high quality, adherent films was observed at substrate temperatures ranging between 400 and 600 °C, demonstrating the possibility of carrying out CVD depositions using involatile precursors *via* aerosol-assisted delivery.

Whilst the solvent could be considered simply as a vehicle for precursor transport, it has been demonstrated that this plays a significant part in film growth and can influence the morphology, crystallographic phase and functional properties of the deposited films. The influence of solvent on film morphology was demonstrated through the deposition of NbS_2 and TaS_2 thin films from precursor solutions of $[M(NMe_2)_5]$ (M = Nb, Ta) and ^tBuSH in both dichloromethane and hexanes.[78] In all cases, the deposition of MS_2 was observed and SEM imaging showed film growth *via* an island growth mechanism (Figure 1.7). NbS_2 clusters were found to be larger for films deposited from hexane, whilst for TaS_2 larger clusters were observed for films deposited from CH_2Cl_2.

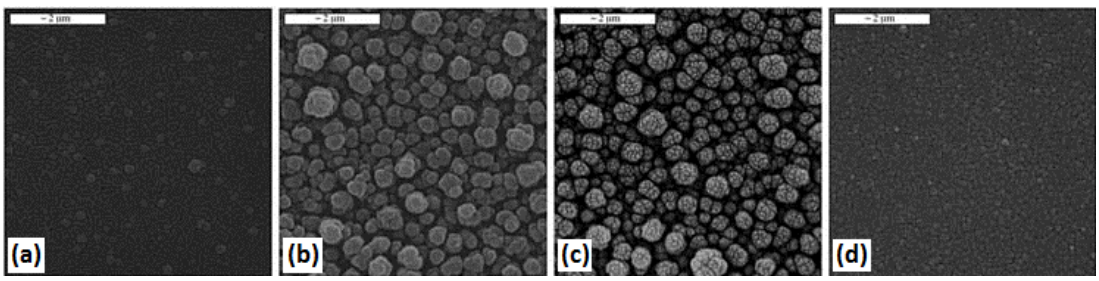

Figure 1.7 - SEM images of NbS_2 films grown in (a) hexane and (b) dichloromethane and TaS_2 films grown in (c) hexane and (d) dichloromethane. Adapted and reproduced from Ref. 78. Copyright 2005 Wiley.

Variation of the solvent used in an AACVD reaction has also been shown to influence the crystallographic phase of the material deposited. For example, the deposition of TiO_2 from solutions of $Ti(O^iPr)_4$ in EtOH, ^{i}PrOH, CH_2Cl_2 and hexane onto steel substrates was found to produce exclusively anatase films, whilst the use of MeOH produced phase-pure rutile TiO_2 thin films.[79] The directing effect of MeOH was further demonstrated by the formation of predominantly rutile films when carrying out depositions from a precursor solution of 10:90 MeOH:EtOH, showing the potential for controlling the crystallographic phase of a deposited material by choice of the precursor solvent. Functional properties can also be influenced by solvent choice, as demonstrated by the AACVD of fluorine-doped tin oxide (FTO) from the precursor ^{n}BuSnCl$_2$F.[80] Depositions were carried out in a range of solvents, with the best film quality, doping efficiency and, subsequently, film performance being found for those deposited from oxygen-containing solvents. The best performing films were those deposited from dioxane and propan-2-ol precursor solutions, with the latter being found to have optical transparency, resistivity, charge carrier density, carrier mobility and haze values significantly higher than for current industry standard materials.

AACVD also presents a route to the formation of some materials which are inaccessible by conventional CVD. The incorporation of nanoparticles into a host matrix to form nanocomposite materials has become an area of interest due to the potential for forming materials with enhanced properties over those of the nanoparticles or the host material alone and has been applied in the field of glazing, semi-conductors, antibacterials and catalysis.[81] One of the major issues with the fabrication of nanocomposite materials is the need to form the nanoparticles either *in situ* or at the same time as the host matrix, which limits the complexity of particles that can be achieved. A more desirable approach would be the separate wet chemical synthesis of particles, following by deposition with or into a thin film. Nanoparticles, however, are incompatible with conventional CVD due to their larger masses and lack of volatility. With AACVD, however, these demands are alleviated and this approach is therefore possible. Palgrave *et al.* showed the potential for this method by the AACVD of TiO_2 and WO_3 incorporating gold nanoparticles from [$Ti(O^iPr)_4$] and [$W(OPh)_6$], respectively, together with a gold colloid solution.[82] Later, the work was extended to the deposition of TiO_2:Au, WO_3:Au and MoO_3:Au

from $[Ti(OiPr)_4]$, $[W(CO)_6]$, $[Mo(CO)_6]$, and $[HAuCl_4]$, where the optical properties of the resulting films were found to be tuneable by variation of the precursor stoichiometries.[77] AACVD can also be used in conjunction with other CVD techniques in so-called 'hybrid' CVD methods, as shown by the hybrid *aerosol assisted-atmospheric pressure* (AA-AP) CVD of gold nanoparticles incorporated into a VO_2 host matrix.[83, 84] The method benefits from the film characteristics offered by APCVD coupled with the precursor versatility of AACVD.

Overall, AACVD is a versatile technique offering many benefits over alternative CVD methods. The major benefit is the alleviation of the need for volatile precursors, thus dramatically expanding the range of available precursors and broadening the scope of CVD for the fabrication of novel materials.

1.3 Precursor Chemistry

For all CVD processes, precursor decomposition is the key step in the formation of thin-films and therefore precursors must be carefully chosen to achieve effective film deposition.[60] It is important that any subsidiary ligands are lost cleanly into the gas phase to avoid contamination of the growing film, however they must also induce the necessary characteristics in the precursor to render it suitably volatile or soluble for efficient transport into the CVD reactor. A number of other considerations must also be taken into account for scaling up CVD processes, such as cost and simplicity of precursor preparation, toxicity, environmental impact and ease of use/safe handling.[60]

For the production of binary materials by CVD, two precursor approaches exist: dual-source and single-source. Dual-source CVD involves the use of separate precursors for each component of the films, whereas single-source precursors are single molecules, which contain pre-formed bonds between all the desired elements of the resultant material. The two approaches are discussed in the following section.

1.3.1 Dual-Source vs. Single-Source

Whilst dual-source CVD has been heavily used for the deposition of high quality materials, issues can arise in the control of film stoichiometry due to complicated gas-phase reaction dynamics and from the need for multiple precursors which can be toxic and/or expensive. In contrast, single-source precursors contain pre-existing,

relatively strong bonds between the desired elements of the target material in predetermined ratios, aiding the repeatable deposition of thin films in the desired stoichiometry.[85] Homogeneity is also improved as the elements of the film are essentially premixed at the molecular level. The high temperatures sometimes associated with dual-source depositions can also be lowered and the precursor delivery is simplified by eliminating the need for multiple bubblers. Whilst single-source precursors themselves can be toxic and expensive, these issues can be addressed and avoided in the design stage of precursor development. The past 25 years has seen enormous interest in the development of single-source precursors for CVD and this application has driven considerable progress in organometallic and coordination chemistry resulting in the synthesis and characterisation of a vast number of novel complexes.

1.3.2 Single-Source Precursor Design

In order to achieve the effective deposition, precursors must satisfy a number of criteria, and thus careful and strategic molecular design is desirable. These requirements for the 'ideal' precursor are, in general, applicable to precursor design for any variant of the CVD process and have been laid out by Jones *et al*:[60, 86]

i) Adequate volatility to achieve acceptable film growth rates at moderate evaporation temperatures.
ii) Thermal stability to allow evaporation without decomposition
iii) A sufficiently large temperature ''window'' between evaporation and thermal decomposition.
iv) Clean decomposition without the incorporation of residual impurities.
v) Good compatibility with co-precursors during the growth of complex oxides.
vi) Long shelf-life, stable in solution for solution-based CVD applications.
vii) Readily manufactured in high yield at low cost.
viii) Non-hazardous or low hazard risk.

Points i) to iii) are relevant only for thermal CVD techniques, where deposition relies on transport of the precursor in the gas phase and hence on the volatility and decomposition characteristics of the precursor. For solution-based CVD processes, such as AACVD, solubility is the important characteristic with regard to the transport of the precursor to the reaction chamber. Clean decomposition of the

precursor is necessary for the formation of high quality films which are free from contamination. Choice of ligands is therefore important not only in achieving the desired thermal characteristics but also for offering clean decomposition pathways, such as β-hydride elimination. Fulfilling as many of the above criteria as possible is the goal of molecular precursor design. Unsurprisingly, the range of compounds which have been developed for application as molecular precursors to group 13 metal oxide and pnictide thin films is vast. The following section discusses some of the most effective and well-established precursors to these materials.

1.3.3 Single-Source Precursors to Group 13 Oxides and Pnictides

Group 13 Pnictides

Much of the pioneering work of single-source precursor chemistry was carried out by Cowley and Jones in the pursuit of more stable and less toxic precursors for the low-temperature deposition of GaAs[85] and their work is discussed briefly here as an illustration of the benefits of the single-source precursor approach. Traditional dual-source approaches to thin film deposition of GaAs relied on the thermal reaction of trialkyl gallium compounds with arsine at temperatures between 600 and 700 °C (Equation 1.1):[87]

$$Me_3Ga + AsH_3 \rightarrow GaAs + 3CH_4 \uparrow \qquad \textbf{(1.1)}$$

However, due to the pyrophoricity of $GaMe_3$ and the toxicity of AsH_3, this route is far from desirable. Initial attempts at the use of single-source precursors focussed on the use of the monomeric, dimeric and trimeric gallium arsenide species, shown in Figure 1.8. The trimer $[Me_2GaAs^iPr_2]_3$ was prepared by the alkane elimination reaction between $GaMe_3$ and $^iPrAsH_2$,[88] however, since alkane elimination becomes less efficient with the increasing steric demands of the substituents, $[R_2GaAs^tBu_2]_2$ and $[Ga(As^tBu_2)_3]$ were synthesised *via* a salt metathesis pathway.[89]

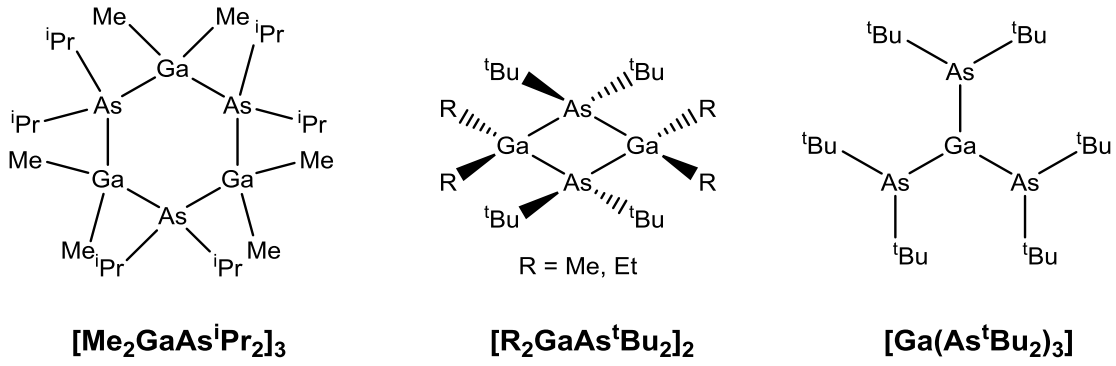

Figure 1.8 – Single-source GaAs precursors synthesised by Cowley et al.[85]

Depositions using these precursors were carried out using MOCVD and chemical beam epitaxy (CBE). Those carried out with $[Me_2GaAs^iPr_2]_3$ and similar trimeric species were found to give poor quality films, which was attributed to the elimination of tetraalkyldiarsines below 100 °C through pyrolysis studies.[85] However, good quality films of GaAs were deposited using both $[R_2GaAs^tBu_2]_2$ and $[Ga(As^tBu_2)_3]$, with the best films arising from CBE of the latter.[90-92] Deposition was achieved at 500 °C which represented a 200 °C decrease in deposition temperature compared with the MOCVD of $GaMe_3$ and AsH_3.

The precursor chemistry of group 13 pnictides, in particular arsenides and phosphides, has been dominated by this type of σ-bonded oligomeric species and has led to the deposition of a full range of III/V materials by CVD.[93]

Group 13 Oxides

Due to the major precursor requirements of volatility (thermal CVD) and solubility (solution-based CVD), much of the work on single-source precursors to group 13 oxides has focussed on the isolation of low mass, monomeric complexes containing pre-formed M-O bonds. The topic of precursors to group 13 oxide materials, in particular Ga_2O_3 and In_2O_3, has been the subject of detailed reviews with three main classes of compounds finding particular attention, namely monodentate alkoxides, donor-functionalised alkoxides and *β*-diketonates (Figure 1.9). [72, 86, 94]

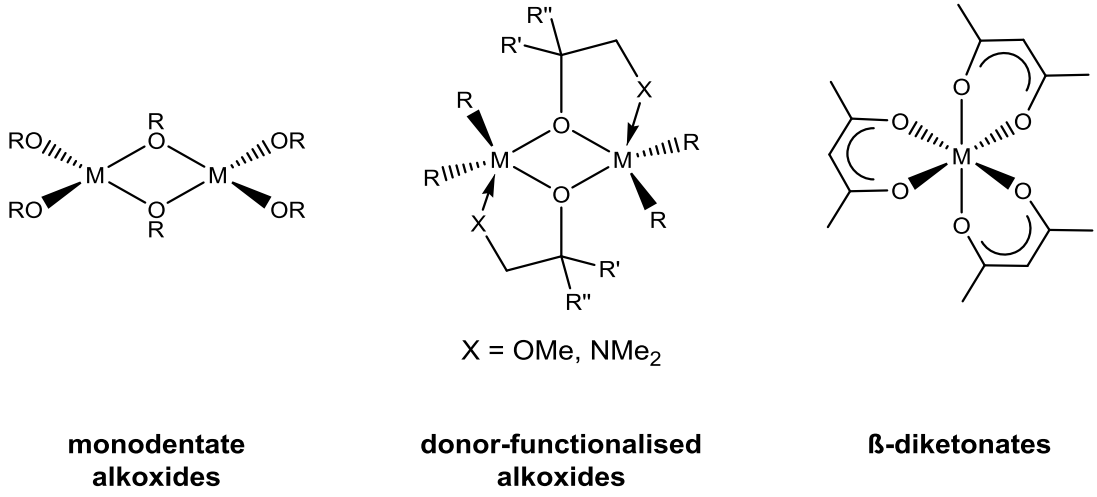

Figure 1.9 - Single-source precursors to group 13 oxide thin films.

Initial synthesis of simple gallium alkoxides was carried out by salt metathesis of $GaCl_3$ with sodium alkoxides NaOEt and NaO^iPr, leading to the corresponding alkoxides $[Ga(OR)_3]$.[94] However, the range of alkoxides was significantly expanded both through alcoholysis of these initial alkoxides, and through amide/alcohol exchange from the starting material $[Ga(NMe_2)_3]_2$.[95-97] Due to its commercial availability, $[Ga(O^iPr)_3]_n$ is a particularly attractive precursor and has been utilised in LPCVD[98] and sol-gel[99] processes for the deposition of Ga_2O_3. Other gallium alkoxides which have been employed in LPCVD include the dimer $[Ga(O^tBu)_3]_2$,[97] the monomeric amine adduct $[\{(CF_3)_2CHO\}_3Ga{\cdot}NHMe_2]$[96] and the tetrametric gallium alkoxide synthesised from $GaMe_3$ and 4-methylbenzyl alcohol, as shown in equation 1.2.[100] The tendency of these alkoxides to oligomerise through the formation of strong alkoxide bridges leads to a diverse array of structural types, often depending on the nature of the alkyl substituents. However, whilst low mass monomers are desirable, the above examples show that it is possible to isolate oligomers which display sufficient volatility for application as CVD precursors.

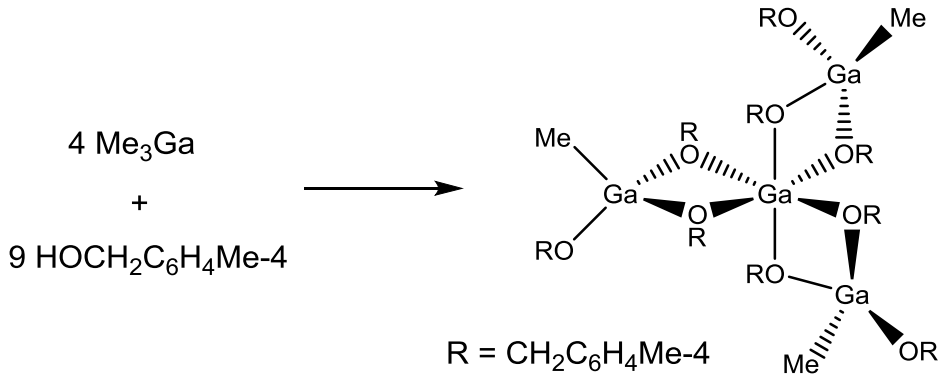

(1.2)

An analogous indium alkoxide was synthesised by the same method, as shown in equation 1.2, again yielding a tetrameric complex, though in this case the terminal indium atoms retain two methyl groups rather than one being replaced by alkoxide, as was seen for gallium. However, in this case LPCVD of In_2O_3 was unsuccessful due to the decomposition of the precursor prior to sublimation. A range of homoleptic indium alkoxide dimers of the form $[In(OR)_3]_2$ (R = ^{t}Bu, CMe_2Et, $CMeEt_2$, $CMe_2{}^i$Pr) were synthesised by Hoffman *et al*. by amide/alcohol exchange of the bulky indium amide $[In\{N^tBu(SiMe_3)\}_3]$.[101] Whilst these were used in the LPCVD of In_2O_3, an additional oxygen source was also used and thus the use of these alkoxides as true single-source precursors was not established.

The use of donor-functionalised alkoxides presents a means to limit oligomerisation by offering an additional donor atom from a substituent alkoxy or amino group, which can coordinate to the metal centre and occupy a coordination site. Furthermore, this additional coordination can help to stabilise alkoxide complexes making them easier to handle and more suitable for scale up. A range of such gallium and indium donor-functionalised alkoxides have been synthesised by Carmalt *et al.* and Chi *et al.* and used in both LP and AACVD processes for the deposition of group 13 oxide thin films.[102-106] Of particular note is the *in situ* precursor formation made possible by the solution-based AACVD process, eliminating the need for prior isolation and purification of the precursor.

The *β*-diketonates are another important class of molecular precursors to thin films of gallium and indium oxide, with the greatest amount of attention being paid to the commercially available acetylacetonate derivatives $[Ga(acac)_3]$ and $[In(acac)_3]$. The first deposition of In_2O_3 from $[In(acac)_3]$ was by LPCVD onto a range of substrates at a range of deposition temperatures.[107] A mixture of amorphous and crystalline

films were produced, with the temperatures required for the production of crystalline In_2O_3 depending largely on the substrate being used. Later studies detailing the APCVD of [In(acac)$_3$] at temperatures ranging from 350 to 500 °C showed the formation of polycrystalline In_2O_3 in all cases.[108] [Ga(acac)$_3$] was first used as a single-source precursor to Ga_2O_3 by spray pyrolysis at relatively low temperatures (<500 °C), however, as expected for Ga_2O_3 at this temperature, the resulting films were amorphous and required an additional annealing step to yield the crystalline material.[109, 110] [Ga(acac)$_3$] has also been employed in a supercritical fluid deposition process using supercritical CO_2 as a medium and whilst this enabled the deposition of films at very low temperatures (decomposition was initialised at 160 °C) the resulting films showed high carbon contamination.[111] The fluorinated analogue [Ga(hfac)$_3$] (Hfac = 1,1,1,5,5,5-hexafluoroacetylacetone) shows improved volatility over the acac derivative and has been shown to be effective towards the deposition of Ga_2O_3 by LPCVD.[112, 113]

1.4 Outlook and Project Aims

As has been demonstrated, the single-source approach to the deposition of thin film materials is highly attractive. The aim of this thesis is to explore further the single-source precursor approach to the deposition group 13 oxide and pnictide materials. Two main areas of research will be discussed:

i) Group 13 metal β-ketoiminate complexes as precursors to the deposition of metal oxides.

While at present the single-source approach to the CVD of main-group metal oxides relies largely on alkoxide and *β*-diketonate compounds, amines have been investigated as versatile alternatives. However, their application has been hindered by variable and less than optimum vapour pressures. The use of β-ketoimines, of general form RC(O)CHC(R′)NHR″ (Figure 1.10), provides a potential solution to this issue.

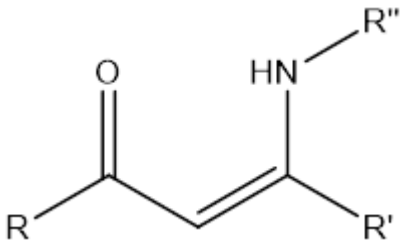

Figure 1.10 - Generic chemical structure of β-ketoimines.

Careful choice of substituents in the R positions, in particular functionalisation of the imino residue, can be used to enable tailoring of the thermal properties of the corresponding main group metal compounds. For example, inclusion of a bulky, aryl substituent can sterically hinder the formation of oligomers. Similarly, substitution with a pendant "arm" containing additional donor atoms, for example an amine group, offers an appendage point for additional intramolecular coordination/saturation of a metal centre, creating a tri-, or even tetradentate system. Small alterations to the ligand system, therefore, can enable tailoring of the coordinative saturation, thermal stability and volatility of the metal complex.

Given this potential versatility as a ligand system and the extensive amount of research that has been carried out on the structurally similar *β*-diketonates and *β*-diketiminates, the relatively small amount of attention that *β*-ketoimines and their main group metal complexes have been afforded is surprising. Simple *β*-ketoimines can be easily synthesised by the condensation reaction between the relevant *β*-diketonate and amine, a reaction which occurs in high yield.

The research in this area is divided into two chapters, one detailing the synthesis of a range of group 13 *β*-ketoiminate complexes and the other exploring their efficacy as molecular precursors to metal oxide thin films.

ii) The AACVD of InAs thin films from single-source organometallic indium arsenide precursors.

The fabrication of III/V semiconductors has been heavily researched over the last three decades owing to the huge technological significance of the applications, with considerable attention being directed towards the development of single-source precursors for the deposition of these materials, in particular gallium arsenide. The single-source deposition of indium arsenide, however, has received notably less attention and no reports exist on the deposition of this material by AACVD. Recent

research by Sathasivam *et al.* has demonstrated the first deposition of GaAs by AACVD, resulting in the production of high quality thin films suitable for application in photovoltaic devices.[114] The aim of this research is to extend the idea to the deposition of InAs, with a view to developing a compatible deposition system to allow the fabrication of mixed-metal $Ga_xIn_{1-x}As$ materials.

The research will be described in a single chapter, detailing the development of a single-source precursor system and subsequently exploring its use in the deposition of InAs by AACVD.

Chapter 2

The Synthesis and Characterisation of Group 13 Metal β-ketoiminates

The following chapter includes a summary of existing literature on the synthesis of group 13 β-ketoiminate complexes and goes on to describe the synthesis of a range of novel group 13 metal β-ketoiminate complexes with a variety of co-ligands, namely chlorides, methyls and hydrides. Characterisation has been carried out using common spectroscopic and analytical techniques, such as ^{1}H & ^{13}C NMR, mass spectrometry and elemental analysis. A number of the complexes have been structurally characterised using crystallographic methods and their molecular structures are discussed. Experimental details of the synthesis of the group 13 metal β-ketoiminate complexes are outlined at the end of the chapter.

2 The Synthesis and Characterisation of Group 13 Metal β-ketoiminates

2.1 Introduction

2.1.1 *β*-ketoimine Complexes of Main Group Metals

The majority of examples of main group metal β-ketoiminate complexes employ one of two types of N-substituents on the imino residue – bulky aryl groups which prevent oligomerisation by steric repulsion and pendant 'arms' containing additional donor atoms, able to occupy coordination sites on the metal centre, again preventing molecular oligomerisation.

Lesikar *et al.* compared the coordination preference of two different β-ketoiminate ligands – the bulky $\mathbf{L^A}$ versus the less bulky, multidentate $\mathbf{L^B}$ – with both indium and antimony. Reaction of the free ligand with ^{n}BuLi formed the lithium salt, which was then added rapidly to a stirring suspension of MCl_3 (M = In, Sb) in THF, affording products **1 - 4** (Scheme 2.1).[115]

The variation in the reactivity of the two ligands with $InCl_3$ was attributed in part to the formation of the preferred trigonal bipyramidal geometry of the indium atom. In **1** this geometry was achieved by bidentate coordination of two ligands, whilst in **2** the coordinating 'arm' is able to occupy a coordination site, preventing further ligand association and achieving a 5-coordinate trigonal bipyramidal geometry without loss of a second chloride. Whilst the reaction of L^BLi with $SbCl_3$ afforded the desired 5-coordinate antimony complex, reaction with L^ALi produced only **3** in low yield (a higher yield of the same product was achieved by reaction of $SbCl_3$ with the free ligand L^AH).

Since this project started, the synthesis of aluminium complexes analogous to **2** and **4** have also been reported. The reaction of $AlMe_2Cl$ with L^BH afforded the five-coordinate aluminium complexes $[L^BAl(Me)X]$, where X is either an additional methyl group, or displays mixed occupancy between methyl and chloride (Me: *ca.* 70%, Cl: *ca.* 30%), depending on the reaction conditions employed.[116] The dichloro derivative $[L^BAlCl_2]$ was also synthesised by reaction of L^BLi with $AlCl_3$, with crystallographic analysis revealing a trigonal bipyramidal geometry around the aluminium metal centre.[117] The formation of mono-ligated products shows the ability

of these tridentate ligand systems to protect the metal centre from further ligand attack.

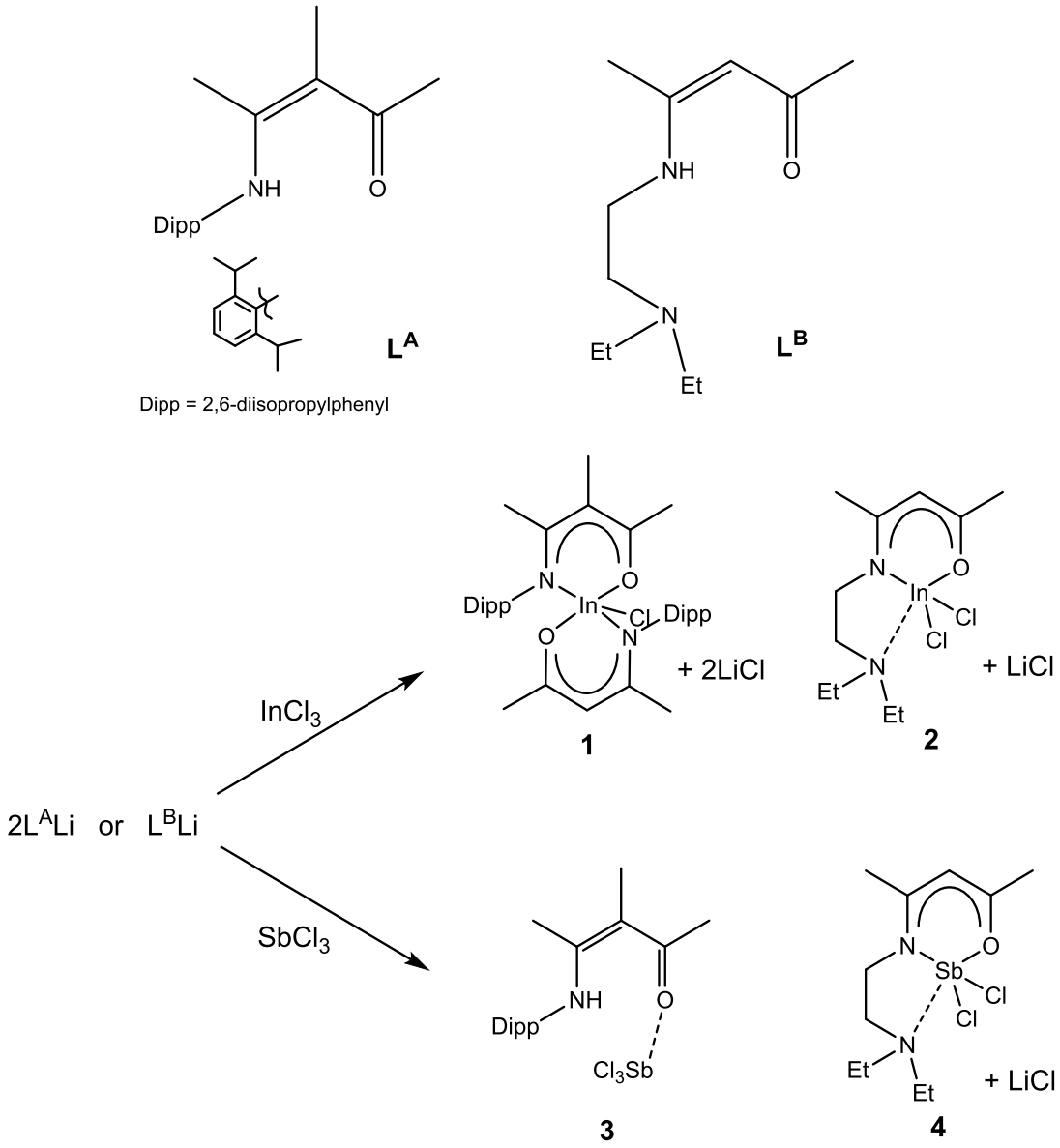

*Scheme 2.1 – The synthesis of β-ketoiminate complexes of indium (**1** and **2**) and antimony (**3** and **4**).*

This work was also extended to further group 13 elements.[116] Reaction of boron trifluoride-diethyl ether with DmpL^{A}Li (dmp = dimethylphenyl) gave rise to the six-membered ring **5** (Equation 2.1). Whist both 1:1 and 1:2 (boron to ligand) reactions yielded the same product (as shown by ^{11}B NMR), a threefold excess of the ligand

lithium salt was required to optimise isolation of crystals of **5**. A series of related difluoroboron ketoiminate complexes have also been previously synthesised by a similar method, using a range of different substituents in order to assess the structural, electrochemical and photophysical impact of altering these substituents.[118]

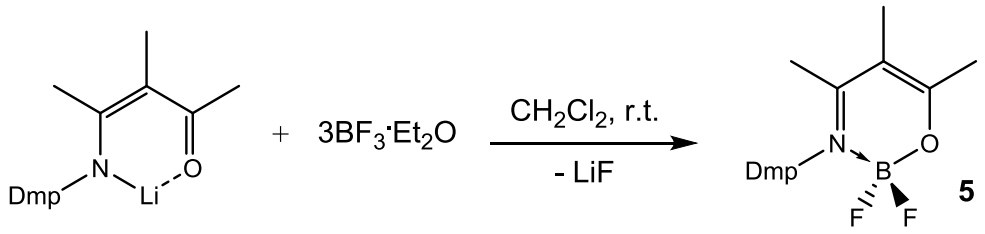

(2.1)

Whilst the difluoroboron reaction yielded the expected chelate compound, similar reactions with $GaCl_3$ and $InMe_3$ showed different results. Instead of the expected salt metathesis reaction, the reaction of $GaCl_3$ with L^ALi produced the ligand-metal halide adduct **6** in low yield, similar to that seen previously with $SbCl_3$ (Equation 2.2). It is noted that in light of the low yield (20%) of crystalline material, **6** is likely to be the minor product in the reaction, with the expected $[L^AGaCl_2]$ the major. This postulation is based on ^1H NMR of the crude reaction product showing a mixture of products, suggesting the desired compound was in fact produced, but the ligand-metal halide adduct was isolated due to its preferential crystallisation.

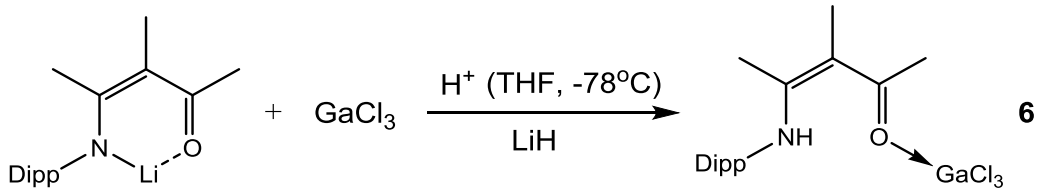

(2.2)

The ligand L^A was successfully employed in the formation of two lithium chloride cages by reaction of the lithium salt with trimethyl indium, which itself was formed *in situ* from $InCl_3$ and MeLi. However, attempts to form similar lithium chloride cages by use of L^B instead afforded the five-coordinate indium complex **7** (Scheme 2.2).

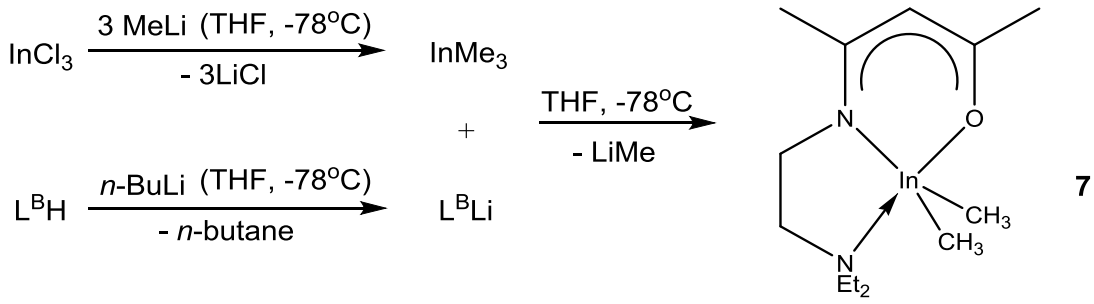

Scheme 2.2 – The synthesis of donor-functionalised β-ketoiminate dimethyl indium complex ***7****.*

Compound **7** structurally resembles the previously reported [$InMe_2$(ketoiminate)] complex, which contains fluorinated methyl groups on the ketoiminate backbone.[119] This fluorinated complex was successfully used for the deposition of In_2O_3 thin films by MOCVD with low level of nitrogen and fluorine incorporation, confirming the effective elimination of the ketoiminate ligand. In addition, the thermal stability of the ketoiminate complex was found to be considerably better upon heating to 300 °C than that of similar aminoalkoxide complexes (of the general form $HOC(CF_3)_2CH_2NHR$, where R = $(CH_2)_2OMe$, Me, ^tBu), an observation attributed to the saturated five-coordinate environment of the ketoiminate complex as opposed to the dimeric structures containing In_2O_2 rings seen for the aminoalkoxides.

There are a number of examples in the literature describing the use of aryl-substituted ketoimines as ligands to stabilise the corresponding main-group metal complexes. Huang *et al*. have employed the same diisopropylphenyl (dipp) substituted ligand as mentioned previously in the formation of a number of four- and five-coordinate aluminium chloride, alkyl[120] and hydride[121] complexes, as shown in Scheme 2.3. The facile reaction between the β-ketoimine ligand and one equivalent of trimethyl- and triethylaluminium yielded **8** and **9**, respectively, in high yield. The formation of **10** and **11** by reaction of trialkylaluminium and ketoimine in 1:2 ratio, required more forcing conditions (refluxing for 3 days in toluene) due to the greater steric hindrance of the complexes. The analogous chloride complexes **12** and **13** were also formed in high yield by reaction of 1 or 2 equivalents of lithiated ketoiminate with aluminium trichloride. Similarly, the hydride complex **14** was formed in the reaction of ketoimine with $LiAlH_4$, again in high yield. The above compounds were made for use in catalysis, since they contain metal atoms surrounded by bulky substituents on one side but left open on the other, thus making

them effective for such applications. Indeed the referenced studies above showed compounds **8** – **13** to be catalytically active towards ring-opening polymerisation reactions, whilst **14** was used successfully in the hydroalumination of carbon dioxide, carbon disulphide and phenyl isocyanate.

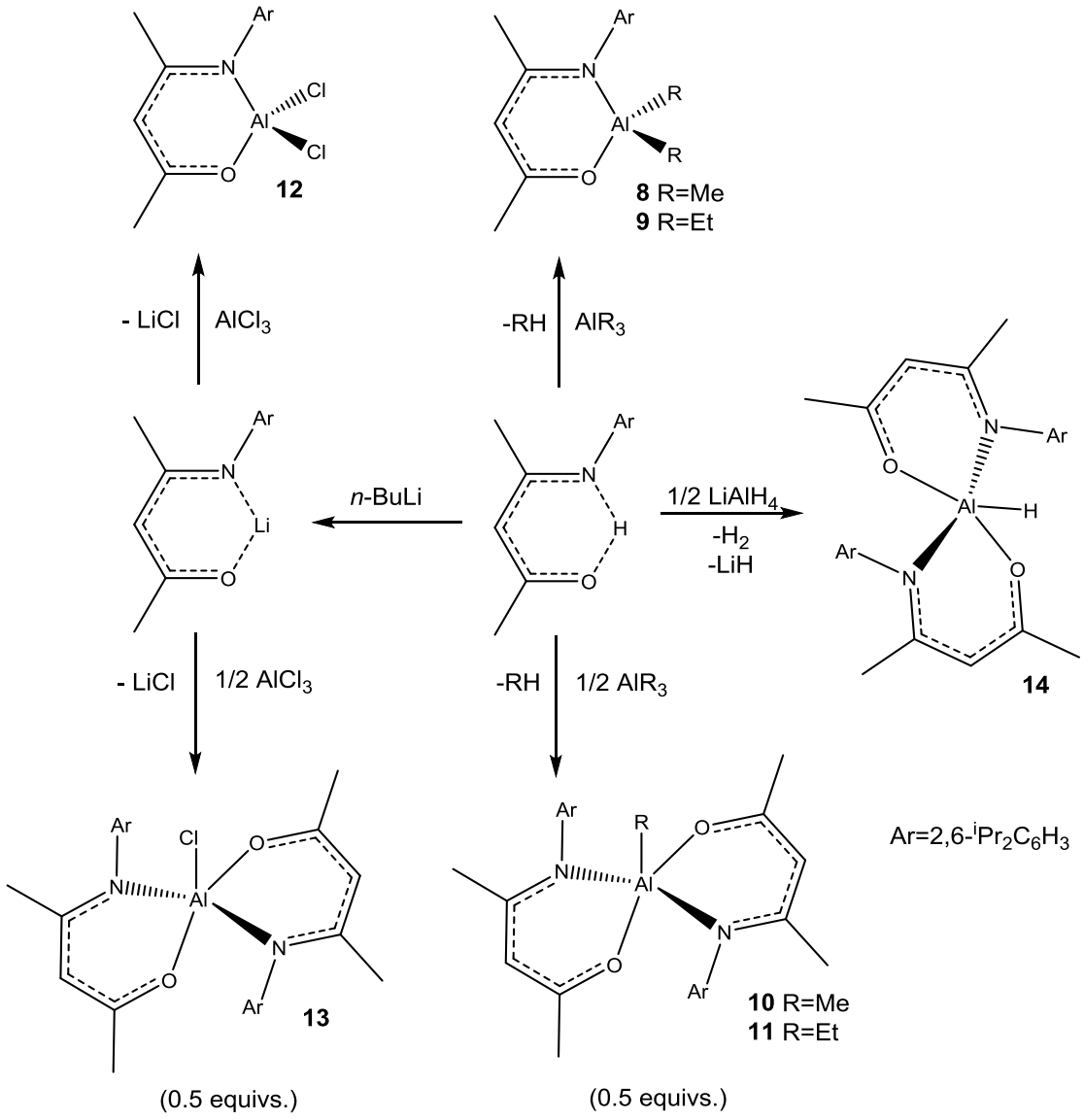

Scheme 2.3 - A range of four- and five-coordinate aluminium complexes based on bulky diisopropylphenyl ketoiminate ligands.

In an attempt to form the equivalent 1:1 and 1:2 complexes by use of a fluorinated aryl substituent (i.e. Ar = *p*-fluorophenyl), it was found that both salt elimination (i) and methane elimination (ii) gave the same five-coordinate complex **15** (Equation 2.3).[122] It is interesting to note the difference in yields from the two methods (i: 2%;

ii: 33%) and the relatively low amount of both in comparison to the series of complexes formed by use of diisopropylphenyl-substituted ketoimine.

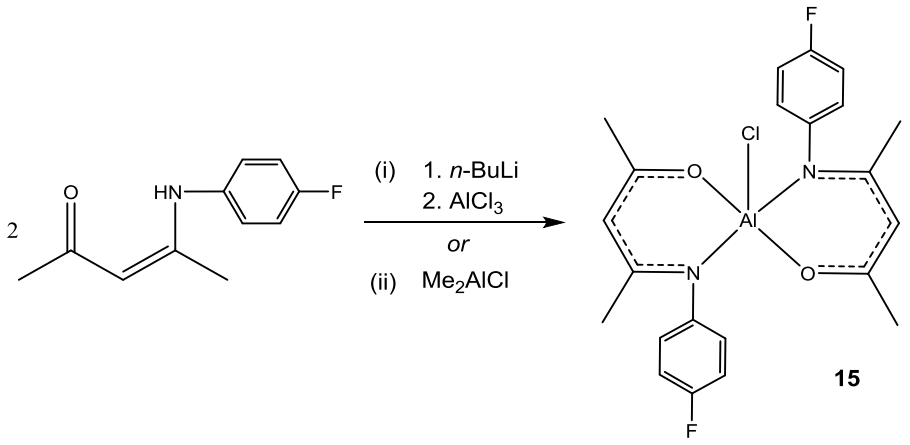

(2.3)

The use of the bulky diisopropylphenyl substituted ligand was further extended to the formation of both Sn(II) and Sn(IV) ketoiminate complexes **16-18**,[123] as shown in Scheme 2.4.

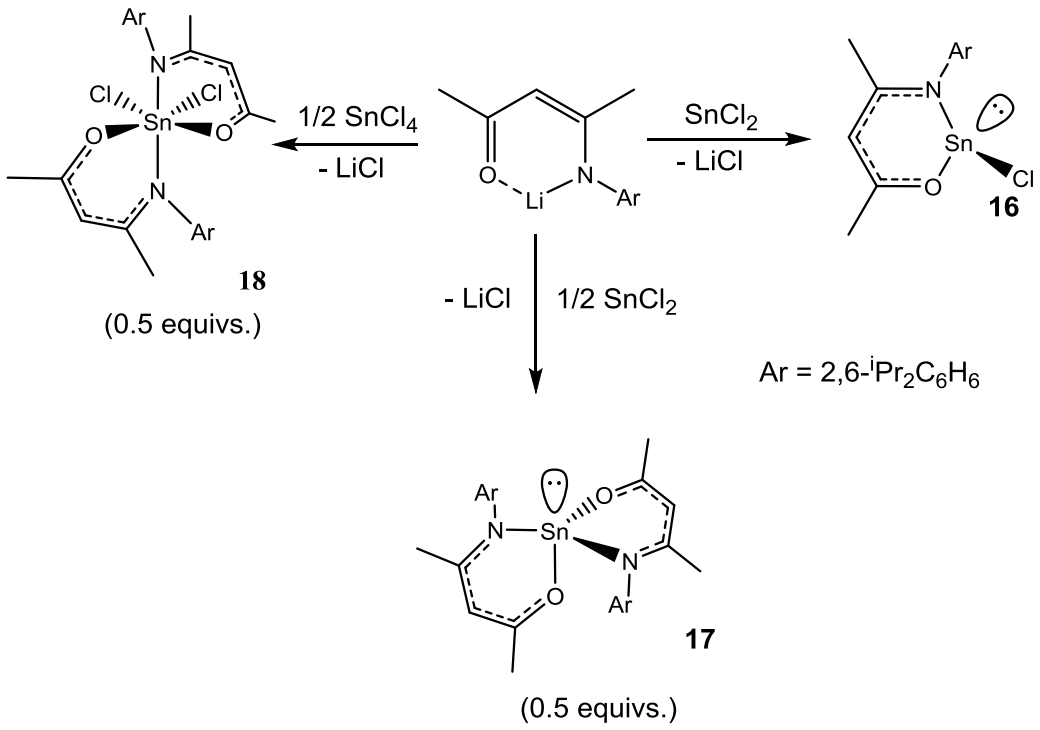

*Scheme 2.4 – The synthesis of tin β-ketoiminate complexes **16** – **18**.*

Three-coordinate **16** has a distorted tetrahedral geometry with a lone pair of electrons occupying one apical position. Similarly, the geometry of **17** can be described as distorted trigonal bipyramidal with one equatorial position being occupied by a lone pair of electrons. The distortion in these geometries arises from the electronic

repulsions between lone pair and bonding electrons, resulting in decreased bond angles around the tin atom. Six-coordinate compound **18** shows distorted octahedral geometry, the two oxygen atoms being *trans* to the two chlorine atoms, and the two nitrogen atoms being *trans* to each other. The above tin complexes were synthesised with a view to their application in lactone and lactide polymerisation reactions, though no further work has to date been reported.

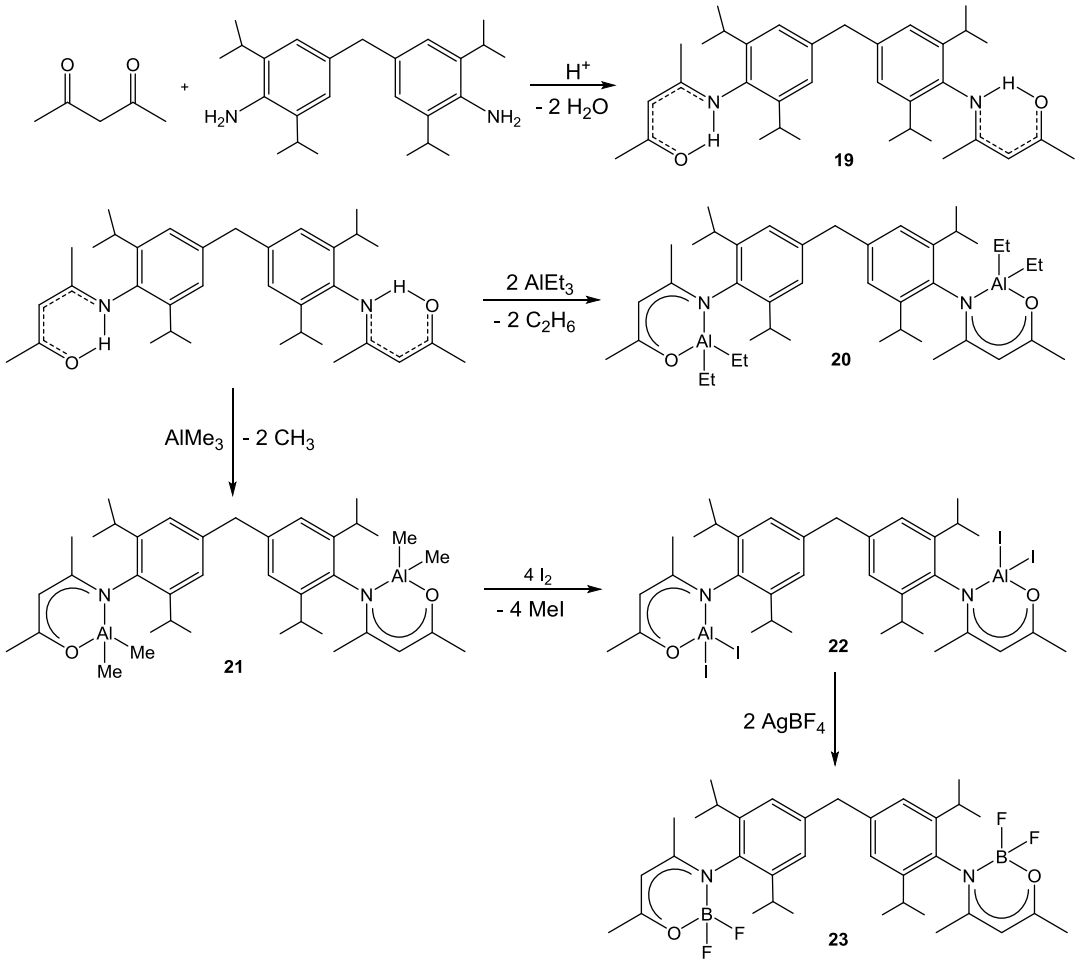

*Scheme 2.5 – The synthesis of bis-β-ketoimine **19** and its aluminium and boron complexes **20** – **23**.*

The use of linked bis-*β*-ketoiminate ligands with group 13 metals has been investigated only briefly. Reaction of acetylacetone with an appropriate diamine results in the formation of ligands capable of binding to a metal centre in a tetradentate manner. Huang *et al*. have investigated some dinuclear metal complexes with bis-multidentate ligands because of their potential use as two-centre Lewis acid catalysts.[124] Reaction of acetylacetone with the bulky amine 4,4'-methylene-bis(diisopropylaniline) yielded the bis(ketoimine) ligand **19** in high yield and purity.

Subsequent reactions afforded dinuclear aluminium and boron complexes as shown in Scheme 2.5.

The dinuclear boron complex **23** was formed as an unexpected product in an attempt to form a cationic aluminium centre by removal of iodide from complex **22**. The formation of a mononuclear complex was not possible due to the bulk of the linking group. However, later work using 1,2-diaminocyclohexane as the amine in the ligand formation reaction showed some different results (Scheme 2.6).[125] Both *cis*- and *trans*-isomers of the *β*-ketoimine **24** were initially formed and were subsequently separated by fractional recrystallisation. Dinuclear complexes were again formed using the *trans*-isomer due to the relative geometry of the two ketoimine groups. However, reaction of the *cis*-isomer with $AlMe_3$ yielded the five-coordinate monomer **26**. A mononuclear complex of the *trans*-isomer could only be formed under harsh conditions (reflux at 110 °C for 96 hours). The formation of these compounds displays the versatile coordination modes of the linked bis-β-ketoiminate ligands with metal centres.

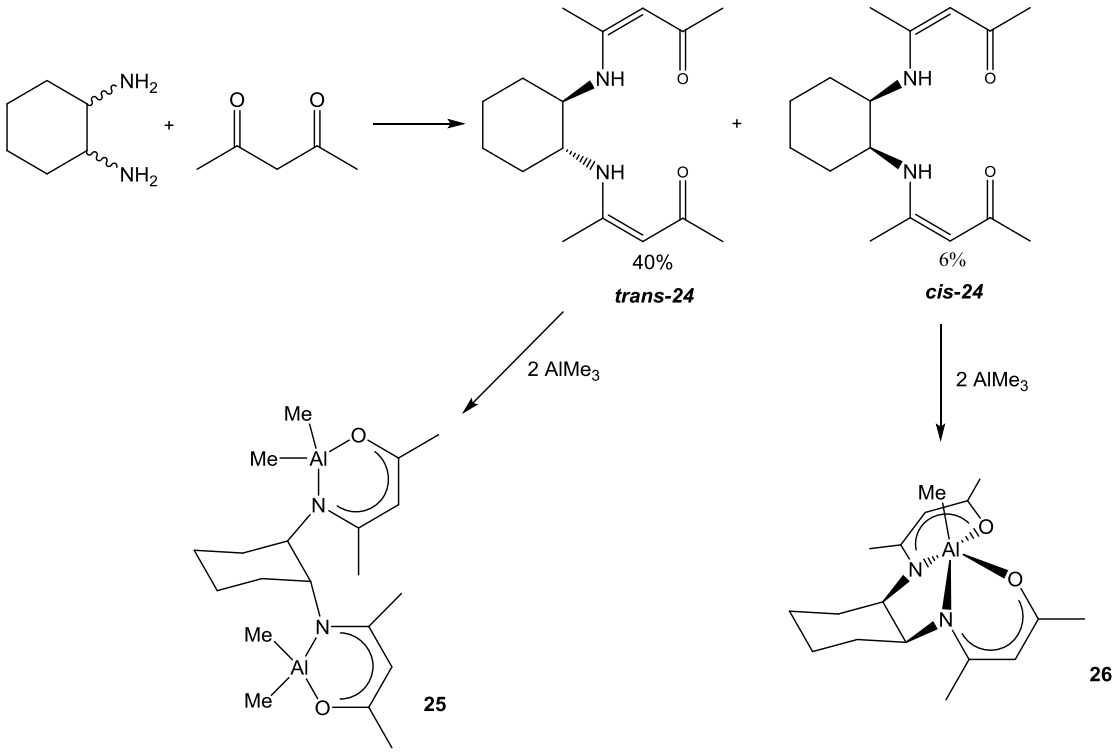

*Scheme 2.6 – The synthesis of cyclohexyl-bridged bis-β-ketoiminate aluminium complexes **24** – **26**.*

The linked-β-ketoimine concept was extended to gallium complexes by use of the tetradentate N,N'-ethylenebis(4-aminopent-3-en-2-one) ligand in the formation of the five-coordinate gallium chloride complex **27** (Equation 2.4).[126] The gallium

complex was formed by simple salt metathesis of the corresponding β-ketoiminate sodium salt with gallium trichloride and purified by recrystallisation *via* sublimation of the crude product, yielding yellow crystals. Crystal structure analysis of the complex revealed a five-coordinate gallium centre in a distorted square pyramidal geometry, though the distortion with a single N_2O_2 four-coordinate ligand is less than found in systems where the ligands are able to move more freely. The complex was made with a view to application as single-source precursors for oxynitride films and nanostructured materials, though no further work using the complex has been reported.

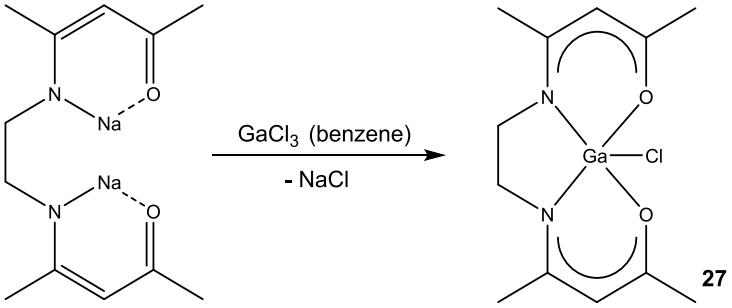

(2.4)

While the number of examples of main group metal β-ketoiminate complexes is relatively limited, those known highlight the great versatility of these ligands towards forming a range of complexes with varying coordination numbers and modes. The potential for manipulation of physical and thermal properties by careful selection of appropriate substituents, particularly of the imino residue, makes the *β*-ketoimines a highly attractive class of ligands for the design of main-group complexes for application in both catalysis and CVD.

2.1.2 The stabilisation of gallium hydrides

Within the design of single-source precursors, the selection of any co-ligand is of great importance to the efficacy of the precursor for the deposition of high quality materials. Hydrides are an attractive class of compound for application as molecular precursors, with advantages including; (i) low molecular masses, (ii) potentially clean decomposition pathways due to the weakness of the Ga-H bond, (iii) ready M-H bond cleavage with respect to M-C and (iv) low levels of carbon contamination within deposited films as a result of the absence of direct metal-carbon bonds within the precursor.[127, 128] Whilst examples of aluminium hydrides are abundant in

literature, isolation and characterisation of hydride derivatives of the heavier group 13 metals (Ga, In, Tl) has been limited by the air/moisture sensitivity and thermal instability of these compounds. The susceptibility of M—H units to oxidation or hydrolysis demands rigorous control of experimental conditions and in some cases the design of all-glass apparatus and special procedures.[129, 130] However, despite the difficulty in synthesis, the past 20 years has seen significant advancement in the development of group 13 hydride derivatives, in particular those of gallium. The focus of the synthetic hydride chemistry within this thesis is on the formation of novel gallium hydride complexes, thus the following discussion will concentrate on the literature relating to gallium hydride derivatives. The topic has been reviewed by Raston *et al.*[128, 131, 132] and Downs *et al.*[130, 133] up to 2001 and herein the literature is summarised with particular attention paid to developments made within the intervening period.

Neutral Adducts of Gallane

One of the most significant areas of interest has been in the stabilisation of gallane *via* adduct formation. Gallane itself ($[GaH_2(\mu\text{-}H)]_2$) is extremely thermally unstable, decomposing to metallic gallium and hydrogen at temperatures above *ca.* 240 K.[129] Stabilisation of the binary hydrides by chemical trapping or protection of reactive fragments can be achieved by electronic or steric means or a combination of the two, with a significant amount of research having been put into the formation of thermally stable adducts of gallane. The simple trimethylamine adduct of gallane ($[H_3Ga(NMe_3)]$), first reported by Greenwood *et al.* in 1963,[134] shows greater thermal robustness and thus presents itself as a more tactile precursor to reactivity studies with gallane than the binary hydride itself.[135] The use of strong Lewis bases is necessary for the formation of room temperature-stable gallane adducts, falling into three main categories: (i) nitrogen donors, (ii) bulky trialkylphosphines and (iii) N-heterocyclic carbenes (Figure 2.1, Table 2.1, page 34).

Table 2.1 lists the reported examples of adduct-stabilised gallanes and comments on their relative stability. As mentioned, the stability of gallane can be significantly improved by formation of the simple trimethylamine adduct, offering a means to explore the further reactivity. This increased stability arises from primary decomposition process for adduct complexes of GaH_3, which is the loss of the Lewis base.[128] A number of other simple amine adducts have been formed, displaying

similar stabilities between 0 °C and room temperature, for example the dimethylbenzylamine adduct **39** and the bimetallic tetramethyl ethylenediamine (TMEDA) adduct **43**.[135, 136]

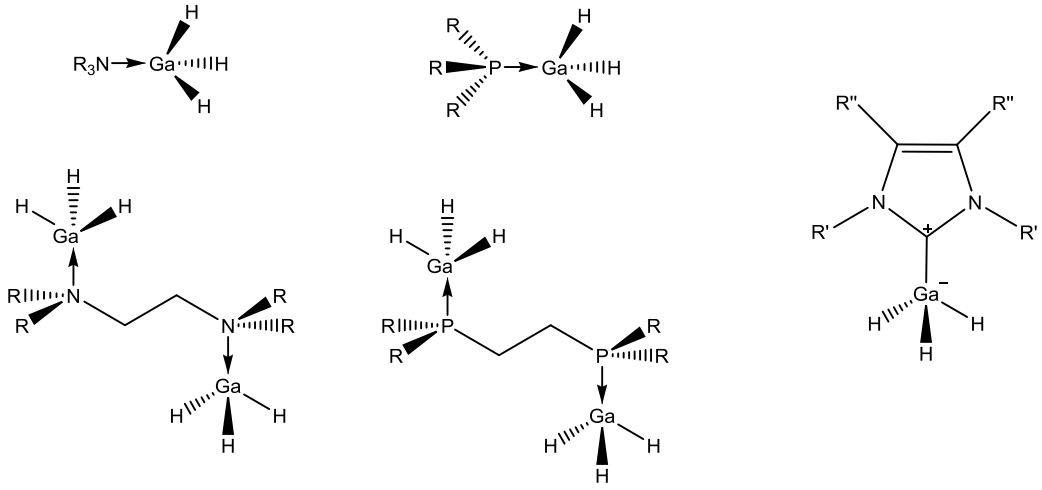

(a) GaH_3/nitrogen donors **(b) GaH_3/phosphorus donors** **(c) GaH_3/N-heterocyclic carbenes**

Figure 2.1 - General structures of gallane adducts stabilised by (a) nitrogen donors; (b) phosphorus donors; and (c) N-heterocyclic carbenes.

Table 2.1 - List of reported neutral adducts of gallane and their relative thermal stabilities. The table presented herein builds on Ref. 133, with decomposition temperatures/relative stability included.

Adduct	Comp. no.	Decomposition temperature (° C) / relative stability	Ref.
Nitrogen donors			
$[H_3Ga{\cdot}NMe_3]$	**28**	> 0	134, 135, 142
$[H_3Ga{\cdot}NEt_3]$	**29**	< $[H_3Ga{\cdot}NC_5H_5]$	143
$[H_3Ga{\cdot}NMe_2H]$	**30**	not long-term	144
$[H_3Ga{\cdot}NMe_2H]_2$	**31**	> - 10	145
$[H_3Ga{\cdot}NEt_2H]$	**32**	< $[H_3Ga{\cdot}NMe_2H]$	143
$[H_3Ga{\cdot}NEt_2Me]$	**33**	light sensitive	143
$[H_3Ga{\cdot}NEtMe_2]$	**34**	unstable at r.t.	143
$[H_3Ga{\cdot}NC_5H_5]$	**35**	< $[H_3Ga{\cdot}NMe_3]$	143
$[H_3Ga{\cdot}\overline{N(Me)CH_2CH_2N(Me)CH_2}CH_2{\cdot}GaH_3$	**36**	unstable at r.t.	143
$[H_3Ga{\cdot}NPh_3]$	**37**	≤ $[H_3Ga{\cdot}NMe_2Ph]$	143

$[H_3Ga{\cdot}NMe_2Ph]$	**38**	< $[H_3Ga{\cdot}NEt_3]$	143
$[H_3Ga{\cdot}NMe_2CH_2Ph]$	**39**	≈ $H_3Ga{\cdot}NMe_3$	135
$[H_3Ga{\cdot}$quinuclidine$]$	**40**	> 100	136
$[H_3Ga{\cdot}Me_2NCH_2NMe_2]$	**41**	not long term	143
$[H_3Ga{\cdot}Me_2NCH_2CH_2NMe_2]$	**42**	unstable at r.t.	136
$[H_3Ga{\cdot}Me_2NCH_2CH_2NMe_2{\cdot}GaH_3]$	**43**	> 20	136
$[H_3Ga{\cdot}Me_2NCH_2CH_2CH_2NMe_2]$	**44**	loss of amine *in vacuo*	143
$[H_3Ga{\cdot}Me_2NCH_2CH_2CH_2NMe_2{\cdot}GaH_3]$	**45**	not long term	143
$[H_3Ga{\cdot}Me_2NCH_2CH_2CH_2NMe_2]_\infty$	**46**	not given	143
$[H_3Ga{\cdot}N(H)C(NMe_2)_2]$	**47**	> 57	137

Phosphorus donors

$[H_3Ga{\cdot}PMe_3]$	**48**	> 77	146, 147
$[H_3Ga{\cdot}PPh_3]$	**49**	> 20	146, 147
$[H_3Ga{\cdot}PCy_2H]$*	**50**	not long term	148
$[H_3Ga{\cdot}PCy_3]$*	**51**	> 130	146
$[H_3Ga{\cdot}P^tBu_3]$	**52**	> 114	149
$[H_3Ga{\cdot}Me_2PCH_2CH_2PMe_2{\cdot}GaH_3]$	**53**	> 100	146, 150
$[H_3Ga{\cdot}^iPr_2PCH_2CH_2P^iPr_2{\cdot}GaH_3]$	**54**	> 130	149
$[H_3Ga{\cdot}Ph_2PCH_2CH_2PPh_2{\cdot}GaH_3]$	**55**	> 0	149

*Cy = cyclohexyl, C_6H_{11}

N-heterocyclic carbenes

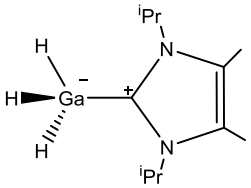	**56**	> 180	151
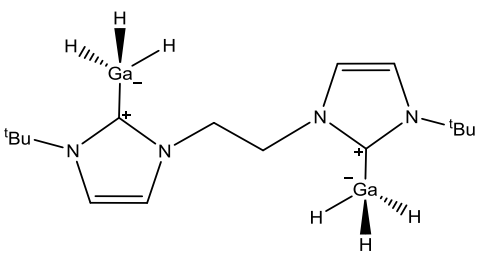	**57**	> 168	152

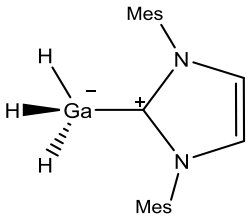	**58**	> 214	140
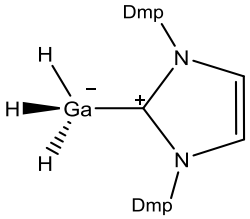	**59**	> 186	153
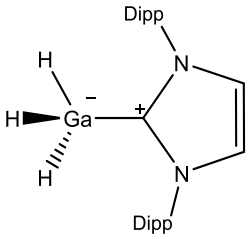	**60**	> 166	153

[ǂ] Mes = $C_6H_2Me_3$-2,4,6; Dmp = $C_6H_3Me_2$-2,6; Dipp = $C_6H_3{}^{i}Pr_2$-2,6

The most stable nitrogen-donor adducts were formed by utilisation of strong bases such as guanidine (**47**) and quinuclidine (**40**), which decompose at temperatures in excess of 57 °C and 100 °C, respectively.[136, 137] The high Lewis basicity of guanidine and quinuclidine, as represented by the pK_a values of their conjugate acids (13.6 and 11.0, respectively, in aqueous solution),[138] clearly shows the importance of the electronic contribution for the stabilisation of these adducts. However, the lower pK_a of quinuclidine (compared to that of guanidine), coupled with the greater stability of the corresponding gallane adduct over the guanidine analogue, implies that steric factors also have significant involvement.

The phosphine adducts in general show much greater stability than the amine analogues, suggesting a stronger Ga-P interaction than observed for Ga-N. Molecular orbital theory would suggest that this stronger interaction is a result of the closer matching of orbital energies between Ga and P compared to those between Ga and N, leading to better orbital overlap and stronger bonding. The relative stability observed between the phosphine adducts themselves can again be attributed to a combination of bulk and basicity. For instance, the stabilities of the triphenyl,

trimethyl and tricyclohexyl phosphine adducts lie in the order $Ph_3P < Me_3P < Cy_3P$, mirroring their pK_a values of 2.73, 8.65 and 9.70, respectively.[139] However, by far the greatest observed stabilities of gallane adducts have been achieved by the use of *N*-heterocyclic carbenes as the stabilising Lewis bases, with decomposition temperatures as high as 214 °C being achieved.[140] This trend is unsurprising given the much higher pK_a values generally displayed by *N*-heterocyclic carbenes (*ca.* 20 – 25) and their significant steric bulk .[141]

Gallium Hydrides Incorporating Ga-O bonds

Mixed hydride species which incorporate other elements bound to the metal are a potentially useful class of compound for use as single-source precursors for the CVD of metal oxides. Of specific interest for this project are those containing bonds to oxygen. Whilst the hydrides will be readily and cleanly lost under thermal decomposition, the strong, inherent M-O bond(s) can stay intact allowing for the formation of the metal oxide material. These types of compounds have generally been synthesised through reaction of gallane with primary alcohols forming species of the type $[H_{3-x}Ga(OR)_x]$ and generally overcome the implied reduction in coordination number at the metal centre by oligomerisation.[133]

Examples of such oxygen-containing mixed hydride species are reasonably scarce (Scheme 2.7). All of the compounds **61 – 65** contain Ga_2O_2 ring units, with two gallium centres bridged by alkoxy groups. The compounds **61** and **62** were synthesised by alcoholysis of freshly prepared ethereal solutions of gallane with precise control over the stoichiometry being necessary for the formation of the correct products.[154] The same was not true, however, in the synthesis of **63**, which was the exclusive product regardless of whether an excess of hydride or ketone was used.[155] It was noted that the inability of hydrido group to reduce additional ketone molecules is likely to be due to the bulk of the alkoxy groups in **63**, as well as the bulk of the ketone itself.

Compounds **64** and **65** were formed by the reaction of $[H_3Ga(NMe_3)]$ with the *bi*- and *tri*-dentate donor-functionalised alcohols $Me_2NCH_2CH_2OH$ and $MeN(CH_2CH_2OH)_2$, respectively.[156] These two complexes represent the only previous examples of the synthesis of precursors based on gallium hydrides for CVD and both were successfully used for the deposition of Ga_2O_3 by AACVD.

Having discussed the literature relating to both the synthesis of main group metal *β*-ketoiminate complexes and the stabilisation of gallium hydrides, in particular those containing preformed Ga-O bonds, the following sections will detail the development of a new class of bis-*β*-ketoiminate ligand and application of this ligand class in the synthesis of a range of group 13 complexes.

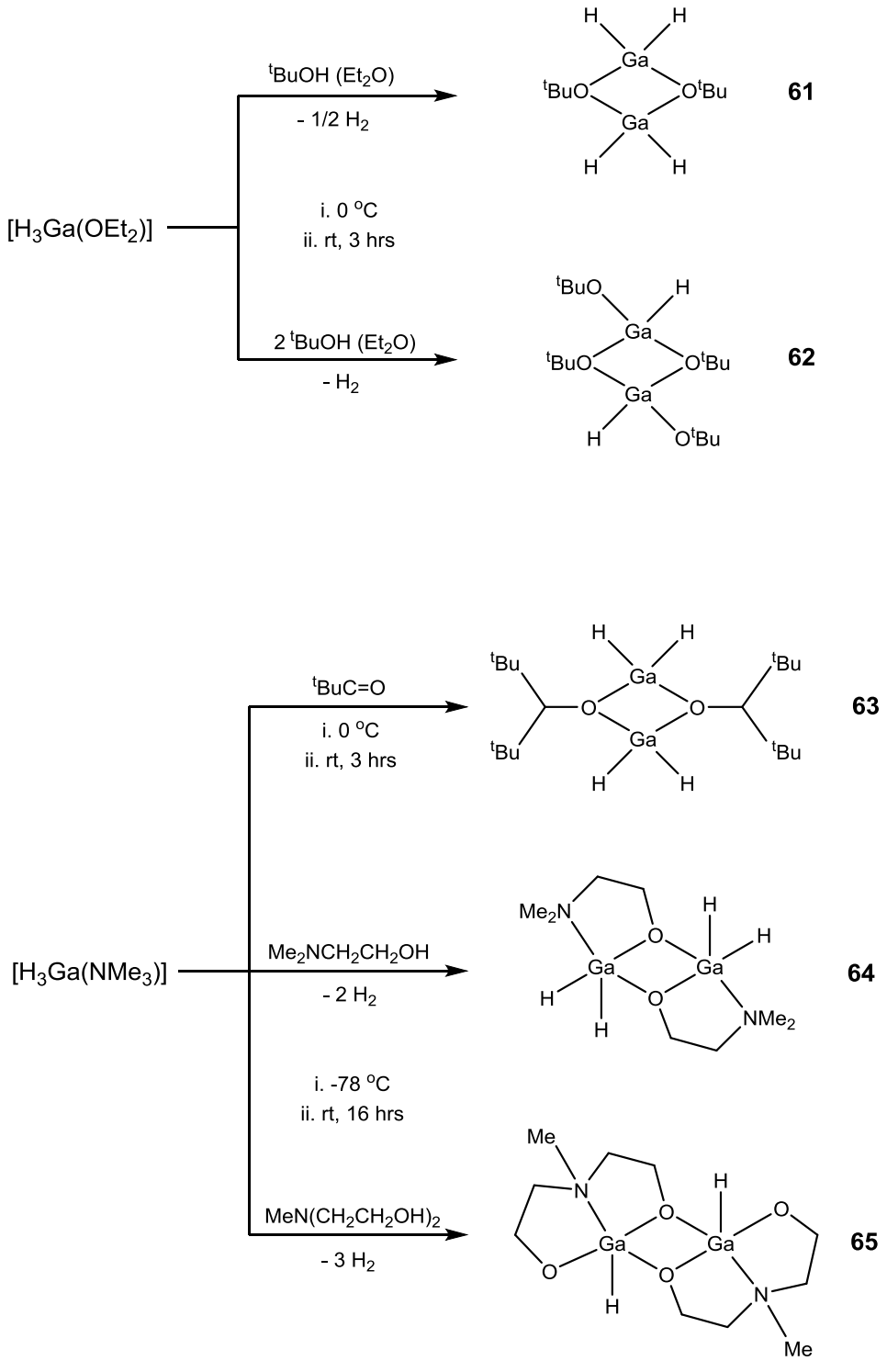

Scheme 2.7 – The synthesis of oxygen-containing gallium hydride derivatives.

2.2 Structural geometries of five-coordinate systems

The following section includes a discussion of the synthesis and structures of a number five-coordinate group 13 metal complexes, which exhibit a range of structural geometries intermediate between the idealised extremes of square-based pyramidal and trigonal bipyramidal. For this purpose, it is useful to define a system for the description of such systems in order to easily identify where the geometry of each complex lies along the spectrum. The method proposed by Addison *et al.* for the classification of five-coordinate geometries will therefore be employed to aid discussion.[157] As shown in Figure 2.2, donor A is chosen such that it is not any of the four which define the two largest angles, α and β. Of the two basal angles, β is the greater (BMC) and α is the lesser (DME). For a perfectly square-based pyramidal system, α = β = 180°, whilst in an ideal trigonal bipyramid α = 120°. As described by Addison *et al.*, in the vast majority of square-based pyramidal systems M is displaced out of the BCDE plane such that α = β < 180°. The geometrical parameter, τ, is thus defined according to equation 2.5 in order to indicate the degree of trigonality within the five-coordinate system.

$$\tau = (\beta - \alpha) / 60 \qquad (2.5)$$

In a square-based pyramidal system (where α = β), τ is equal to zero, whilst for a trigonal bipyramidal system (α = 120°, β = 180°) τ becomes unity, giving a useful numerical value describing the geometry of the system.

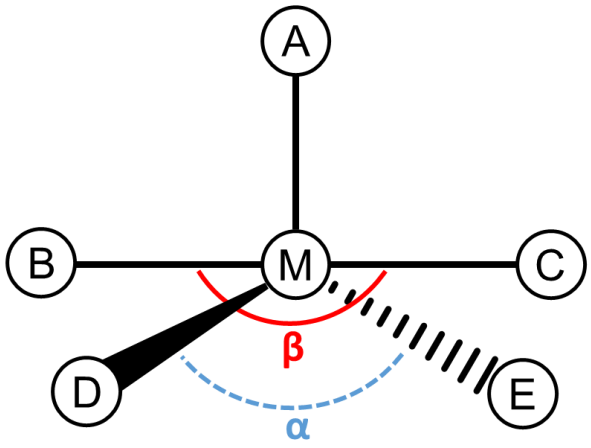

Figure 2.2 - The geometrical classification of five-coordinate systems

2.3 Results and Discussion

2.3.1 The Synthesis of β-ketoimine Ligands

The synthesis of *β*-ketoimines can be achieved through the facile condensation reaction of *β*-diketones with primary amines, as shown in Scheme 2.8. A range of methods have been developed and reported for the synthesis of *β*-ketoimines, including iodine-catalysed and microwave-accelerated processes.[158, 159] However, in the synthesis of basic acac-derived *β*-ketoimines, the simple solvent-free reaction was found to be sufficient for the isolation of the desired compounds in high yield and purity. A range of methods were employed for the removal of water as a reaction by-product, such as drying with magnesium sulphate and *in situ* distillation by fitting of a Dean-Stark condenser. However, in most cases drying the products *in vacuo* post-synthesis was found to be sufficient for the removal of any residual water, as determined by ^{1}H NMR spectroscopy.

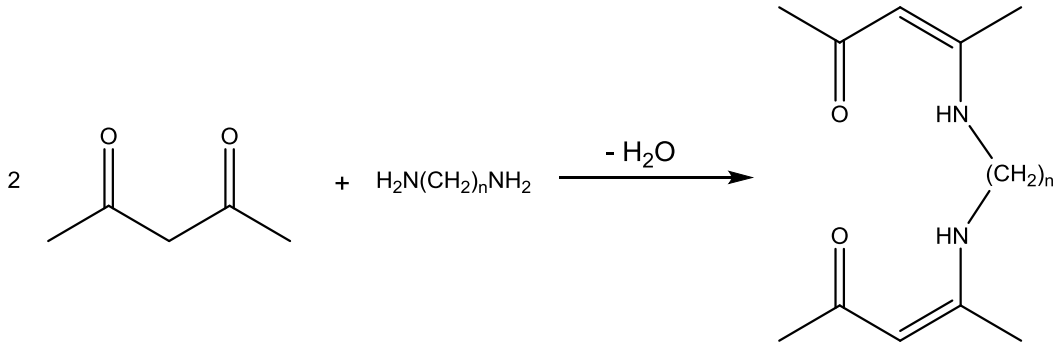

Scheme 2.8 - Reaction scheme for the synthesis of β-ketoimines by the condensation reaction between β-diketones and diamines.

Table 2.2 - Experimental conditions and yields for the synthesis of bis-β-ketoimines L^nH_2, where n = 2, 3, 4.

Ligand	n	Solvent	T (°C)	Time (hrs)	Yield (wt.%)
L^2H_2	2	neat	150	4	98%
L^3H_2	3	neat	RT	4	99%
L^4H_2	4	toluene	Reflux	4	81%

As described in section 1.4, functionalization of the imino moiety of *β*-ketoimines can offer a means to tailoring the compounds as ligands in the complexation of monomeric metal species. Functionalisation with bulky aryl groups can sterically

occupy the coordination sphere of the metal centre, whilst inclusion of a coordinating pendant arm in this position offers the potential to occupy a further coordination site on the metal centre, both of which can encourage the formation of monomeric species. The latter approach led to the development of a series of bis-*β*-ketoimines, offering a dianionic, tetradentate ligand system with potential to fill the coordination sphere of metal centres, encouraging the formation of monomeric metal complexes by the chelate effect.

The bis-*β*-ketoimines $\mathbf{L^2H_2}$, $\mathbf{L^3H_2}$ and $\mathbf{L^4H_2}$ were synthesised in good yield by the condensation reaction between two equivalents of acac with diamino-ethane, -propane and -butane, respectively. Formation of the desired products was easily identified by ^{1}H NMR spectroscopy through the observation of characteristic NH proton resonances, appearing between δ 10.80 – 10.96 ppm. This dramatic downfield chemical shift arises from intramolecular hydrogen bonding with the carbonyl oxygen, resulting in significant deshielding of the hydrogen atom. It is likely that the *β*-ketoimines exist in two rapidly interconverting tautomeric forms, with proton exchange occurring between the nitrogen and oxygen atoms, as illustrated in Scheme 2.9. The presence of just one resonance corresponding to a heteroatomic proton suggests that this interconversion occurs very quickly with respect to the NMR timescale, resulting in the appearance of a single broad peak.

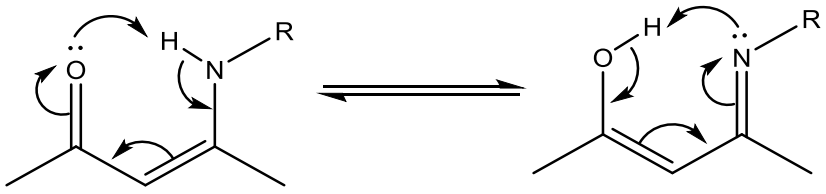

Scheme 2.9 - Interconversion of tautomeric forms of β-ketoimines

Whilst the bis-*β*-ketoimines L^nH_2 (n = 2,3,4) are well known,[228,229] to the best of the author's knowledge the exact methods of synthesis described herein have not been reported previously and thus a short description of their synthesis is included.

2.3.1.1 N,N'-ethylenebis(4-aminopent-3-en-2-one) (L^2H_2)

The reaction of 1,2-diaminoethane with acetylacetone at 150 °C in the absence of solvent afforded $\mathbf{L^2H_2}$ as a light yellow solid after cooling to room temperature, which was purified by washing with CH_2Cl_2 and hexane. The resulting yellow solid product was synthesised in high purity and high yield (98%). Formation of L^2H_2 was

confirmed by the presence of peaks at δ1.89, 1.98, 3.39, 4.99 and 10.96 ppm in the ^{1}H NMR spectrum in a 3:3:2:1:1 ratio, corresponding to the hydrogen environments C*H*$_3$CO, C*H*$_3$CN, C*H*$_2$C*H*$_2$, C*H* and N*H* respectively. ^{13}C{^{1}H} NMR peaks at δ18.8 (*C*H$_3$CO), 28.9 (*C*H$_3$CN), 43.6 (*C*H$_2$*C*H$_2$), 96.3 (*C*H), 163.0 (CH$_3$*C*N), 195.6 ppm (CH$_3$*C*O) were also consistent with the formation of **L^{2}H$_2$**. Mass spectrometry revealed a parent ion of mass 225, which was in agreement with the calculated value for L^{2}H$_2$.

2.3.1.2 N,N'-1,3-propylenebis(4-aminopent-3-en-2-one) (L^{3}H$_2$)

In contrast to the ethylene derivative, synthesis of **L^{3}H$_2$** by the same method resulted in a sticky brown product, which melted easily to give an oil. Attempts to purify the product by recrystallisation and by the same method as used for **L^{2}H$_2$** were unsuccessful. An alternative synthetic procedure was therefore developed where the two reagents were mixed slowly with external cooling in an ice bath. Initially, a white precipitate formed rapidly, though due to the exothermic nature of the reaction, the product soon melted and was stirred to allow the reaction to carry on to completion. The pure, pale yellow solid product was separated from the oily impurities by extraction with Et$_2$O and all solvents removed *in vacuo*. A broad peak at δ10.80 ppm in the ^{1}H NMR spectrum corresponding to NH (H$_c$, Figure 2.4) confirmed the formation of the *β*-ketoimine, as shown in Figure 2.3. Proton resonances at δ4.92 (C*H*), 3.28 (C*H*$_2$CH$_2$C*H*$_2$), 1.92 (C*H*$_3$CO), 1.84 (C*H*$_3$CN) and 1.68 (quintet - CH$_2$C*H*$_2$CH$_2$) in a 1:2:3:3:1 ratio were all consistent with the formation of **L^{3}H$_2$**, as were ^{13}C{^{1}H} NMR, mass spectrometry and elemental analysis. The multiplet at 3.28 ppm corresponds to the two terminal CH$_2$ groups of the propylene bridging group (H$_b$, Figure 2.4) , with the observed coupling arising from second order effects of the magnetically inequivalent protons.

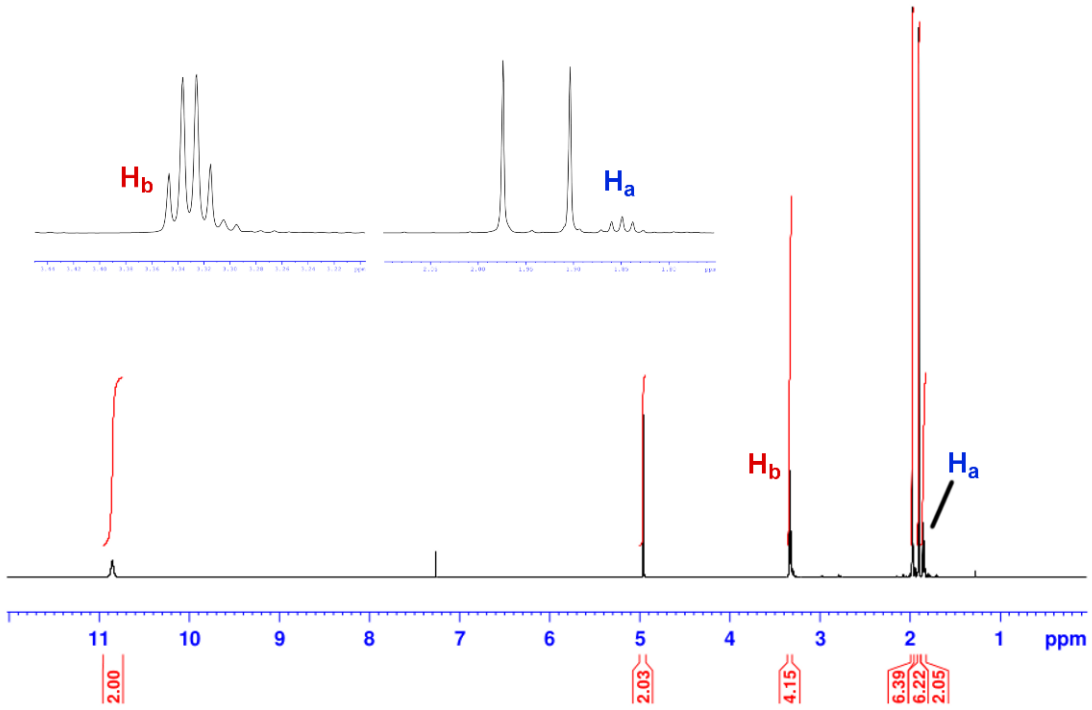

Figure 2.3 - ^{1}H NMR spectrum of $L^{3}H_{2}$.

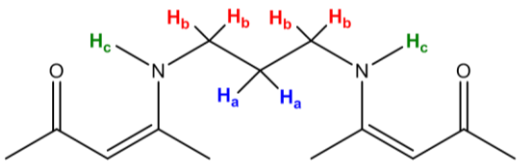

Figure 2.4 – Diagram of $L^{3}H_{2}$, with protons labelled for reference in the text.

2.3.1.3 N,N'-tetramethylenebis(4-aminopent-3-en-2-one) ($L^{4}H_{2}$)

The synthesis of $L^{4}H_{2}$ was carried out in toluene owing to the solid nature of the diamine starting material. After reaction, the product was recrystallised by cooling of the toluene solution affording a highly pure product in 81% yield. The lower yield with comparison to the ethylene and propylene derivatives is likely to be due to the inefficiency of the recrystallisation step, however, the yield could be increased by repeated recrystallisations. ^{1}H NMR analysis was in keeping with the formation of the desired product, the spectrum displaying the expected low field broad singlet at δ10.86 ppm corresponding to the two amino protons. The product can be

distinguished from the propylene derivative by the increased magnitude of the integral of the CH_2 peak appearing at δ 1.66 ppm.

2.3.2 Group 13 β-ketoiminate Chloride Complexes: Synthesis, Structures and Characterisation

With a view to utilising the synthesised ligand systems in the formation of group 13 metal complexes, attention turned to the synthesis of di-substituted chlorides *via* deprotonation and subsequent salt metathesis with the relevant metal trichloride. Scheme 2.10 shows the general pathway for this reaction, which was employed in the formation of aluminium, gallium and indium complexes, though optimum reaction conditions were dependent on the specific systems and are described in the following sections. The deprotonation stage is entropically highly favourable due to the formation of hydrogen gas as a by-product, whilst the metathesis is driven by the formation of sodium chloride. The formation of the comparatively insoluble sodium chloride also assists in reaction work up, allowing reaction products to be separated by simple solvent extraction and filtration with the use of a solvent of appropriate polarity.

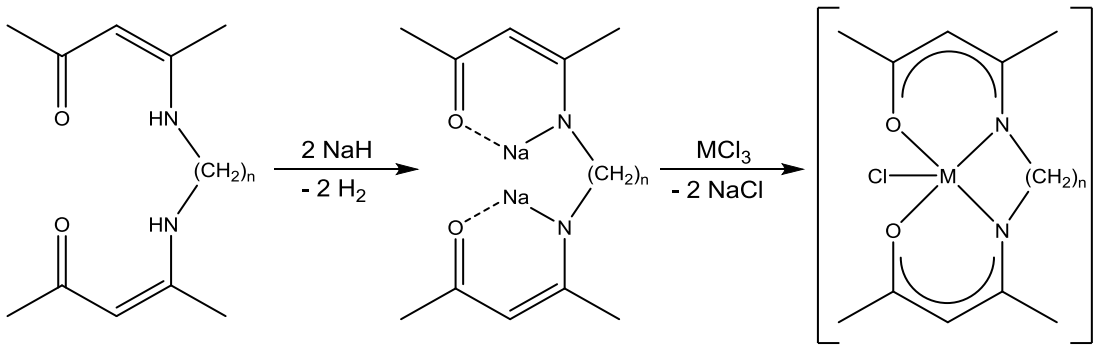

Scheme 2.10 - General reaction scheme for the synthesis of group 13 β-ketoiminate chloride complexes.

2.3.2.1 Synthesis of [Al(L^2)Cl]

The aluminium β-ketoiminate complex [Al(L^2)Cl] was synthesised by salt metathesis from the reaction of the sodium salt L^1Na_2, itself formed by deprotonation of the proligand with NaH, with $AlCl_3$ (Scheme 2.10). Though multiple attempts were made to recrystallise the complex, these were unsuccessful in obtaining sufficiently large crystals to gain a crystal structure. However, the formation of [Al(L^2)Cl] was confirmed *via* spectroscopic methods. ^{1}H NMR spectroscopy of the complex showed separation of the two backbone CH_2 resonances to give two broad singlet peaks at

δ2.65 and 3.21 ppm, implying coordination to the aluminium centre and a resultant inequivalence of the two proton environments. The remaining ^{1}H NMR peaks, $^{13}C\{^{1}H\}$ NMR spectroscopy, mass spectrometry and elemental analysis were all consistent with the formation of the five-coordinate aluminium complex.

2.3.2.2 Synthesis of [Al(L^3)Cl]

The complex [Al(L^3)Cl] was also prepared by the transmetallation of L^3Na_2 with $AlCl_3$ in refluxing THF. The ligand deprotonation was carried out *in situ*, demonstrating the ability to synthesise the *β*-ketoiminate chloride complexes without the need for isolation of the intermediate ligand sodium salt. This is significant towards the possibility of scaling up the synthetic procedure for application in an industrial process. Whilst the yield of the recrystallised product was low (16%), this is simply due to the inefficiency of the recrystallisation process. The crude product displayed high purity negating the need for further purification and the yield in this case was significantly higher (72%). ^{1}H and ^{13}C NMR showed only the presence of very low-level impurities in addition to the expected resonances. Elemental analysis was consistent with the proposed formation.

The ^{1}H NMR spectrum of [Al(L^3)Cl] showed the expected absence of the NH protons. A singlet peak at 5.20 ppm (C*H*), and two further singlets at 2.034 and 2.030 ppm (CH_3CO and CH_3CN) in a 1:3:3 ratio are also in agreement with the formation of the desired product. Of particular interest, however, are the changes observed within the propylene bridging group with respect to the proton NMR of the free ligand L^3H_2 (Figure 2.5). Within the free ligand, the protons of the two terminal CH_2 groups were equivalent and appeared as a single quartet resonance at 3.28 ppm. Upon coordination to the aluminium centre, these two resonances become separated and appear as two broad singlets at 3.40 and 3.70 ppm. Coordination results in the proton environments becoming inequivalent and their broad nature suggests a degree of fluxionality. The implied fluxionality is a likely effect of a Berry pseudorotation mechanism common in 5-coordinate systems and could be further probed by variable temperature (VT) NMR studies. A similar separation was observed between the resonances corresponding to the two protons of the internal propylene CH_2 group, appearing as broad singlets at 2.22 and 1.87 ppm, as shown in Figure 2.5.

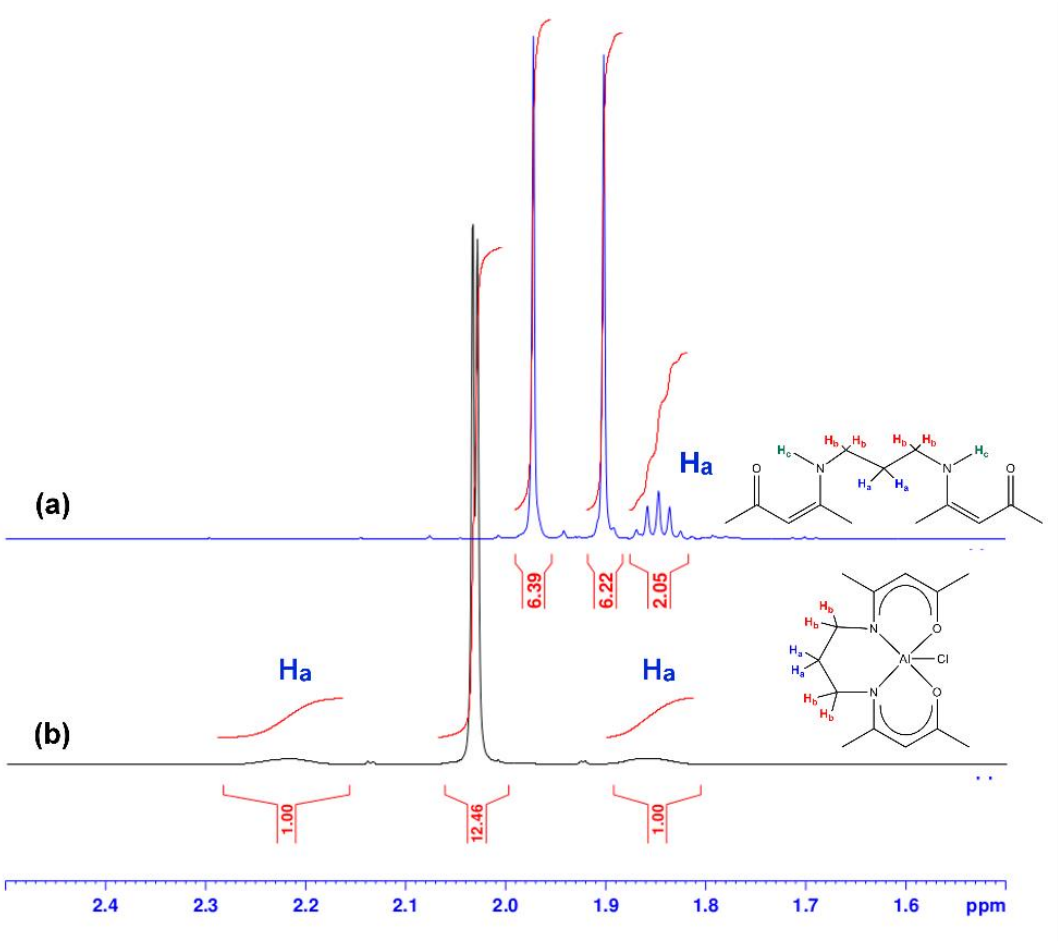

Figure 2.5 - ^{1}H NMR spectrum of (a) $L^{3}H_{2}$ and (b) $Al(L^{3})Cl$.

2.3.2.3 Synthesis of [Al(L^{4})Cl]

The tetramethylene derivative [Al(L^{4})Cl] was synthesised by the same procedure employed for the propylene analogue. Colourless crystals were formed from a concentrated toluene solution of the complex cooled to -20 °C, which were analysed by single crystal X-ray crystallography.

Figure 2.6 shows the X-ray crystal structure of [Al(L^{4})Cl] and selected bond lengths and angles are given in Table 2.4.

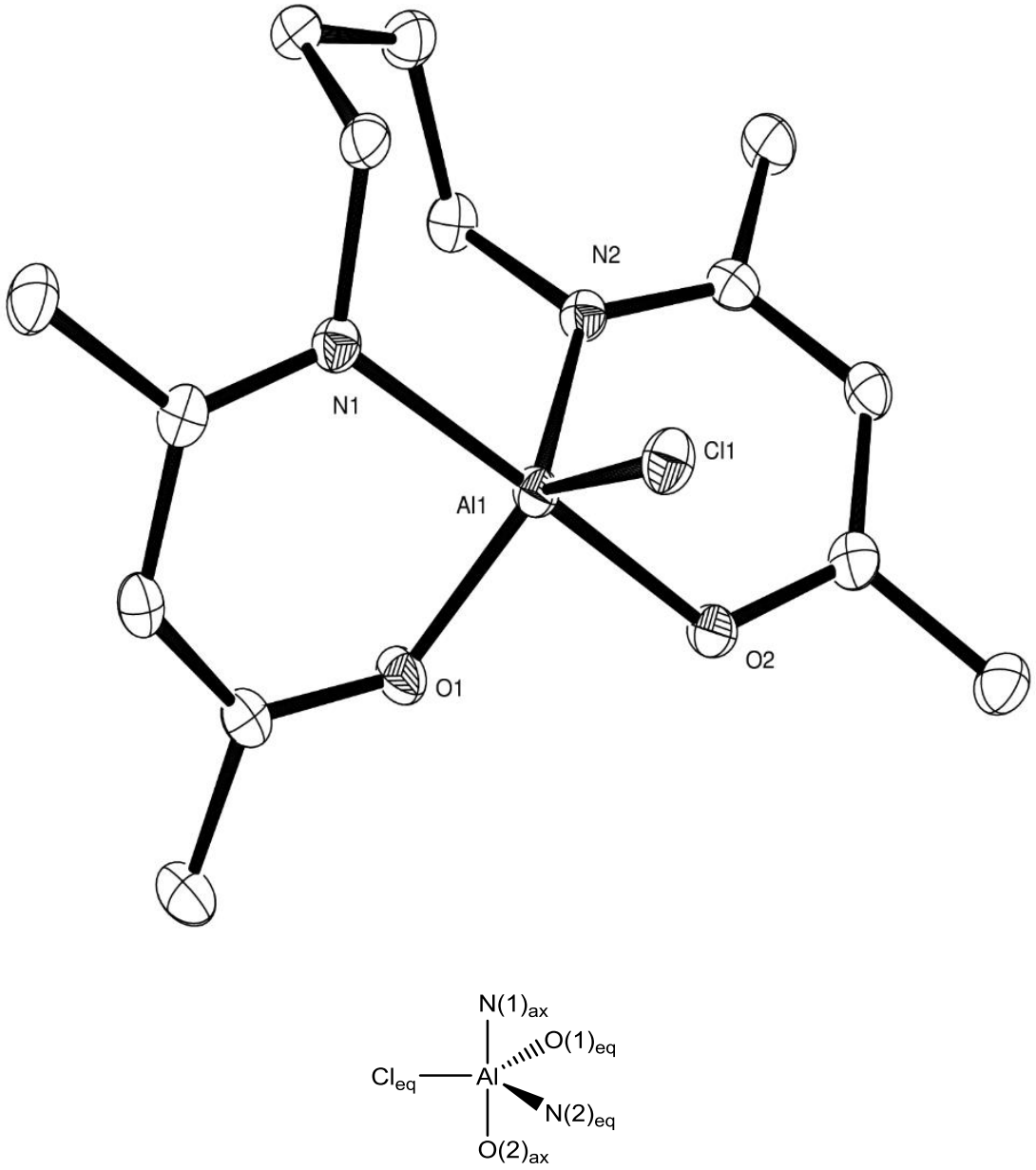

Figure 2.6 - X-ray crystal structure of Al(L[4])Cl. Includes line drawing to clarify axial/equatorial positioning of atoms within the structure. Data collection was carried out by the National Crystallography Service, Southampton. Structure solution was carried out by the author.

Table 2.3 - Crystal data for Al(L[4])Cl

Crystal system	Triclinic	
Space group	P-1	
Unit cell dimensions	a = 8.6638(5) Å	α= 80.362(6)°
	b = 9.2573(5) Å	β= 77.955(6)°
	c = 10.9227(7) Å	γ= 64.890(5)°

Table 2.4 - Selected bond lengths (Å) and angles (°) for Al(L^4)Cl

Cl(1)-Al(1)	2.2391(11)	N(1)-C(6)	1.4796(18)
Al(1)-O(1)	1.7895(13)	C(1)-C(2)	1.496(2)
Al(1)-O(2)	1.8427(12)	C(2)-C(3)	1.365(2)
Al(1)-N(2)	1.9355(14)	C(6)-C(7)	1.531(2)
Al(1)-N(1)	1.9979(14)	C(4)-C(3)	1.429(2)
O(1)-C(2)	1.3121(16)	C(7)-C(8)	1.529(2)
O(2)-C(13)	1.3008(17)	C(8)-C(9)	1.535(2)
N(1)-C(4)	1.3160(18)		
O(1)-Al(1)-O(2)	87.82(5)	N(2)-Al(1)-N(1)	92.10(6)
O(1)-Al(1)-N(2)	118.39(5)	O(1)-Al(1)-Cl(1)	123.73(5)
O(2)-Al(1)-N(2)	90.94(6)	O(2)-Al(1)-Cl(1)	89.73(4)
O(1)-Al(1)-N(1)	91.11(5)	N(2)-Al(1)-Cl(1)	117.86(4)
O(2)-Al(1)-N(1)	176.93(5)	N(1)-Al(1)-Cl(1)	88.47(4)

The value of τ was found to be 0.89, indicating a distorted trigonal bipyramidal geometry surrounding the aluminium centre. Axial positions are occupied by one oxygen atom (O(2)) and one nitrogen atom (N(1)) of the *β*-ketoiminate ligand, with the angle between the two being 176.93(5)°. The equatorial positions are taken up by the remaining oxygen and nitrogen atoms and the chloride.

Upon coordination, the aluminium centre forms two six-membered rings with the *β*-ketoiminate moieties of the ligand. Within these rings, a delocalisation of electron density is evident by analysis of the bond lengths within the ring. Carbon-carbon bond lengths of 1.365 and 1.429 Å are intermediate between the values expected for single and double bonds, as are the observed carbon-oxygen and carbon-nitrogen bonds lengths ranging between 1.78 and 2.00 Å.[160] Aluminium-oxygen and aluminium–nitrogen bonds lengths are in keeping with those found in related aluminium *β*-ketoiminate complexes.[120] However the observed aluminium-chlorine

bond length of 2.2391(11) Å is notably longer than the bond length of 2.170(6) Å that is found within the bis-ligated aluminium *β*-ketoiminate chloride complex $[Al(L)_2Cl]$, stabilised by two bulky aryl-substituted monoanionic *β*-ketoiminate ligands.[120] Since there is a noticeable variation in literature values for Al-Cl bond lengths for similar complexes,[117] it is likely that the longer bond length observed in $[Al(L^4)Cl]$ is a result of crystal packing effects.

Once again, the identity of the product was confirmed by ^1H, $^{13}C\{^1H\}$ NMR, mass spectrometry and elemental analysis. For comparison, Figure 2.7 shows the ^1H NMR spectra of $[Al(L^2)Cl]$, $[Al(L^3)Cl]$ and $[Al(L^4)Cl]$. The most notable differences within the ^1H NMR spectra of the three complexes lie within the alkyl bridging groups of the *β*-ketoiminate ligand. Within these bridges, terminal methylene groups have been referred to as H_a and internal methylene groups as H_b. As has been discussed in section 2.3.2.2, the propylene complex displayed a separation of the two internal CH_2 protons (H_b), however the tetramethylene derivative shows no such separation, with the four protons appearing as a broad singlet at 1.76 ppm. This is attributed to the relative proximity of the protons to the metal centre within the two species. Within $[Al(L^4)Cl]$, the protons are further removed from the metal, thus any difference in magnetic environment is negligible and the chemical shifts the same, resulting in a single peak being observed. Similarly, a convergence of the resonances corresponding to the terminal methylene groups (H_a) is observed for $[Al(L^4)Cl]$, in contrast to the separate resonances seen within the ^1H NMR spectra of $[Al(L^2)Cl]$ and $[Al(L^3)Cl]$ (Figure 2.7). As for $[Al(L^3)Cl]$, the broad nature of the protons resonances associated with the bridging group suggest that the solid-state structure does not hold in solution and that fluxionality (likely to be in the form of Berry pseudorotation) is present.

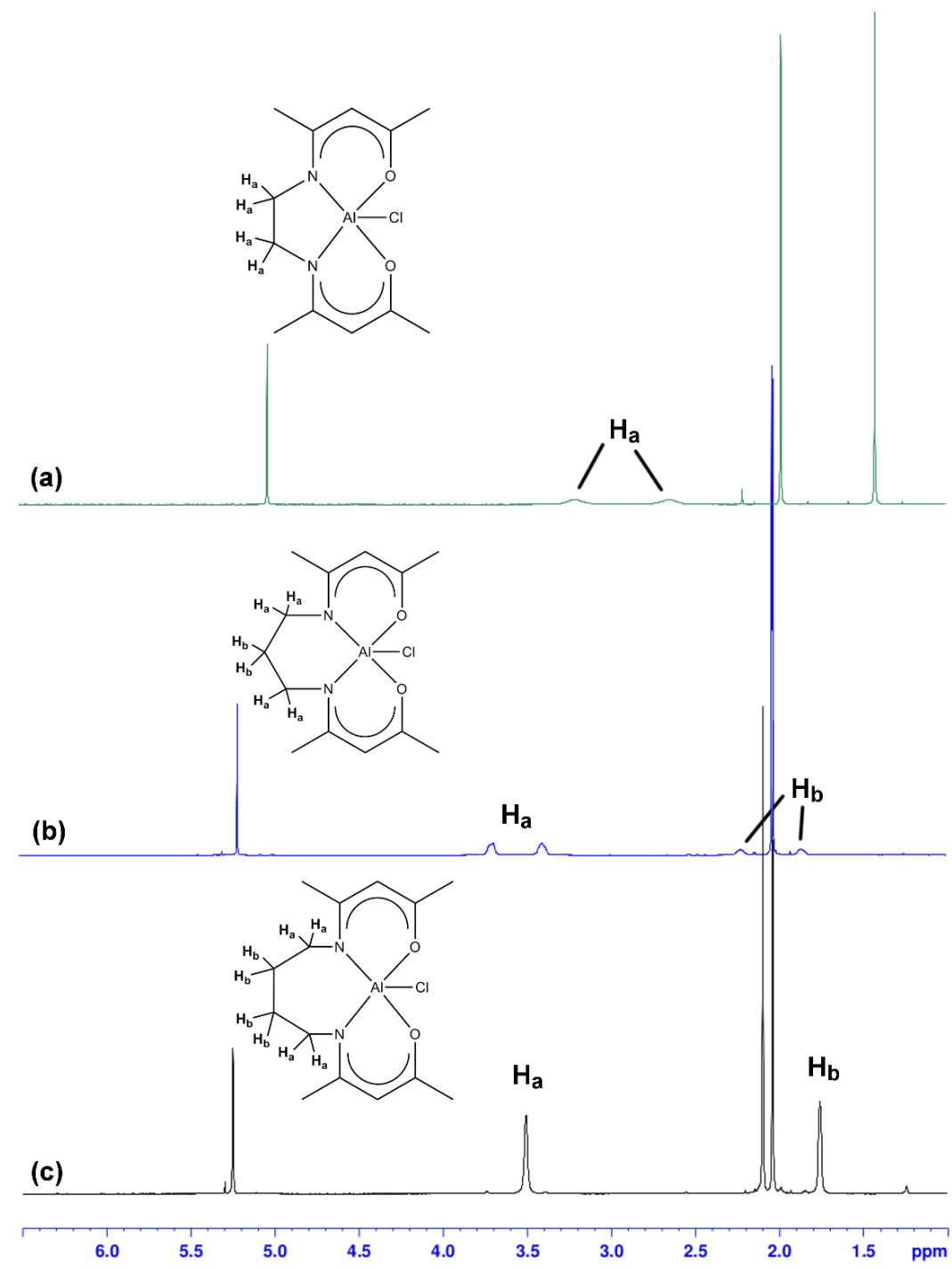

Figure 2.7 - ^{1}H NMR spectra of (a) Al(L^{2})Cl; (b) Al(L^{3})Cl; and (c) Al(L^{4})Cl.

2.3.2.4 Synthesis of [Ga(L^{2})Cl]

The synthesis of [Ga(L^{2})Cl] and its structural characterisation has previously been reported, though no reference to further analysis (except single-crystal X-ray crystallography) or discussion of its chemistry or application was made.[126] A discussion of further characterisation is therefore made herein. The original synthetic

method involved initial deprotonation of the free ligand L^2H_2 with NaH to form the intermediate sodium salt L^2Na_2. Subsequent room temperature salt metathesis of the sodium salt with $GaCl_3$ in hexane yielded the desired product, as determined by ^{1}H NMR, ^{13}C NMR, mass spectrometry and elemental analysis, in low yield (20%). The likely cause of the low yield was the limited solubility of the reagents in hexane and the low reaction temperature used. The synthesis was therefore repeated, the deprotonation reaction carried out *in situ* and the metathesis reaction carried out in refluxing THF, resulting in a significant increase in yield to 70%. The ^{1}H NMR spectrum of [Ga(L^2)Cl] showed a downfield shift compared to the free ligand for all proton resonances due to the electron-withdrawing nature of the gallium(III) centre. Multiplet peaks at δ3.51 and 3.62 ppm correspond to the two C$\underline{H}_2$ proton environments of the ligand diamine backbone, which become inequivalent upon coordination to the gallium(III) centre and are thus observed as separate resonances, compared to the single 4H resonance seen in the spectrum of the corresponding *β*-ketoimine. Other peaks at δ2.02, 2.08 and 5.26 ppm, corresponding to C$\underline{H}_3$CO, C$\underline{H}_3$CN and C$\underline{H}$ respectively, in addition to peaks in the ^{13}C{^{1}H} NMR spectrum at δ22.6 ($\underline{C}$H$_3$CO), 26.7 ($\underline{C}$H$_3$CN), 45.1 ($\underline{C}$H$_2$*C*H$_2$), 98.8 ($\underline{C}$H), 173.3 (CH$_3\underline{C}$N) and 183.6 ppm (CH$_3\underline{C}$O), which are also consistent with the formation of the desired product. Crystal structure analysis revealed a five-coordinate gallium(III) centre in a distorted square-pyramidal geometry, in agreement with the findings of Vohs *et al.*[126]

2.3.2.5 Synthesis of [Ga(L^3)Cl]

The compound [Ga(L^3)Cl] was similarly synthesised *via* deprotonation of L^3H_2 followed by salt metathesis with $GaCl_3$ in hexane, according to Scheme 2.10. After formation and isolation of L^2Na_2, reaction with $GaCl_3$ afforded yellow crystals of the five-coordinate gallium complex. The product was formed in relatively low yield, as was found for the ethylene analogue when the metathesis reaction was carried out in hexane. Whilst it was later found that greater yields can be achieved by simple adaptation of the synthetic procedure (see section 2.3.2.4), [Ga(L^3)Cl] was formed in sufficient yield by this method to gain full characterisation of the complex and thus no further synthesis was needed.

The crystal structure of [Ga(L^3)Cl] was determined by X-ray crystallography, confirming its structure to be that of the mononuclear complex shown in Figure 2.8. Selected bond lengths and angles are given in Table 2.5. Using the method defined by Addision *et al.* and described in section 2.2, the gallium atom was found to be in a slightly distorted trigonal bipyramidal geometry ($\tau = 0.86$).[157] The axial positions are occupied by one oxygen and one nitrogen atom of the ligand, with a bond angle of 172.66(5)° (O(1)-Ga(1)-N(2)). Equatorial positions are occupied by the remaining oxygen and nitrogen atoms, as well as one chlorine atom, with O(2)-Ga(1)-N(1), O(2)-Ga(1)-Cl(1) and N(1)-Ga(1)-Cl(1) bond angles of 121.30(5), 114.59(4) and 123.42(4)° respectively. Average C-C (1.399 Å), C-O (1.303 Å) and C-N (1.316 Å) bond lengths lie between the expected values for single and double bonds, demonstrating the delocalisation of electron density within the ketoimine moiety of the ligand. Whilst there is no structural data available for the free ligand in the literature, the data are consistent with those reported for [Ga(L^2)Cl], which differs only in the number of carbon atoms linking the two ketoimine moieties.[126] As expected, Ga-O bond lengths of 1.8754 (11) and 1.9759(11) Å show the bonds to be weaker than found in similar gallium donor-functionalised alkoxide complexes (average bond length 1.8415 Å)[103] but to be of comparable magnitude to structurally similar gallium β-diketonates, which have an average bond length of 1.950Å.[161]

^{1}H and ^{13}C NMR were consistent with the formation of [Ga(L^3)Cl], however it should be noted that separation of the pure product from the ligand starting material was difficult and the NMR spectra showed a mixture of the two. Peaks for the quaternary carbons in the ^{13}C NMR spectrum were notably absent and could not be detected by increasing the number of scans. Elemental analysis of the pure sample provided further evidence for the composition of [Ga(L^3)Cl] as shown in the crystal structure in Figure 2.8.

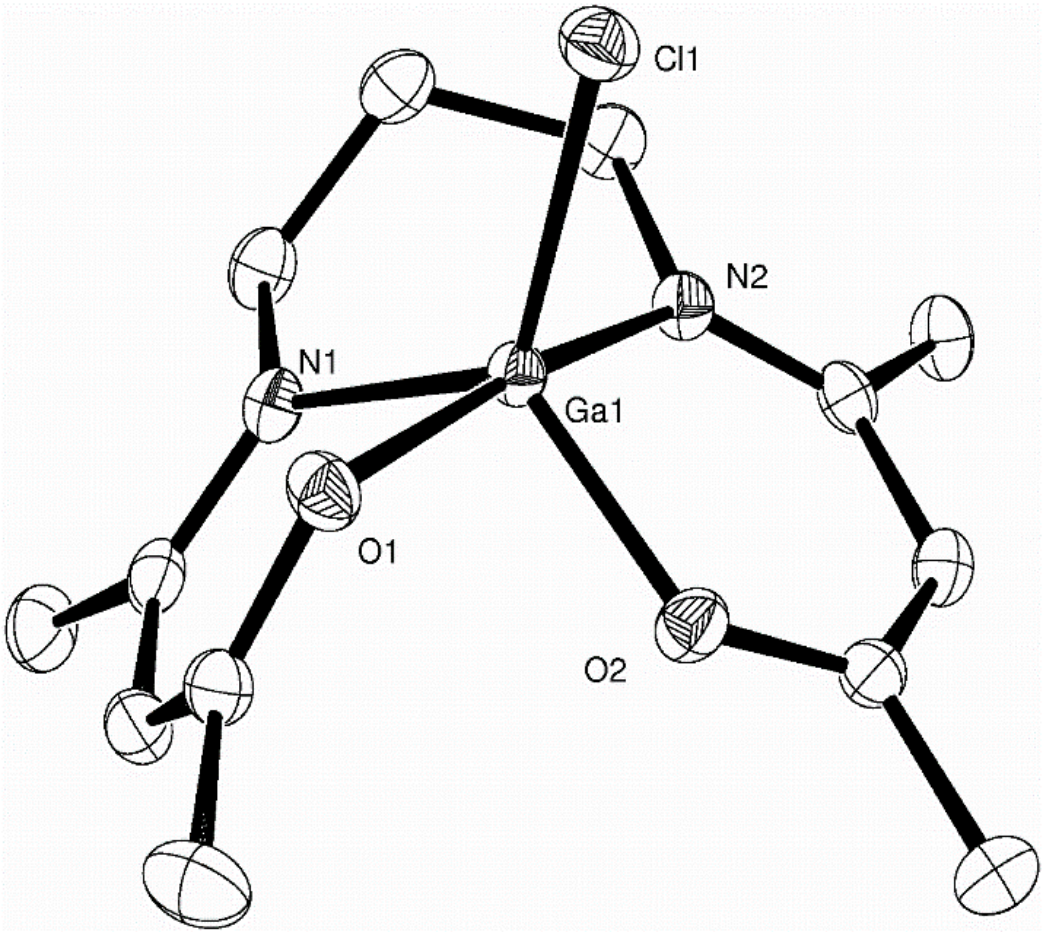

Figure 2.8 - The X-ray crystal structure of Ga(L^3)Cl. Data collection and structure solution was carried out by Dr. David Pugh.

Table 2.5 - Crystal data for Ga(L^3)Cl

Crystal system	Triclinic	
Space group	P-1	
Unit cell dimensions	a = 7.4177(9) Å	α = 72.534(2)°
	b = 8.6862(11) Å	β = 75.996(2)°
	c = 12.4715(15) Å	γ = 77.103(2)°

Table 2.6 - Selected bond lengths (Å) and angles (°) for Ga(L^3)Cl

Ga(1)-O(1)	1.9759(11)	C(9)-C(10)	1.511(2)
Ga(1)-O(2)	1.8754(11)	C(10)-C(11)	1.434(2)
Ga(1)-N(1)	1.9824(13)	C(11)-C(12)	1.362(2)
Ga(1)-N(2)	2.0229(13)	C(12)-C(13)	1.502(2)
Ga(1)-Cl(1)	2.2317(5)	O(1)-C(2)	1.2972(19)
C(1)-C(2)	1.502(2)	O(2)-C(12)	1.308(2)
C(2)-C(3)	1.380(2)	N(1)-C(4)	1.323(2)
C(3)-C(4)	1.418(2)	N(2)-C(10)	1.309(2)
C(4)-C(5)	1.509(2)		
O(2)-Ga(1)-N(1)	121.30(5)	O(1)-Ga(1)-Cl(1)	91.24(3)
O(2)-Ga(1)-Cl(1)	114.59(4)	O(2)-Ga(1)-O(1)	83.41(5)
N(1)-Ga(1)-Cl(1)	123.42(4)	O(2)-Ga(1)-N(2)	92.71(5)
O(1)-Ga(1)-N(2)	172.66(5)	N(1)-Ga(1)-N(2)	89.64(5)
O(1)-Ga(1)-N(1)	87.07(5)	N(2)-Ga(1)-Cl(1)	96.05(4)

2.3.2.6 Synthesis of [Ga(L^4)Cl]

The synthesis of [Ga(L^4)Cl] was achieved in good yield (67%) by the same method employed for the aluminium complexes [Al(L^3)Cl] and [Al(L^4)Cl]. Colourless, crystalline blocks were formed by slow solvent diffusion of hexane into a concentrated CH_2Cl_2 solution of the crude product, which were suitable for analysis by single crystal X-ray diffraction. Figure 2.9 shows the molecular structure of [Ga(L^4)Cl] and selected bond lengths and angles are given in Table 2.8.

The monomeric [Ga(L^4)Cl] complex crystallised as a five-coordinate species in the triclinic P-1 space group, with the gallium cation in a slightly distorted trigonal bipyramidal geometry (τ = 0.86).[157] Chloride, as the largest ligand, predictably occupies one of the equatorial sites, with the other two sites being occupied by one oxygen and one nitrogen of the chelating *β*-ketoiminate ligand. Individual angles between these three show a deviation from ideal trigonality, however the sum of the

angles is very close to 360°. The axial positions are again occupied by the remaining donor atoms of the *β*-ketoiminate ligand, with the O(1)-Ga-N(2) angle bending away from linear to 175.21°.

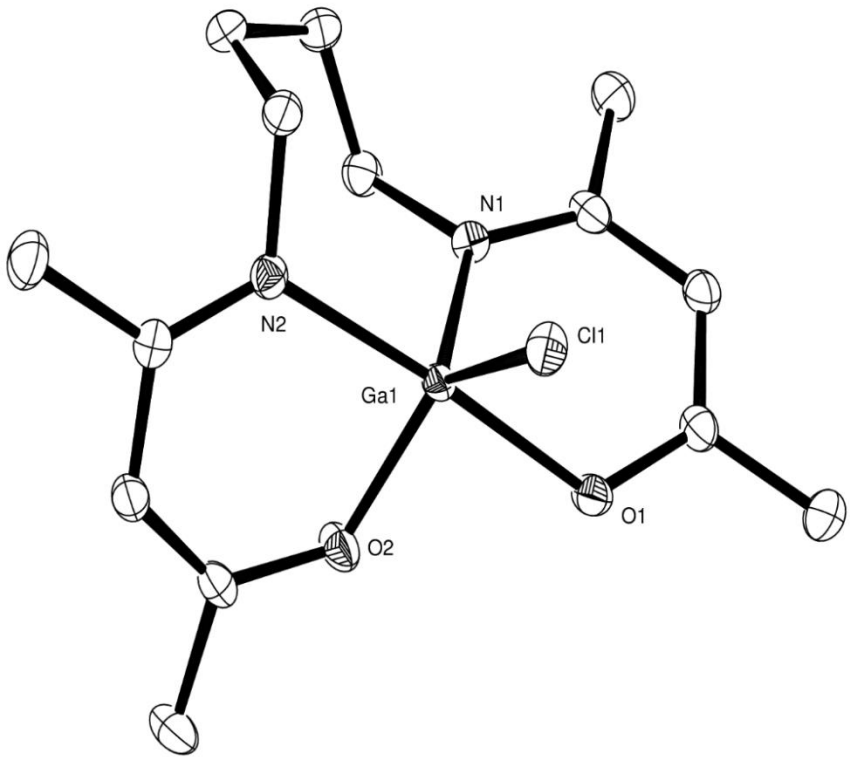

Figure 2.9 - X-ray crystal structure of Ga(L^4)Cl. Data collection was carried out by the National Crystallography Service, Southampton. Structure solution was carried out by the author.

Table 2.7 - Crystal data for Ga(L^4)Cl

Crystal system	Triclinic	
Space group	P-1	
Unit cell dimensions	a = 8.64560(10) Å	α = 79.7260(3)°
		β = 77.4020(3)°
	b = 9.21790(10) Å	γ = 65.5730(3)°
	c = 11.0432(2) Å	

Bond lengths within the complex are consistent with those found within the propylene analogue [Ga(L^3)Cl]. As expected, bond lengths within the ketoimine moieties are intermediate between those of single and double bonds, suggesting the delocalisation of electron density. As discussed for the propylene analogue, Ga-O

bond lengths show good agreement with similar gallium *β*-diketonate complexes, whilst being longer than Ga-O bond lengths within gallium alkoxide complexes. This is a result of the bidentate, monoanionic nature of the bonding, making each individual Ga-O bond weaker.

Table 2.8 - Selected bond lengths (Å) and angles (°) for Ga(L^4)Cl

Ga(1)-O(2)	1.878(2)	N(2)-C(9)	1.478(4)
Ga(1)-O(1)	1.950(2)	O(2)-C(13)	1.315(4)
Ga(1)-N(1)	1.967(3)	N(1)-C(4)	1.329(4)
Ga(1)-N(2)	2.029(3)	N(1)-C(6)	1.467(4)
Ga(1)-Cl(1)	2.2619(9)	C(2)-C(3)	1.377(5)
O(1)-C(2)	1.299(4)	C(4)-C(3)	1.420(5)
N(2)-C(11)	1.310(5)		
O(2)-Ga(1)-O(1)	85.03(11)	N(1)-Ga(1)-N(2)	93.56(12)
O(2)-Ga(1)-N(1)	117.71(12)	O(2)-Ga(1)-Cl(1)	123.63(9)
O(1)-Ga(1)-N(1)	91.02(11)	O(1)-Ga(1)-Cl(1)	88.99(8)
O(2)-Ga(1)-N(2)	91.59(11)	N(1)-Ga(1)-Cl(1)	118.40(8)
O(1)-Ga(1)-N(2)	175.21(10)	N(2)-Ga(1)-Cl(1)	90.06(8)

The ^{1}H NMR spectrum of the complex showed the expected pattern, most notably the absence of an NH proton. This is a good indication that the *in situ* deprotonation reaction had gone to completion and no free ligand remained within the reaction mixture. Singlet peaks were observed at 5.1, 2.06 and 2.03 ppm corresponding to the methine and two methyl groups of the *β*-ketoiminate ligand backbone. Similar to the observations made for the analogous aluminium complex [Al(L^4)Cl] (section 2.3.2.3), the methylene groups of the tetramethylene bridging moiety were observed as two broad singlet peaks at 3.52 and 1.78 ppm (central and terminal respectively). This is in contrast to the observed separation of the methylene resonances within the methylene and propylene derivatives, [Ga(L^2)Cl] and [Ga(L^3)Cl]. The tertiary carbons $CH_3\underline{C}N$ and $CH_3\underline{C}O$ are again observed at very high chemical shift within the ^{13}C NMR spectrum (174.9 and 182.9 ppm, respectively) due to deshielding arising from the inductive effect of the electronegative heteroatoms N and O, to which they are bonded. The anisotropic effect of the π-electrons within the area of

delocalised electron density across the *β*-ketoiminate backbone also contributes towards the deshielding of the nuclei, which is also the cause of the large downfield shift observed for the tertiary methine carbons (99.5 ppm). The two terminal methyl carbons of the *β*-ketoiminate backbone appear as signals at 26.6 and 22.5 ppm and the tetramethylene bridging group appears as two resonances at 48.7 and 28.6 ppm.

Mass spectrometry showed the presence of the parent ion, in addition to various ions resulting from the fragmentation of the complex, in particular the loss of Cl and CH_3 groups.

2.3.2.7 Synthesis of [In(L^2)Cl]

In an attempt to synthesise the ethylene indium derivative, the salt metathesis reaction between an isolated sample of L^2Na_2 and $InCl_3$ was carried out in hexane. Purification of the crude product was initially attempted by recrystallisation from THF, however, this was unsuccessful. The product was recrystallised by solvent diffusion of hexane into a concentrated CH_2Cl_2 solution, which yielded yellow crystals after 2 days. Initial characterisation was carried out by ^{1}H NMR, which indicated the formation of the desired product, [In(L^2)Cl]. Of particular significance, however, was the presence of multiplets at δ1.85 and 3.74 ppm, characteristic of THF, which were initially attributed to residual THF in the sample after the first attempt at recrystallisation. However, closer inspection of the integrals showed the presence of THF in a 1:1 ratio with respect to the ligand resonances. Determination of the crystal structure revealed the coordination of one THF molecule to the indium centre, forming the six-coordinate indium complex [In(L^2)Cl·THF], shown in Figure 2.10. Selected bond lengths and angles are given in Table 2.10.

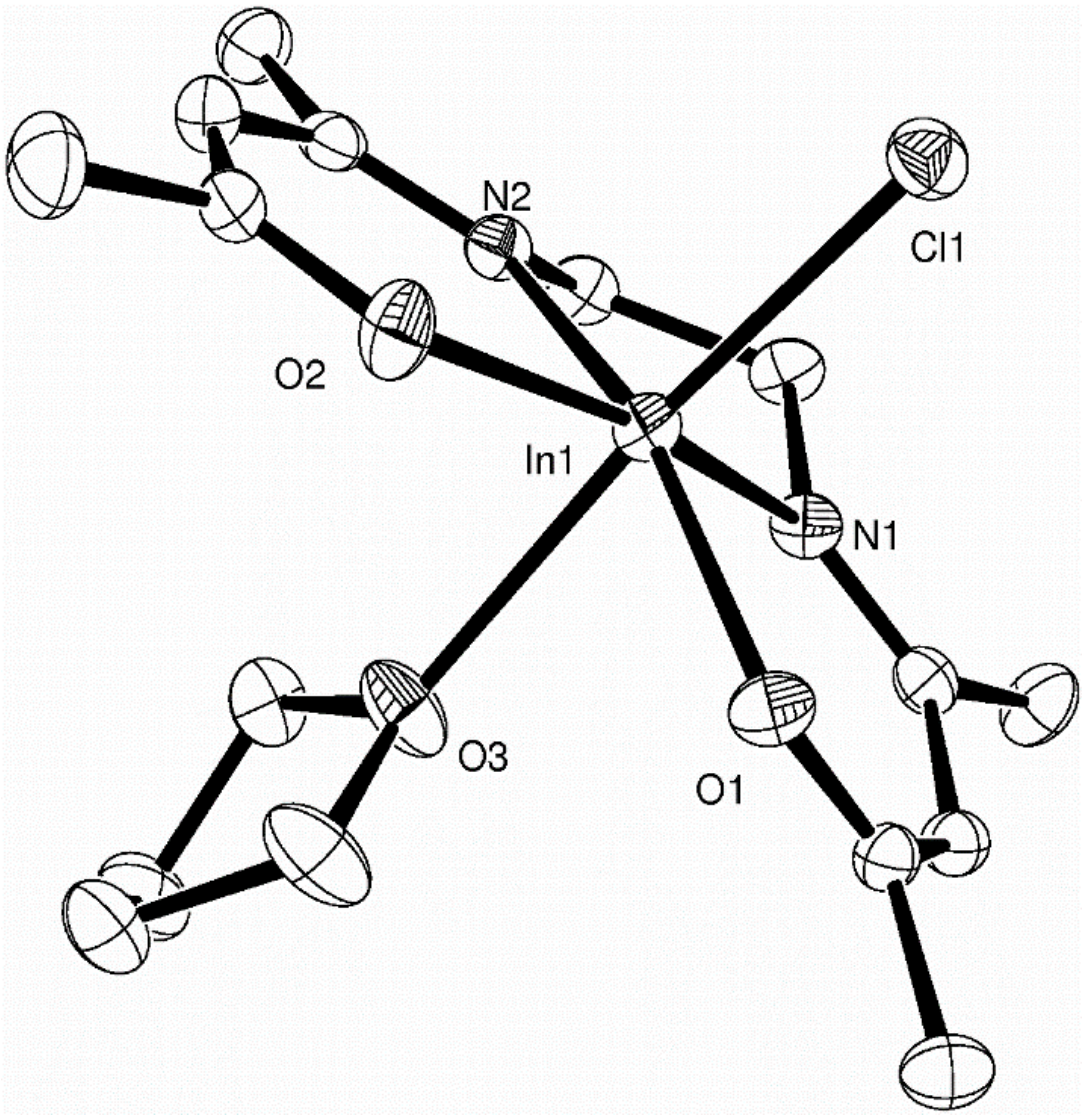

Figure 2.10 - The X-ray crystal structure of [In(L^2)Cl·THF]. Data collection was carried out by the National Crystallography Service, Southampton. Structure solution was carried out by Dr. David Pugh.

Table 2.9 - Crystal data for [In(L^2)·THF].

Crystal system	Monoclinic	
Space group	$P2_1/c$	
Unit cell dimensions	a = 8.017(3) Å	α = 90°
	b = 14.760(5) Å	β = 114.81°
	c = 17.112(5) Å	γ = 90°

Table 2.10 - Selected bond lengths (Å) and angles (°) for [In(L^2)Cl·THF]

In(1)-O(1)	2.0965(19)	C(6)-C(7)	1.532(4)
In(1)-O(2)	2.101(2)	C(8)-C(9)	1.515(4)
In(1)-O(3)	2.413(2)	C(9)-C(10)	1.424(4)
In(1)-N(1)	2.171(2)	C(10)-C(11)	1.386(4)
In(1)-N(2)	2.183(2)	C(11)-C(12)	1.510(4)
In(1)-Cl(1)	2.4538(8)	N(1)-C(4)	1.300(4)
C(1)-C(2)	1.509(4)	N(2)-C(9)	1.304(4)
C(2)-C(3)	1.371(4)	O(1)-C(2)	1.299(3)
C(3)-C(4)	1.427(4)	O(2)-C(11)	1.293(4)
C(4)-C(5)	1.513(4)		
O(1)-In(1)-O(2)	98.66(8)	O(1)-In(1)-N(1)	89.72(8)
O(2)-In(1)-N(2)	89.43(8)	O(3)-In(1)-Cl(1)	172.68(6)
N(1)-In(1)-N(2)	78.41(9)		

The indium atom of [In(L^2)Cl·THF] lies in a 6-coordinate, distorted octahedral geometry. The equatorial positions are occupied by the N_2O_2 plane of the ligand, whilst the chlorine atom and the oxygen atom of the coordinated THF molecule occupy the two axial positions. The bond angles O1-In-N1, N1-In-N2 and N2-In-O2 (89.72°, 78.41° and 89.43° respectively) are below 90° due to the geometry of the ligand, whilst the sum of the angles between the equatorial heteroatoms is less than 360° (356.13°) due to the indium atom sitting slightly above the N_2O_2 plane. The equatorial In-O bond lengths of 2.0965(19) and 2.101(2) Å are consistent with those seen in related indium β-diketonate complexes (2.110(5) - 2.140(5) Å).[161] These values lie in between that of shorter In-O bond lengths in alkoxide complexes (1.94(2) - 2.1237(18) Å)[162] and the dative In-O3 of the coordinated THF molecule (2.413(2) Å). The In-Cl bond length of 2.4538(8) Å is longer than would be expected, compared to values of 2.153(3) and 2.156(3) Å in a similar indium β-ketoiminate complex.[116] This could be attributed to the structural *trans*-influence

brought about by the presence of the coordinating THF molecule, though it could also be due to a crystal packing effect. All ligand bond lengths are consistent with those found in the free ligand and suggest a delocalisation of electron density within each 6-membered ring formed between the indium, nitrogen, oxygen and internal carbon atoms of the ligand system.[163] The average C-C bond length of 1.402 Å within this ring, consistent with that of 1.418 Å in the free ligand, is shorter than the average single bond length of 1.512 Å seen in the terminal C-C bonds of the ligand backbones (C1-C2, C4-C5, C8-C9, C11-C12), whilst being longer than expected for a standard C=C double bond. Evidence for a delocalised ring system also exists in the C-O and C-N bond lengths (average distance 1.296 and 1.302 Å respectively), which again lie in between those expected for C-E single and double bonds (E = O, N).[160]

The formation, in this case, of the THF adduct displays the preference of the larger indium(III) ion to form a six-coordinate compound where a suitable coordinating solvent is present, compared to the smaller gallium(III) atom, which formed the 5-coordinate compound [Ga(L^2)Cl] despite the use of THF in its synthesis.

In an attempt to circumvent the preference of this system to form six-coordinate complexes, the reaction between the ligand sodium salt and $InCl_3$ was repeated in Et_2O. It was expected that Et_2O would coordinate to the indium centre, however due to its relatively low boiling point with respect to THF, exposure to reduced pressure could result in evaporation of the solvent and formation of the desired 5-coordinate species. The reaction between $InCl_3$ and L^1Na_2 in Et_2O was carried out and the product recrystallised by slow diffusion of hexane into a concentrated CH_2Cl_2 solution by layering, affording yellow crystals of the dimeric species [In(L^2)Cl]$_2$. ^{1}H and ^{13}C NMR were able to confirm the metathesis reaction had taken place, however the characterisation of the structural composition of the complex was achieved by single crystal X-ray diffraction. Figure 2.11 shows the crystal structure of [In(L^2)Cl]$_2$ and selected bond lengths and angles are given in Table 2.12. Again, instead of the desired monomeric 5-coordinate species, a dimeric species was formed with two indium centres in a distorted octahedral geometry. In the absence of any coordinating solvent molecules the coordination sphere of each indium centre is filled by coordination of one oxygen atom of the opposite ligand moiety bridging between the two. The bridging In-O bonds (2.1809(15) Å) are longer than those to the non-

bridging oxygen atoms (2.1054(16) Å), which is expected due to the weaker nature of the bridging bonds. A slight increase in the In-N bond length to the bridging ketoimine moiety is also observed, which can be attributed to a removal of electron density from the delocalised system forming a 6-membered ring with the central indium atom. The bond lengths between the indium centre and the heteroatoms of the non-bridging ketoimine moiety are in good agreement with those found for [In(L^2)Cl·THF].

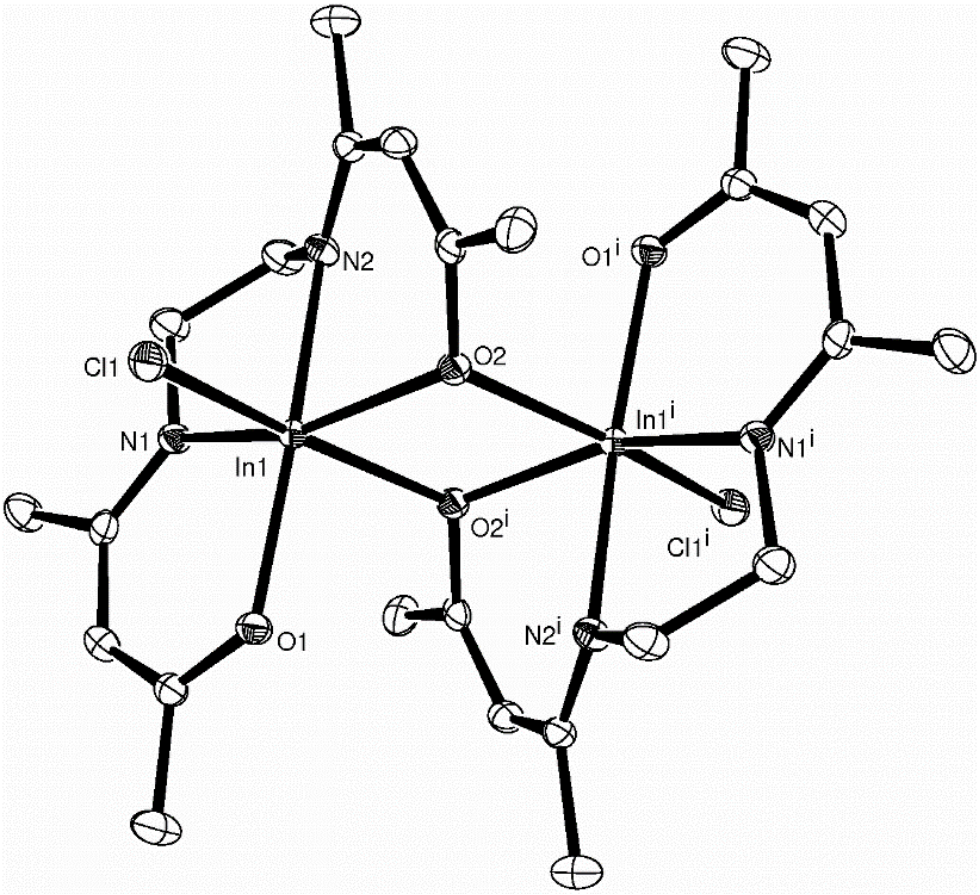

Figure 2.11 - The X-ray crystal structure of [In(L^2)Cl]$_2$. Data collection was carried out by the National Crystallography Service, Southampton. Structure solution was carried out by Dr. David Pugh.

Table 2.11 - Crystal data for [In(L^2)Cl]$_2$.

Crystal system	Monoclinic	
Space group	$P2_1/c$	
Unit cell dimensions	a = 11.276(4) Å	α = 90°
	b = 11.797(4) Å	β = 120.50(2)°
	c = 12.513(3) Å	γ = 90°

Table 2.12 - Selected bond lengths (Å) and angles (°) for $[In(L^2)Cl]_2$

N(1)-In(1)	2.1854(19)	O(2)-In(1)	2.1809(15)
N(2)-In(1)	2.2150(19)	Cl(1)-In(1)	2.4420(9)
O(1)-In(1)	2.1054(16)	O(2)-In(1)^{i}	2.2571(15)
O(1)-In(1)-O(2)	111.88(6)	N(1)-In(1)-O(2)^{i}	95.97(7)
O(1)-In(1)-N(1)	88.67(7)	N(2)-In(1)-O(2)^{i}	88.61(6)
O(2)-In(1)-N(1)	155.84(6)	O(1)-In(1)-Cl(1)	92.91(5)
O(1)-In(1)-N(2)	164.06(7)	O(2)-In(1)-Cl(1)	90.72(5)
O(2)-In(1)-N(2)	80.23(6)	N(1)-In(1)-Cl(1)	101.17(6)
N(1)-In(1)-N(2)	77.44(7)	N(2)-In(1)-Cl(1)	97.38(5)
O(1)-In(1)-O(2)^{i}	85.05(6)	O(2)^{i}-In(1)-Cl(1)	162.70(4)
O(2)-In(1)-O(2)^{i}	74.25(7)		

In the synthesis of a number of the aluminium and gallium analogues, the *in situ* deprotonation was found to be a viable route to the formation of the metal chloride *β*-ketoiminate complexes, notably simplifying the synthetic method. The attempted synthesis of $[In(L^2)Cl]_2$ by this method, however, resulted in the formation of a bimetallic species consisting of two six-coordinate indium centres linked by a bridging ligand group coordinating to the indium centres by the terminal oxygen atoms (Figure 2.12). Selected bond lengths and angles can be found in Table 2.14. The formation of $[\{In(L^2)Cl\}_2(L^2H_2)]$ was confirmed by ^{1}H and ^{13}C NMR and elemental analysis. The likely cause of this is incomplete conversion of the free ligand into its sodium salt, resulting in excess ligand being present in the subsequent reaction with $InCl_3$ and the formation of $[\{In(L^2)Cl\}_2(L^2H_2)]$ was found to be repeatable by reaction of the ligand sodium salt with $InCl_3$, with the deliberate addition of excess free ligand. The result displays the tendency of indium to form six-coordinate systems where a suitable coordinating molecule is present.

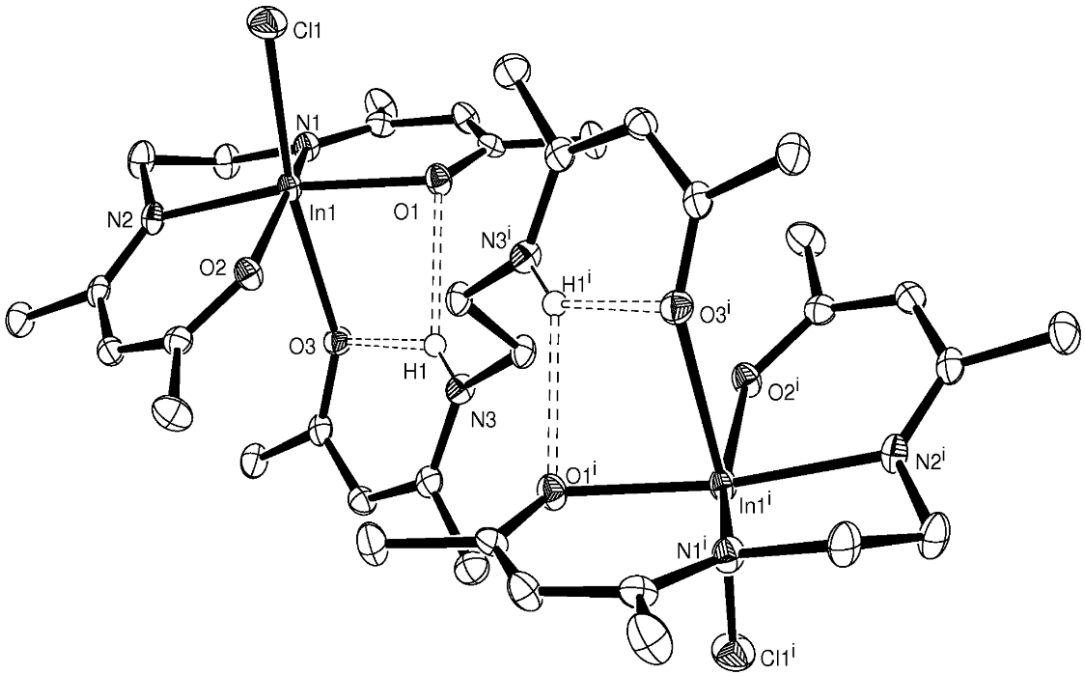

Figure 2.12 - The X-ray crystal structure of [{In(L^2)Cl}$_2$(L^2H_2)]. Data collection was carried out by the National Crystallography Service, Southampton. Structure solution was carried out by Dr. David Pugh.

Table 2.13 - Crystal data for [{In(L^2)Cl}$_2$(L^2H_2)].

Crystal system	Triclinic	
Space group	P-1	
Unit cell dimensions	a = 8.21910(10) Å	α = 73.9820(10)°
	b = 9.4727(2) Å	β = 75.8890(10)°
	c = 14.0874(2) Å	γ = 86.4360(10)°

Table 2.14 - Selected bond lengths (Å) and angles (°) for [{In(L^2)Cl}$_2$(L^2H_2)].

N(1)-In(1)	2.1859(15)	O(2)-In(1)	2.1134(13)
N(2)-In(1)	2.1815(15)	O(3)-In(1)	2.3865(13)
O(1)-In(1)	2.1248(13)	Cl(1)-In(1)	2.4488(5)
O(3)-In(1)-Cl(1)	168.40(3)	O(2)-In(1)-O(1)	101.40(5)
O(1)-In(1)-N(1)	89.01(5)	O(2)-In(1)-N(2)	87.10(5)
N(2)-In(1)-N(1)	78.43(6)		

2.3.2.8 Synthesis of [In(L^3)Cl]

Owing to the formation of the THF adduct [In(L^2)Cl·THF] and the implied preference of indium to form six-coordinate complexes where a suitable coordinating solvent is present, the synthesis of [In(L^3)Cl] was carried out in the absence of THF. Salt metathesis from the sodium salt L^3Na_2 and $InCl_3$ was again employed to drive the reaction forward by formation of the energetically favourable NaCl as a by-product. Yellow crystals were formed by dissolving the crude product in dichloromethane and layering with hexane. ^1H and $^{13}C\{^1H\}$ NMR spectra and elemental analysis were all consistent with the formation of [In(L^3)Cl]. The crystal structure of [In(L^3)Cl] was obtained by X-ray crystallography, confirming the formation of the expected five-coordinate indium complex. Selected bond lengths and angles are given in Table 2.16(A) and Table 2.16(B).

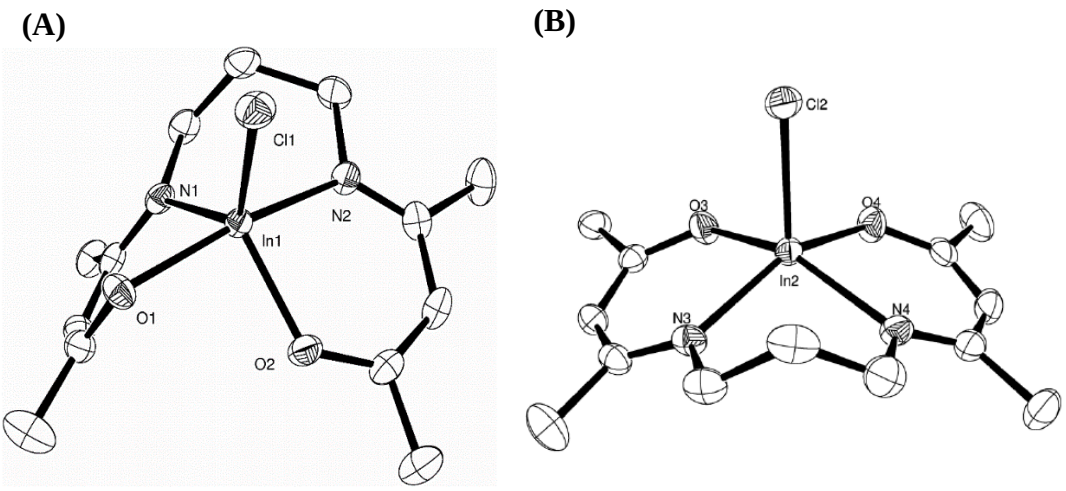

Figure 2.13 - X-ray crystal structure of [In(L^3)Cl](A) and [In(L^3)Cl](B). Data collection and structure solution was carried out by Dr. David Pugh.

Table 2.15 - Crystal data for [In(L^3)Cl].

Crystal system	Triclinic	
Space group	P-1	
Unit cell dimensions	a = 8.8098(8) Å	α = 94.3270(10)°
	b = 12.6328(11) Å	β = 95.4480(10)°
	c = 14.7568(13) Å	γ = 110.0580(10)°

The complex [In(L^3)Cl] crystallised into the triclinic crystal system with two molecules in the asymmetric unit with different geometries. The first showed a trigonal bipyramidal geometry ([In(L^3)Cl](A), Figure 2.13,

Table 2.16) whilst the second has a geometry half way between trigonal bipyramidal and square based pyramidal ([In(L^3)Cl](B)). The structure of [In(L^3)Cl](A) closely resembles that of the analogous gallium complex [Ga(L^3)Cl], as discussed in detail in section 2.3.2.5. Using the same method of geometry determination,[157] [In(L^3)Cl](A) was also found to adopt a distorted trigonal bipyramidal geometry (τ = 0.75), though not as close to perfect as that of [Ga(L^3)Cl] (τ = 0.86). As before, the equatorial positions are occupied by one nitrogen and one oxygen atom of opposite ketoimine moieties within the ligand, as well as the chlorine anion. The remaining nitrogen and oxygen atoms occupy the axial sites, with a O(1)-In(1)-N(2) bond angle of 166.56(8)°.

Table 2.16(A) - Selected bond lengths (Å) and angles (°) for In(L^3)Cl[A]

O(1)-In(1)	2.1222(18)	C(9)-C(10)	1.512(4)
O(2)-In(1)	2.0749(18)	C(10)-C(11)	1.429(4)
N(1)-In(1)	2.164(2)	C(11)-C(12)	1.363(4)
N(2)-In(1)	2.181(2)	C(12)-C(13)	1.505(4)
Cl(1)-In(1)	2.3826(7)	C(2)-O(1)	1.296(3)
C(1)-C(2)	1.499(4)	C(12)-O(2)	1.313(3)
C(2)-C(3)	1.378(4)	C(4)-N(1)	1.313(4)
C(3)-C(4)	1.423(4)	C(10)-N(2)	1.308(4)
C(4)-C(5)	1.508(4)		
O(2)-In(1)-N(1)	121.35(8)	N(1)-In(1)-Cl(1)	124.30(6)
O(2)-In(1)-Cl(1)	114.13(6)	O(1)-In(1)-N(2)	166.56(8)

Bond lengths within the molecular structure of [In(L^3)Cl](A) are very close to those found in both [In(L^2)Cl·THF] and [Ga(L^3)Cl]. Internal C-C bond lengths (1.398 Å)

suggest the same delocalisation of the ligand ketoimine moieties, whilst In-O and In-N bond lengths are of comparable magnitude to those in [In(L^2)Cl·THF]. The nature and magnitude of the bond lengths and the subsequent inferences follow the same pattern as found in [Ga(L^2)Cl] and [In(L^2)Cl·THF], a detailed discussion of which can be found in sections 2.3.2.4 and 2.3.2.7, respectively. Bonds lengths within the 6-membered ring formed by the indium cation and the ketoiminate ligand show a delocalisation of the electron density within the ring.

The bond lengths in the second geometrically distinct molecule within the assymetric unit, [In(L^3)Cl](B), are very similar to those in [In(L^3)Cl](A), though bond angles are more distorted towards a square-based pyramidal geometry (τ = 0.03, Table 2.16(B)).

Table 2.16(B) - Selected bond lengths (Å) and angles (°) for In(L^3)Cl[B].

O(3)-In(2)	2.0964(19)	N(4)-In(2)	2.196(2)
O(4)-In(2)	2.1132(19)	Cl(2)-In(2)	2.4002(7)
N(3)-In(2)	2.183(2)		
O(3)-In(2)-N(4)	153.78(9)	N(3)-In(2)-N(4)	90.81(9)
O(4)-In(2)-N(3)	151.70(8)	O(3)-In(2)-Cl(2)	99.38(6)
O(3)-In(2)-O(4)	82.71(8)	O(4)-In(2)-Cl(2)	101.06(6)
O(3)-In(2)-N(3)	87.63(8)	N(3)-In(2)-Cl(2)	106.74(6)
O(4)-In(2)-N(4)	86.44(9)	N(4)-In(2)-Cl(2)	106.12(7)

The formation of a 5-coordinate monomeric species is in contrast to the pattern observed when employing the ethylene-bridged ligand (L^2H_2), where the exclusive formation of 6-coordinate species was observed by a range of synthetic procedures. When considering the ethylene-bridged ligand systems, it was determined that the ligand lacked the flexibility to 'wrap around' the larger indium cation (compared to the analogous gallium species), thus leaving space within the coordination sphere for the coordination of additional molecules. In contrast, it has been observed that the additional length and flexibility of the linking group offered by the propylene-based ligand system is sufficient to fill the coordination sphere of the indium cation and

thus prevent either oligomerisation or additional coordination of solvent molecules. This observation is of significance in the design of molecular precursors for CVD applications, given the influence of oligomerisation on the thermal properties of a compound. The ability to tune the length of the bridging group to the size of the metal cation has, in this case, enabled the formation of a monomeric indium species and thus displays the potential 'tuneability' of the class of ligand for the synthesis of molecular precursors.

2.3.2.9 Synthesis of [In(L^4)Cl]

Given the ability of the propylene-bridged ligand system to stabilise a 5-coordinate indium chloride complex (in contrast to the ethylene-bridged systems which formed exclusively 6-coordinate species), it was anticipated that the larger tetramethylene-bridged ligand derivative, L^4H_2, would also be suitable for the formation of a 5-coordinate, monomeric complex. The synthesis was therefore carried out by the same synthetic pathway employed for the other metal chloride complexes (Scheme 2.10), with the *in situ* deprotonation of L^4H_2 in THF followed by salt metathesis with $InCl_3$ in refluxing THF. Whilst it was possible to recrystallise the crude product by solvent diffusion of hexane into a concentrated CH_2Cl_2 solution, the purified product was microcrystalline and not suitable for single crystal X-ray diffraction analysis.

^{1}H NMR spectroscopy indicated the formation of the desired indium chloride complex [In(L^4)Cl] on the basis of the absence of an NH resonance and the characteristic downfield chemical shift of other ligand resonances observed upon coordinate to a metal centre. Of note was the absence of any resonances corresponding to a coordinated THF molecule, (*cf.* [In(L^2)Cl·THF], section 2.3.2.7), or of any resonances that could be attributed to presence of excess free ligand (*cf.* [{In(L^2)Cl}$_2$(L^2H_2)], section 2.3.2.7). Whilst no diffraction data is available for the determination of the molecular structure of the complex, should the 5-coordinate monomer not be stable it would be expected that the sixth coordination site of the indium cation would be filled by a coordinating THF molecule in preference to dimerisation, as has been previously observed in the formation of the ethylene-bridged analogue. ^{1}H NMR shows this not to be the case. ^{13}C NMR, elemental analysis and mass spectroscopy also supported the formation of the expected

product, though the structural identity cannot be unconditionally confirmed in the absence of further structural characterisation.

2.3.2.10 Attempted chloride-replacement reactions

The dianionic nature of the ligand systems coupled with the trivalency of the metal centres (M^{3+}) allows for further manipulation of the precursor through the variation of the third 'co-ligand'. Indeed, choice of the co-ligand has the potential to significantly influence the volatility, solubility, decomposition profile and general deposition efficacy of the precursor and is thus of key importance. Since the co-ligand forms a direct M-E bond with the metal centre, there is also potential for incorporation/contamination of the bonded element, E, in the deposited film. Whilst the presence of direct M-Cl bonds gives rise to the potential for chlorine contamination in the resultant films, this is not necessarily an issue and reports exist on the chlorine-free deposition of group 13 based materials from single-source precursors containing direct M-Cl bonds.[164] However, substitution in this position does offer the potential for tuning the precursor and thus attention was directed towards the reactivity of the chloride complexes to ligand substitution. In particular, the inclusion of additional oxygen donors was of interest owing to the potential to increase the metal to oxygen ratio within the precursor and encouraging the deposition of stoichiometric M_2O_3 films.

Initial attempts to replace the chloride focussed on transmetallation with a range of sodium and potassium alkoxides, according to equation 2.6:

$$M(L)Cl + M'OR \rightarrow M(L)OR + M'Cl \downarrow \qquad (2.6)$$

where M = Al, Ga, In; M' = Na, K; R = ^{i}Pr, ^{t}Bu.

To ensure their purity, the metal alkoxides were freshly sublimed under vacuum onto a cold finger prior to use. Whilst in most cases a reaction was observed to take place, as evidenced by the precipitation of the metal chloride by-product, the products obtained were in all cases isolated as highly impure oils which could not be purified by washing with solvents, crystallisation or sublimation. In some cases ^{1}H and ^{13}C NMR indicated the formation of the desired products, however a significant number of impurities were also found to be present and further analysis by mass spectrometry and elemental analysis did not provide satisfactory data to support their

formation. Attempts at transmetallation with alkali metal amides afforded similar results and no complexes of the form $[M(L)NR_2]$ could be formed with sufficient characterisation.

An alternative route to the alkoxide derivatives was thus attempted *via.* direct reaction of the *β*-ketoimine ligands with the metal *tris*-alkoxides (Equation 2.7):

$$M(OR)_3 + LH_2 \rightarrow M(L)OR + 2\ ROH \uparrow \qquad (2.7)$$

where M = Al, Ga, In; R = ^{i}Pr, ^{t}Bu.

Starting materials were again purified via sublimation prior to use, however the reactions again only afforded highly impure, oily products which could not be fully characterised. Attention was therefore directed towards the synthesis of organometallic group 13 *β*-ketoiminate complexes, as discussed in the following section.

2.3.3 Organometallic group 13 metal β-ketoiminate complexes

Whilst the use of MCl_3 starting reagents provides a simple and clean route to the corresponding metal chloro-*β*-ketoiminate complexes, the presence of chloride ions is not necessarily ideal in the formation of precursors suitable to CVD applications, as has been discussed. The synthesis of analogous complexes with alternative groups to chloride which are more likely to be removed during a decomposition process was therefore attempted. For this reason, focus turned to the synthesis of organometallic group 13 *β*-ketoiminate containing alkyl co-ligands.

2.3.3.1 The synthesis of [Ga(L^2)Me] and [L^2(GaMe$_2$)$_2$]

The methyl complex [Ga(L^2)Me] was formed by the methane elimination reaction between $GaMe_3$ and one equivalent of the ligand L^2H_2, as shown in Equation 2.8.

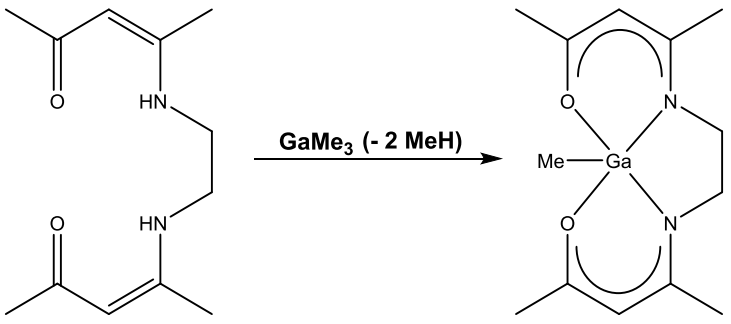

(2.8)

Due to the reactivity of $GaMe_3$, the addition was carried out at -78 °C and the reaction mixture subsequently warmed to room temperature, before being further heated to reflux. Evolution of gas was observed from the reaction solution at *ca.* 60 °C, attributed to the production of methane. After refluxing for 16 hours, ^{1}H NMR analysis of the product showed the presence of two sets of resonances, one set corresponding to residual free ligand within the reaction mixture, and the other implying the formation of the desired product. Due to similarity in the solubilities of the product and the free ligand, complete separation by solvent extraction was not possible. A hot hexane solution of the mixture was allowed to cool very slowly to room temperature, yielding yellow crystals which were suitable for single crystal X-ray analysis. Structural characterisation by this method showed the formation of the desired monomeric, 5-coordinate gallium methyl complex [Ga(L^2)Me]. Figure 2.14 shows the crystal structure of [Ga(L^2)Me] and selected bond lengths and angles are given in Table 2.18.

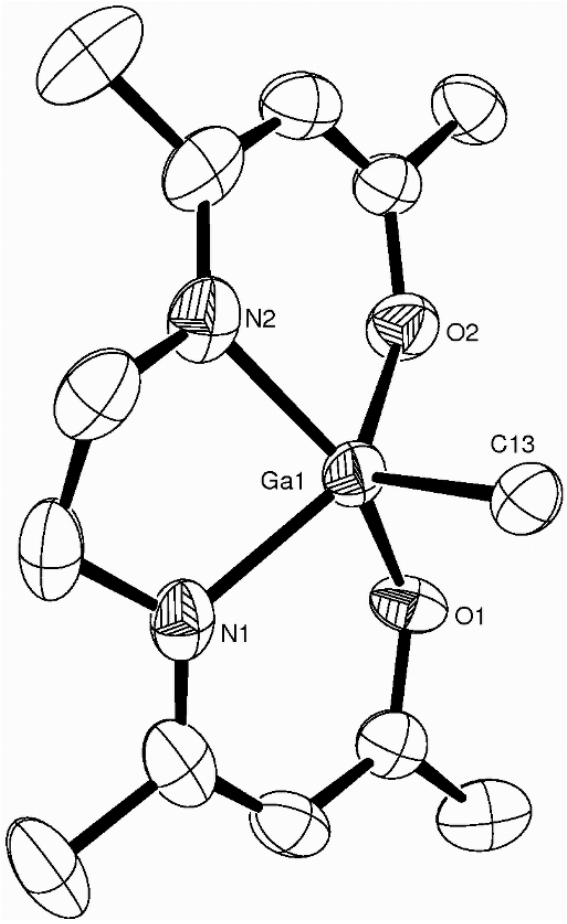

Figure 2.14 - X-ray crystal structure of Ga(L^2)Me. Data collection was carried out by the National Crystallography Service, Southampton. Structure solution was carried out by Dr. David Pugh.

Table 2.17 - Crystal data for Ga(L^2)Me.

Crystal system	Monoclinic	
Space group	$P2_1/c$	
Unit cell dimensions	a = 8.148(2) Å	α = 90°
	b = 13.014(3) Å	β = 110.298(11)°
	c = 14.885(3) Å	γ = 90°

Table 2.18 - Selected bond lengths (Å) and angles (°) for Ga(L^2)Me.

Ga(1)-O(1)	1.947(4)	C(8)-C(9)	1.515(8)
Ga(1)-O(2)	1.942(4)	C(9)-C(10)	1.415(8)
Ga(1)-N(1)	2.034(5)	C(10)-C(11)	1.365(8)
Ga(1)-N(2)	2.030(5)	C(11)-C(12)	1.495(7)
Ga(1)-C(13)	1.971(5)	O(1)-C(2)	1.295(6)
C(1)-C(2)	1.500(8)	O(2)-C(11)	1.302(6)
C(2)-C(3)	1.374(7)	N(1)-C(4)	1.303(7)
C(3)-C(4)	1.412(8)	N(2)-C(9)	1.312(7)
C(4)-C(5)	1.514(7)		
O(2)-Ga(1)-N(1)	137.68(16)	O(1)-Ga(1)-C(13)	101.8(2)
O(2)-Ga(1)-C(13)	109.1(2)	O(2)-Ga(1)-O(1)	81.70(15)
C(13)-Ga(1)-N(1)	108.8(2)	O(2)-Ga(1)-N(2)	88.28(17)
O(1)-Ga(1)-N(2)	149.39(17)	N(1)-Ga(1)-N(2)	80.37(19)
O(1)-Ga(1)-N(1)	87.75(17)	N(2)-Ga(1)-Cl(1)	113.18(19)

The bond lengths found in the crystal structure of [Ga(L^2)Me] show a similar pattern to those seen in the related chloride complex [Ga(L^3)Cl]. The average Ga-O bond distance of 1.94 Å is only slightly longer than the 1.92 Å average bond distance seen in [Ga(L^3)Cl]. However, [Ga(L^2)Me] shows two identical Ga-O bond lengths, whereas [Ga(L^3)Cl] has a difference of 0.1 Å between the two. The large thermal ellipsoids observed within the structure suggest some thermal motion within the

crystal and thus the identical Ga-O bond lengths are also likely to arise from this thermal motion. The bond lengths between the carbons of the ketoimine moiety backbone again display the delocalised nature of the bonding within the 6-membered ring formed of the three central carbon atoms and the nitrogen, oxygen and gallium atoms. The terminal C-C bond lengths (e.g. C1-C2) are in keeping with the expected bond lengths for a C-C single bond (average 1.506Å) whereas the C-C bond lengths within the 'rings' (average 1.3915 Å) lie in between those expect for C-C single and double bonds (*ca.* 1.5 and 1.3 Å respectively).[160] This same pattern is seen for the C-O and C-N bond lengths (average 1.2985 and 1.3075 Å respectively), as was also discussed for the chloride complex [Ga(L^3)Cl], once again showing the delocalisation of bonding within this 'ring'. The Ga-C bond length of 1.971 Å is consistent with those seen for similar alkyl-substituted gallium complexes.[165] Using Addison's method of analysis for the determination of the geometry of the central gallium atom,[157] [Ga(L^2)Me] was found to have $\tau = 0.19$ indicating the gallium atom lies in a slightly distorted square-based pyramidal geometry.[157] The basal plane is formed of the N_2O_2 unit of the ketoiminate ligand, with the substituent methyl group occupying the axial position. This is in contrast to the geometries seen for the majority of chloride complexes discussed earlier, which tended towards trigonal bipyramidal geometries.

As discussed, complete separation of the product from the free ligand starting material was not possible. ^{1}H and ^{13}C NMR analysis of the crystals formed by cooling of a hexane solution still showed the presence of a small amount of the free ligand. However, the resonances corresponding to the product were in agreement with the findings of the structural characterisation and could easily be distinguished from those corresponding to the free ligand. Resonances in the ^{1}H NMR spectrum at 4.9 ppm (2H, singlet, C*H*), 3.39 – 3.51 ppm (4H, multiplet, CH_2CH_2), 2.01 ppm (6H, singlet, CH_3CO) and 1.96 ppm (6H, singlet, CH_3CN) in a 1:2:3:3 ratio showed the expected chemical shift with respect to the free ligand and were consistent with the formation of [Ga(L^2)Me]. The formation of a mono-methyl complex was confirmed by the presence of a three-proton singlet appearing at -0.46 ppm, corresponding to Ga-CH_3. Within the ^{13}C NMR spectrum, resonances at 182.1 and 171.0 ppm signified the *C*O and *C*N carbons of the *β*-ketoiminate backbone respectively, the central methine of the backbone was observed at 97.5 ppm and the terminal methyl

carbons at 26.9 and 21.6 ppm. The ethylene bridging group displayed a resonance at 45.9 ppm.

Mass spectrometry showed the protonated parent ion at 307 *m/z*, as well as the loss of CH_3 by a fragment at 291 *m/z*. Elemental analysis of the sample gave values close to those expected, though a slight discrepancy was found, likely to be due to the presence of remnant free ligand within the sample.

The reaction was repeated and the reflux allowed to continue for 64 hours in an attempt to drive the reaction to completion. ^{1}H NMR analysis of the reaction product showed only trace amounts of free ligand remaining, as determined by the absence of the characteristic NH resonance. However, two sets of resonances were again observed in a ratio of *ca.* 1:4 indicating the formation of two products. The major product was identified as [Ga(L^2)Me] by comparison of the two ^{1}H NMR spectra. By analysis of the integrals of the second set of resonances, the minor product was identified as the bimetallic species [L^2($GaMe_2$)$_2$], as shown in Equation 2.9, formed by the reaction of two equivalents of $GaMe_3$ with one equivalent of L^2H_2. To confirm this observation, the reaction was again repeated with a $GaMe_3$ to L^2H_2 ratio of 2:1 and under milder conditions (Equation 2.9). The ^{1}H NMR spectrum of the product was consistent with the formation of [L^2($GaMe_2$)$_2$] as the major product, though resonances corresponding to a small amount of free ligand were also present. As shown in Figure 2.15, peaks were observed at δ 4.89 (C*H*), 3.35 (C*H*$_2$C*H*$_2$), 2.00 (C*H*$_3$CO) and 1.93 ppm (C*H*$_3$CN) in a 1:2:3:3 ratio, as expected for the *β*-ketoiminate ligand. However, the identity of the bimetallic product was determined by the presence of a 12H singlet at δ -0.34 ppm, corresponding to $GaMe_2$.

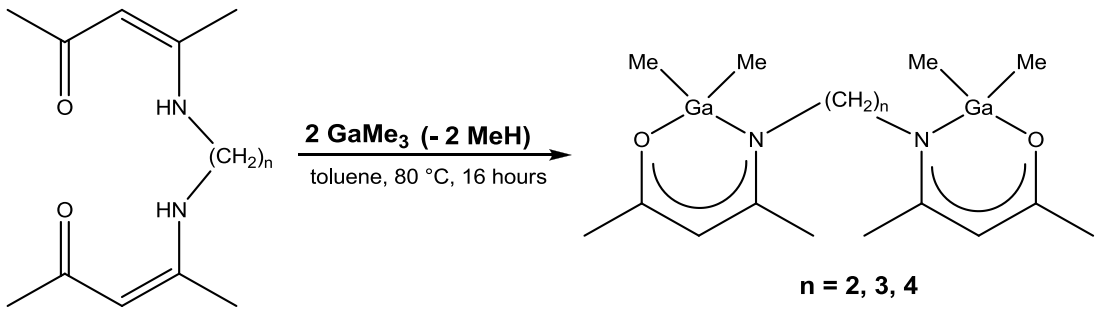

(2.9)

The enhanced resolution offered by ^{13}C NMR enabled clear separation of the resonances associated with [L^2($GaMe_2$)$_2$] and those of the free ligand (Figure 2.16).

Resonances were observed at δ 181.4 ($CH_3\underline{C}O$), 172.4 ($CH_3\underline{C}N$), 98.4 ($\underline{C}H$), 48.0 ($\underline{C}H_2\underline{C}H_2$), 26.6 ($\underline{C}H_3CN$) and 21.2 ppm ($\underline{C}H_3CO$), consistent with the formation of $[L^2(GaMe_2)_2]$ and only one Ga-CH_3 resonance was present at δ -7.1 ppm, indicating that none of the monomeric species $[Ga(L^2)Me]$ was present in the mixture. Heteronuclear single quantum coherence (HSQC) spectroscopy was used to correlate those resonances belonging to $[L^2(GaMe_2)_2]$ and those belonging to the free ligand with the resonances found in the ^1H NMR spectrum (Figure 2.17).

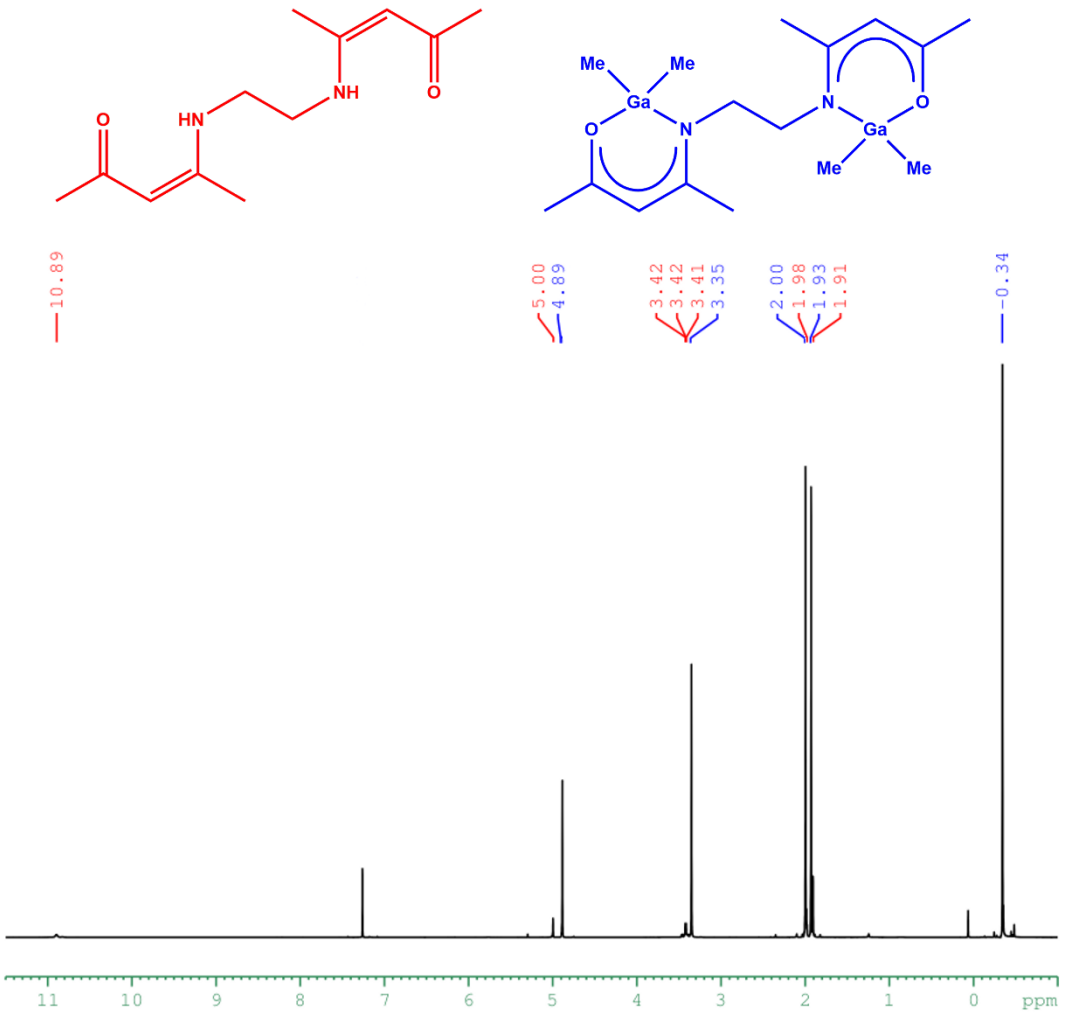

Figure 2.15 - ^1H NMR spectrum of a mixture of the bimetallic species $[L^2(GaMe_2)_2]$ (blue) and the free ligand L^2H_2 (red).

Mass spectrometry was consistent with the formation of the bimetallic species, showing a fragment at 407 *m/z*, corresponding to the loss of a methyl group from the parent ion. A fragment at 307 *m/z* could either correspond to the loss of $GaMe_3$ from $[L^2(GaMe_2)_2]$, or from the presence of the monomeric species $[Ga(L^2)Me]$, however

the former is most likely given the absence of any resonances associated with [Ga(L^2)Me] in the NMR spectra. Further loss of CH_3 gave rise to the only other significant peak at 291 *m/z*. Elemental analysis showed good agreement for H and N ratios, however the proportion of carbon within the sample was not in agreement with the calculated values. (Anal. calcd. for $C_{16}H_{30}N_2O_2Ga_2$: C, 45.55; H, 7.17; N, 6.64. Found: C, 43.37; H, 7.03; N, 6.69) This is likely to be a result of the inability to separate the components of the product mixture leading to an impure sample being submitted for analysis.

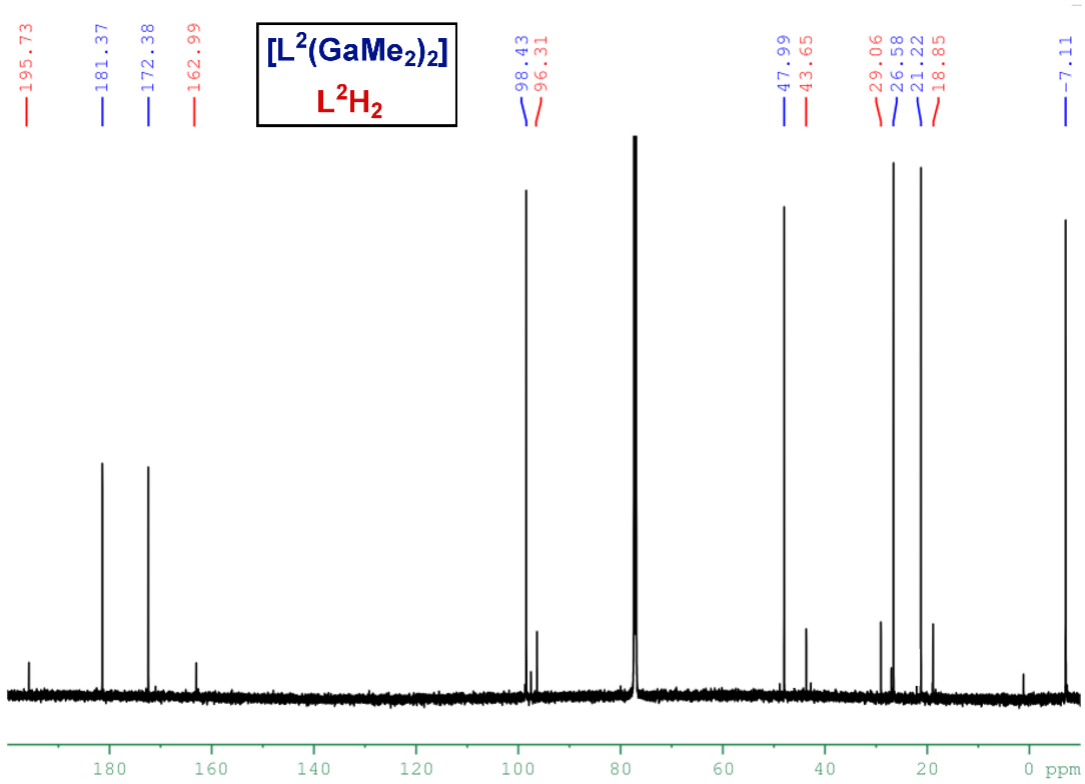

Figure 2.16 - ^{13}C NMR spectrum of a mixture of the bimetallic species [$L_2(GaMe_2)_2$] (blue) and the free ligand L_2H_2 (red).

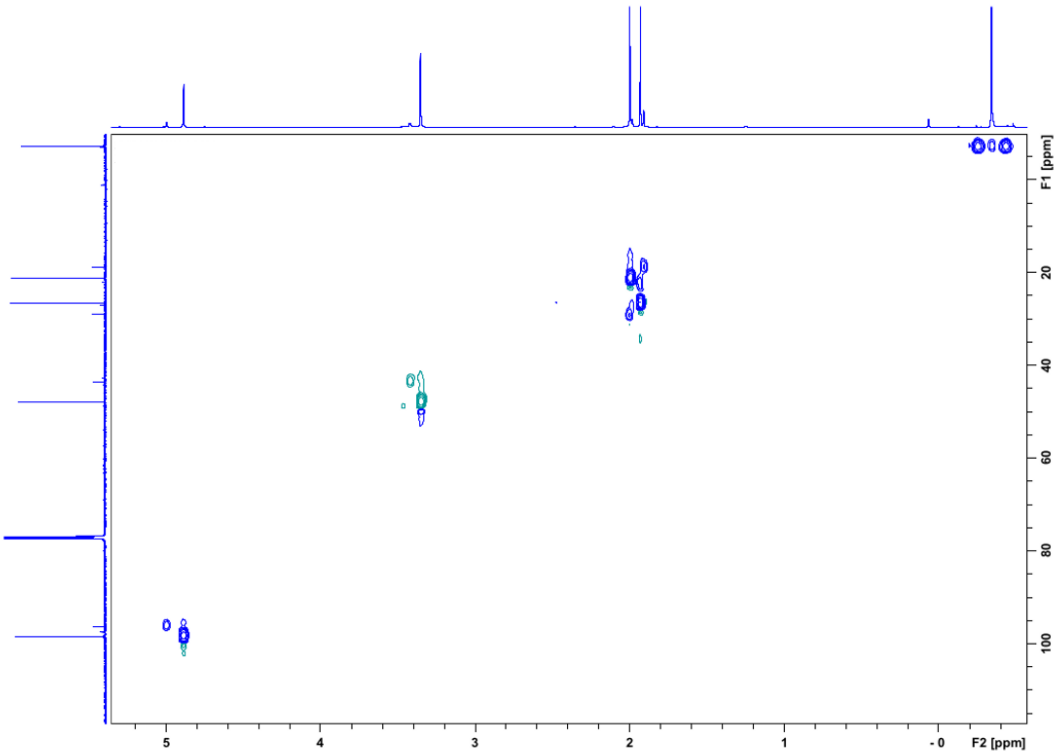

Figure 2.17 - HSQC spectrum showing proton-carbon correlation within a sample mixture of [$L^2(GaMe_2)_2$] and L^2H_2. X-axis: ^1H NMR spectrum; Y-axis: ^{13}C NMR spectrum.

2.3.3.2 Synthesis of [$L^n(GaMe_2)_2$] (n = 3, 4)

In an attempt to form the propylene and tetramethylene analogues of the mono-metallic methyl gallium complex, the reactions between trimethyl gallium and the free ligands L^3H_2 and L^4H_2 were carried out by the same method used for the synthesis of [Ga(L^2)Me]. The ligands were added to trimethyl gallium in toluene at -78 °C, before being warmed slowly to *ca.* 80 °C. The evolution of gas was observed at *ca.* 50 – 60 °C, suggesting that the methane elimination reaction had taken place. Having been stirred at an elevated temperature for *ca.* 16 hours, the reaction mixture was filtered and solvent removed from the filtrate *in vacuo*. ^1H NMR of both reaction products showed the presence of two sets of resonances, the first corresponding to the free ligand (including the presence of the characteristic NH proton) and the second presumably corresponding to the methane elimination product. In both cases the ratio between the two sets of resonances was 1:1. An incomplete reaction was one possible explanation for these observations, however, since the evolution of methane gas had ceased by the time the reaction was stopped this seemed unlikely. Furthermore, the peak corresponding to the organometallic protons (Ga-Me) showed an integration of 12H, as opposed to the expected 3H for

the formation of the desired product. This led to the conclusion that a mono-substitution had taken place with each equivalent of the free ligand reacting with two equivalents of $GaMe_3$, resulting in the formation of the bimetallic species $[L^n(GaMe_2)_2]$ (where n = 3, 4), as shown in Equation 2.9.

To confirm this conclusion, the reactions were repeated with a ligand to metal stoichiometry of 1:2, resulting in the formation of the bimetallic species. The analytical data for both propylene and tetramethylene derivatives were very similar, thus only data relating to the propylene derivative $[L^3(GaMe_3)_2]$ will be used in this discussion. Full analytical details can be found in the following experimental section.

The absence of any resonances corresponding to the presence of the free ligand (in particular that of the NH protons) within the ^1H NMR spectrum immediately confirmed that the reaction had gone to completion. A 12H peak at -0.38 ppm corresponds to the organometallic methyl protons, which show a slight upfield shift with respect to the unreacted starting material $GaMe_3$ (-0.18 ppm).[166] The upfield chemical shift of the resonance arises from the inductive effect of the electropositive gallium centre. The added electron density donated on coordination of the *β*-ketoiminate ligand provides further shielding of the methyl protons, resulting in an upfield chemical shift with respected to $GaMe_3$.

Mass spectrometry confirmed the formation of the bimetallic product by the detection of a fragment at 419 *m/z*, corresponding to the molecular ion with loss of a CH_3 group. A fragment at 321 *m/z* corresponds to the loss of $GaMe_3$, perhaps forming the stable $[Ga(L^3)Me]$ in the fragmentation process, and loss of a further CH_3 resulted in the detection of a fragment at 305 *m/z*. The mass spectrum of $[L^4(GaMe_2)_2]$ shows an identical fragmentation pattern, again confirming the formation of the bimetallic species. Elemental analysis for both products showed a discrepancy from the calculated values (>0.5 %), which is attributed to the retention of solvent within the sample given the absence of impurities suggested by the other characterisation data.

2.3.3.3 Synthesis of [In(L^n)Me] (n = 2, 3)

In the same way as for the analogous gallium complex $[Ga(L^2)Me]$ discussed above, $[In(L^2)Me]$ and $[In(L^3)Me]$ were both synthesised by methane elimination from the reaction of $InMe_3$ with the ligands L^1H_2 and L^2H_2 respectively. Unlike the gallium

complex, however, in the case of both indium complexes 16 hrs was sufficient for the reactions to go to completion. Both yielded products showing no residual ligand within their NMR spectra. Attempts to recrystallise the indium complexes by the same method used for [Ga(L^2)Me] were unsuccessful and thus neither indium compound has been crystallographically characterised. NMR data are consistent with the formation of the desired product, with both compounds showing a resonance correlating to the In-CH_3 protons in the expected ratio at δ -0.46 and -0.07 ppm for [In(L^2)Me] and [In(L^3)Me] respectively. Mass spectrometry also suggested the monomeric species were formed by the presence of the parent ion peaks in both cases. However, elemental analysis to determine the composition of the products was in both cases inconsistent with the theoretical percentages calculated for the desired products. Whilst this is likely to be due to either significant levels of impurities or residual solvent within the samples or to decomposition of the compounds during the analytical procedure, recrystallisation of the products to yield crystals suitable for crystallographic analysis is still desired in order to provide sufficient evidence for the structural nature of these indium complexes.

2.3.4 β-ketoiminate-stabilised gallium hydride complexes

As discussed earlier, group 13 metal hydrides are attractive as potential precursors for the deposition of high quality materials due to the low mass and clean decomposition offered by hydride as a co-ligand. With a view to synthesising such hydride complexes by ligand substitution, the gallium chloride complexes [Ga(L^2)Cl] and [Ga(L^3)Cl] were reacted with a variety of hydride sources (LiH, NaH, $NaBH_4$, $LiAlH_4$, $NaBEt_3H$) in THF (Scheme 2.11). However, no reaction was observed in all cases and ^{1}H NMR analysis showed only the presence of starting material. A similar result was found in the attempted chloride replacement reactions of similar donor-functionalised alkoxide gallium complexes.[156]

Owing to the low reactivity of the chloride complexes towards ligand exchange, attention was turned to the use of the trimethylamine adduct of gallane [$GaH_3(NMe_3)$] as a starting material. Given the thermal instability of the gallane adduct, it was prepared freshly as an ethereal solution prior to its use according to a literature procedure.[135] Lithium gallium hydride ($LiGaH_4$) was synthesised by the reaction of $GaCl_3$ with a large excess of LiH in Et_2O at -78 °C, which was allowed to warm to room temperature and stirred overnight. The Et_2O solution of $LiGaH_4$ was

then filtered from the excess LiH / LiCl residue, cooled again to -78 °C and reacted directly with a single equivalent of the relevant *β*-ketoimine, according to Scheme 2.11. Since the reagents and products of this reaction are highly sensitive to air and moisture, it was necessary to carry out all manipulations using strict experimental procedures. All synthetic work was carried out using standard Schlenk techniques and all glassware was flame-dried prior to use. Without such precautions, decomposition of the materials was observed by the formation of grey, metallic gallium within the reaction mixture. Particular complications with decomposition arose during the filtration steps. Initially supernatants were isolated by filtration through a fritted funnel fitted with celite, however, this often resulted in decomposition, presumably due to the inability to completely remove all traces of moisture from the glassware and/or celite by flame drying prior to use. Eventually the most practical method was found to be filtration *via* cannula, which was fitted with a glass filter paper and dried for a number of hours. It was also necessary to allow the cannula to cool under nitrogen prior to use, as the reagents also showed significant thermal sensitivity, often decomposing on exposure to temperatures in excess of *ca.* 25 °C.

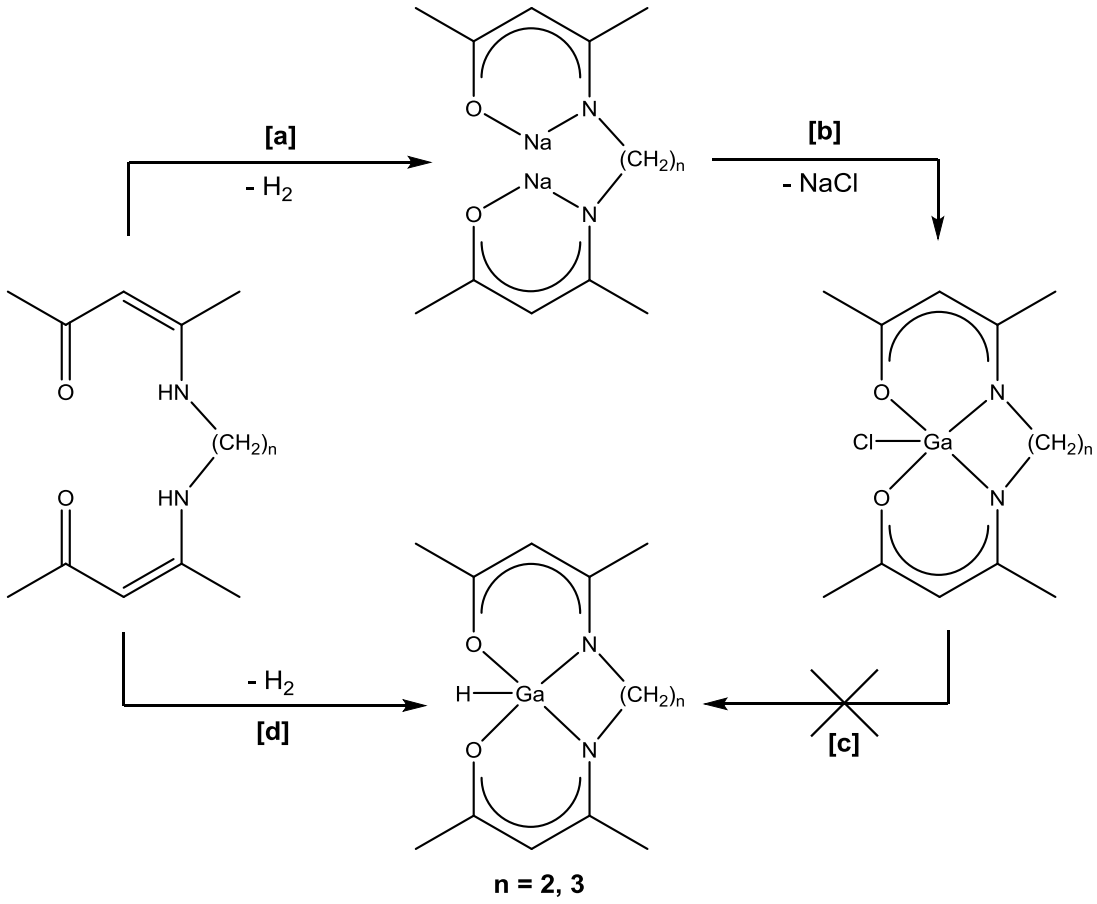

Scheme 2.11 - Reaction scheme for the synthesis of gallium β-ketoiminate hydride complexes. Conditions: [a] 2 NaH, THF, RT; [b] hexane, RT / THF, reflux; [c] LiH/NaH/$NaBH_4$/$LiAlH_4$/$NaBEt_3H$, THF, −78 °C – RT; [d] [GaH_3·NMe_3], Et_2O, −78 °C – RT.

2.3.4.1 Synthesis of [Ga(L^2)H]

The initial synthesis of [Ga(L^2)H], including reactivity studies of [Ga(L^2)Cl] with reducing agents, was carried out by David Pugh. However, the synthesis was repeated by the author in order to gain crystallographic analysis.

The β-ketoiminate-stabilised hydride complex [Ga(L^2)H] was synthesised by the direct reaction of *β*-ketoimine L^2H_2 with a freshly prepared ethereal solution of [$GaH_3(NMe_3)$] in Et_2O, as shown in Scheme 2.11 and described above. The reaction was initially cooled to -78 °C and allowed to warm very slowly to room temperature after the addition had taken place. On warming, the evolution of gas from the reaction mixture was observed, correlating to the production of H_2 as a reaction by-product, as well as the release of trimethylamine from the gallane adduct upon reaction. Initial attempts to crystallise the reaction product from a concentrated

toluene solution cooled to -20 °C only resulted in the formation of a microcrystalline solid, however yellow platelet crystals were formed by slow evaporation of CH_2Cl_2 from a solution of the product over a number of days, which were suitable for single crystal X-ray diffraction. Figure 2.18 shows the X-ray crystal structure of [Ga(L^2)H] and selected bond lengths and angles are given in Table 2.20.

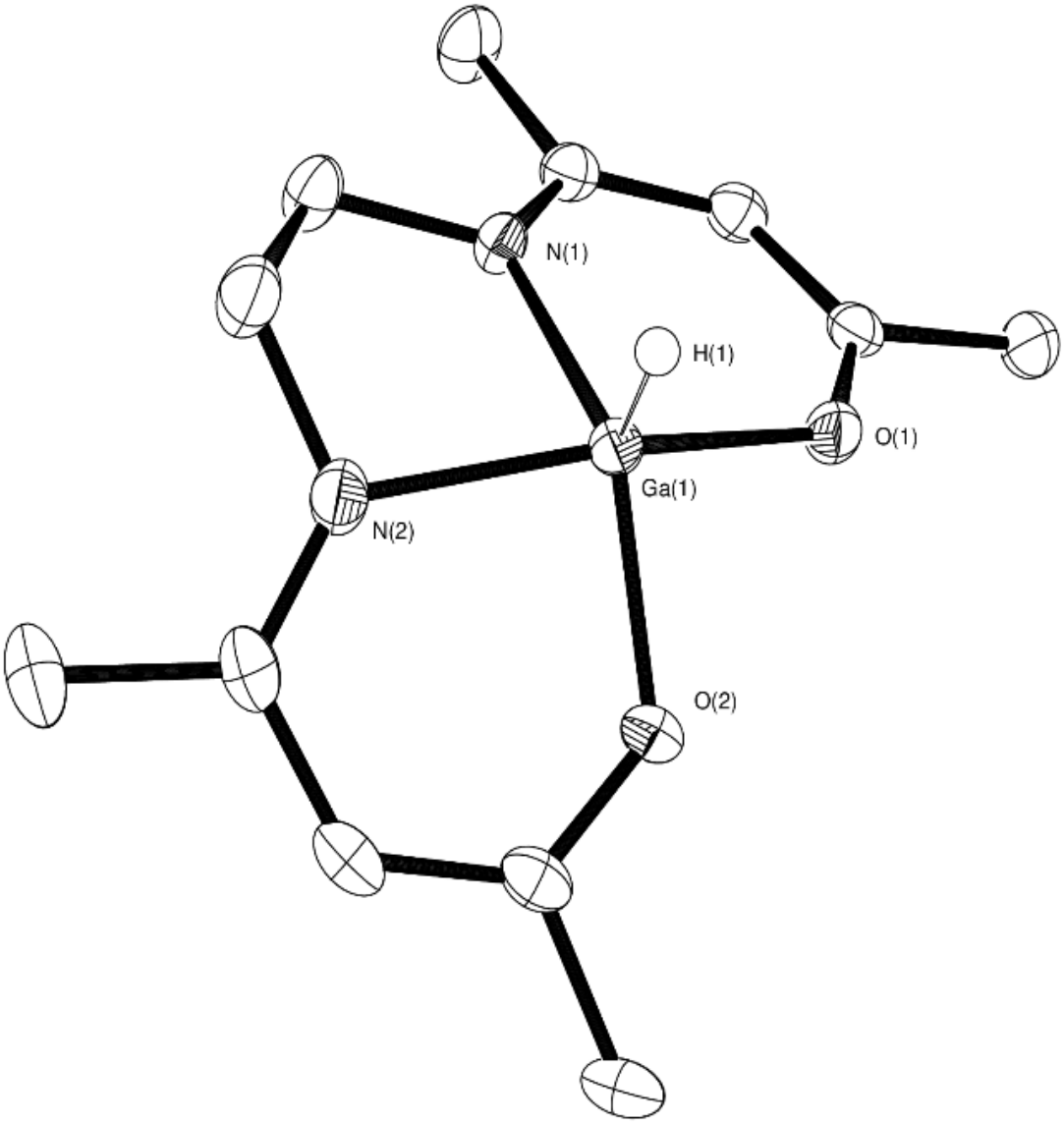

Figure 2.18 - X-ray crystal structure of Ga(L^2)H. Data collection was carried out by the National Crystallography Service, Southampton. Structure solution was carried out by the author.

Table 2.19 - Crystal data for [Ga(L^2)H]

Crystal system	Monoclinic	
Space group	$P2_1/c$	
Unit cell dimensions	a = 7.9220(2) Å	α = 90°
	b = 12.0209(3) Å	β = 93.0450(18)°
	c = 13.5746(5) Å	γ = 90°

Table 2.20 - Selected bond lengths (Å) and angles (°) for [Ga(L^2)H].

Ga(1)-O(1)	1.9563(17)	N(1)-C(4)	1.312(3)
Ga(1)-N(1)	2.0242(19)	C(1)-C(2)	1.506(3)
Ga(1)-O(2)	1.9368(16)	C(2)-C(3)	1.377(3)
Ga(1)-N(2)	2.043(2)	C(3)-C(4)	1.415(3)
Ga(1)-H(1)	1.56(2)	C(5)-C(4)	1.507(3)
O(1)-C(2)	1.289(3)	C(6)-C(7)	1.519(4)
O(2)-Ga(1)-O(1)	85.18(7)	N(1)-Ga(1)-N(2)	79.58(8)
O(2)-Ga(1)-N(1)	136.57(8)	O(2)-Ga(1)-H(1)	113.2(8)
O(1)-Ga(1)-N(1)	89.98(7)	O(1)-Ga(1)-H(1)	109.3(8)
O(2)-Ga(1)-N(2)	88.80(8)	N(1)-Ga(1)-H(1)	109.1(8)
O(1)-Ga(1)-N(2)	157.49(8)	N(2)-Ga(1)-H(1)	93.0(8)

Initial characterisation of the product was carried out by ^{1}H NMR in C_6D_6, showing no resonance associated with the NH proton. The formation of the desired product was further indicated by the presence of a very broad singlet peak at 5.56 ppm, characteristic of a gallium hydride.[129, 136, 144, 156, 167-170] The broadening is due to the two quadrupolar gallium nuclei, ^{69}Ga and ^{71}Ga, with I = 3/2. The identity of the hydride complex was confirmed by the presence of a singlet at 4.80 ppm (C<u>*H*</u>), multiplets at 2.80-2.89 and 2.58-2.68 ppm (C<u>*H*</u>$_2$C<u>*H*</u>$_2$), and singlets at 1.90 and 1.39 ppm (COC<u>*H*</u>$_3$ and CNC<u>*H*</u>$_3$ respectively) in a 1:2:2:3:3 ratio. ^{13}C NMR further confirmed the formation of the desired product by the presence of the expected peaks

and elemental analysis gave the anticipated proportions of C, H and N within the product. IR spectroscopy showed a broad band at 1865 cm^{-1}, characteristic of a Ga-H stretch.[154]

As shown in Figure 2.18, X-ray crystallographic analysis confirmed the formation of the desired five-coordinate, monomeric gallium monohydride. In contrast to the structures observed for chloride and methyl complexes discussed earlier, which tend to display geometries only slightly distorted from either of the idealised extremes of trigonal bipyramidal and square-based pyramidal, [Ga(L^2)H] exhibits a geometry much more intermediate between the two. This is quantified by a τ value of 0.35, inferring a considerably distorted square-based pyramidal geometry around the gallium metal centre. Interestingly, this observation is true of both the ethylene-bridged methyl complex [Ga(L^2)Me] reported earlier, as well as the chloride complex [Ga(L^2)Cl] reported by Vohs *et al.*[126] The basal plane is made up of the four heteroatoms of the *β*-ketoiminate ligand, whilst the axial position is occupied by the hydride co-ligand. Bond angles between the four heteroatoms are all only slightly less than 90°, with the exception of N(1)-Ga-N(2), which has an angle of 79.58°. This is presumably a result of the constraint imposed by the relatively short ethylene bridging group between the two nitrogen atoms.

The observed Ga-H bond length of 1.56(2) Å is in keeping with literature values.[133] Other bond lengths are consistent with the results found for the chloride and methyl complexes previously discussed, with C-C, C-O and C-N bond lengths within the *β*-ketoiminate ring system showing values intermediate of single and double bonds, exhibiting the delocalisation of electron density.

2.3.4.2 Synthesis of [Ga(L^3)H]

The propylene derivative [Ga(L^3)H] was synthesised by the same procedure outlined for [Ga(L^2)H] above. Colourless platelet crystals were obtained by crystallisation from a concentrated toluene solution cooled to -20 °C. The formation of the desired hydride was again confirmed by the presence of a very broad, single proton resonance (Ga-H), as well as the absence of any NH proton in the ^{1}H NMR spectrum of the product. In the same way as seen for the aluminium chloride complex, [Al(L^3)Cl], the two central protons of the propylene bridging group are observed as two distinct broad singlets at *ca.* 2.17 and 1.14 ppm, having become separated upon

coordination to the metal centre. Whilst this is an interesting characteristic observed more than once for the propylene ligand derivative, it is not universally true of its metal complexes. The formation of the hydride was further indicated by the presence of a sharp singlet at 4.85 ppm (CH), two multiplets at 2.80 – 2.89 and 2.79 – 2.85 ppm (C$\underline{H_2}$CH$_2$C$\underline{H_2}$) and two further sharp singlets at 1.98 and 1.36 ppm (C$\underline{H_3}$CO and C$\underline{H_3}$CN, respectively) in a 1:1:1:3:3 ratio.

The crystals formed were suitable for X-ray crystallographic analysis and results are shown in Figure 2.19 and Table 2.22.

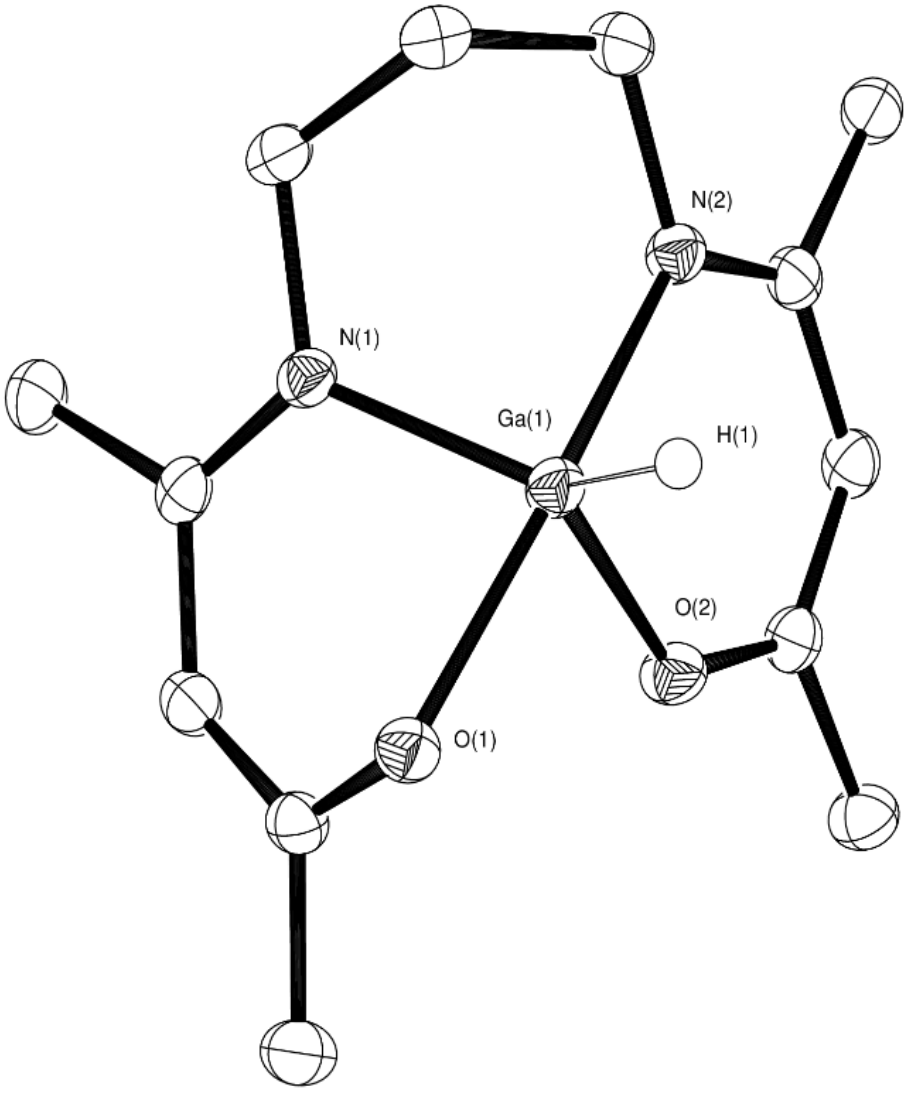

Figure 2.19 - X-ray crystal structure of Ga(L^3)H. Data collection was carried out by the National Crystallography Service, Southampton. Structure solution was carried out by the author.

Table 2.21 - Crystal data for [Ga(L^3)H].

Crystal system	Monoclinic	
Space group	$P2_1/c$	
Unit cell dimensions	a = 7.4450(5) Å	α = 90°
	b = 15.1760(9) Å	β = 97.1120(10)°
	c = 12.4920(8) Å	γ = 90°

Table 2.22 - Selected bond lengths (Å) and angles (°) for [Ga(L^3)H].

Ga(1)-N(1)	1.992(2)	C(6)-N(1)	1.482(3)
Ga(1)-O(1)	2.0231(16)	C(1)-C(2)	1.508(3)
Ga(1)-O(2)	1.9150(19)	C(2)-C(3)	1.371(3)
Ga(1)-N(2)	2.080(2)	C(3)-C(4)	1.428(3)
Ga(1)-H(1)	1.78(2)	C(4)-C(5)	1.502(3)
C(2)-O(1)	1.293(3)	C(6)-C(7)	1.514(3)
C(4)-N(1)	1.317(3)	C(7)-C(8)	1.529(4)
O(2)-Ga(1)-N(1)	117.83(9)	O(1)-Ga(1)-N(2)	165.36(8)
O(2)-Ga(1)-O(1)	81.86(8)	O(2)-Ga(1)-H(1)	112.9(7)
N(1)-Ga(1)-O(1)	85.94(7)	N(1)-Ga(1)-H(1)	128.5(7)
O(2)-Ga(1)-N(2)	89.50(8)	O(1)-Ga(1)-H(1)	93.1(7)
N(1)-Ga(1)-N(2)	87.71(8)	N(2)-Ga(1)-H(1)	101.2(7)

Similarly to the ethylene analogue, the geometry of the metal centre is far more intermediary than seen previously for the chloride and methyl derivatives. However, with a τ value of 0.61, the gallium of the propylene complex [Ga(L^3)H] lies in a distorted trigonal bipyramidal geometry in contrast to the slight tendency towards square-based pyramidal shown by its ethylene sister complex. The axial positions are occupied by one oxygen and one nitrogen of the *β*-ketoiminate, whilst the equatorial positions are occupied by the remaining heteroatoms and the hydride co-ligand. The

significant distortion away from an idealised trigonal bypyramid is demonstrated by the axial bond angle (O(1)-Ga-N(2)) of 165.36°.

In general, bond lengths within the complex mirror those of the ethylene analogue. However, of note is the significantly longer Ga-H bond length of 1.78(2) Å (*cf.* 1.56(2) Å in [Ga(L^2)H]). Whilst this is also much longer than the majority of structurally characterised gallium hydride complexes,[133] it is most closely comparable to the amido-bridged dimer $[H_2GaNEt_2]_2$ (1.72 Å).[133,171] It is likely that this abnormally long Ga-H bond is simply a result of crystal packing effects arising from the different geometry of the complex.

The identity of the product was further confirmed by mass spectrometry, showing a fragment at 305 *m/z* corresponding to parent ion minus the hydride co-ligand. IR spectroscopy showed a broad band at 1867 cm^{-1}, characteristic of a Ga-H stretch.[154] It should be noted that a small discrepancy (>0.5 %) was observed within the elemental analysis data compared to the theoretical values for the C, H and N content of the compound. A likely source of this discrepancy is the degredation of the complex during the analytical procedure due to the air and moisture sensitivity of gallium hydride species. The rentention of solvent within the sample and the presence of trace impurities are also possible causes.

The hydride showed good stability at room temperature over a period of a few weeks under an inert atmosphere. As expected, the complex is susceptible to hydrolysis on exposure to air and moisture. Thermogravimetric analysis was carried out to establish some of the thermal properties and decomposition characteristics of the hydride complexes, which will be discussed in greater detail in chapter 3. However, the onset of decomposition was not observed until *ca.* 210 °C, showing considerable thermal stability. Whilst the thermal stability of the hydride complexes is comparable to that of some Lewis base-stabilised adducts of gallane discussed earlier, in particular those of *N*-heterocyclic carbenes, the overall synthetic procedure (including the synthesis of the ligand) offers a considerably easier route to hydride complexes of reasonable robustness. This presents such gallium hydride compounds as feasible precursors for the deposition of gallium oxide by CVD.

Having synthesised a range of group 13 metal *β*-ketoiminate complexes, the following chapter will discuss some investigation into their thermal properties and their application as precursors for the deposition of metal oxide thin films.

2.4 Summary

The synthesis of main group *β*-ketoiminate complexes remains a surprisingly little studied field of chemistry given the versatility of the ligand class towards complexation of main group metals. The applications of those examples of main group *β*-ketoiminates that do exist are largely limited to the field of catalysis and there are very few reports of the use of such species in the development of precursors for CVD.

In the design of molecular precursors to main group oxide materials, the formation of monomeric species is desirable for the formation of low mass, volatile species where traditional thermal CVD techniques are employed, and for enhancing the solubility where solution-based processes are chosen. Given the tendency of species such as main group alkoxides or amides to oligomerisation, there remains interest in the development of new compound classes containing inherent M-O bonds which are suitable for application as single-source precursors. The potential for functionalisation, in particular of the imino residue, makes *β*-ketoimines a potentially useful class of ligand for synthesising tuneable precursors. Two approaches have generally been employed for the synthesis of monomeric *β*-ketoiminate complexes: a) the use of bulky substituents to sterically hinder oligomerisation; and b) the inclusion of pendant ‘arms’ containing additional donors atoms (i.e. N or O), which are able to coordinate to the metal centre, occupy a vacant coordination site and thus fill up the coordination sphere of the metal, preventing oligomerisation.

With these considerations in mind, a class of bis-*β*-ketoimine ligands have been developed, offering dianionic, tetradentate binding to a metal centre. Such ligand systems are rare in literature and thus exploration of their reactivity towards group 13 metals was of great interest. Ligand synthesis has been achieved on a large scale in high yield and purity, through the facile condensation reaction of *β*-diketonates with ethylene-, propylene- and tetramethylene-diamine. The ligands have subsequently been used in the formation of three main classes on group 13 metal compounds, namely chlorides, methyls and hydrides. The isolation of relatively

stable gallium hydride complexes is of particular significance owing to the extreme difficulty in their synthesis arising from their high thermal and air/moisture sensitivity. This difficulty in synthesis is exemplified by the relative scarcity of examples of gallium hydride in the literature. Extension to the formation of stable indium hydrides has been unsuccessful to this date.

Characterisation of the complexes has been carried out by ^{1}H & ^{13}C NMR, mass spectrometry, elemental analysis and IR spectroscopy, where relevant. Many of the complexes have been structurally characterised by single-crystal X-ray crystallography, revealing, in general, the formation of a number of monomeric, five-coordinate species. Geometries were observed showing distortion form the idealised extremes of square-based pyramidal and trigonal bipyramidal, as well as geometries in between the two. Some indium complexes were observed to adopt six-coordinate geometries, either through adduct formation or dimerisation. This was attributed to the larger size of the indium cation over those of aluminium and gallium and was easily overcome through increasing the size of the carbon chain linking the two *β*-ketoimine moieties of the ligand.

Having developed a range of group 13 metal *β*-ketoiminate complexes, attention was then focussed towards their application as single-source precursors for the deposition of group 13 metal oxide thin films by CVD. The following chapter describes efforts made in this regard and the characterisation of a number of films deposited.

2.5 Experimental

2.5.1 N,N'-ethylenebis(4-aminopent-3-en-2-one) (L^2H_2)

1,2-diaminoethane (0.1 mol, 6.7 ml) was added dropwise to acetylacetone (0.2 mol, 20.54 ml) in a round-bottom flask cooled in an ice and salt water bath. Precipitation of a pale yellow solid was observed immediately upon addition. The reaction mixture was heated to 130 °C for 4 hours in an oil bath before being left to stir at room temperature overnight. Upon cooling a pale orange/yellow solid was formed. The crude product was dissolved in CH_2Cl_2 (ca. 20 ml) and precipitated by rapid addition of hexane (ca. 200 ml) with stirring. The mixture was filtered and the solid product dried *in vacuo* to give a purified yellow solid product. Yield: 21.92 g, 98%. **^{1}H NMR δ/ppm ($CDCl_3$):** 1.89 (s, 6H, C$\underline{H}_3$CO), 1.98 (s, 6H, C$\underline{H}_3$CN), 3.39 (s br, 4H, C$\underline{H}_2$C$\underline{H}_2$), 4.99 (s, 2H, C$\underline{H}$), 10.96 (s (broad), 2H, N$\underline{H}$). **^{13}C{^{1}H} NMR δ/ppm ($CDCl_3$):** 18.8 ($\underline{C}H_3$CO), 28.9 ($\underline{C}H_3$CN), 43.6 ($\underline{C}H_2\underline{C}H_2$), 96.3 ($\underline{C}$H), 163.0 ($CH_3\underline{C}$N), 195.6 ($CH_3\underline{C}$O). **MS (m/z; found):** 225 [M] + H^+, 112 [M] – CH_2N(H)C(Me)CHC(O)Me, 98 [M] – CH_2CH_2N(H)C(Me)CHC(O)Me. **Anal. Calcd. For $C_{12}H_{20}N_2O_2$:** C, 64.26; H, 8.99; N, 12.49. **Found:** C, 63.63; H, 8.99; N, 12.66.

2.5.2 N,N'-1,3-propylenebis(4-aminopent-3-en-2-one) (L^3H_2)

1,3-diaminopropane (2.1 ml, 0.025 mol) was added dropwise to acetylacetone (5.13 ml, 0.05 mol), in a round-bottom flask cooled in an ice and salt water bath. Precipitation of an off-white solid product was observed immediately upon addition. The reaction mixture was warmed to room temperature and allowed to stir for *ca.* 2 hours affording an oily yellow product. The product was then dissolved in diethyl ether, leaving a small amount of insoluble oily residue. The diethyl ether solution was decanted into a second flask and the solvent removed by rotary evaporation, affording an pale yellow waxy solid product. Yield: 5.95 g, >99%. **^{1}H NMR δ/ppm ($CDCl_3$):** 1.68 (2H, quin, J = 7 Hz, $CH_2C\underline{H}_2CH_2$), 1.84 (6H, s, C$\underline{H}_3$CN), 1.92 (6H, s, C$\underline{H}_3$CO), 3.28 (4H, q, J = 6 Hz, C$\underline{H}_2CH_2C\underline{H}_2$), 4.92 (2H, s, C$\underline{H}$), 10.80 (2H, br s, N$\underline{H}$). **^{13}C{^{1}H} NMR δ/ppm ($CDCl_3$):** 18.9 ($\underline{C}H_3$CO), 28.9 ($\underline{C}H_3$CN), 30.3 ($CH_2\underline{C}H_2CH_2$), 39.7 ($\underline{C}H_2CH_2CH_2\underline{C}H_2$), 95.7 ($\underline{C}$H), 163.3 (CH$\underline{C}$N), 195.2 ($CH_3\underline{C}$O). **MS (m/z; found):** 238 [M], 126 [M] - $CH_3C(O)CHC(CH_3)NHCH_2$, 98 [M] -

$CH_3C(O)CHC(CH_3)NHCH_2CH_2CH_2$. **Anal. Calcd. For $C_{13}H_{22}N_2O_2$:** C, 65.52; H, 9.30; N, 11.75. **Found:** C, 63.03; H, 9.15; N, 11.73.

2.5.3 N,N'-tetramethylenebis(4-aminopent-3-en-2-one) (L^4H_2)

Acetylacetone (14.6 mL, 141.5 mmol) was added to a stirring solution of 1,4-diaminobutane (6.26 g, 70.7 mmol) in toluene (*ca.* 100 mL), upon which precipitation of a white solid product was immediately observed. The reaction mixture was then brought to reflux for 2 hours before being cooled slowly to -20 °C. After *ca.* 2 hours a pale coloured precipitate had formed, which was isolated by filtration and dried *in vacuo*. Yield: 14.43 g, 81%. **^{1}H NMR δ/ppm ($CDCl_3$):** 1.65 (4H, m, $CH_2C\underline{H_2}C\underline{H_2}CH_2$), 1.89 (6H, s, $C\underline{H_3}CN$), 1.97 (6H, s, $C\underline{H_3}CO$), 3.24 (4H, m, $C\underline{H_2}CH_2CH_2C\underline{H_2}$), 4.94 (2H, s, C*H*). **^{13}C{^{1}H} NMR δ/ppm ($CDCl_3$):** 18.9 ($\underline{C}H_3CO$), 27.6 ($CH_2\underline{C}H_2\underline{C}H_2CH_2$), 28.9 ($\underline{C}H_3CN$), 42.7 ($\underline{C}H_2CH_2CH_2\underline{C}H_2$), 95.49 ($\underline{C}H$), 163.14 ($CH\underline{C}N$), 195.0 ($CH_3\underline{C}O$). **MS (m/z; found):** 253 [M] + H^+. **Anal. Calcd. For $C_{14}H_{24}N_2O_2$:** C, 66.63; H, 9.59; N, 11.10. **Found:** C, 66.56; H, 9.71; N, 11.17.

2.5.4 [Al(L^2)Cl]

NaH (20.4 mmol, 0.49 g) was suspended in THF and added dropwise *via* cannula to a stirring solution of L^2H_2 (10.2 mmol, 2.29 g), upon which evolution of hydrogen gas was immediately observed. The addition was carried out slowly such that an excess of NaH was not allowed to build up within the reaction mixture. The mixture was allowed to stir for *ca.* 16 hours, after which a large amount of pale coloured precipitate had formed within the orange solution. The solid *β*-ketoiminate sodium salt (L^2Na_2) was isolated by removal of solvent by filtration and dried *in vacuo*. L^2Na_2 (2 mmol, 0.54 g) was then suspended in hexane and added slowly to a stirring solution of $AlCl_3$ (0.27 g, 2 mmol) in hexane at -78 °C for 30 mins before being warmed slowly to room temperature and left to stir for *ca.* 16 hours. Hexane was removed *in vacuo* and toluene was added to the remaining solid product. The mixture was then filtered to give a yellow filtrate and a residual white solid product (NaCl). The yellow toluene solution was then concentrated *in vacuo* and cooled at -20 °C for 2 days, yielding a yellow crystalline material. Yield: 0.20 g, 35% (based on $AlCl_3$). **^{1}H NMR δ/ppm ($CDCl_3$):** 1.43 (s, 6H, $C\underline{H_3}CO$), 1.99 (s, 6H, $C\underline{H_3}CN$), 2.65 (s (broad), 2H, $C\underline{H_2}CH_2$), 3.21 (s (broad), 2H, $CH_2C\underline{H_2}$), 5.04 (s, 2H, C*H*). **^{13}C{^{1}H} NMR δ/ppm ($CDCl_3$):** 22.4 ($\underline{C}H_3CN$), 25.8 ($\underline{C}H_3CO$), 45.8 ($\underline{C}H_2\underline{C}H_2$), 100.7 ($\underline{C}H$),

173.6 ($CH_3\underline{C}N$), 180.6 ($CH_3\underline{C}O$). **MS (m/z; found):** 284 [M], 249 [M] – Cl. **Anal. Calcd. For $C_{12}H_{18}N_2O_2Al$:** C, 50.62; H, 6.37; N, 9.84. **Found:** C, 49.71; H, 6.49; N, 9.28.

2.5.5 [Al(L^3)Cl]

L^3Na_2 was prepared *in situ* by the room temperature reaction of L^3H_2 (2.38 g, 10 mmol) with NaH (0.49 g, 20.5 mmol) in THF for 4 hours. The freshly prepared THF solution of L^3Na_2 was then added dropwise to a stirring solution of $AlCl_3$ (1.33 g, 10 mmol) in THF cooled to -78 °C, stirred for 30 mins before being warmed slowly to room temperature and subsequently brought to reflux for *ca.* 16 hours. THF was removed *in vacuo*, CH_2Cl_2 added to the dry product mixture and the white supernatant filtered off, leaving a white solid residue (NaCl). The CH_2Cl_2 solution was concentrated *in vacuo* and placed in the freezer for a number of days, after which small yellow crystals were formed. Yield: 0.49 g, 16% (based on $AlCl_3$). **^{1}H NMR δ/ppm ($CDCl_3$):** 1.87 and 2.22 (each 1H, br s, $CH_2C\underline{H_2}CH_2$), 2.030 (6H, s, $C\underline{H_3}CN$), 2.034 (6H, s, CH_3CO), 3.40 and 3.70 (each 2H, br s, $C\underline{H_2}CH_2C\underline{H_2}$), 5.20 (2H, s, $C\underline{H}$). **^{13}C{^{1}H} NMR δ/ppm ($CDCl_3$):** 21.7 ($\underline{C}H_3CO$), 25.7 ($\underline{C}H_3CN$), 26.3 ($CH_2\underline{C}H_2CH_2$), 45.7 ($\underline{C}H_2CH_2\underline{C}H_2$), 101.1 ($\underline{C}H$), 173.7 ($\underline{C}N$), 180.0 ($\underline{C}O$). **MS (m/z; found):** 263 [M] – Cl, 239 [L^3H_2] + H^+ **Anal. Calcd. For $C_{13}H_{20}N_2O_2AlCl$:** C, 52.27; H, 6.75; N, 9.38. **Found:** C, 51.93; H, 6.96; N, 9.54.

2.5.6 [Al(L^4)Cl]

L^4Na_2 was prepared *in situ* by the room temperature reaction of L^4H_2 (2.52 g, 10 mmol) with NaH (0.49 g, 20.5 mmol) in THF for 4 hours. The freshly prepared THF solution of L^4Na_2 was then added dropwise to a stirring solution of $AlCl_3$ (1.33 g, 10 mmol) in THF cooled to -78 °C, stirred for 30 mins before being warmed slowly to room temperature and subsequently brought to reflux for *ca.* 16 hours. THF was removed *in vacuo*, CH_2Cl_2 added to the dry product mixture and the white supernatant filtered off, leaving a white solid residue (NaCl). CH_2Cl_2 was removed *in vacuo*, the product dissolved in minimal toluene and cooled to -20 °C. The solution was left at this temperature overnight, after which colourless crystalline blocks had formed. Yield = 0.66 g, 21%.**^{1}H NMR δ/ppm ($CDCl_3$):** 1.76 (4H, br s, $CH_2C\underline{H_2}C\underline{H_2}CH_2$), 2.03 (6H, s, $C\underline{H_3}CN$), 2.10 (6H, s, $C\underline{H_3}CO$), 3.51 (4H, br s, $C\underline{H_2}CH_2CH_2C\underline{H_2}$), 5.25 (2H, s, $C\underline{H}$),.**^{13}C{^{1}H} NMR δ/ppm ($CDCl_3$):** 22.1 ($\underline{C}H_3CO$),

25.6 ($\underline{C}H_3CN$), 29.43 ($CH_2\underline{C}H_2CH_2$), 48.7 ($\underline{C}H_2CH_2\underline{C}H_2$), 101.6 ($\underline{C}H$), 175.3 ($\underline{C}N$), 179.3 ($\underline{C}O$),. **MS (m/z; found):** 312 [M], 297 [M] – CH_3, 281 [M] – CH_3 – O, 277 [M] – Cl, 253 [L^4H_2], 154 [L^4H_2] – $CH_3COCHC(CH_3)NH$, 110 [L^4H_2] – $CH_3COCHC(CH_3)NHCH_2CH_2$ – O. **Anal. Calcd. For $C_{14}H_{22}N_2O_2AlCl$:** C, 53.76; H, 7.09; N, 8.96. **Found:** C, 52.13; H, 7.23; N, 8.32.

2.5.7 [Ga(L^2)Cl]

L^2H_2 (10.2 mmol, 2.29 g) was dissolved in THF and was transferred by cannula to a stirring suspension of NaH (20.4 mmol, 0.49 g) in THF and the mixture was allowed to stir for a few hours until the evolution of hydrogen gas had ceased. The mixture was then transferred slowly by cannula to a stirring solution of $GaCl_3$ (10 mmol, 1.76 g) in THF at -78 °C for ca. 30 mins. The mixture was then allowed to warm slowly to room temperature before being refluxed at 85 °C overnight, during which time a white precipitate was formed in a yellow/brown solution. The mixture was filtered and the resulting white solid product washed with THF before being filtered for a second time. Solvent was removed from the yellow/brown filtrate *in vacuo*, the yellow solid product dissolved in minimal CH_2Cl_2 and precipitated out by rapid addition of hexane affording the purified gallium complex. Yield: 2.29 g, 70% (based on $GaCl_3$). **^{1}H NMR δ/ppm ($CDCl_3$):** 2.02 (s, 6H, $C\underline{H}_3CO$), 2.08 (s, 6H, $C\underline{H}_3CN$), 3.51 (m, 2H, $C\underline{H}_2CH_2$), 3.62 (m, 2H, $CH_2C\underline{H}_2$), 5.26 (s, 2H, $C\underline{H}$). **^{13}C{^{1}H} NMR δ/ppm ($CDCl_3$):** 22.6 ($\underline{C}H_3CO$), 26.7 ($\underline{C}H_3CN$), 45.1 ($\underline{C}H_2\underline{C}H_2$), 98.8 ($\underline{C}H$), 173.3 ($CH_3\underline{C}N$), 183.6 ($CH_3\underline{C}O$). **Anal. Calcd for $C_{12}H_{18}N_2O_2Ga$:** C, 44.01; H, 5.54; N, 8.55. **Found:** C, 43.00; H, 5.49; N, 8.26. **MS (m/z; found):** 326 [M], 291 [M] – Cl, 275 [M] – Cl – O, 202 [M] + H^+ - $MeC(O)CH(C(Me)NCH_2CH_2^+$.

2.5.8 [Ga(L^3)Cl]

NaH (12 mmol, 0.29 g) was suspended in THF and added to a stirring solution of L^3H_2 (5 mmol, 1.19 g) in THF and was allowed to stir overnight. The resulting suspension was then filtered and solvent removed *in vacuo* from the filtrate affording a dark yellow solid product, L^3Na_2. The sodium salt (2 mmol, 0.57 g) was then suspended in hexane, which was then transferred slowly by cannula to a solution of $GaCl_3$ (2 mmol, 0.352 g) in hexane at -78 °C. The mixture was allowed to warm slowly to room temperature and was left to stir overnight. The mixture was then filtered, solvent removed from the filtrate and the resulting yellow/brown solid

product dissolved in minimal dichloromethane, before being filtered for a second time and layered with hexane. The product was left at room temperature for 2 days, during which time yellow crystals of [Ga(L^3)Cl] were formed. Yield: 0.27 g, 38% (based on $GaCl_3$). **^{1}H NMR δ/ppm ($CDCl_3$):** 1.87 (2H, quintet, *J* = 6.5 Hz, $CH_2C\underline{H}_2CH_2$) 2.00 (6H, s, $CNC\underline{H}_3$), 2.01 (6H, s, $COC\underline{H}_3$), 3.46 and 3.71 (each 2H, br s, $C\underline{H}_2CH_2C\underline{H}_2$), 5.06 (2H, s, C*H*). **^{13}C{^{1}H} NMR δ/ppm ($CDCl_3$):** 18.8 ($CO\underline{C}H_3$), 26.5 ($CN\underline{C}H_3$), 30.3 ($CH_2\underline{C}H_2CH_2$), 47.2 ($\underline{C}H_2CH_2\underline{C}H_2$), 98.8 (*C*H) ppm; *C*O and *C*N not detected. **Analysis Calc. for $C_{13}H_{20}N_2O_2GaCl$:** C 45.75; H 5.90; N 8.20. Found: C 45.44; H 6.04; N 8.28.

2.5.9 [Ga(L^4)Cl]

NaH (1 g, 42 mmol) was suspended in THF and added to a stirring solution of L^4H_2 (5 g, 19.8 mmol) in THF and was allowed to stir overnight. Solvent was removed from the resulting suspension *in vacuo* affording a pale yellow solid product, L^4Na_2. L^4Na_2 (0.59 g, 2 mmol) was then suspended in THF and added slowly to a stirring solution of $GaCl_3$ (0.35 g, 2 mmol) in THF at -78 °C. The mixture was stirred for *ca.* 30 mins before being warmed slowly to room temperature and subsequently brought to reflux for 16 hours. The resulting yellow supernatant was separated from the white solid precipitate (NaCl) by filtration and solvent removed *in vacuo* affording a solid yellow crude product. The product was then dissolved in minimal CH_2Cl_2 (*ca*. 3 mL), filtered into a narrow Schlenk flask and layered with hexane (*ca.* 10 mL). The product was left overnight, after which colourless crystalline blocks had formed. Yield = 0.71 g, 67% (based on $GaCl_3$). **^{1}H NMR δ/ppm ($CDCl_3$):** 1.78 (4H, br s, $CH_2C\underline{H_2}C\underline{H_2}CH_2$), 2.03 (6H, s, $C\underline{H}_3CN$), 2.06 (6H, s, $C\underline{H}_3CO$), 3.52 (4H, br s, $C\underline{H_2}CH_2CH_2C\underline{H_2}$), 5.10 (2H, s, C*H*),. **^{13}C{^{1}H} NMR δ/ppm ($CDCl_3$):** 22.5 ($\underline{C}H_3CO$). 26.6 ($\underline{C}H_3CN$), 28.6 ($CH_2\underline{C}H_2CH_2$), 48.7 ($\underline{C}H_2CH_2\underline{C}H_2$), 99.5 (*C*H), 174.9 (*C*N), 182.9 (*C*O). **MS (m/z; found):** 354 [M], 339 [M] – CH_3, 319 [M] – Cl, 311 [M] – CH_3CO. **Anal. Calcd for $C_{12}H_{18}N_2O_2Ga$:** C, 47.17; H, 6.50; N, 7.86. **Found:** C, 46.72; H, 6.20; N, 6.17.

2.5.10 [In(L^2)Cl·THF]

L^2H_2 (5 mmol, 1.12 g) was dissolved in THF and added to a stirring solution of NaH (12 mmol, 0.29 g) and was allowed to stir overnight. The mixture was then filtered and solvent removed *in vacuo* from the resulting brown precipitate, affording a

brown solid sodium salt of the β-ketoimine. The sodium salt (2 mmol, 0.54 g) was then suspended in hexane and added to a stirring solution of $InCl_3$ (2 mmol, 0.44 g) in hexane at -78 °C. The solution was warmed to room temperature and allowed to stir overnight, yielding a white precipitate (NaCl). The product was extracted with hexane (3 x 20 mL) and the solvent was removed from the combined yellow filtrate *in vacuo* yielding a pale yellow solid crude product. Attempts to recrystallise the compound from THF were unsuccessful. The crude product was finally dissolved in a minimum amount of dichloromethane and was layered with hexane, from which yellow crystals were formed. Yield: 0.093 g, 14%. **^{1}H NMR δ/ppm ($CDCl_3$):** 1.85 (m, 4H, C$\underline{H}_2$(3,4) – *THF*), 2.00 (s, 6H, C$\underline{H}_3$CO), 2.02 (s, 6H, C$\underline{H}_3$CN), 3.58 (m, 4H, C$\underline{H}_2$C$\underline{H}_2$), 3.74 (m, 4H, C$\underline{H}_2$(2,5) – *THF*), 4.97 (s, 2H, C$\underline{H}$). **^{13}C{^{1}H} NMR δ/ppm ($CDCl_3$):** 22.5 (C$\underline{C}$H$_3$CO), 25.58 (C$\underline{C}$H$_2$(3,4), THF), 27.9 (C$\underline{C}$H$_3$CN), 46.6 (C$\underline{C}$H$_2$C$\underline{C}$H$_2$), 68.0 (C$\underline{C}$H$_2$(2,5), THF), 98.7 (C$\underline{C}$H) 174.8 (CH$_3$C$\underline{C}$N), 184.7 (CH$_3$C$\underline{C}$O). **MS (m/z; found):** 372 [M] – THF, 337 [M] – THF – Cl, 111 MeC(O)CHC(Me)NCH$_2^+$.

2.5.11 [{In(L^2)Cl}$_2$(L^2H_2)]

L^2Na_2 was formed *in situ* by the slow addition of a toluene suspension of NaH (12 mmol, 0.29 g) to a stirring solution of L^2H_2 (5 mmol, 1.12 g). Evolution of hydrogen gas was observed upon addition and the mixture was allowed to stir at room temperature for 16 hours. The resulting L^2Na_2 toluene suspension was added slowly to a stirring solution of $InCl_3$ (1.11 g, 5mmol) in toluene at -78 °C, before being warmed to room temperature and subsequently brought to reflux for 4 hours. The resulting solution was filtered and solvent removed from the filtrate *in vacuo* yielding a solid yellow product. The product was dissolved in minimal CH_2Cl_2 (*ca.* 3 mL), filtered into a narrow Schlenk flask and layered with hexane (*ca.* 10 mL). Yellow crystals of the product were formed after a number of days. Yield = 0.53 g, 22% (based on $InCl_3$). **^{1}H NMR δ/ppm ($CDCl_3$):** 1.97 (6H, s, CNC$\underline{H}_3$ anionic), 2.05 (6H, s, CNC$\underline{H}_3$ bridging), 2.06 (12H, s, CNC$\underline{H}_3$ bridging), 2.07 (12H, s, COC$\underline{H}_3$ anionic), 3.47 (4H, t, *J* = 3.0 Hz, C$\underline{H}_2$C$\underline{H}_2$ bridging), 3.60 (8H, s, C$\underline{H}_2$C$\underline{H}_2$ anionic), 5.07 (4H, s, C$\underline{H}$ anionic), 5.08 (2H, s, C$\underline{H}$ bridging), 10.98 (2H, s, N$\underline{H}$). **^{13}C{^{1}H} NMR δ/ppm ($CDCl_3$):** 18.6 (CO$\underline{C}$H$_3$ bridging), 22.3 (CO$\underline{C}$H$_3$ anionic), 27.4 (CN$\underline{C}$H$_3$ anionic), 28.4 (CN$\underline{C}$H$_3$ bridging), 43.5 ($\underline{C}$H$_2$ bridging), 46.7 ($\underline{C}$H$_2$ anionic), 95.9 ($\underline{C}$H bridging), 98.2 ($\underline{C}$H anionic), 164.5 ($\underline{C}$N bridging), 175.0 ($\underline{C}$N anionic),

183.9 (*C*O anionic), 195.0 (*C*O bridging). **Analysis: Calc. for $C_{18}H_{28}N_3O_3InCl$:** C, 44.60; H, 5.82; N, 8.67. **Found:** C 44.49; H 5.73; N 8.78.

2.5.12 $[In(L^2)Cl]_2$

A suspension of L^2Na_2 (2.68 g, 10 mmol) in hexane was added to a suspension of $InCl_3$ (2.21 g, 10 mmol) in hexane at -78 °C and stirred for *ca.* 30 mins. The reaction was warmed slowly to room temperature and then refluxed for 16 hours. The reaction was cooled and filtered and the resulting NaCl was washed with further hexane. The filtrates were combined, solvents removed *in vacuo* and the resulting yellow solid product dissolved in minimal CH_2Cl_2 (*ca.* 10 mL). Yellow crystals were formed through vapour diffusion of hexane into the CH_2Cl_2 solution. Yield: 1.67 g, 45%. **^{1}H NMR δ/ppm ($CDCl_3$):** 2.02 (6H, s, CNC*H*$_3$), 2.08 (6H, s, COC*H*$_3$), 3.51 and 3.62 (each 2H, m, C*H*$_2$), 5.26 (2H, s, C*H*). **^{13}C{^{1}H} NMR δ/ppm ($CDCl_3$):** 22.6 (CO*C*H$_3$), 26.7 (CN*C*H$_3$), 45.1 (*C*H$_2$), 98.8 (*C*H), 173.3 (*C*N), 183.6 (*C*O). **Anal. Calcd for $C_{12}H_{18}N_2O_2Ga$:** C, 38.69; H, 4.87; N, 7.52. **Found:** C, 38.82; H, 5.01; N, 7.46. **MS (m/z; found):** 372 $[M]^+$, 337 $[M - Cl]^+$.

2.5.13 $[In(L^3)Cl]$

A suspension of L^2Na_2 (0.57 g, 2 mmol) in hexane was added slowly to a stirring suspension of $InCl_3$ (2 mmol, 0.44 g) in hexane at -78 °C. The mixture was allowed to warm slowly to room temperature and was left to stir overnight. The mixture was filtered and hexane removed from the filtrate *in vacuo*. The resulting yellow solid product was dissolved in minimal dichloromethane, the solution filtered and layered with hexane, forming yellow crystals after 2 days at room temperature. Yield: 0.27 g, 35%. **^{1}H NMR δ/ppm ($CDCl_3$):** 1.99 (s, 6H, C*H*$_3$CO), 2.02 (s, 6H, C*H*$_3$CN), 2.63 (br, 2H, CH$_2$C*H*$_2$CH$_2$), 3.47 (br, 2H, C*H*$_2$CH$_2$CH$_2$), 3.76 (br, 2H, CH$_2$CH$_2$C*H*$_2$), 4.94 (s, 2H, C*H*). **^{13}C{^{1}H} NMR δ/ppm ($CDCl_3$):** 23.2 (*C*H$_3$CO), 27.6 (*C*H$_3$CN), 29.1 (CH$_2$*C*H$_2$CH$_2$), 51.9 (*C*H$_2$CH$_2$*C*H$_2$), 98.0 (*C*H), 176.0 (CH$_3$*C*N), 185.8 (CH$_3$*C*O). **Anal. Calcd. For $C_{13}H_{20}N_2O_2In$:** C, 40.39; H, 5.21; N, 7.25. **Found:** C, 40.17; H, 5.30; N, 7.59. **MS (m/z; found):** 386 [M], 351 (351) [M] – Cl, 238 $L^2H_2^+$, 126 (126) MeC(O)CHC(Me)NHCH$_2$CH$_2^+$, 98 MeC(O)CHC(Me)NH$^+$.

2.5.14 $[In(L^4)Cl]$

L^4Na_2 was prepared *in situ* by the room temperature reaction of L^4H_2 (2.52 g, 10 mmol) with NaH (0.49 g, 20.5 mmol) in THF for 4 hours. The freshly prepared THF

solution of L^4Na_2 was then added dropwise to a stirring solution of $InCl_3$ (2.21 g, 10 mmol) in THF cooled to -78 °C, stirred for 30 mins before being warmed slowly to room temperature and subsequently brought to reflux for *ca.* 16 hours. THF was removed *in vacuo*, DCM added to the dry product mixture and the supernatant filtered off, leaving a white solid residue (NaCl). The solution was concentrated by evaporation of the solvent *in vacuo* and layered with hexane. After one day a yellow microcrystalline material had formed, which was unsuitable for crystallographic analysis. Yield: 1.64 g, 41%. **^{1}H NMR δ/ppm ($CDCl_3$):** 1.91 (4H, br s, $CH_2C\underline{H_2}C\underline{H_2}CH_2$), 2.02 (6H, s, $C\underline{H_3}CN$), 2.03 (6H, s, $C\underline{H_3}CO$), 3.54 (4H, br s, $C\underline{H_2}CH_2CH_2C\underline{H_2}$), 4.95 (2H, s, C*H*). **^{13}C{^{1}H} NMR δ/ppm ($CDCl_3$):** 23.2 ($\underline{C}H_3CO$), 26.8 ($\underline{C}H_3CN$), 27.9 ($CH_2\underline{C}H_2CH_2$), 49.2 ($\underline{C}H_2CH_2\underline{C}H_2$), 98.8 (<u>*C*</u>H), 176.0 (<u>*C*</u>N), 185.3 (<u>*C*</u>O). **MS (m/z; found):** 401 [M] + H^+, 365 [M] – Cl, 253 [L^4H_2] + H^+. **Anal. Calcd for $C_{12}H_{18}N_2O_2Ga$:** C, 41.97; H, 5.54; N, 6.99. **Found:** C, 41.89; H, 5.80; N, 6.71.

2.5.15 [Ga(L^2)Me]

L^2H_2 (7.8 g, 34.8 mmol) was dissolved in anhydrous toluene and added slowly to a stirring solution of $GaMe_3$ (4 g, 34.8 mmol) in toluene at -78 °C. The mixture was allowed to stir at -78 °C for *ca.* 30 mins before being warmed slowly to room temperature. The reaction mixture was then heated to 80 °C in an oil bath and allowed to stir at this temperature for 16 hours. The resulting dark yellow/orange solution was filtered and toluene was removed under reduced pressure yielding a dark yellow waxy product. ^{1}H NMR of the crude product showed formation of the desired product with a small amount of residual free ligand. The product was dissolved in a minimum volume of hexane with gentle heating and was left to cool to room temperature, during which time needle-like, yellow crystals formed. Yield = 8.16 g (77%). **^{1}H NMR δ/ppm ($CDCl_3$):** -0.45 (s, $GaC\underline{H_3}$), 1.94 (6H, s, $C\underline{H_3}CN$), 1.99 (6H, s, $C\underline{H_3}CO$), 3.37 – 3.46 (4H, m, $C\underline{H_2}C\underline{H_2}$), 4.91 (2H, s, C*H*). **^{13}C{^{1}H} NMR δ/ppm ($CDCl_3$):** -7.1 ($Ga\underline{C}H_3$), 21.6 ($\underline{C}H_3CO$), 26.9 ($\underline{C}H_3CN$), 45.9 ($\underline{C}H_2\underline{C}H_2$), 97.5 (<u>*C*</u>H), 171.0 ($CH_3\underline{C}N$), 182.1 ($CH_3\underline{C}O$). **MS (m/z; found):** 307 [M + H]$^+$, 291 [M- CH_3]$^+$. **Analysis**: **Calc. for $C_{13}H_{21}GaN_2O_2$**: C, 50.85; H, 6.89; N, 9.12. **Found**: C, 49.23; H, 7.29; N, 9.24.

2.5.16 [L^3{$GaMe_2$)$_2$}]

L^3H_2 (0.60 g, 2.5 mmol) was dissolved in anhydrous toluene and added slowly to a stirring solution of $GaMe_3$ (0.57 g, 5 mmol) in toluene at -78 °C. The mixture was allowed to stir at -78 °C for *ca.* 30mins before being warmed slowly to room temperature. The reaction mixture was then heated to *ca.* 80 °C and allowed to stir at this temperature for 16 hours. The yellow solution was cooled to room temperature, filtered and solvent removed from the filtrate *in vacuo*. Recrystallisation of the resulting yellow solid powder was unsuccessful from a range of solvent and temperature combinations. Yield = 0.63 g, 58%). **^{1}H NMR δ/ppm ($CDCl_3$):** 4.85 (2H, s, C*H*), 3.23 – 3.27 (4H, m, C*H*$_2$CH_2C*H*$_2$), 1.96 (6H, s, C*H*$_3$CO), 1.91 (6H, s, C*H*$_3$CN), 1.70 – 1.80 (2H, m, CH_2C*H*$_2$$CH_2$), -0.38 (12H, s, Ga(C*H*$_3$)$_2$). **^{13}C{^{1}H} NMR δ/ppm ($CDCl_3$):** -7.3 (Ga(*C*H_3)$_2$), 20.9 (*C*H_3CO), 26.4 (*C*H_3CN), 30.5 (CH_2*C*$H_2$$CH_2$), 46.4 (*C*$H_2$$CH_2$*C*$H_2$), 98.2 (*C*H), 171.5 (*C*N), 180.4 (*C*O). **MS (m/z; found):** 421 [M] - CH_3, 321 [M] - $GaMe_3$, 305 [M] - $GaMe_3$ - CH_3. **Anal. Calcd for $C_{17}H_{32}N_2O_2Ga_2$:** C, 46.84; H, 7.40; N, 6.43. **Found:** C, 45.30; H, 8.01; N, 6.28. Poor fit attributed to the retention of solvent within the sample.

2.5.17 [L^4{$GaMe_2$)$_2$}]

L^4H_2 (0.63 g, 2.5 mmol) was dissolved in anhydrous toluene and added slowly to a stirring solution of $GaMe_3$ (0.57 g, 5 mmol) in toluene at -78 °C. The mixture was allowed to stir at -78 °C for *ca.* 30mins before being warmed slowly to room temperature. The reaction mixture was then heated to *ca.* 80 °C and allowed to stir at this temperature for 16 hours. The yellow solution was cooled to room temperature, filtered and solvent removed from the filtrate *in vacuo*. Recrystallisation of the resulting yellow solid powder was unsuccessful from a range of solvent and temperature combinations. Yield = 0.89 g, 79%. **^{1}H NMR δ/ppm ($CDCl_3$):** -0.38 (12H, s, Ga(C*H*$_3$)$_2$), 1.53 (2H, br s, CH_2C*H*$_2$$CH_2$), 1.92 (6H, s, C*H*$_3$CN), 1.96 (6H, s, C*H*$_3$CO), 3.28 (4H, br s, C*H*$_2$$CH_2$C*H*$_2$), 4.85 (2H, s, C*H*). **^{13}C{^{1}H} NMR δ/ppm ($CDCl_3$):** -7.4 (Ga(*C*H_3)$_2$), 21.2 (*C*H_3CO), 26.4 (*C*H_3CN), 27.9 (CH_2*C*$H_2$$CH_2$), 48.6 (*C*$H_2$$CH_2$*C*$H_2$), 98.3 (*C*H), 171.3 (*C*N), 180.0 (*C*O). **MS (m/z; found):** 435 [M] – CH_3, 335 [M] – $GaMe_3$, 319 [M] – $GaMe_3$ – CH_3. **Anal. Calcd for $C_{18}H_{34}N_2O_2Ga_2$:** C, 48.05; H, 7.62; N, 6.23. **Found:** C, 47.15; H, 7.81; N, 6.15.

2.5.18 [In(L^2)Me]

L^1H_2 (2.8 g, 12.5 mmol) was dissolved in anhydrous toluene and added slowly to a stirring solution of $InMe_3$ (2 g, 12.5 mmol) in toluene at -78 °C. The mixture was allowed to stir at -78 °C for *ca.* 30 mins before being warmed slowly to room temperature. The reaction mixture was then heated to 80 °C in an oil bath and allowed to stir at this temperature for 16 hours. The resulting yellow solution containing a small quantity of dark precipitate was filtered and toluene was removed under reduced pressure yielding a pale yellow solid product. Crystals of [In(L^2)Me] suitable for X-ray crystallography could not be grown by the same method used for the analogous gallium complex [Ga(L^2)Me]. Yield = 3.11 g, 71%. **^{1}H NMR δ/ppm ($CDCl_3$):** -0.46 (3H, s, InC$\underline{H}_3$), 1.95 (6H, s, C$\underline{H}_3$CN), 2.00 (6H, s, C$\underline{H}_3$CO), 3.44 (4H, m, C$\underline{H}_2$C$\underline{H}_2$), 4.91 (2H, s, C$\underline{H}$). **^{13}C{^{1}H} NMR δ/ppm ($CDCl_3$):** -11.5 (In$\underline{C}H_3$), 22.0 ($\underline{C}H_3$CO), 27.9 ($\underline{C}H_3$CN), 47.7 ($\underline{C}H_2\underline{C}H_2$), 97.64 ($\underline{C}$H), 172.4 ($\underline{C}$N), 183.3 ($\underline{C}$O). **MS (m/z; found):** 352 $[M]^+$, 337 $[M - CH_3]^+$. **Analysis**: **Calc. for $C_{13}H_{21}InN_2O_2$:** C, 44.34; H, 6.01; N, 7.96. **Found:** C, 36.71; H, 5.34; N, 6.15. Large discrepancy in theoretical and experimental values suggests the presence of impurities within the product. Retention of solvent and decomposition of the complex during the analytical procedure are also possible sources of discrepancy.

2.5.19 [In(L^3)Me]

L^2H_2 (1.19 g, 5 mmol) was dissolved in toluene and added slowly to a solution of $InMe_3$ (0.8 g, 5 mmol) at -78 °C and allowed to stir for *ca.* 0.5 hours. The mixture was then allowed to warm slowly to room temperature before being heated to 100 °C in an oil bath and stirred for 16 hours. As the oil bath temperature reached *ca.* 60 °C, bubbles of gas began to evolve from the reaction mixture. The resulting yellow solution was filtered and solvent removed from the filtrate under reduced pressure yielding a yellow solid product. Recrystallisation of the product was not attempted due to the sufficient purity of the crude sample. Yield = 0.83 g, 45%. **^{1}H NMR δ/ppm ($CDCl_3$):** -0.07 (3H, s, InC$\underline{H}_3$), 1.89 (6H, s, C$\underline{H}_3$CN), 3.43 (2H, s br, C$\underline{H}_2$), 1.93 (6H, s, C$\underline{H}_3$CO), 3.60 (2H, s br, C$\underline{H}_2$), 4.79 (2H, s, C$\underline{H}$). **^{13}C{^{1}H} NMR δ/ppm ($CDCl_3$):** -6.9 (In$\underline{C}H_3$) 22.6 ($\underline{C}H_3$CO), 27.6 ($\underline{C}H_3$CN), 29.1 ($CH_2\underline{C}H_2CH_2$), 51.8 ($\underline{C}H_2CH_2\underline{C}H_2$), 97.2 ($\underline{C}$H), 173.3 ($\underline{C}$N), 184.0 ($\underline{C}$O). **MS (m/z; found):** 366 $[M]^+$, 351 $[M - CH_3]^+$. **Analysis**: **Calc. for $C_{13}H_{21}InN_2O_2$:** C, 45.92; H, 6.33; N, 7.65. **Found:** C, 42.27; H, 6.04; N, 6.15. Large discrepancy in theoretical and

experimental values suggests the presence of impurities within the product. Retention of solvent and decomposition of the complex during the analytical procedure are also possible sources of discrepancy.

2.5.20 [Ga(L^2)H]

A freshly prepared solution of [$GaH_3(NMe_3)$] (5.0 mmol) in Et_2O (50 mL) was cooled to −78 °C and added to a suspension of L^2H_2 (1.12 g, 5.0 mmol) in Et_2O (20 mL) at −78 °C. The suspension was stirred for 15 min, then warmed to RT and stirred for 16 hours. After this time, a yellow solution with a white suspension had formed. The reaction was filtered, and volatiles were removed *in vacuo*, affording 1.04 g of a yellow solid in 71% yield. Yellow crystals were subsequently grown by slow evaporation of a CH_2Cl_2 solution of the product. **^{1}H NMR δ/ppm (C_6D_6):** 1.39 (6H, s, CNC*H*$_3$) ppm, 1.90 (6H, s, COC*H*$_3$), 2.80 - 2.89 and 2.58 - 2.68 (each 2H, m, C*H*$_2$), 4.80 (2H, s, C*H*), 5.56 (1H, v br s, Ga*H*). **^{13}C{^{1}H} NMR δ/ppm (C_6D_6):** 21.5 (CO*C*H$_3$), 26.7 (CN*C*H$_3$), 45.3 (*C*H$_2$), 97.6 (*C*H), 171.3 (*C*N), 182.5 (*C*O). **Analysis Calcd. for $C_{12}H_{19}N_2O_2Ga$:** C, 35.69; H, 6.99; N, 6.94. **Found:** C, 35.75; H, 6.91; N, 7.06. **MS (m/z; found):** 291 [M] – H$^+$. **IR υ(cm^{-1}):** 1865 (br, Ga-H).

2.5.21 [Ga(L^3)H]

A freshly prepared solution of [$GaH_3(NMe_3)$] (5.0 mmol) in Et_2O (50 mL) was cooled to − 78 °C and added to a suspension of L^3H_2 (1.19 g, 5.0 mmol) in Et_2O (20 mL) at − 78 °C. The suspension was stirred for 15 min, then warmed to RT and stirred for 16 h. After this time, a pale yellow solution with a white suspension had formed. The reaction was filtered, volatiles were removed *in vacuo* and the crude product was dissolved in minimal toluene. The toluene solution was cooled to -20 °C, from which colourless crystals were formed overnight. Yield = 0.91 g, 59% (based on $GaCl_3$). **^{1}H NMR δ/ppm (C_6D_6):** 2.15 – 2.19 and 1.12 – 1.16 (each 1H, m, $CH_2CH_2CH_2$), 1.36 (6H, s, CNC*H*$_3$), 1.98 (6H, s, COC*H*$_3$), 2.80−2.89 and 2.79−2.85 (each 2H, m, C*H*$_2$CH$_2$C*H*$_2$), 4.85 (2H, s, C*H*), 5.83 (1H, v br s, Ga*H*). **^{13}C{^{1}H} NMR δ/ppm (C_6D_6):** 21.2 (CO*C*H$_3$), 26.5 ($CH_2CH_2CH_2$), 26.8 (CN*C*H$_3$), 49.0 ($CH_2CH_2CH_2$), 97.9 (*C*H), 171.1 (*C*N), 182.95 (*C*O). **Anal. Calcd for $C_{13}H_{21}N_2O_2Ga$:** C, 50.85; H, 6.89; N, 9.12. **Found:** C, 49.56; H, 7.31; N, 8.48. **MS (m/z; found):** 305 [M] – H$^+$. **IR υ(cm^{-1}):** 1867 (br, Ga-H). A significant discrepancy

between theoretical and experimental values was observed. This is attributed to degradation of the complex occurring during the analytical procedure.

Chapter 3

The Application of Group 13 Metal *β*-ketoiminates as Precursors for the Deposition of Group 13 Oxide Thin Films

Following the successful synthesis of a range of group 13 metal β-ketoiminate complexes, as described in Chapter 2, the following chapter concerns the investigation of their suitability as single-source precursors for the deposition of group 13 metal oxide thin films by CVD. Thermal properties of the precursors are studied by thermogravimetric analysis (TGA), giving an initial indication of decomposition temperatures and pathways, as well as the influence of variations within the β-ketoiminate and of the co-ligand on the decomposition properties of the complexes. The attempted growth of metal oxide thin films by use of the precursors in an AACVD process and the characterisation and analysis of functional properties is then discussed.

3 The Application of Group 13 Metal *β*-ketoiminates as Precursors for the Deposition of Group 13 Oxide Thin Films

3.1 Introduction

3.1.1 Deposition of Gallium Oxide

Given the range of applications for thin films of gallium oxide, as discussed in Chapter 1 (section 1.1.2), it is no surprise that a number of techniques have been explored for the deposition of the material. Common fabrication techniques such as sputtering,[47] sol-gel processes,[49] spray pyrolysis,[53] screen printing,[58] atomic layer deposition,[62] as well as chemical vapour deposition (CVD) processes including low pressure (LP),[96] atmospheric pressure (AP)[172] and aerosol assisted (AA)[103] CVD have all been reported for thin films of Ga_2O_3.

Amongst the many available techniques for the deposition of group 13 metal oxides, CVD is favourable due to the production of high quality, uniform films free from contamination, although it can be more complicated and expensive than other available options. AACVD, a process which has been discussed in length in Chapter 1, relies on the solubility of the chosen precursor rather than depending on its volatility, broadening the range of potential precursors which can be employed. Furthermore, the solution based process offers an additional means to controlling film morphology and concurrently its properties and is therefore of great interest in the deposition of materials.[72]

The first example of the deposition of Ga_2O_3 by AACVD was reported by Basharat *et al.,* from the *in situ* reaction of $[Ga(NMe_2)_3]_2$ with donor-functionalised alcohols ROH (R = $CH_2CH_2NMe_2$, $CH(CH_2NMe_2)_2$, CH_2CH_2OMe, $CH(CH_3)CH_2NMe_2$).[103] Previous studies had identified that the room temperature reaction of $[Ga(NMe_2)_3]_2$ with ROH afforded the dimeric gallium alkoxides $[Ga(OR)_3]_2$.[165] The work demonstrated the possibility of carrying out Ga_2O_3 depositions without the need for prior isolation of the precursor, considerably simplifying the entire process. The work was later extended to show the deposition of Ga_2O_3 from the monoalkoxogallane $[Me_2Ga(OC(CH_3)_2CH_2OMe)]_2$, *via* the *in situ* reaction of $GaMe_3$ and $HOC(CH_3)_2CH_2OMe$), again without the need for prior isolation of the precursor.[105] Pugh *et al.* reported the formation of the complexes

[{$GaH_2(Me_2NCH_2CH_2O)$}$_2$], [(GaH{$(OCH_2CH_2)_2NMe$}$)_2$], [$Ga(OCH_2CH_2NMe_2)_3$] and [(GaMe{$(OCH_2CH_2)_2NMe$}$)_2$], which showed promising thermal decomposition properties for the formation of Ga_2O_3 at low deposition temperatures.[156] However, deposition in a LPCVD process was hampered by decomposition of the precursors and thus AACVD was instead used, enabling the transport of the precursors to the reaction chamber as an aerosol. Thin films of Ga_2O_3 were deposited in all cases, with the best results being observed for the tris-alkoxide complex [$Ga(OCH_2CH_2NMe_2)_3$].

The use of single-source precursors which contain existing M-O (M = main group metal) bonds and can decompose cleanly leaving a thin film of the desired material is an attractive approach to CVD. This approach can eliminate the need for multiple precursors which can be expensive and/or toxic and thus present problems with safe handling, as well as difficulties in the control of film stoichiometry.[85] As eluded to above, the combination of this approach with AACVD offers the benefits of single-source deposition coupled with the simplicity of *in* situ precursor formation. However, the single-source approach is by no means limited to solution-based CVD process and a considerable amount of literature has been dedicated to the formation and application of such precursors by a range of CVD and other deposition processes. Whilst a large number of precursors have been employed for this method, the single-source approach largely relies on the use of alkoxides (including donor-functionalised alkoxides) and *β*-diketonates of the main group metals.[94] (The literature relating to the single-source deposition of group 13 oxides has been discussed in greater detail in chapter 1).

Given the successful application of donor-functionalised alkoxides and *β*-diketonates as single-source precursors to gallium oxide, the aim of this project was the investigation of structurally similar *β*-ketoiminates for the same purpose. The following section discusses previous reports of the use of *β*-ketoiminate complexes spanning the periodic table in CVD.

3.1.2 *β*-ketoiminates in CVD

The application of *β*-ketoiminate complexes of various metals has largely been limited to the field of catalysis. However, a number of examples of metal-*β*-ketoiminate compounds being employed as precursors for the production of thin films by CVD exist in literature. The following section discusses the scope of their

application in this process for the production of materials based on alkaline earth, transition metal and rare earth metals.

Alkaline earth Metals

The need for volatile, fluorine-free MOCVD precursors of barium led to the development of a number of barium β-ketoiminate complexes containing linked polyether "lariats", the type and lengths of which offered a potential means to tailoring thermal characteristics of the complex.[173, 174] The ligands were synthesised according to Scheme 3.1, and the corresponding barium complexes formed by refluxing the free ligand with BaH_2.

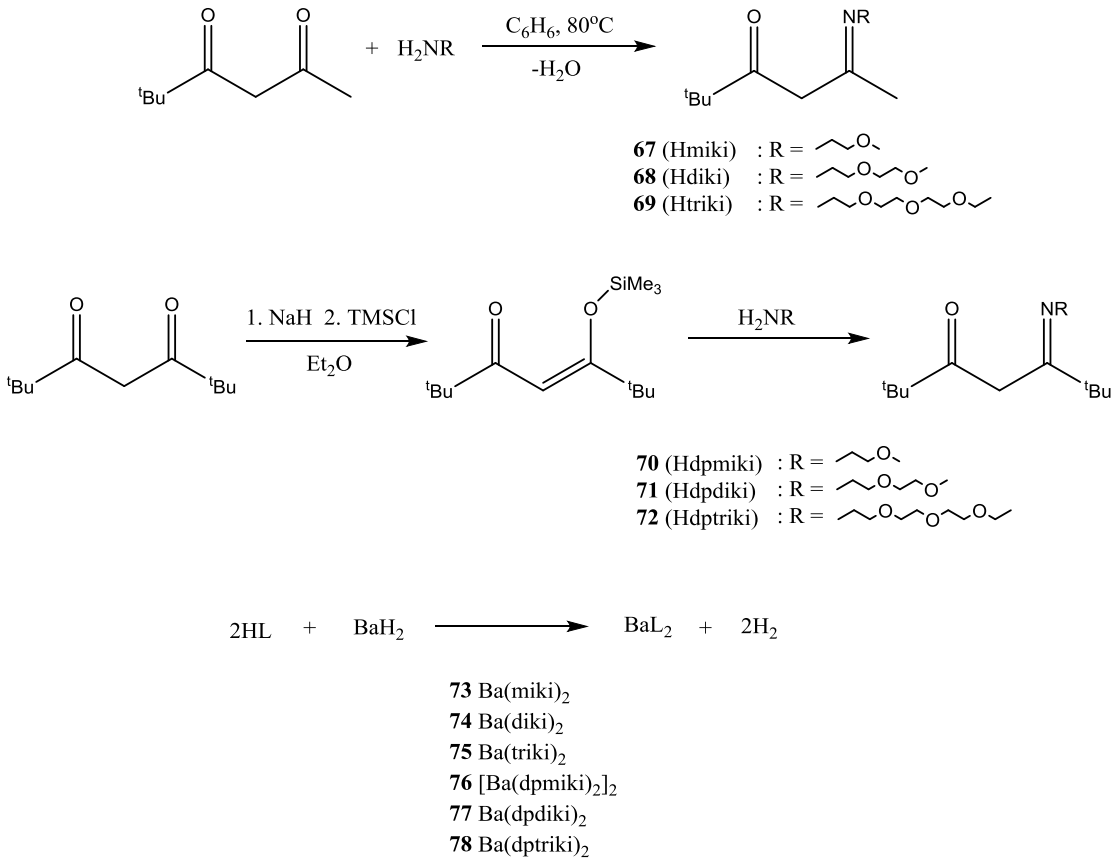

*Scheme 3.1 - Synthesis of poly-ether functionalised β-ketoimines **67** – **72** and their corresponding barium complexes **73** – **78**.*

Single crystal X-ray diffraction studies of **74** and **75** showed both to be monomeric, eight-coordinate barium complexes, whereas that of **76** showed the complex to be dimeric, containing two 6-coordinate barium centres bridged by ketoiminyl oxygen

atoms (Figure 3.1). Each barium centre is coordinated by two ligand molecules, one of which coordinates by all three heteroatoms, the other coordinates through the ketoiminyl oxygen and the oxygen of the appended ether group.

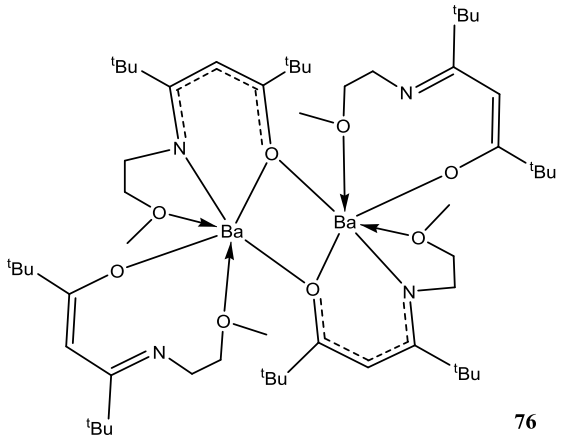

76

*Figure 3.1 -Crystal structure of [Ba(dpmiki)$_2$]$_2$ (**76**)*

Thermogravimetric analysis of compounds **73** – **78** showed that the thermal properties were significantly dependent upon the nature of the ligand system. Both the percentage residue at 500 °C and T_{50} (the temperature at which 50 wt% of the material had been lost) were found to decrease with increasing length of the polyether lariat, with the exception of **76**. Melting points followed the same pattern with the exception of **73**. The anomalous behaviour of **73** and **76** were thought to be a result of their dimeric nature. Compound **74** was subsequently used successfully in the deposition of $BaPbO_3$ thin films on MgO substrates by MOCVD, using a lead diketonate as the lead source and water-saturated O_2 as an oxidising agent. Deposition was carried out at 450 °C before a 10 min post-anneal at 890 °C in air afforded crystalline thin film of $BaPbO_3$ containing traces of BaO, as determined by X-ray diffraction studies.

The work was later extended to the use of linked *β*-ketoiminate-polyether-*β*-ketoiminate ligands, designed to encapsulate alkaline-earth cations which have low charges and large ionic radii.[175] Barium complexes **79** – **82** (Figure 3.2) were synthesised in the same way as outlined above. In all cases, initial syntheses gave low yields of barium-β-ketoiminate product (10-26%), however the yield of **81** was improved to 64% by multiple solvent extraction steps to remove the product from unreacted BaH_2 solid starting material. Crystal structure analysis revealed complex

81 to have a nine-coordinate, tricapped trigonal prismatic coordination geometry and complex **82·2DMSO** to have a ten-coordinate, distorted tetracapped trigonal prismatic coordination geometry. To investigate their efficacy towards MOCVD, TGA analysis was carried out on compounds **79** and **81**, owing to their superior volatility over the other two complexes. Compound **81** showed much greater thermal stability than **79**, and was subsequently used in combination with [Ti(dipivaloylmethanate)$_2$(isopropoxide)$_2$] for the deposition of $BaTiO_3$ epitaxial films on MgO, with N_2O and O_2 employed as oxidising gases. These examples prove the potential for use of *β*-ketoimine ligands in the fine tuning of the thermal properties of metal complexes, and subsequently their suitability as MOCVD precursors.

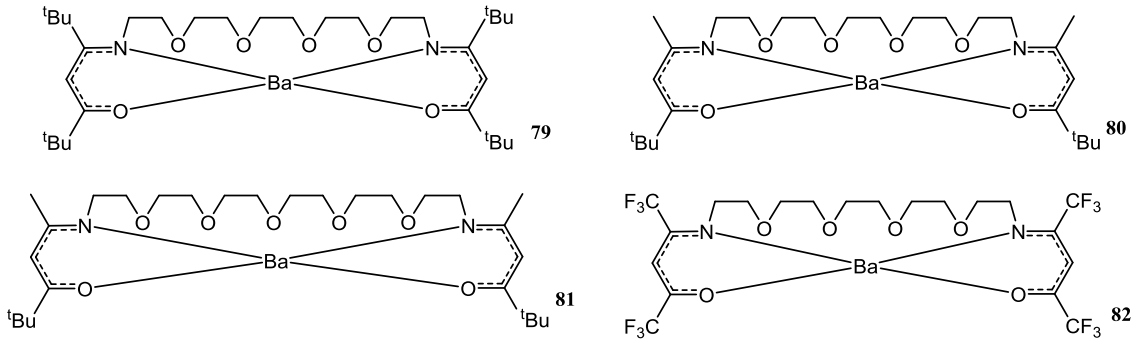

*Figure 3.2 – Structure of barium β-ketoiminate complexes **79** - **82***

The utility of *β*-ketoiminate ligands containing pendant amine 'arms' was applied to group 2 metals calcium, strontium and barium.[176] The synthetic strategy used in this case employed reaction of the metal with the free ligand in the presence of ammonia to activate the metal (probably due to the formation of amide/imide intermediates), resulting in the formation of metal *β*-ketoiminate complexes of the general form $[ML_2]_m$ (Equation 3.1), in a range of yields (**83** 60%, **84** 20%, **85**, 44%).

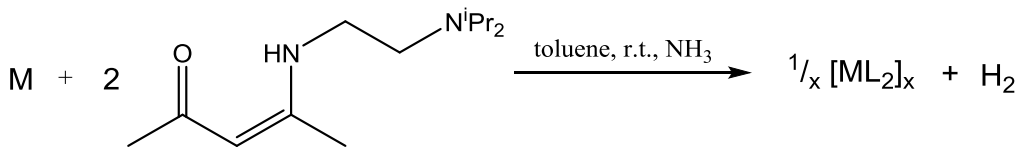

M = Sr (**83**), Ca (**84**), Ba (**85**) (3.1)

Strontium complex **83** exists as a trimer with hexacoordinated Sr atoms, the two terminal Sr atoms being bonded to three ketoiminate ligands in a "three blade propeller" mode. The central Sr atom is bonded to six oxygen atoms of the ketoiminate ligands and has trigonal antiprismatic geometry. NMR analysis of **83** and **85** show all ligands to be magnetically equivalent, whereas that of **84** showed two sets of resonances in a 1:2 ratio. The volatility of the complexes was found to be poor; however the strontium and calcium derivatives may still have application in liquid injection MOCVD due to their high solubility in organic solvents.

The first example of a magnesium β-ketoiminate complex, reported by Matthews *et al.*,[177] involved the formation of β-ketoimine **86** by the condensation reaction between the relevant *β*-diketone and diamine, followed by reaction with half an equivalent of dibutylmagnesium forming the 6-coordinate complex **87** (Equation 3.2). The magnesium lies in an octahedral geometry with both axial positions occupied by nitrogen atoms belonging to the pendant 'arm' moieties of the β-ketoiminate ligand, which form dative bonds to the magnesium centre as evidenced by the longer than normal Mg-N bond lengths. TGA showed sublimation of the precursor in a one-step event without decomposition. CVD of stoichiometric MgO was achieved using the precursor without the need for any addition oxygen source. The observed carbon contamination levels of 7% were three to five times lower than typically seen in metal oxide films.

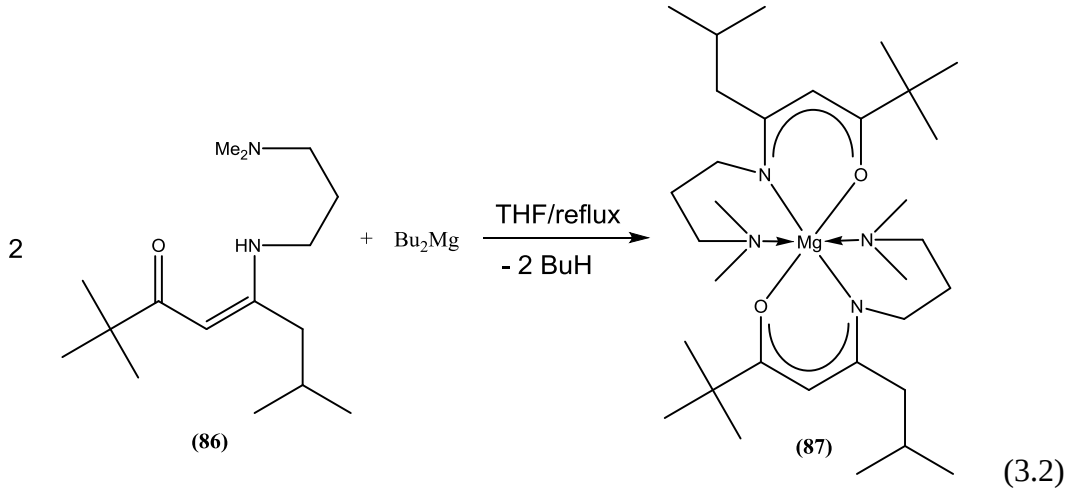

(3.2)

Lanthanides

In an attempt to design a fluorine-free ligand system which met all the requirements for CVD precursors and which could be applied across the lanthanide series, Edleman *et al.* developed a series of ether-functionalised *β*-ketoimines and utilised them in the formation of monomeric species of Ce, Nd, Gd and Er (Scheme 3.2 – *Note: not all ether oxygen atoms coordinated in all cases*).[178] Compounds **88** – **96** were synthesised by the amine elimination reaction between the relevant lanthanide tris[bis(trimethylsilyl)amide] and *β*-ketoimine in xylenes under reflux, as outlined in Scheme 3.2. The products were easily purified by recrystallization from pentane affording monomeric complexes. Studies into the thermal properties of this wide range of complexes revealed the ability to fine-tune the thermal properties by substitution of a variety of alkyl moieties in the keto, imino and ether sites, providing the ability to customise the ligand for any given system. For example, the melting points were found to increase with the introduction of larger alkyl groups in the R_2 position. The potential of this class of complex was demonstrated by the deposition of CeO_2 on YSZ at relatively low temperatures.

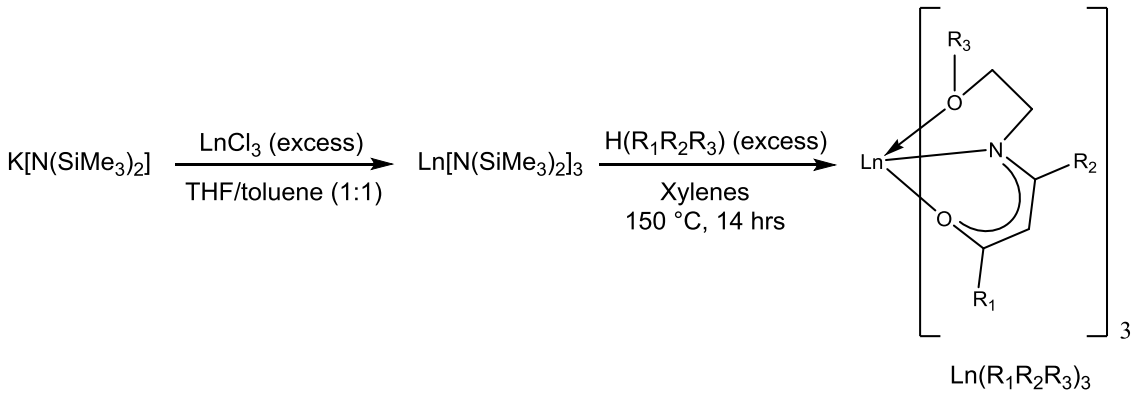

88: Ce(^{t}BuMeMe) **91**: Er(^{t}BuMeMe) **94**: Er(^{t}BuEtMe)
89: Nd(^{t}BuMeMe) **92**: Ce(^{t}BuEtMe) **95**: Nd(^{t}Bu^{t}BuMe)
90: Gd(^{t}BuMeMe) **93**: Nd(^{t}BuEtMe) **96**: Er(^{t}Bu^{t}BuMe)

*Scheme 3.2 - Synthesis of lanthanide β-ketoiminate complexes **88** – **96**.*

Transition Metals

The effect of ligand substituents on the thermal properties of *β*-ketoiminate complexes has also been investigated thoroughly for some transition metal elements.[179] A series of *N*-alkoxy-β-ketoiminato titanium complexes were prepared by the reaction of titanium *iso*-propoxide with the free ligand. Dimers and monomers could be formed depending on the stoichiometry and the reaction conditions (Scheme

3.3). Analysis of the thermal characteristics showed the dimeric species to undergo disproportionation followed by successive evaporation of $Ti(O^iPr)_4$ and [Ti(*N*-alkoxy-*β*-ketoiminate)$_2$]. The substituents on the backbone of alkoxy moiety of the monomeric species were found to have a noticeable influence on the thermal characteristics of the compound, such as melting points, evaporation temperatures and decomposition residue. In particular, the introduction of alkyl substituents on the alkoxy backbones tends to lead to lower vapourisation temperatures and the formation of 6,5-chelate rings offers enhanced thermal stability and higher volatility over 6,6-chelate ring systems.

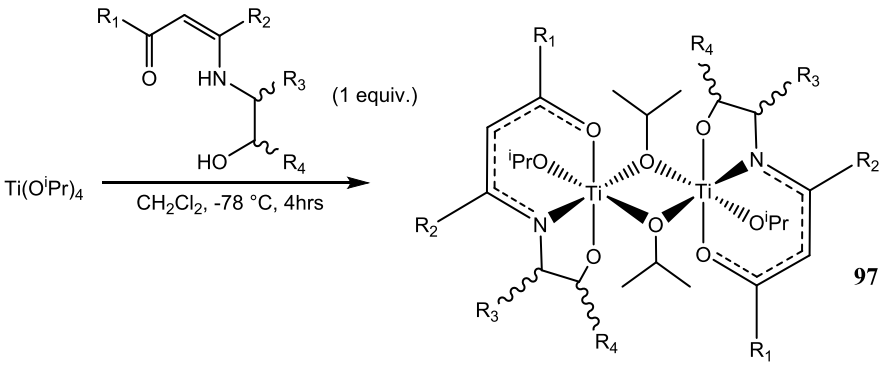

Compound no.	R_1	R_2	R_3	R_4
97a	Me	Me	H	H
97b	Me	Me	Me	H
97c	Me	Me	H	Me
97d	^{i}Pr	^{i}Pr	H	H
97h	^{i}Pr	^{i}Pr	H	Me

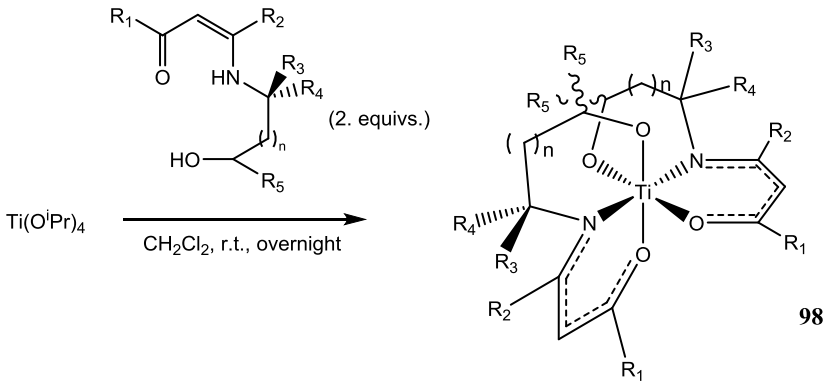

Compound no.	R_1	R_2	R_3	R_4	R_5	n
98a	Me	Me	H	H	H	0
98b	Me	Me	H	H	Me	0
98c	Me	Me	Me	H	H	0
98d	Me	Me	Me	Me	H	0

98e	Me	Me	H	H	H	1
98f	Me	Me	Et	H	H	0
98h	^{i}Pr	^{i}Pr	H	H	Me	0
98i	^{i}Pr	^{i}Pr	Me	H	H	0
98j	^{t}Bu	^{t}Bu	H	H	H	0
98k	^{t}Bu	^{t}Bu	H	H	Me	0

*Scheme 3.3 - Synthesis of dimeric (**97**) and monomeric (**98**) titanium N-alkoxy-β-ketoiminate complexes with varying ligand substituents R_1 - R_5.*

Such complexes have been found to be suitable for use in CVD. The deposition of $Ba_xSr_{1-x}TiO_3$ by a liquid-source (LS) MOCVD process using the monomeric complex **98b** as the titanium source was found to produce ultra-smooth films.[180] The titanium content of the films was not found to vary significantly with varying deposition temperatures, unlike other commercially available precursors. The dimeric precursors **97b** and **97c** have also been used to deposit TiO_2 by LSMOCVD, with **97b** displaying a faster deposition rate than commercially available precursors.[179] It is suggested that the dimer undergoes disproportional rearrangement under elevated temperatures and that the formation of $Ti(O^{i}Pr)_4$ in this process is the cause of the improved deposition rates.

Thin films of palladium have been of interest for application in the fields of microanalysis and catalysis. However, deposition of Pd films by CVD has been limited by a lack of suitable precursors, as most Pd complexes are insufficiently volatile under normal CVD conditions or are sensitive to air and moisture, presenting difficulties in handling of the precursors. Liu *et al.* synthesised the four-coordinate, fluorinated bis-*β*-ketoiminato palladium complex **99** (Figure 3.3, R = $(CH_2)_2OMe$) by the reaction of $Li_2[PdCl_4]$ with two equivalents of the ligand potassium salt, which was itself prepared *in situ* by the deprotonation of the free ligand with KOH.[181] The product was purified by vacuum sublimation, yielding a pure orange-red product, after which single crystals suitable for X-ray crystallography were grown by recrystallization from a CH_2Cl_2/heptane solution, revealing a palladium centre in square-planar geometry forming two slightly distorted hexagonal 6-membered rings with each *β*-ketoiminate ligand. Compound **99** was successfully used in the deposition of a Pd thin film on a Si substrate at 350 °C using O_2 as a carrier gas.

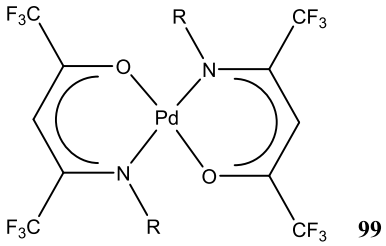

99

Figure 3.3 – Chemical structure of palladium β-ketoiminate complex ***99*** *(R = $CH_2)_2OMe$).*

In recent years, a great deal of attention has been paid to ZnO as a material useful for a wide range of important applications. With MOCVD an attractive method of deposition due to capability of large area growth, conformal coverage, good control of film thickness, preferred orientation and quick deposition rates, substantial research has been carried out into identifying suitable precursors. The first example of the use of *β*-ketoiminate complexes for the deposition of ZnO was carried out by Matthew *et al.*, involving the synthesis of zinc bis-*β*-ketoiminates **100 - 101** containing simple alkyl groups substituted on the ligand imino moiety.[182] These compounds were formed by the facile reaction between the relevant free ligands with diethyl zinc, eliminating ethane (Equation 3.3).

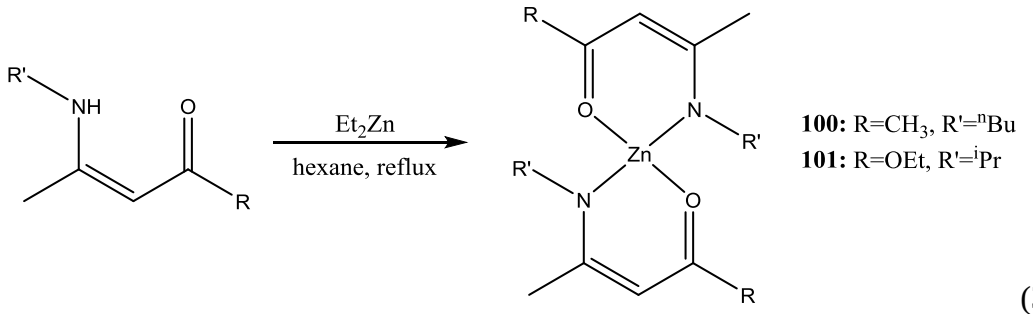

(3.3)

Thermal analysis of the zinc precursors showed that both were volatilized without decomposition supporting their potential as precursors for APCVD. Both compounds **100** and **101** were used for the deposition of ZnO on Si substrates at atmospheric pressure without the use of an addition oxidant, though films deposited with **100** showed a much higher carbon content than those of **101**. This is attributed to the presence of addition oxygen in the precursor aiding the deposition of ZnO. The results show the potential of using single-source precursors containing oxygen as an alternative to deposition processes carried out in the presence of an addition oxidant such as O_2.

Later, two similar zinc *β*-ketoiminate precursors were synthesised containing longer chain ether groups attached to the imino moiety of the ligand.[183] These were again formed by the ethane elimination reaction between the free ligands and diethyl zinc (Equation 3.4). Thermal analysis showed the compounds to have low melting points, good volatility and clean decomposition characteristics, whilst also being attractive due to good stability to humidity making them easy to handle, as well as showing good solubility in common organic solvents. Both precursors were used for the deposition of pure, stoichiometric ZnO films on silicon and borosilicate substrates at temperatures between 400 and 700 °C with the use of O_2 as a reactive gas.[184] Unlike the previous example, deposition was not attempted in the absence of an additional oxidant, however the potential of such ligand systems for developing suitable precursors for the deposition of metal oxide was again demonstrated.

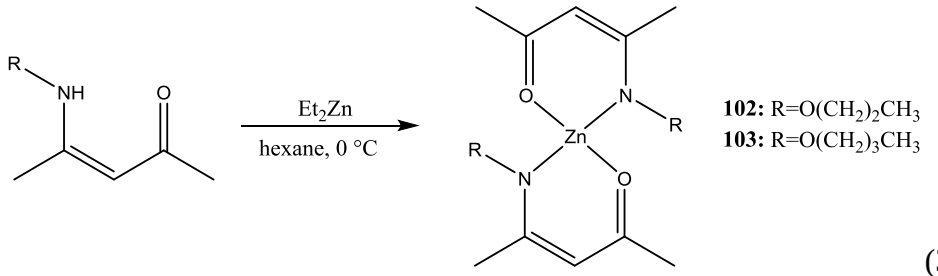

(3.4)

The above examples display the potential of the *β*-ketoiminate class of ligands to be used in the formation of metallic complexes across the entire periodic table, which are suitable for use as precursors for the deposition of thin films of a variety of materials by a range of different CVD techniques. The possibility of *N*-derivatisation enables the ligand to be adapted to meet the needs of each specific system, both fulfilling the coordination preferences of each individual metal in order to form monomeric species, whilst also tailoring the thermal properties to enhance the suitability of each precursor for CVD purposes. Inclusion of heteroatomic appendages such as ether groups can both enable coordinative saturation of the metal centre to prevent oligomerisation, as well as eliminating the need for additional reactive gases (oxidants for the purposes of metal-oxide film deposition) in the deposition process. This potential for tailoring makes metal *β*-ketoiminates an attractive class of compound for application in CVD, though their use in the deposition of group 13 oxides is relatively unexplored.

3.2 Results & Discussion

3.2.1 Thermal Decomposition Analysis

The thermal decomposition properties of the gallium *β*-ketoiminate complexes (the synthesis and characterisation of which has been discussed in Chapter 2) were studied by thermogravimetric analysis (TGA) and differential scanning calorimetry (DSC). TGA is a technique which allows the continuous measurement of the mass of a sample with increasing temperature. In the case of such complexes as those being studied, decomposition occurs through loss of organic ligands, resulting in a decrease in the mass of the sample. By plotting sample mass (or % mass) as a function of increasing temperature, it is possible to gain information about the decomposition characteristics exhibited by the complex, such as decomposition temperature ranges, decomposition stages, sublimation and total mass loss. DSC can be carried out simultaneously, which measures the difference in the amount of energy required to increase the temperature of a sample with comparison to a reference, also as a function of temperature. This is particularly useful for determining phase transitions (i.e. melting points, boiling points), where the endothermic reaction demands more energy.

Carrying out such analysis on the complexes provides a means to make an initial assessment of the complexes as potential precursors for the CVD of metal oxides. Ideal precursors would exhibit clean, low temperature decomposition, with a sufficient temperature window between melting and the onset of decomposition in order to allow the transfer of the precursor in the gas phase to the reaction chamber without unwanted decomposition. (The latter is relevant only for conventional thermal CVD processes, however thermal analysis will allow an assessment of which techniques would be suitable for a given precursor.) Furthermore, calculation of the residual mass post-decomposition will allow an estimation as to whether complete decomposition to the metal oxide can be achieved at such temperatures.

Due to the air and moisture sensitivity of the complexes, all analyses were carried out in sealed aluminium crucibles, meaning that the highest temperature to which the samples could be heated was 600 °C due to the melting point of aluminium (660 °C). However, since the thermal decomposition properties of the complexes were being studied with a view to carrying out CVD on glass substrates, which have a maximum

temperature of 600 °C before warping is observed, this is an appropriate ceiling temperature for the thermal analyses.

Figure 3.4 shows the TGA profile for the three gallium *β*-ketoiminate chloride complexes, [Ga(L^n)Cl] (where n = 2 -4). The melting points of the complexes were found to be in the range 161 – 200 °C, as determined by the presence of endotherms within the DSC profile. Both [Ga(L^2)Cl] and [Ga(L^3)Cl] displayed a slow mass loss at temperatures above *ca.* 150 °C, indicating sublimation of the complexes prior to decomposition. The profile for [Ga(L^3)Cl] (red) also shows a small mass loss between 70 and 150 °C, which is most likely to be due to the loss of residual solvent within the sample. The fact that no apparent sublimation was observed for the tetramethylene derivative [Ga(L^4)Cl] could be a result of the slightly higher molecular mass. The onset of decomposition was observed at similar temperatures for all three complexes, 285 °C for [Ga(L^2)Cl], 268 °C for [Ga(L^3)Cl] and 241 °C for [Ga(L^4)Cl]. The large gap between the melting point and the onset of decomposition suggests that the complexes could be successfully used in a thermal CVD process, with successful transfer of the precursor to the reaction chamber in the gas phase.

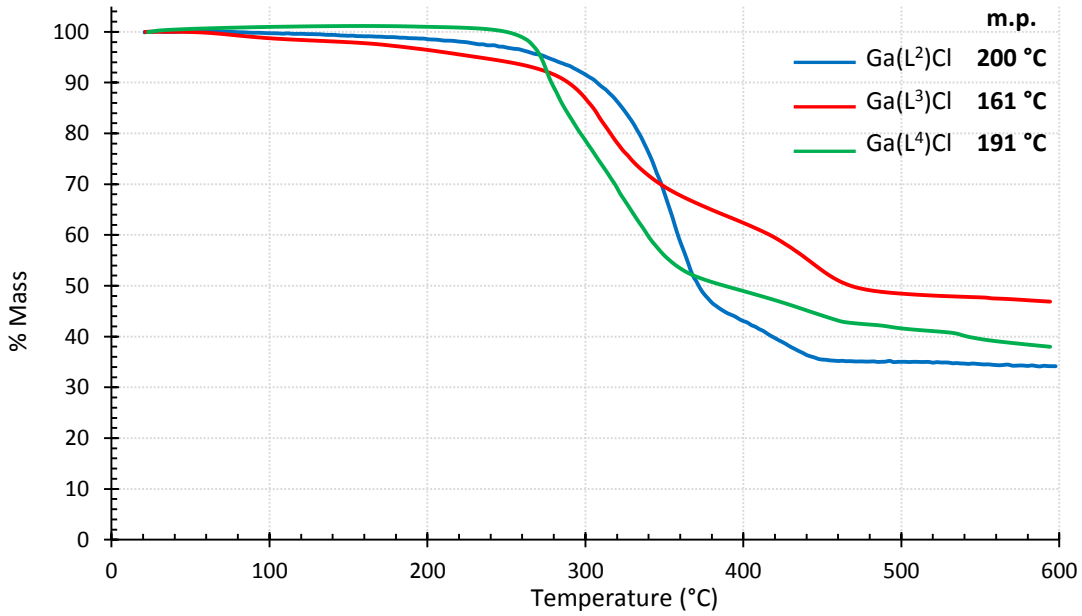

Figure 3.4 - TGA of gallium β-ketoiminate chloride complexes. Melting points of the complexes are indicated in the legend.

Decomposition of all three complexes does not occur through a particularly clean pathway and occurs in a number of stages. The first and largest stage is likely to correspond to decomposition and loss of some of the organic ligand. In all three cases, a smaller mass loss of *ca.* 11% is observed between 350 and 450 °C, which corresponds well to the loss of the chloride co-ligand (calculated values for chloride loss are: [Ga(L^2)Cl], -10.8%; [Ga(L^3)Cl], -10.4%; and [Ga(L^4)Cl], -10.0%).

An important characteristic of a precursor's thermal decomposition properties is the full decomposition to the desired material, i.e. gallium oxide (Ga_2O_3). The residual mass left over after the TGA experiment allows an estimation of whether or not complete decomposition has taken place. For the three chloride complexes [Ga(L^2)Cl], [Ga(L^3)Cl] and [Ga(L^4)Cl], $GaO_{1.5}$ (i.e. ½ Ga_2O_3, where 2 mol precursor are required for the formation of 1 mol oxide) accounts for 29, 27 and 26% of the total mass, whilst the residual masses post-decomposition were 34, 47, and 48%, respectively. This shows that full decomposition to gallium oxide has not taken place. Data suggest that these chloride complexes could be successful in the deposition of thin films at temperatures below 500 °C, though some contaminants may remain since the observed mass loss was not sufficient for the formation of Ga_2O_3.

TGA of the methyl complexes showed much cleaner decomposition pathways than were observed for the chloride complexes (Figure 3.5). The complexes [Ga(L^2)Me], [L^3($GaMe_2$)$_2$] and [L^4($GaMe_2$)$_2$] all showed very similar decomposition profiles, as displayed in the blue, red and green data sets, respectively. Decomposition occurs in a single, clean step between 230 and 360 °C, followed by residual mass loss up to 550 °C. The total mass losses for these three complexes were 77, 76 and 75%, respectively, compared to the calculated values of 69, 57 and 58% for complete decomposition to Ga_2O_3. In all three cases, the observed mass loss was significantly higher than would be expected for the formation of Ga_2O_3, suggesting some sublimation of the precursor has occurred leading to excess mass loss. The excess mass losses for the mononuclear complex was only 8%, whereas that of two dinuclear species were 19 and 17%. This difference can be understood by looking at the measured melting points of the compounds from DSC of 120, 65 and 73 °C. The higher melting point of the mononuclear complex results in less sublimation prior to

decomposition than for the two dinuclear complexes and thus less mass is lost by this process. In all cases, a good temperature window exists between the melting point of the precursors and the onset of decomposition suggesting that these could be successfully transferred to a CVD reaction chamber in the gas phase without decomposition.

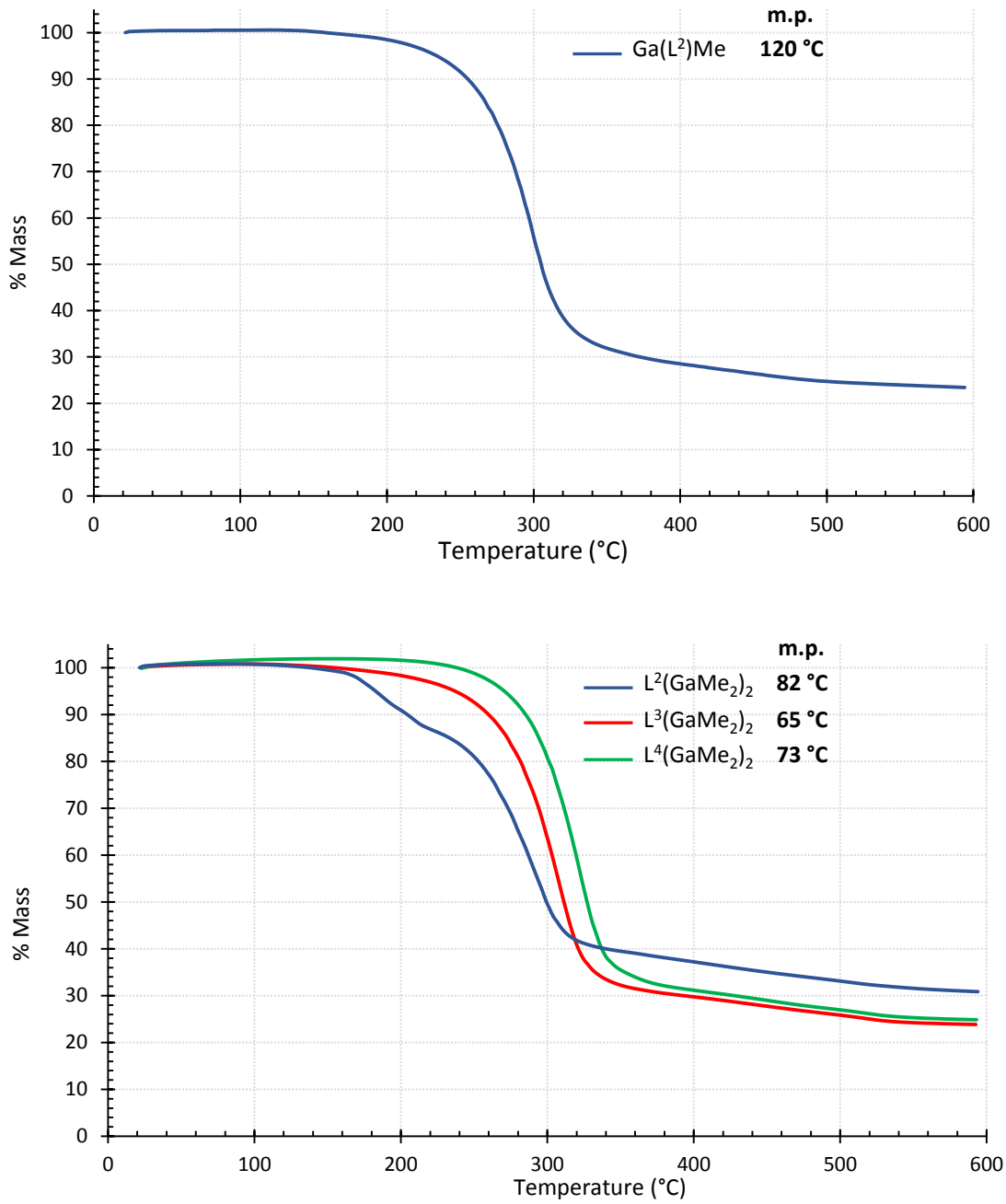

Figure 3.5 - TGA of gallium β-ketoiminate methyl complexes. Melting points of the complexes are indicated in the legend.

The thermal decomposition of the ethylene-bridged dinuclear complex $[L^2(GaMe_2)_2]$ showed a slightly different pathway to the other methyl complexes (Figure 3.5, blue

curve). In this case, decomposition occurs in two discrete stages, the first between 160 and 230 °C, followed by the major mass loss between 230 and 330 °C. The initial smaller mass loss of *ca*. 12% occurs at too high a temperature to be a result of residual solvent loss and thus must be a decomposition process. The major mass loss of 46% is followed by residual mass loss up to 520 °C, resulting in a total mass loss of 69%, compared to the calculated value of 56% for Ga_2O_3. Given the observed melting point of 82 °C, this agrees well with the data for the other three methyl complexes and suggests the excess mass loss is a result of precursor sublimation. The temperature window between the melting point and the onset of decomposition is not as large as that of the other three complexes, though is still sufficiently large to allow precursor sublimation prior to decomposition.

Finally, TGA analysis was carried out on the two hydride complexes, [Ga(L^2)H] and [Ga(L^3)H]. Except for the initial loss of residual solvent within the sample of [Ga(L^2)H], both hydride complexes showed clean, single-step decomposition pathways, as shown in Figure 3.6. The melting points of the two complexes, as determined by DSC analysis, were very similar at 126 and 127 °C and the onset of decomposition was observed at *ca.* 240 °C, once again indicating a sufficient temperature window for transfer of the precursor to the CVD reactor in the gas phase. However, very different observations were made for the two complexes with regards to the total mass loss in the decomposition process.

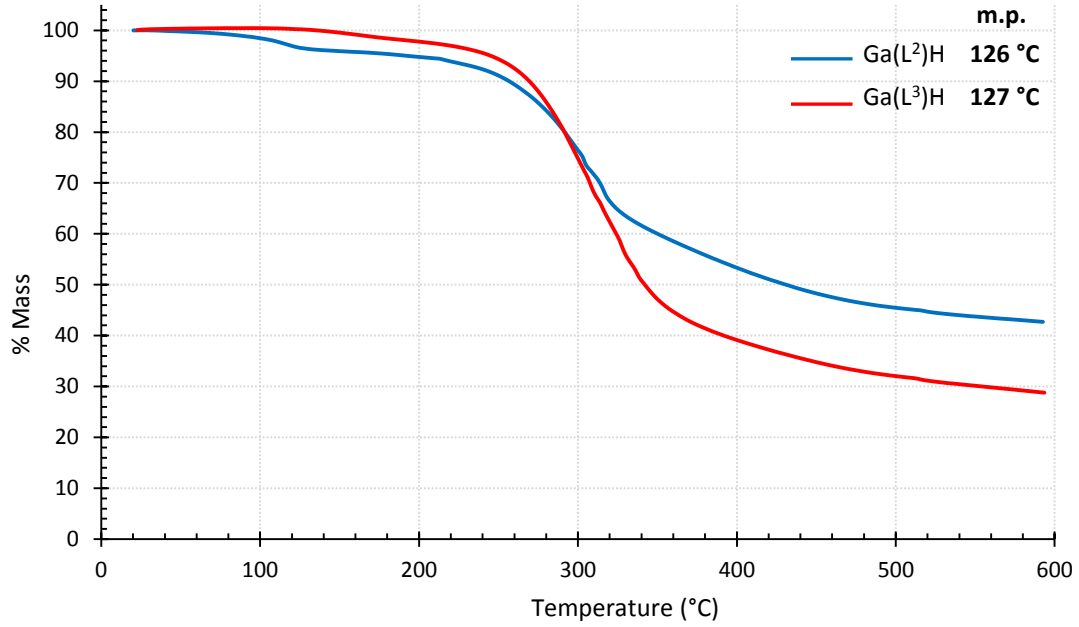

Figure 3.6 - TGA of gallium β-ketoiminate hydride complexes. Melting points of the complexes are indicated in the legend.

[Ga(L^3)H] showed an overall mass loss of 71%, which when compared to the expected mass loss of 69% for decomposition to Ga_2O_3 gives the precursor good potential for the deposition of uncontaminated thin films. The ethylene derivative [Ga(L^2)H], however, showed a mass loss of just 57%, versus the required loss of 68% for Ga_2O_3. This implies that the nature of the bridging group has a notable influence on the decomposition characteristics of the precursor. As discussed previously, a similar observation was made for the ethylene derivative of the dinuclear methyl complex [$L^n(GaMe_2)_2$], whose decomposition pathway differed from that of the propylene and tetramethylene analogues. This seems to suggest that the ligand bridge moiety plays a key part in the decomposition of the precursor and variation of the length of this linker can influence the decomposition characteristics significant. This provides support for the careful design of precursors, showing that small adaptation have an impact not only on the structural and geometrical characteristics of the complex itself (see discussion in chapter 2), but also on the decomposition characteristics of the complex as a potential precursor.

Whilst this thermal analysis provides some insight into the decomposition characteristics of the gallium *β*-ketoiminate complexes, it should be noted that the mechanism of decomposition for such systems is not well understood. It would be pertinent, therefore, for a detailed study of the decomposition of gallium *β*-

ketoiminates to be carried out *via* pyrolysis and/or trapping of CVD reaction products in order to better understand the process.

3.2.2 Aerosol-Assisted Chemical Vapour Deposition (AACVD)

Given the observation of a significant temperature window between melting and decomposition found through TGA and DSC analysis, initial attempts at the deposition of Ga_2O_3 were made with the hydride precursor [Ga(L^2)H], using a simple low pressure (LP)CVD tube furnace. However, it was found that the precursor decomposed before any significant sublimation occurred. In order to aid the transport of the precursors into the reaction chamber, attention was turned to the use of AACVD. A detailed overview of AACVD is given in Chapter 1. The process utilises a solution of the precursor in a suitable organic solvent, which is then nebulized to yield an aerosol precursor 'mist' and transferred into the reaction chamber by use of a carrier gas. One of the major benefits of the technique is the alleviation of the need for highly volatile precursors, since the main requirement is good solubility in the chosen solvent, broadening the range of potential precursor candidates.

3.2.2.1 Chlorides

Despite the suggestion from TGA of the chloride precursors that decomposition occurs within the desired temperature window for the deposition of Ga_2O_3, no deposition was observed for any of the chloride complexes under any experimental conditions employed. The substrate temperature was varied between 400 and 600 °C, flow rates between 0.2 and 1 L min^{-1} and quantities of precursor between 0.2 and 0.6 g. It was initially thought that the lack of film growth was due to insufficient solubility of the precursor in toluene, owing to the presence of a residue of the precursor within the AACVD flask after the nebulisation and transport of the solvent to the CVD reactor. However, use of a number of alternative solvents, namely CH_2Cl_2, THF and MeOH, in which the solubility of the precursors was sufficient for no residue to be left after the nebulisation and transport process, did not lead to any observable deposition. The higher decomposition temperatures observed for the chloride species by TGA/DSC analysis suggest that deposition does not occur due to insufficient temperatures within the reactor for decomposition of the precursors. Whilst higher deposition temperatures could be explored through the use of

alternative substrates (e.g. quartz), attention was turned to methyl and hydride precursor derivatives.

3.2.2.2 Methyls

Given the clean and relatively low temperature decomposition of the methyl complexes observed by TGA, it was expected that deposition of gallium oxide would be possible by use of these complexes as precursors. The precursors $[L^2(GaMe_2)_2]$ and $[L^3(GaMe_2)_2]$ were synthesised as described in Chapter 2, dissolved in anhydrous toluene and stored as stock solutions at a concentration of 0.02 g mL^{-1}. Initial depositions were attempted at substrate temperatures of 400 – 500 °C, however no film growth was observed at the lower end of the temperature range for either precursor.

At 500 °C a small amount of deposition was observed near the reactor outlet, suggesting that higher temperatures were required for deposition with good coverage over the entire substrate. Increasing the temperature to 550 °C resulted in improved coverage, however the best results in both cases were observed at a substrate temperature of 600 °C. Table 3.1 summarises the experimental conditions under which the most effective depositions were achieved.

Despite the good decomposition characteristics found for the monomeric complex $[Ga(L^2)Me]$, isolation of the monomer required recrystallisation and it was not possible to obtain sufficient quantities to carry out CVD studies by this method. The complex remains a suitable candidate for the deposition of Ga_2O_3 and further work could be directed towards the isolation of the precursor in order to carry out CVD studies.

Previous reports of the deposition of Ga_2O_3 *via* AACVD of dialkylalkoxogallanes of the type $[R_2Ga(OR')]$ (where R = Me, Et; R′ = $CH_2CH_2NMe_2$, CH_2CH_2OMe etc.) often resulted in the production of grey or brown films indicative of carbon contamination arising from the retention of the Ga-C bond.[34, 104] In contrast, films grown *via* AACVD of $[L^2(GaMe_2)_2]$ and $[L^3(GaMe_2)_2]$ resulted in the production of adherent, transparent films (visible by the appearance of interference fringes on the surface of the substrate), with no observable evidence of carbon contamination, though optical analysis of the as-deposited films (discussed later in 3.2.3.5) did suggest some carbon contamination. The films were determined to be adherent by

the Scotch™ tape test, however were easily scratched by a brass or stainless steel stylus.

Table 3.1 - AACVD conditions for the production of Ga_2O_3 thin films from methyl gallium β-ketoiminate precursors.

Experiment No.	Precursor	Mass (g)	Solvent	Volume (mL)	N_2 flow rate (L/min)	Deposition time (hours)	Substrate Temperature (°C)
1	$[L^2(GaMe_2)_2]$	0.2	Toluene	30	0.5	2	600
2	$[L^2(GaMe_2)_2]$	0.4	Toluene	60	0.5	4	600
3	$[L^3(GaMe_2)_2]$	0.2	Toluene	30	0.5	2	550
4	$[L^3(GaMe_2)_2]$	0.2	Toluene	30	0.5	2	600

Attempts to deposit thin films of In_2O_3 from the precursors $[In(L^2)Me]$ and $[In(L^3)Me]$ were unsuccessful, with no deposition observed under any conditions. It is likely that temperatures in excess of 600 °C would be necessary for effective decomposition of the complexes, however such temperatures would result in warping of the glass substrates. Whilst this could be explored further by use of alternative substrate materials, attention was focussed on the deposition of Ga_2O_3 and the characterisation and analysis of those films produced.

3.2.2.3 Hydrides

Gallium hydride complexes stabilised by donor-functionalised alkoxides have recently been successfully employed in the AACVD of Ga_2O_3.[156] As mentioned earlier, attempts at film growth from $[Ga(L^2)H]$ in a low pressure (LP)CVD process resulted only in decomposition of the precursor before any significant sublimation was able to occur. Thus attention was turned to AACVD to facilitate transport of the precursor into the reactor.

Optimum conditions for deposition with $[Ga(L^2)H]$ were found to be at a substrate temperature of 450 °C and a carrier gas flow rate of 1 L min^{-1}, resulting in the deposition of an adherent, transparent film with good coverage over the substrate. Full deposition conditions are given in Table 3.2. Deposition from the propylene analogue $[Ga(L^3)H]$, however, was not so facile and required more intense conditions to achieve optimum deposition. A higher substrate temperature (500 °C), lower carrier gas flow (0.5 L min^{-1}) and greater mass of precursor (0.6 g, *cf.* 0.3 g used with $[Ga(L^2)H]$) were all necessary to achieve good coverage over the

substrate. The films produced from both precursors showed good transparency and were visible by the appearance of the expected interference fringes. Similarly to the films produced from methyl precursors, both films passed the Scotch™ tape test but could be easily scratched by a brass or stainless steel stylus.

Table 3.2 - AACVD conditions for the production of Ga_2O_3 thin films from β-ketoiminate-stabilised gallium hydride precursors

Experiment / Film No.	Precursor	Mass (g)	Solvent	Volume (mL)	N_2 flow rate (L/min)	Deposition time (hours)	Substrate Temperature ('C)
5	[Ga(L^2)H]	0.3	Toluene	30	1	2	450
6	[Ga(L^3)H]	0.6	Toluene	40	0.5	2.5	500

3.2.3 Gallium Oxide Thin Film Analysis

3.2.3.1 Glancing angle powder X-ray diffraction (pXRD)

Glancing angle powder X-ray diffraction was carried out on all samples as an initial tool for characterisation. However, in all cases the films were found to be amorphous as-deposited. This is not unusual for the growth of Ga_2O_3 at substrate temperatures below *ca*. 700 °C.[72, 100, 165] In order to obtain crystalline Ga_2O_3, experiment **5** was repeated on a quartz substrate and the film was successfully annealed affording crystalline Ga_2O_3 as determined by pXRD (Figure 3.7).

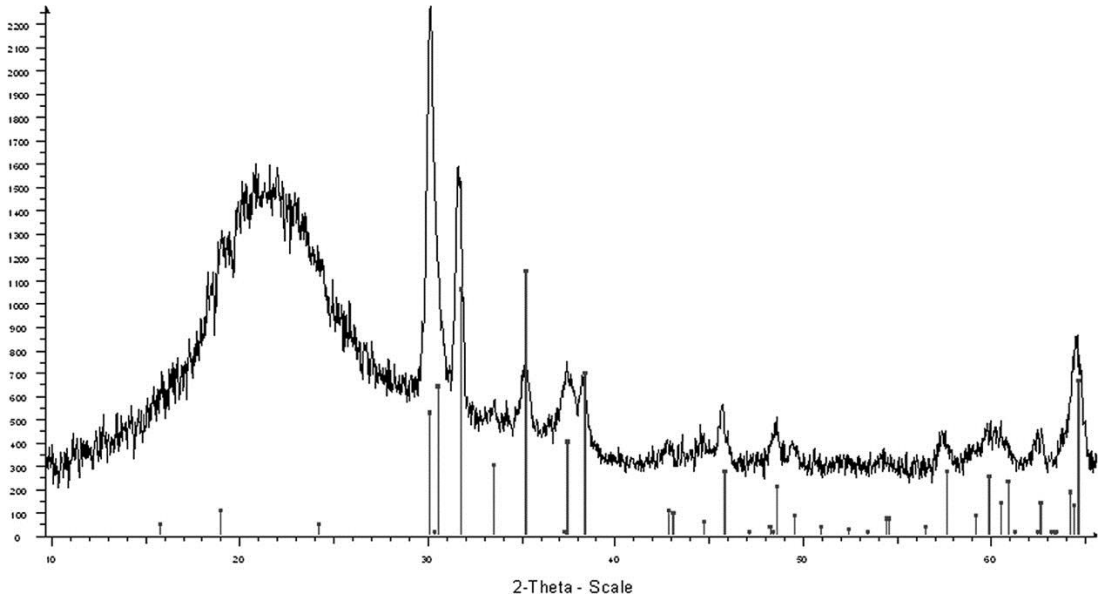

Figure 3.7 - XRD pattern of the film deposited on quartz by AACVD of [Ga(L^2)H] after annealing at 1000 °C for 12 h, consistent with crystalline Ga_2O_3 (solid bars).

3.2.3.2 Energy Dispersive X-Ray Analysis (EDXA)

Energy dispersive X-ray analysis (EDXA) was carried out on all films in order to determine the elemental composition of the films. Analysis confirmed the presence of both gallium and oxygen in the films, however breakthrough to the glass substrates prevented a reliable calculation of the atomic ratios of the elements.

3.2.3.3 Scanning Electron Microscopy (SEM)

Figure 3.8 shows the SEM images produced from films **1** – **6**. In all cases the films were found to be made up of spherical particles, indicating that film growth has occurred *via* a Volmer-Weber type island growth mechanism. Films **1** and **2** were both grown at a substrate temperature of 600 °C using 0.2 g and 0.4 g of the precursor [$L^2(GaMe_2)_2$], respectively. The concentration of the precursor solution was kept constant by doubling the volume of toluene used for the second deposition. Both films are made up of spherical particles and do not exhibit any significant surface features. Film **1** shows very small grain sizes (< 100 nm), however this size is fairly uniform across the film. In contrast, film **2** shows a greater variation in grain size, with some much larger grains of *ca.* 250 nm being visible in the SEM image (Figure 3.8(b)). Larger grain sizes are indicative of slower growing films, which is consistent with these observations given the larger amount of precursor, the greater volume of precursor solution and the longer deposition time involved in the formation of film **2**.

Films **3** and **4**, shown in Figure 3.8 (c) and (d), were those grown using the precursor [$L^3(GaMe_2)_2$] at substrate temperatures of 550 and 600 °C, respectively. Whilst film **3** exhibited very small grain sizes, film **4** displayed much larger grain sizes as high as 600 nm in diameter. Normal grain growth is driven by the minimisation of the overall free energy of the system and larger grain sizes are concurrent with fewer high energy grain boundaries.[185] The increased substrate temperature used in the deposition of film **4** provides adatoms at the surface greater kinetic energy, allowing them to find the lowest energy sites prior to nucleation, resulting in a film with larger grains and fewer grain boundaries.

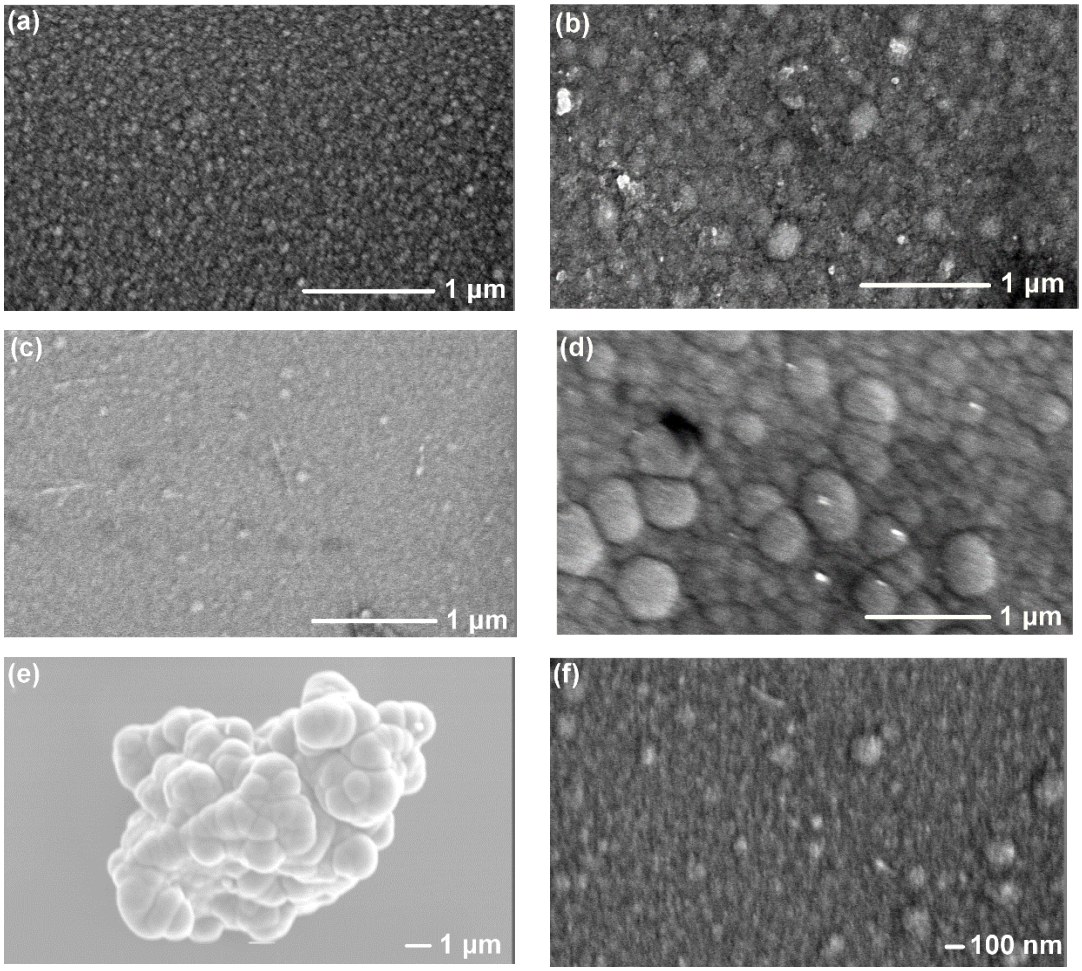

Figure 3.8 - SEM images of Ga_2O_3 films grown under (a) condition 1 (x30,000 magnification); (b) condition 2 (x30,000); (c) condition 3 (x30,000); (d) condition 4 (x30,000); (e) condition 5 (x6,000); and (f) condition 6 (x40,000).

Optimum depositions for the two hydride species [Ga(L^2)H] and [Ga(L^3)H] were found to differ. Film **5** was grown using a toluene solution of the ethylene derivative at a concentration of 0.01 g mL^{-1}, at a N_2 flow rate of 1 L min^{-1} and a substrate temperature of 450 °C. As shown in Figure 3.8 (e), the as-deposited film consisted of large globular surface features made up of smaller spherical particles. In contrast, film **6** was grown from a 0.015 g mL^{-1} toluene solution of [Ga(L^3)H], at a substrate temperature of 500 °C and under a N_2 flow rate of 0.5 L min^{-1} and the surface morphology was found to be more consistent with the results for film **1** – **4**, showing a much smoother surface made up of spherical particles. Whilst this result is slightly anomalous, it is most likely that the globular particle aggregates found at the surface of film **5** arise as a result of the higher carrier gas flow rate employed in the deposition, leading to a very fast deposition rate.

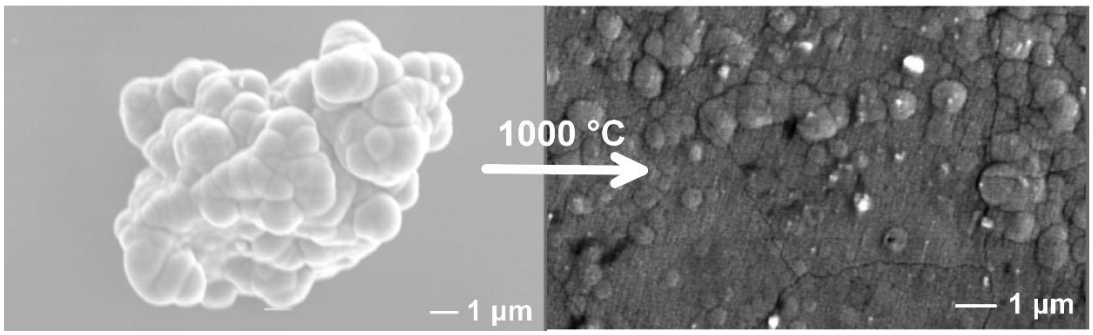

Figure 3.9 - SEM images of the films grown under condition 5. Left: As-deposited on glass. Right: On quartz, followed by annealing in air at 1000 °C.

As discussed in section 3.2.3.1, deposition under condition **5** was repeated on a quartz substrate, which allowed a post-deposition annealing step in air at 1000 °C to be carried out, affording a thin film of crystalline gallium oxide (Film **5a**). SEM imaging of the annealed film (Figure 3.9) showed a loss of the globular surface features and the formation of a much smoother, more uniform film. The increased temperature allows migration of the particles to the lowest energy sites at the substrate surface giving rise to the more uniform coverage.

3.2.3.4 X-Ray Photoelectron Spectroscopy (XPS)

All XPS data were collected by Dr. Sanjay Sathasivam, with data processing and manipulation being carried out by the author.

Ga_2O_3 Standard

To aid the fitting process, a standard sample of Ga_2O_3 powder (99.99%) was analysed by XPS. The results are discussed briefly here for reference when discussing the analysis of the deposited films later. The presence of Ga_2O_3 was confirmed by the presence of a doublet of peaks for Ga $3d_{5/2}$ and $3d_{3/2}$ at 19.41 and 19.92 eV, respectively, as shown in Figure 3.10. These correspond to literature values for Ga_2O_3 3d peaks of 20.07 and 20.52 eV,[186] with the small shift likely to arise from instrumental differences. The presence of another gallium species was also indicated by the presence of a doublet at 18.21 and 18.66 eV, likely to be metallic gallium by comparison to the Ga $3d_{5/2}$ binding energy of 18.4 eV reported for elemental gallium.[187] The observation of this impurity was also reported by Ghosh *et al.* in the XPS analysis of a Ga_2O_3 standard.[186] The oxygen 1s peak of Ga_2O_3 is reported to appear at a binding energy of *ca.* 531 eV,[188, 189] therefore a peak observed at 530.5 eV was attributed to O 1s of the Ga-O bond of the native oxide. A

small additional O 1s peak at 532.04 eV was attributed to the presence of small amounts of another oxygen-containing impurity within the sample.[189] The gallium to oxygen ratio within the relevant peaks was 0.67, once again consistent with Ga_2O_3 (Table 3.3). Having carried out the XPS fitting for the standard sample of Ga_2O_3, the same constraints were used for the analysis of the films deposited under conditions **1** – **4** and **6**.

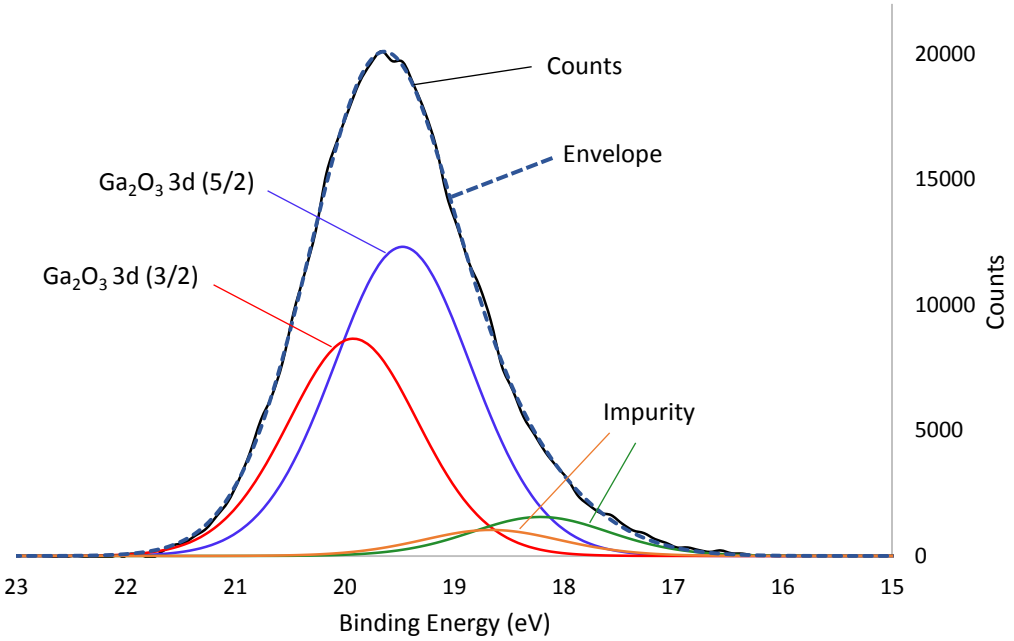

Figure 3.10 - XPS peaks for Ga 3d from standard powder sample of Ga_2O_3 (99.99%). 3d peaks are at 19.41 ($3d_{5/2}$) and 19.92 eV ($3d_{3/2}$). A small amount of an unidentified impurity (possibly metallic gallium) gave rise to a doublet at 18.21 and 18.66 eV in the fitting process.

Films 1 & 2 – $[L^2(GaMe_2)_2]$

Films **1** and **2** were both deposited by AACVD at 600 °C from the precursor $[L^2(GaMe_2)_2]$, using a mass of 0.2 g and 0.4 g, respectively. The resulting films were analysed by XPS to determine their elemental composition. Figure 3.11 shows the peaks found in the Ga 3d region. In both films, Ga $3d_{5/2}$ peaks at 19.33 eV corresponded well to the standard, indicating the presence of Ga_2O_3. As for the standard, an additional doublet at lower binding energy showed the presence of a small amount of impurity, likely to be metallic gallium. O 1s peaks were also observed at 530.35 and 530.22 eV for films **1** and **2** respectively, also corresponding well to the value for Ga_2O_3 within the standard sample of 530.52 eV and agreeing with literature values of *ca.* 531 eV.[188]

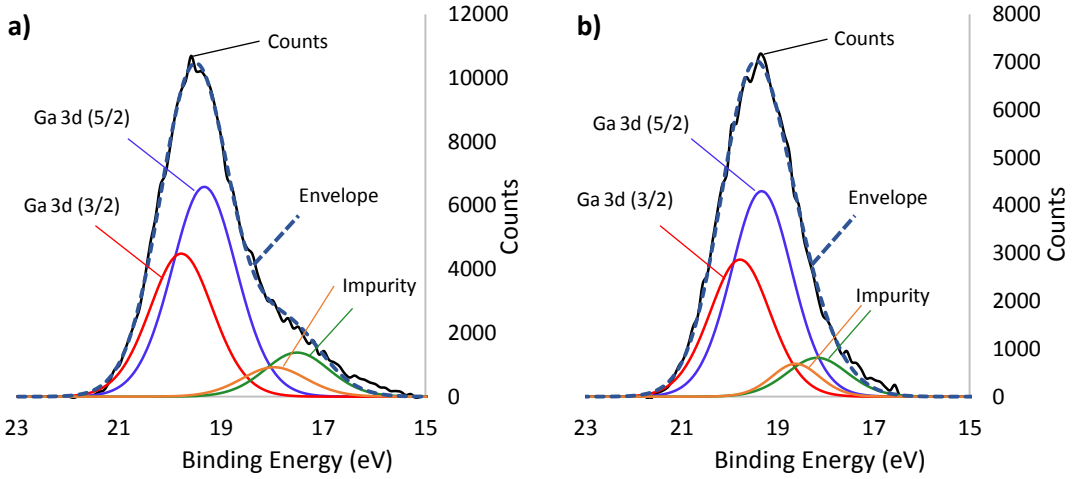

*Figure 3.11 - XPS peaks for Ga 3d at surface of (a) film **1**; and (b) film **2**.*

Whilst the peak positions suggested the formation of Ga_2O_3, the elemental ratios calculated from these peaks were not in the expected ratios for the native oxide (Table 3.3). The calculated Ga:O ratios were calculated as 0.46 and 0.55, significantly lower than required for Ga_2O_3 (0.66), suggesting an excess of oxygen. Furthermore, both films also displayed additional O 1s peaks at 531.96 and 531.76 eV (**1** and **2**, respectively) of considerable intensity, which could not be attributed to any Ga-O species. These latter two observations prevent the reliable characterisation of the film as phase pure Ga_2O_3, thus the analysis can only act to confirm EDXA results which show the presence of both gallium and oxygen within the film. Since all deposition conditions were kept constant except the mass of precursor used, it is unsurprising that the XPS analyses of the two films show very similar patterns.

*Table 3.3 - Ga:O ratios within films **1** - **4** and **6**, as determined by XPS surface analysis.*

Ga_2O_3 standard	**Film 1**	**Film 2**	**Film 3**	**Film 4**	**Film 6**
0.66	0.46	0.55	0.62	0.74	0.95

Films 3 and 4 – $[L^3(GaMe_2)_2]$

Films **3** and **4** were deposited by the AACVD of $[L^3(GaMe_2)_2]$ at 550 and 600 °C, respectively. As shown in Figure 3.12, Ga $3d_{5/2}$ peaks were observed at 19.87 and 19.69 eV for **3** and **4**, respectively, in agreement with values for the standard (19.41 eV) and found within literature (20.07 eV)[186] for Ga^{3+} within the native oxide Ga_2O_3. Peaks at 530.44 (**3**) and 530.46 eV (**4**) corresponded to the presence of O 1s within

Ga_2O_3 by comparison to the standard sample, in which O1s was observed with a binding energy of 530.52 eV, as well as the literature value of 530.6 eV.[189] Whilst the presence of an additional oxygen species was detected by the presence of peaks at *ca.* 532 eV, these were much smaller than those found for films **1** and **2**.

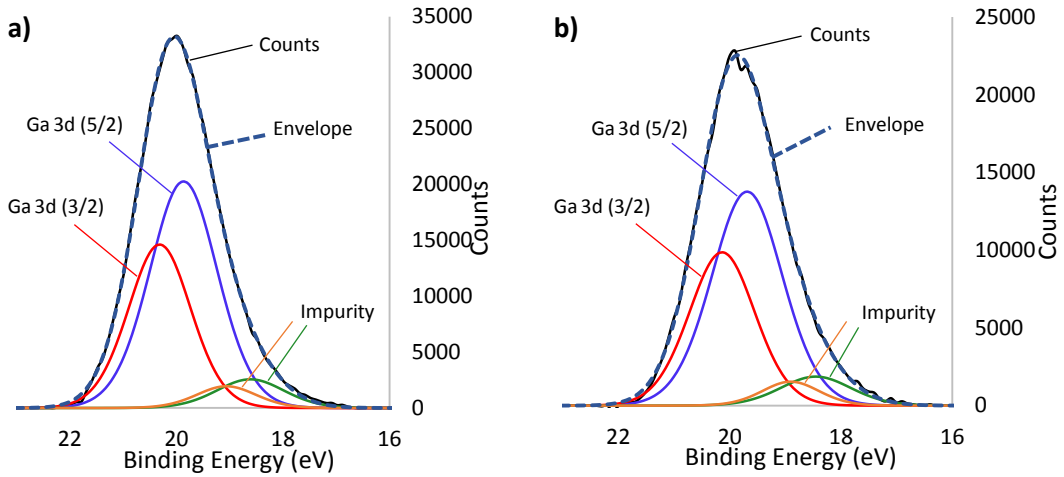

*Figure 3.12 - XPS peaks for Ga 3d at surface of (a) film **3**; and (b) film **4**.*

As shown in Table 3.3, the Ga:O ratios for films **3** and **4** were calculated as 0.62 and 0.74, compared to the theoretical value of 0.66 for Ga_2O_3. Whilst **3** is close to the theoretical stoichiometry, **4** shows a higher than expected gallium content indicating the formation of an oxygen-deficient film. This is unsurprising given the gallium to oxygen ratio of 1:1 within the dimeric precursor. XPS analysis of films **1** – **4** shows those deposited from $[L^3(GaMe_2)_2]$ to be of much better quality than those from $[L^2(GaMe_2)_2]$. This acts in agreement with TGA analysis of the two precursors, as discussed in section 3.2.1, which showed that $[L^3(GaMe_2)_2]$ has a cleaner decomposition pathway than $[L^2(GaMe_2)_2]$, as well as a greater overall mass loss.

Film 6 – [Ga(L^3)H]

XPS analysis of film **6** showed a similar pattern to films **3** and **4**. A Ga $3d_{5/2}$ peak was observed at 19.54 eV (Figure 3.13), corresponding well to the data for the Ga_2O_3 standard (19.41 eV). O 1s was observed at 530.35 eV, also in good agreement with the standard value of 530.52 eV, both of which strongly suggest the formation of Ga_2O_3. The Ga:O ratio of 0.96 was significantly higher than the theoretical value of 0.66, again suggesting the formation of highly oxygen deficient films.

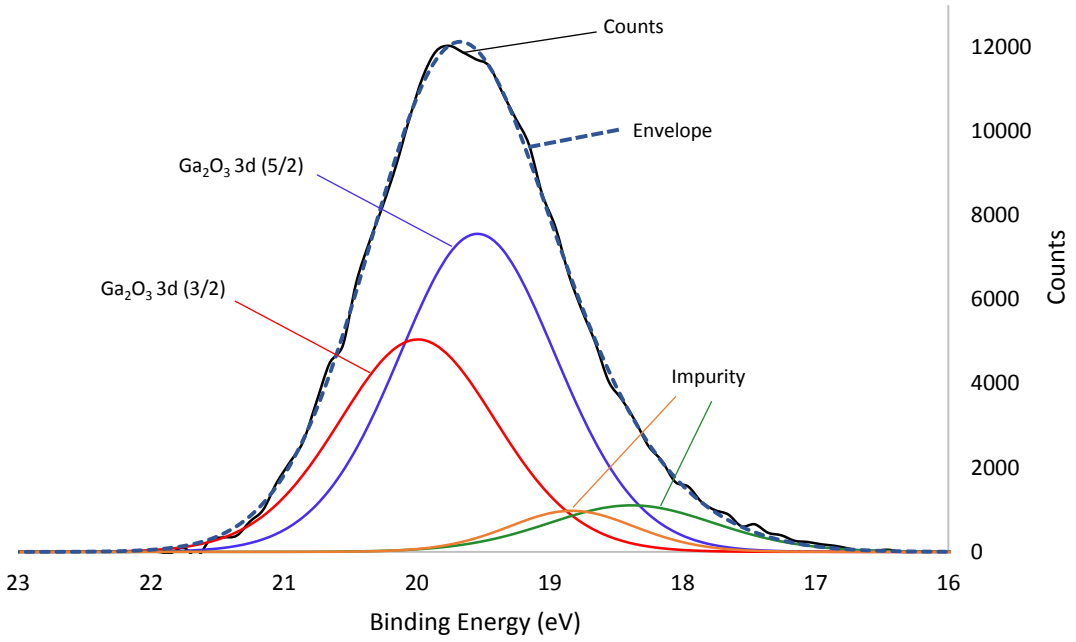

*Figure 3.13 - XPS peaks for Ga 3d at surface of film **6**.*

3.2.3.5 Optical analysis

Transmission and reflectance measurements were carried out on as-deposited films **1** – **4** and **6** between 320 and 2000 nm, as shown in Figure 3.14. Since the transmittance of glass overlaps with that of Ga_2O_3, accurate band gaps could not be calculated from UV/visible data. As shown in Figure 3.14, transmission in the visible region for films **1** and **2** was poor (5 – 40 %), reflecting the poor quality of the films as indicated by XPS analysis. Films **4** and **6**, which were found to be oxygen deficient Ga_2O_3 by XPS, showed improved transmission (20-60%), whilst the highest transmission (60-80%) was found for film **3**, which was also determined to be the best quality Ga_2O_3 film by XPS. However, all the films showed comparatively poor transmission to industrial standard transparent oxides (>80%), likely to be due to carbon contamination resulting from the deposition process. Reflectivity of the films was typically low, ranging between 10 and 20%.

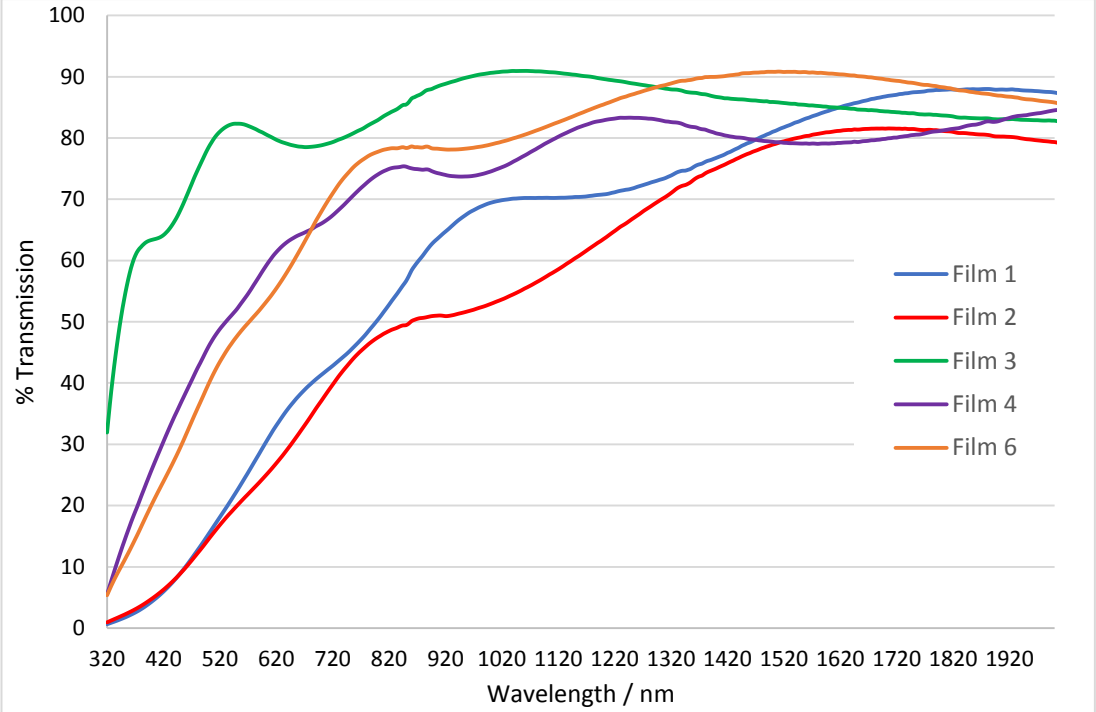

Figure 3.14 - Transmission spectra of films 1 - 4 and 6.

Film **5b** which was deposited on quartz from the precursor [Ga(L^2)H] was analysed by UV/visible spectroscopy between 90 and 1100 nm. Conducting a Tauc plot of the UV/visible data enabled the calculation of band gap of the film, which was found to be *ca.* 4.65 eV.[190] This value is in keeping with literature values for the band gap of Ga_2O_3, ranging between 4.2 and 4.9 eV.[13, 172, 191]

Transmission and reflectance measurements between 200 and 2250 nm showed that film **5b** has minimal reflectance (5 – 10%) and was highly transparent, with transmission values between 80 and 90% in the visible region (Figure 3.15). The deposition of Ga_2O_3 by AACVD has been previously reported using dialkylalkoxogallanes of the type $[R_2Ga(OR')]_2$ (R = Me, Et; R′ = $CH_2CH_2NMe_2$, CH_2CH_2OMe, etc.), which typically has resulted in the formation of grey or brown coloured films.[103-105] By comparison, the as-deposited films **5** and **5b** (pre-annealing) were notably transparent with minimal discolouration. This suggests very low carbon contamination which can be attributed to the lack of direct Ga-C bonds within the precursor.

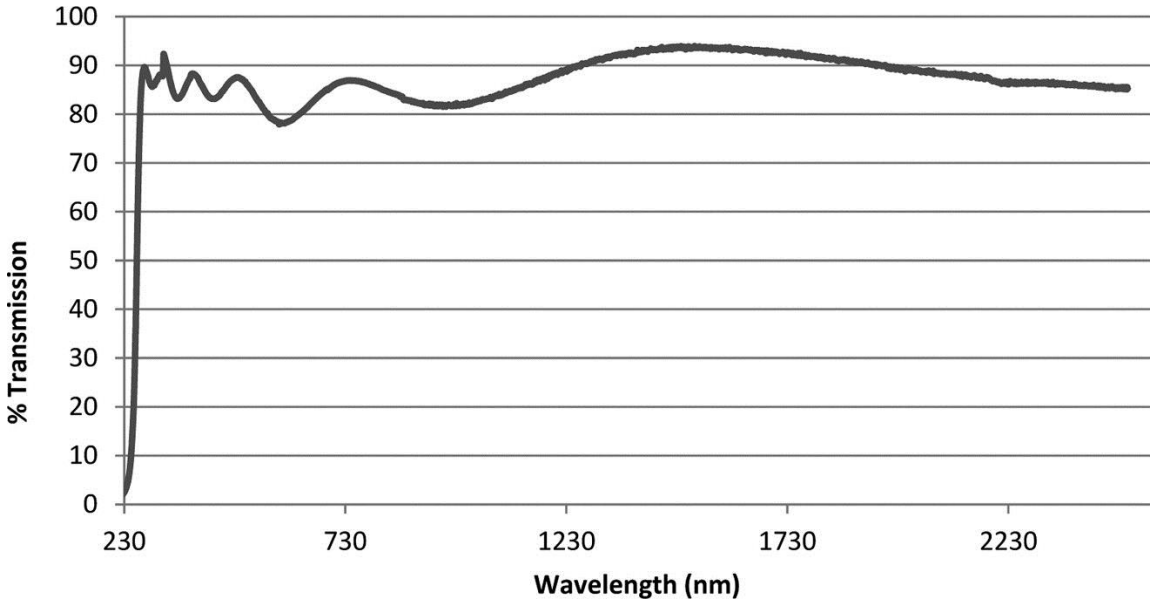

Figure 3.15 - Transmission spectrum of film 5b, grown by AACVD of a toluene solution of [Ga(L^2)H].

3.3 Summary

A range of gallium *β*-ketoiminate complexes have been tested for their suitability as precursors to the deposition of gallium oxide thin films by CVD. Initially, thermal decomposition properties were analysed by TGA, showing in all cases decomposition at temperatures below 600 °C, however decomposition pathways were found to differ between precursor types. The cleanest, lowest temperature decomposition was observed by methyl complexes of the form $[L^n(GaMe_2)_2]$, where n = 3, 4, and $[Ga(L^2)Me]$.

Initial attempts at deposition by LPCVD proved unfruitful due to decomposition of the precursors prior to any significant sublimation, thus attention was turned to AACVD to enable successful transport of the precursor to the reaction chamber. It was found that temperatures approaching 600 °C were necessary for film growth from methyl and hydride precursors, whilst no deposition was achieved from complexes utilising chloride as a co-ligand.

Deposited films were analysed by a range of techniques including EXDA, SEM, pXRD, XPS and transmission/reflectance. All films were amorphous as deposited. As suggested by TGA analysis of the precursors, the best quality films were deposited using the methyl precursor $[L^3(GaMe_2)_2]$. However, in all cases the deposited films were extremely thin and attempts to anneal films deposited on quartz in most cases resulted in complete removal of the oxide film. Film **5b**, however, was successfully grown on quartz and annealed 1000 °C, affording crystalline Ga_2O_3 with high transmission (80-90%), low reflectivity (5-10%) and minimal carbon contamination.

Whilst the deposition of Ga_2O_3 from *β*-ketoiminate precursors has been achieved, further work would be needed to achieve films of sufficient quality for application, for example investigating alternative solvents or liquid deposition techniques. However, it has been shown that small changes in the nature of the ligand have the potential to alter decomposition properties and ultimately the quality of the deposited films and thus it should be possible to optimise the precursor systems, through adaptation of the *β*-ketoimine ligand or selection of alternative co-ligands, to achieve the deposition of high quality Ga_2O_3 thin films.

3.4 Experimental Methods

3.4.1 General Procedures - AACVD

The precursors employed in the thin film depositions were synthesised as described in Chapter 2. Depositions were carried out using the AACVD process, which is described in detail in Chapter 1 and is drawn schematically in Figure 3.16.

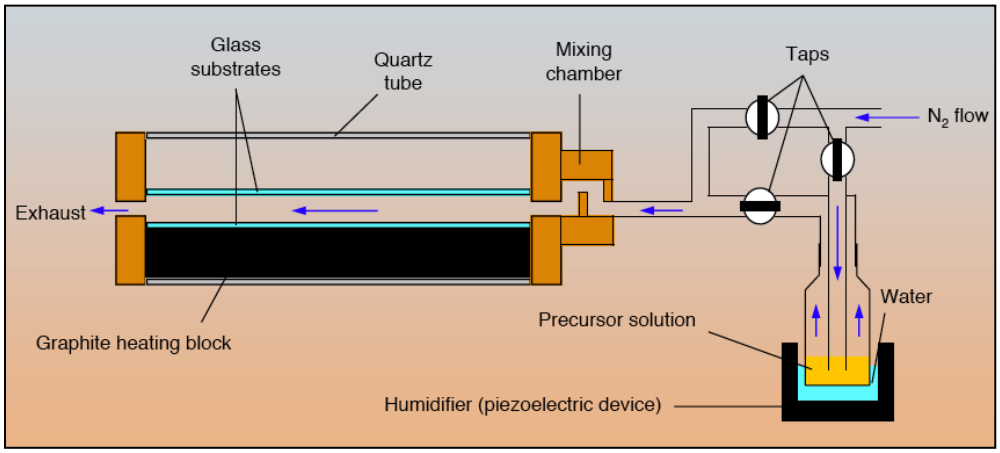

Figure 3.16 - Schematic diagram of an AACVD reactor.

Nitrogen (99.99%) was obtained from BOC and passed through activated molecular sieves to remove moisture. All solvents were dried over activated alumina by the Grubbs method using anhydrous engineering equipment, such that the water concentration was 5 – 10 ppm.[192] Films were grown on SiO_2 coated float-glass substrates supplied by Pilkington Group Ltd, of dimensions *ca.* 90 mm x 45 mm x 4 mm. Prior to use the substrates were cleaned using water and detergent, propan-2-ol and acetone and were dried in air. For each deposition, two substrates were placed within the reactor with the lower surface of the 'top-plate' sitting at a distance of *ca.* 8 mm above the upper surface of the 'bottom-plate'. The reactor was heated to the relevant temperature by a graphite block containing a Whatman cartridge heater and the temperature of the block was monitored by a Pt-Rh thermocouple. All deposition temperatures quoted refer to this temperature. The temperature of the top-plate was generally found to be *ca.* 50 – 70 °C higher than that of the bottom-plate. After reaching the desired temperature, the temperature within the reactor was allowed to equilibrate for 30 mins prior to commencing the deposition.

The precursors were dissolved in anhydrous solvent using standard Schlenk techniques, from which an aerosol was generated at room temperature by use of an

ultrasonic humidifier. The aerosol was carried into the reactor using nitrogen through a brass baffle to obtain laminar flow. The total time for each deposition was dependent upon the solvents, volumes and flow rates being used. Depositions were carried out at substrate temperatures ranging between 400 – 600 °C. Table 3.4 outlines the experimental conditions which afforded the best quality films.

Table 3.4 - Experimental conditions for the AACVD of Ga_2O_3 from β-ketoiminate precursors

Experiment No.	Precursor	Mass (g)	Solvent	Volume (mL)	N_2 flow rate (L/min)	Deposition time (hours)	Substrate Temperature ('C)
1	[Ga(L^2)Me]	0.2	Toluene	30	0.5	2	600
2	[Ga(L^2)Me]	0.4	Toluene	60	0.5	4	600
3	[Ga(L^3)Me]	0.2	Toluene	30	0.5	2	550
4	[Ga(L^3)Me]	0.2	Toluene	30	0.5	2	600
5	[Ga(L^2)H]	0.3	Toluene	30	1	2	450
6	[Ga(L^3)H]	0.6	Toluene	40	0.5	2.5	500

3.4.2 Analysis Techniques

Thermogravimetric analysis was carried out on a Netzsch system from 20 °C to 600 °C. Samples of *ca.* 10 – 20 mg were run under an inert atmosphere of helium in sealed aluminium pans.

Scanning Electron Microscopy (SEM) was performed to determine surface morphology and film thickness using a JEOL JSM-6301F Field Emission SEM at an accelerating voltage of 5 keV. Images were captured using SEMAfore software. Samples were cut to 10 mm x 10 mm coupons and coated with a fine layer of gold to avoid charging.

X-ray photoemission spectroscopy (XPS) was performed using a Thermo Scientific K-alpha photoelectron spectrometer using monochromatic Al-K_α radiation. Survey scans were collected in the range 0–1100 eV (binding energy) at a pass energy of 160 eV. Higher resolution scans were recorded for the principal peaks of Ga (3d), O (1s) and C (1s) at a pass energy of 50 eV. Peak positions were calibrated to carbon and plotted using the CasaXPS software.

Energy dispersive (EDX) analysis was carried out on a JEOL JSM-6301F Field Emission instrument with acceleration voltage of 20 kV.

UV/Vis transmittance and reflectance spectra were obtained on a Perkin Elmer Lambda 950 spectrometer using an air background and were recorded between 250 and 2000 nm.

Chapter 4

The Single-Source Precursor Approach to the AACVD of Indium Arsenide Thin Films

The following chapter discusses the development of a single-source precursor for the deposition of InAs by AACVD. The methane elimination reaction between $InMe_3$ and $^tBuAsH_2$ is investigated, leading to the isolation of an oligomeric InAs cluster complex, the molecular structure of which has been determined by X-ray crystallography and is herein discussed. The deposition of InAs by AACVD from a single-source precursor has been optimised and the properties of the resulting film analysed by a range of characterisation techniques including glancing angle powder X-ray diffraction, X-ray photoelectron spectroscopy, energy dispersive X-ray analysis, scanning electron microscopy and Hall effect.

4 The Single-Source Precursor Approach to the AACVD of Indium Arsenide Thin Films

4.1 Introduction

4.1.1 Deposition of III/V Semiconductor Materials

As discussed in chapter 1, III/V materials are of particular importance within the optoelectronics industry[1, 40] and as such much research has been directed towards their deposition. The dominant processes used for the fabrication of III/V materials are molecular beam epitaxy (MBE) and CVD. Whilst MBE is a useful tool for the development of novel materials, the scale of materials fabrication by this method is limited. CVD, in contrast, offers good potential for large scale production of such materials. However, the majority of examples employ dual precursors, utilising reaction pathways such as that shown in equation 4.1, for the deposition of the binary material.

$$In(CH_3)_{3\,(g)} + AsH_{3\,(g)} \rightarrow InAs_{\,(s)} + 3\,CH_{4\,(g)} \qquad (4.1)$$

This process, however, is far from ideal given the extreme toxicity and high vapour pressure of arsine as a precursor and the pyrophoric nature of MMe_3 (M = Al, Ga, In). Difficulties can also arise in control of film stoichiometry when using dual source precursors. As a result, there has been significant research interest in the development of III/V compounds containing preformed bonds between the desired elements (M-E, where M = group 13 metal and E = pnictogen) for potential application as single-source precursors to the relevant III/V material, bypassing the complications arising from the use of highly toxic precursors. Particular credit should be directed towards the work of Cowley and Jones with regard to the development of such precursors.[85]

4.1.2 Indium Arsenide Compounds

Organometallic InAs compounds are a potentially useful source of InAs in deposition processes and this has driven the development of a range of complexes, taking the form of monomeric, oligomeric and cage structures. Simple monomeric adducts, such as $[(^tBu)_3In{\cdot}As(SiMe_3)_3]$[193] and $[(Me_3SiCH_2)_3In{\cdot}As(SiMe_3)_3]$[194] are seemingly a good starting point for such precursor chemistry, given their low molecular masses and correct stoichiometry. However, the application of such

adducts is thwarted by the weakness of the In-As dative interaction, in comparison to the σ-bond interactions of In-C and As-Si, which allow facile dissociation under elevated temperatures. Indeed, similar titanium and tin arsenide adducts yielded only TiO_2 and SnO_2, respectively, when used as precursors to the corresponding arsenides.[195, 196]

Dimeric species of the form $[R_2InAsR'_2]_2$ (Figure 4.1) are the most common examples of potential InAs precursors, a number of which are summarised in Table 4.1. Three main synthetic pathways are employed towards the synthesis of these complexes, namely alkane elimination (equation 4.2), salt methathesis (equation 4.3) and dehalosilylation (equation 4.4).

$$2\ InR_3 + 2\ As(R')_2H \rightarrow [R_2InAsR'_2]_2 + 2\ RH \qquad (4.2)$$

$$2\ R_2InCl + 2\ LiAsR'_2 \rightarrow [R_2InAsR'_2]_2 + 2\ LiCl \qquad (4.3)$$

$$2\ R_2InCl + 2\ As(SiMe_3)_3 \rightarrow [R_2InAs(SiMe_3)_2]_2 + 2\ Me_3SiCl \qquad (4.4)$$

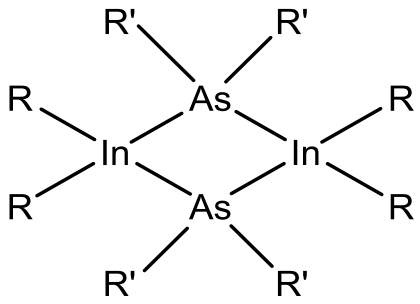

Figure 4.1 – Molecular structure of dimeric InAs species.

Higher oligomers have also been synthesised and structurally characterised, including the trimer $[Me_2InAsMe_2]_3$,[209] which exists as a six-membered ring, as well as a number of cage complexes which have been reviewed by Neumüller *et al*.[210]

Whilst a range of potential precursors have been developed, few reports exist into their application as single-source precursors. Compound **11** has been employed in the deposition of InAs into nanostructured templates by supercritical fluid deposition, however the resulting films were found to be poorly adherent.[206]

Table 4.1 - Examples of dimeric InAs species.

R	R′	Compound no.	Reference
Cl	^{t}Bu	**1**	197
Me	$SiMe_3$	**2**	198
Et	^{t}Bu	**3**	199
Ph	$SiMe_3$	**4**	200
$^{t}BuCH_2$	$SiMe_3$	**5**	201
Me_3SiCH_2	$SiMe_3$	**6**	202
Me_3SiCH_2 / Ph	$SiMe_3$	**7**	203
Me_3SiCH_2 / Me	$SiMe_3$	**8**	203
$PhCh_2$	^{t}Bu	**9**	204
Et	$SiMe_3$	**10**	205
^{n}Bu	^{t}Bu	**11**	206
Me	Ph	**12**	207
Me	Me	**13**	208

4.1.3 Outlook and Project Aims

Recent research has highlighted the potential of single-source GaAs precursors for the deposition of high quality GaAs thin films by AACVD, suitable for application in photovoltaic devices.[114] The aim of this work was to investigate the methane elimination reaction between $InMe_3$ and $^{t}BuAsH_2$ with a view to synthesising a suitable single-source precursor for the deposition of thin films of InAs by AACVD, owing to the recent success of the analogous route for the deposition of GaAs.[114]

4.2 Results and Discussion

4.2.1 Precursor Synthesis

With a view to synthesising a single-source InAs precursor, trimethylindium was reacted with a slight excess of *tert*-butylarsine in toluene, according to equation 4.5. *Tert*-butylarsine was chosen as an arsenic source owing to its wide use in the deposition of arsenide materials and low pyrolysis temperatures.[213,225,226] Both molecular dynamics studies and partial pressure analysis suggest a combination of free radical and β-elimination mechanisms in the decomposition process.[226,227]

The initial reaction was carried out at -78 °C, before being allowed to warm slowly to room temperature. Upon warming, the evolution of gas was observed, presumed to be the release of methane upon formation of the product. The reaction was gently warmed to 80 °C and allowed to stir at this temperature for 16 hours, during which time gas was evolved more readily. After 16 hours gas evolution ceased and the reaction mixture was cooled to room temperature, filtered and the solvent was removed from the filtrate *in vacuo*.

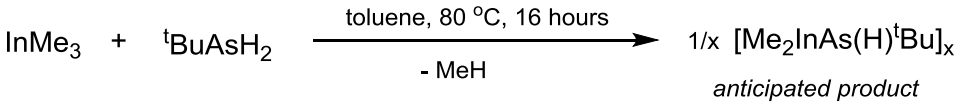

(4.5)

The ^{1}H and $^{13}C\{^{1}H\}$ NMR spectra of the crude product showed a large number of resonances in the InMe, As^{t}Bu and AsH regions, suggesting either the formation of a large oligomeric species, or probably the formation of a number of different species. Resonances in the ^{1}H NMR spectrum in the region 0.42 - 0.86 ppm were attributed to InMe, those in region 1.31 - 1.62 ppm to As^{t}Bu and two peaks at 2.51 and 2.52 ppm to AsH. Likewise, the $^{13}C\{^{1}H\}$ NMR spectrum showed resonances in the region -5.2 - -2.0 ppm (InMe) and 31.3 – 40.4 ppm (As^{t}Bu). These resonances are all in agreement with NMR data for related InAs clusters.[198, 206]

The product was re-dissolved in minimal toluene and cooled to -20 °C for a number of days, after which time small, yellow, rod-like crystals formed, which were suitable for single crystal X-ray diffraction. The analysis confirmed the formation of

the cluster shown in Figure 4.3 (hydrogen atoms omitted for clarity). Crystal data are given in Table 4.2 and selected bond lengths and angles are given in Table 4.3.

The centrosymmetric InAs cluster crystallised into the monoclinic space group $P2_1/c$. Figure 4.2 shows a simplified drawing of the complex with alkyl and hydride groups omitted for clarity. The structure can be considered as two conjoined units containing eight In/As centres (Figure 4.2(a)). Each unit consists of a six-membered In-As ring in a distorted boat conformation, with each atom being four-coordinate, possessing three bonds to an adjacent As or In atom, and one further bond to either a methyl (In) or *tert*-butyl (As) group. Each ring is arched by a [-In$(Me)_2$-As(^{t}Bu)H-] bridge. The two major units are linked by four In-As bonds between the two rings (Figure 4.2(b)) forming two additional In-As four-membered rings.

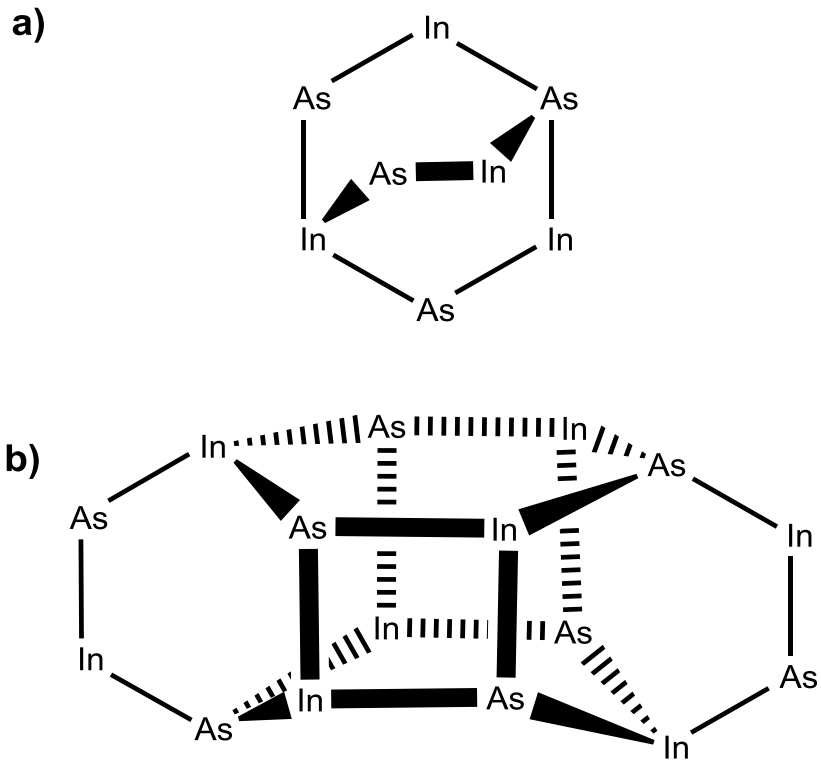

Figure 4.2 - Structural representation of the oligomeric indium arsenide precursor complex, showing a) an isolated eight-membered unit; and b) the two interconnected units, linked through In-As bonding. Alkyl substituents have been omitted for clarity.

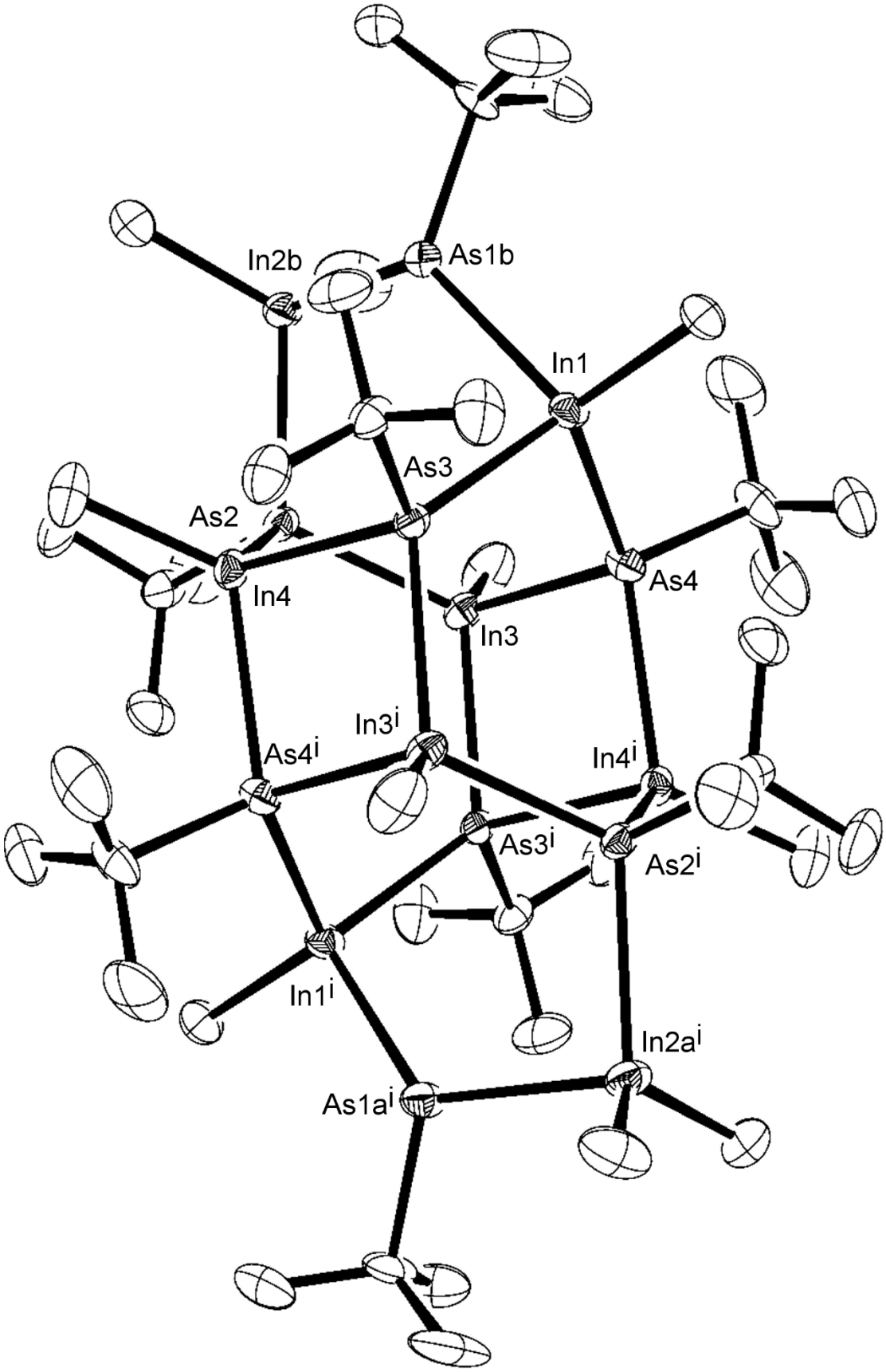

Figure 4.3 - X-ray crystal structure of the indium arsenide precursor complex.

Table 4.2 - Crystal data for indium arsenide cage complex.

Crystal system	Monoclinic	
Space group	$P2_1/c$	
Unit cell dimensions	a = 14.4602(10) Å	α = 90°
	b = 12.4339(9) Å	β = 107.5640(10)°
	c = 23.7507(17) Å	γ = 90°

Each In and As centre is four-coordinate, with the indium atoms utilising their vacant p-orbitals in order to increase their coordination number from 3 to 4. Bond angles around the indium centres show a significant distortion from tetrahedral geometry, with angles ranging from 97.99° to 118.32° around In(1), which are typical for all the indium centres. The arsenic centres show a lesser degree of distortion, with typical values ranging between 104.81 and 114.08° for As(2). The In-As bond lengths were somewhat varied ranging between 2.6202(5) and 2.6836(5) Å. The In-As bonds involved in the four-member rings which link the two units are reasonably short (average 2.67 Å) for such species, by comparison to simple dimeric species $[Me_2InAs(SiMe_3)_2]_2$ (2.70 Å), $[Et_2InAs^tBu_2]_2$ (2.70 Å) and $[^nBu_2InAs^tBu_2]_2$ (2.72 Å), which all contain four-membered In-As rings.[198, 199, 206] Whilst this might seem surprising given the anticipated increase in steric crowding for the larger oligomer in comparison to smaller dimeric structures, steric crowding is in fact less in this case due to the presence of just one alkyl substituent per In/As centre, resulting in less steric hindrance and shorter In-As bonds. The In-As bonds involving In2 and As1 were shorter than those found within the four-membered rings, at an average bond length of 2.63 Å, which was similar to the observations made for the related dianionic complex $[(InCl)_4(InCl_2)_2(As^tBu)_6]^{2-}$, reported by Dashti-Mommertz *et al.*[197] The longest values were those observed within the $[-In(Me)_2-As(^tBu)H-]$ moiety that arches over the 6-membered ring (2.68 Å). All In-C bonds were very similar in length and were in keeping with literature values for related InAs clusters.[200, 206, 211] As-C bonds are similar in magnitude, though slightly larger, to those of 2.014 Å within the As-^{t}Bu units of the dimeric species $[(CH_2)_4GaAs^tBu_2]_2$ reported by Cowley *et al.*[212] Interestingly, these bond lengths within oligomeric structures containing four-coordinate As atoms are larger than those of 1.982 Å

found in the monomeric species $[(^tBu)_2GaAs(^tBu)_2]$, where As is only three coordinate. This is presumably a result of the removal of electron density from the As centre on becoming four-coordinate.

Table 4.3 - Selected bond lengths (Å) and angles (°) for indium arsenide cage complex $[InAs]_8$.

As(1B)-In(1)	2.6642(10)	As(2)-In(3)	2.6218(6)
As(1B)-In(2B)	2.684(2)	As(2)-In(4)	2.6337(5)
As(3)-In(1)	2.6202(5)	As(3)-In(3)#1	2.6655(5)
As(3)-In(4)	2.6587(5)	As(4)-In(4)#1	2.6835(5)
As(4)-In(1)	2.6327(6)	In(3)-As(3)#1	2.6653(5)
As(4)-In(3)	2.6595(5)	In(4)-As(4)#1	2.6836(5)
As(2)-In(2B)	2.680(2)		
C(1)-In(1)	2.175(4)	C(5)-In(4)	2.179(5)
C(2B)-In(2B)	2.178(10)	C(6B)-As(1B)	2.036(11)
C(3B)-In(2B)	2.176(8)	C(14)-As(3)	2.023(5)
C(1)-In(1)-As(3)	118.32(13)	As(3)-In(1)-As(4)	102.871(16)
C(1)-In(1)-As(4)	118.01(14)	As(3)-In(1)-As(1B)	97.99(5)
C(1)-In(1)-As(1B)	109.54(13)	As(4)-In(1)-As(1B)	107.93(6)
C(10)-As(2)-In(3)	107.13(14)	In(3)-As(2)-In(4)	114.079(17)
C(10)-As(2)-In(4)	107.66(12)	In(3)-As(2)-In(2B)	104.81(9)
C(10)-As(2)-In(2B)	108.76(13)	In(4)-As(2)-In(2B)	114.11(7)

Whilst this particular oligomer has been isolated and structurally characterised, it is unlikely that it is the only oligomer formed, only that this particular oligomer has preferentially crystallised. Indeed, in solution it is likely that a number of oligomers exist in equilibrium, as would be suggested by the large number of peaks present in the NMR spectra. Integration of peaks in the InMe, As^{t}Bu and AsH regions of the ^{1}H NMR spectrum were in a roughly 1:36:15 ratio, which is consistent with the formation of the above complex. Furthermore, elemental analysis showed carbon to be present at 24.24% and hydrogen at 5.06%, in good agreement with the calculated values of 23.71 and 4.93%, respectively. Mass spectrometry did not show the

presence of the parent ion for the cluster, displaying instead a large degree of fragmentation. The only peak of significant intensity was observed at 145 *m/z*, corresponding to [$InMe_2$]. Despite the uncertainty over the exact nature of the precursor, it is clear that the formation of a number of cluster complexes occurs during the synthetic procedure, containing a large number of In-As linkages and an In to As ratio of 1. This presents the precursor as potentially suitable for the formation of stoichiometric InAs *via* thermal decomposition.

Attempts to isolate monomeric species by addition of the Lewis base 4-(dimethylamino)pyridine (dmap) were carried out by addition of dmap to both the reaction mixture and the isolated product, a method well utilised by Schulz *et al.* in the isolation of monomeric III/V compounds.[230] However, these attempts were unsuccessful with analysis continuing to show a complex mixture of products.

4.2.2 Thermogravimetric Analysis (TGA)

In order to study the thermal decomposition characteristics of the precursor, thermogravimetric analysis (TGA) was carried out on a 9.9 mg sample of the crude (i.e. un-crystallised) product (Figure 4.4). A small initial mass loss of 3% was observed between *ca.* 70 and 200 °C, presumably due to the loss of a small amount of residual solvent within the sample or sublimation. The major decomposition process occurs between 200 and 300 °C, with a mass loss of 27%. Further residual mass loss was seen up to 480 °C (6%), after which a final decomposition process afforded a 7% mass loss. The limiting temperature of the experiment was 600 °C due to the aluminium crucibles used, however this is appropriate for the investigation of the precursor with a view to carrying out depositions on glass, since 600 °C is also the ceiling temperature above which glass would begin to warp.

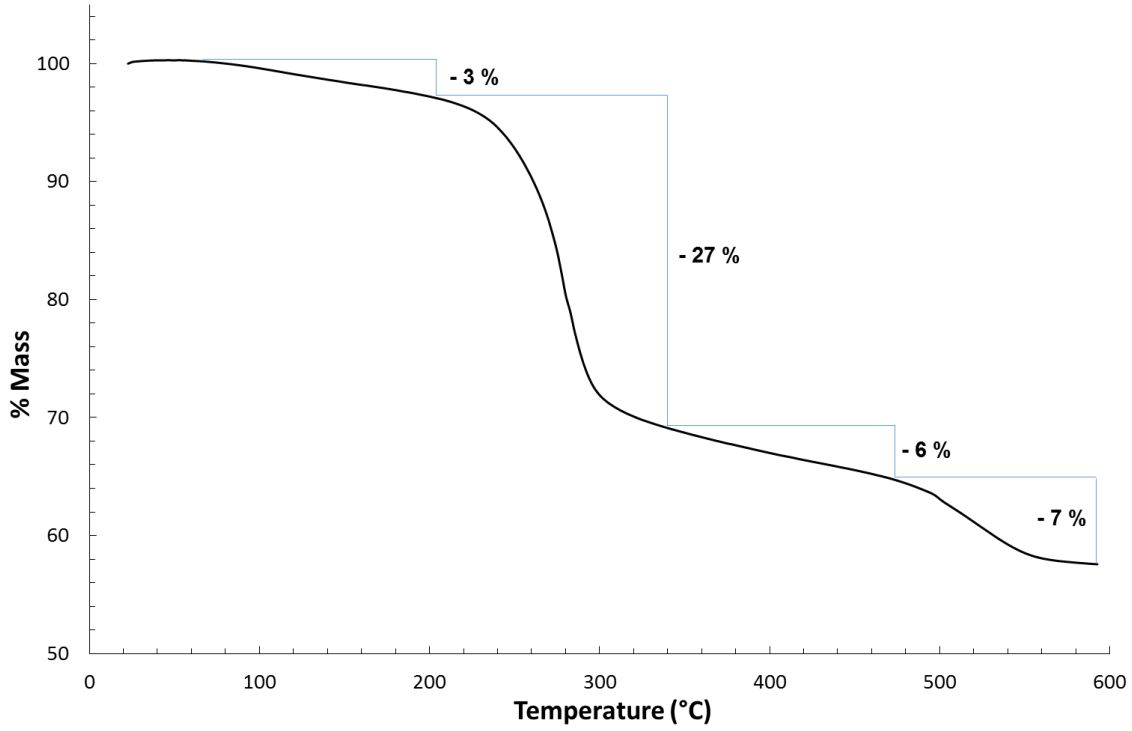

Figure 4.4 – Thermogravimetric analysis of InAs precursor showing % mass loss with increasing temperature.

The total mass loss incurred through the thermal decomposition was 43%, leaving a residual mass of 57% post-decomposition. Within any oligomer of the empirical formula $[Me_2InAs(H)^tBu]_x$, InAs contributes 68% of the mass, whilst in the large 16-metal cluster whose structure was discussed earlier in section 4.2.1, InAs contributes 71% of the total mass of the complex. Indeed, for any of the likely products formed, the total InAs content can be said to be *ca.* 70% of the total mass. Thus the expected mass loss on removal of the organic ligands would be *ca.* 30%, as opposed to the observed 43% which was observed through experiment. This extra mass loss can be attributed to the presence of residual solvent within the sample, as well as sublimation of some of the precursor within the aluminium crucible prior to decomposition. However, in spite of this the TGA results suggest the potential of the precursor for the deposition of InAs by CVD at temperatures below 600 °C.

4.2.3 Aerosol-Assisted Chemical Vapour Deposition (AACVD)

As discussed, organometallic group 13 metal arsenide clusters have proven to be very useful precursors for the depositions of III/V materials by CVD. Much attention has been paid to the deposition of GaAs from single-source precursors by CVD processes, however examples of the production of indium-based materials by such methods are much rarer. The groups of Cowley and Bradley both independently

reported the deposition of InP from the single-source precursor $[Me_2InPMe_2]_2$ by MOCVD and molecular bean epitaxy, respectively.[90, 213, 214] In the latter case, indium-rich films were formed at all temperatures and the use of excess phosphine was required in the deposition process in order to achieve stoichiometric InP films. More recently, both InP and InAs were successfully deposited from the similar dimeric organometallic species $[^nBu_2InAs^tBu_2]_2$ *via* supercritical chemical fluid deposition though the arsenide films were found to be poorly adherent to the substrate. The good solubility of such organometallic complexes in non-polar solvents offers the added potential for application in solution-based CVD processes, in particular AACVD. The proficiency of this technique towards the single-source deposition of III/V materials has been recently demonstrated by Sathasivam in the production of high quality thin films of GaAs from $[R_2GaAs(H)^tBu]_2$ (R = Me, Et).[114]

Growth of InAs films *via* AACVD was initially carried out at a range of temperatures to determine the optimum conditions for growth of InAs using this precursor (Table 4.4). Depositions were carried out at substrate temperatures of 400, 450 and 500 °C with 0.2 g of precursor in 30 mL of anhydrous toluene. In all cases, growth of blue, metallic films indicated the deposition of InAs. Whilst substrate coverage was good at all three temperatures, the best coverage was found at a temperature of 450 °C (condition **2**). Depositions carried out at 400 (condition **1**) and 500 °C (condition **3**) afforded film growth near the reaction chamber outlet and inlet, respectively.

Having determined 450 °C as the optimum temperature, deposition was then carried out with a higher quantity of precursor (0.5 g, condition **4**), again yielding a blue metallic film with good coverage over the substrate. Finally, to determine the effect of the precursor synthesis conditions on the efficacy of the precursor, the methane elimination reaction was carried out at room temperature over a period of 72 hours (condition **5**) and 2 hours (condition **6**). Condition **5** again yielded a good quality blue metallic film, similar to those deposited through the previous experiments, however, no deposition was observed under condition **6**. This observation was confirmed through three repetitions of the experiment. Under this condition, the reaction between $^tBuAsH_2$ and $InMe_3$ was only allowed to stir at room temperature for 2 hours prior to carrying out the deposition, suggesting that the reaction had not

gone to completion. It is possible that this observation is a result of the immediate formation of the adduct [$Me_3In(AsH_2{}^tBu)$] prior to methane elimination taking place. The weak dative bond between As and In then readily dissociates under elevated temperatures and thus no deposition of InAs is observed. Similar observations were made in the attempted deposition of both titanium and tin arsenide by AACVD from precursors based on arsine adducts of titanium and tin chloride, respectively.[195, 196] In both cases, only deposition of the respective oxides was seen as a result of the ready dissociation of the M-As bonds (M = Ti, Sn).

Table 4.4- Experimental conditions for the AACVD of InAs.

Condition/ Film No.	Precursor Synthesis Conditions	Mass (g)*	Substrate Temperature (°C)
1	a	0.2	400
2	a	0.2	450
3	a	0.2	500
4	a	0.5	450
5	b	0.5	450
6	c	0.5	450

In all cases, the precursor was dissolved in toluene (30 mL) and the aerosol transported using N_2 carrier gas at a flow rate of 0.5 L/min. The total deposition time was 2 hours.
* Mass quoted refers to the mass of crude precursor reaction product used for the deposition.

a) toluene, 80 °C, stir, 16 hours

b) toluene, r.t., stir, 72 hours

c) toluene, r.t., stir, 2 hours

These results imply that for the deposition of InAs by the single-source precursor route, design of the precursor to incorporate pre-existing In-As sigma bonds is important for successful deposition, in order to prevent ready dissociation of any dative In-As linkages.

Having deposited a number of films under varying conditions, characterisation and analysis of the films and their properties was then carried out by a range of techniques, as described in the following sections.

4.2.4 Indium Arsenide Thin Film Analysis

4.2.4.1 Glancing Angle Powder X-Ray Diffraction

Glancing angle powder X-ray diffraction (XRD) of the films grown under the 5 successful deposition conditions (**1** – **5**) confirmed the formation of crystalline InAs for all 5 films. Figure 4.5 shows the XRD diffractograms recorded for the 5 films. In all cases, peaks were observed at 2θ values of 25.44°, 42.15° and 49.89°, corresponding to the lattice planes (111), (220) and (311) of cubic InAs, respectively.

The degree of crystallinity, as determined by the breadth of the peaks, was found to differ according to the deposition conditions used. Conditions **1** – **3** show the effect of increasing the deposition temperature on film growth, keeping all other deposition variables the same. Whilst the formation of InAs was observed at 400 °C, the crystallinity of the film was quite poor and could be improved by increasing the temperature to 450 °C and 500 °C. However, the film grown at 500 °C showed additional peaks at 2θ = 30.57°, 32.96°, 35.40° and 51.23° corresponding to the concurrent formation of In_2O_3 within the film.

Increasing the amount of precursor used in the deposition process to 0.5 g (condition **4**) resulted in a dramatic improvement in film crystallinity, as demonstrated in Figure 4.5(d). The greater intensity of the peaks reflects the formation of thicker films, which is an unsurprising result of increasing the amount of precursor. Figure 4.5(e) shows the XRD pattern of the film produced when altering the reaction conditions used in the synthesis of the precursor. In this case, the reaction mixture was not heated, instead it was allowed to stir at room temperature for 72 hours before being isolated (condition **5**). A larger amount of the precursor was again used in the deposition (0.5 g), however the resulting film showed much poorer crystallinity than observed for condition **4**.

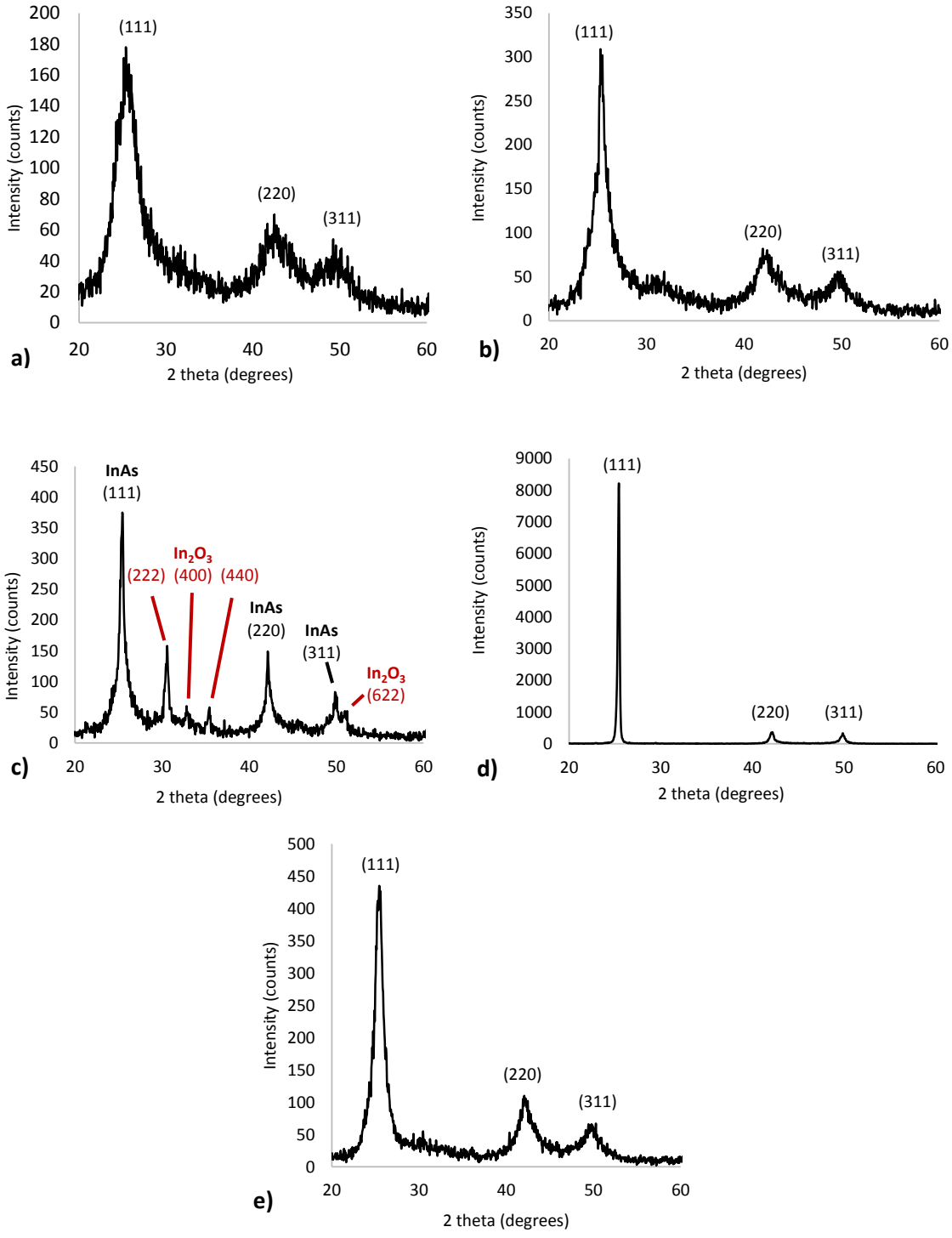

Figure 4.5 - XRD pattern of InAs films grown under conditions (a) 1; (b) 2; (c) 3; (d) 4; and (e) 5.

The varying relative intensities of the peaks show that there is differing preferred orientation from film to film. This can be quantified by calculation of the intensity ratio (α) of each peak, according to equation 4.6:

$$\alpha = \frac{I_{(h'k'l')}}{\Sigma\, I_{(hkl)}} \qquad (4.6)$$

[150]

where $I_{(h'k'l')}$ is the intensity of the peak of interest and $\Sigma I_{(hkl)}$ is the sum of the intensities of all the peaks. Table 4.5 gives the intensity ratios for the films grown under conditions **1 - 5**, displaying in all cases preferred orientation in the (111) plane. The extent of this preference, however, differs between samples with the greatest preference being shown by the highly crystalline sample grown under condition **4**.

Table 4.5 - Intensity ratios (α) showing preferred orientation of InAs films, calculated according to equation 4.6.

	Intensity ratio (α)		
Condition	(1,1,1)	(2,2,0)	(3,1,1)
1	0.60	0.23	0.17
2	0.71	0.18	0.11
3	0.63	0.25	0.13
4	0.95	0.03	0.03
5	0.73	0.17	0.10

The breadth of the peak in a diffraction pattern is inversely proportional to the size of the crystallite, i.e. the larger the crystallites, the narrower the observed XRD peak, as quantified in the Scherrer equation.[215] It is thus possible to make a judgement about the average size of the crystallites within a sample from the breadth of the XRD peaks. The film grown under condition **4** shows the narrowest peaks (Figure 4.5(d)) and hence can be assumed to have the largest crystallites. This is unsurprising given the greater amount of precursor that was used in the deposition process.

4.2.4.2 Energy Dispersive X-Ray Analysis (EDXA)

Table 4.6 gives the results of Energy dispersive X-ray analysis (EDXA) for films grown under conditions **1 - 5**. In all cases, the indium to arsenic ratios within the films deviate from stoichiometry, with considerably more indium being present than would be expected for InAs. These results can be easily understood by comparison to the XPS data, which showed the presence of In_2O_3 at the surface of the films. Since EDXA is a surface technique, the elemental ratios given below refer only to the surface of the films, rather than to the bulk. Thus the apparent excess of indium can be attributed to the formation of the native oxide at the surface. The film showing an In:As ratio closest to unity was that grown under condition **4**, which was also observed by XPS to have the least amount of In_2O_3.

Table 4.6 - EDXA analysis of InAs films grown under conditions 1 - 5, showing atomic percentages of indium and arsenic.

Condition 1			**Condition 2**		
Region	**As (atomic%)**	**In (atomic%)**	**Region**	**As (atomic%)**	**In (atomic%)**
1	34.80	65.20	1	34.91	65.09
2	34.61	65.39	2	34.48	65.52
3	34.77	65.23	3	34.04	65.96
Average	34.73	65.27	Average	34.48	65.52
Condition 3			**Condition 4**		
Region	**As (atomic%)**	**In (atomic%)**	**Region**	**As (atomic%)**	**In (atomic%)**
1	26.84	73.16	1	43.82	56.18
2	26.86	73.14	2	44.59	55.41
3	27.13	72.87	3	44.5	55.5
Average	26.94	73.06	Average	44.30	55.70
Condition 5					
Region	**As (atomic%)**	**In (atomic%)**			
1	29.17	70.83			
2	29.37	70.63			
3	29.42	70.58			
Average	29.32	70.68			

4.2.4.3 X-Ray Photoelectron Spectroscopy (XPS)

X-ray photoelectron spectroscopy (XPS) was carried out on the deposited films in order to determine the composition of the indium and arsenic species within them. All XPS data were collected by Dr. Sanjay Sathasivam, with data processing and manipulation being carried out by the author.

Condition 1

Figure 4.6 shows the XPS analysis of the surface of the film grown under condition **1**, where (a) shows the peaks for In 3d and (b) gives those for As 3d. Two In species were observed at the surface of the film by the presence of two sets of $3d_{5/2}$ and $3d_{3/2}$ peaks, each set with a doublet separation of 7.6 eV. These two sets of peaks can be identified by the binding energy of the $3d_{5/2}$ peaks, matching literature values for In in the form of InAs at 443.99 eV and In_2O_3 at 444.79 eV.[216, 217] The surface ratio of InAs to In_2O_3 was calculated as 1:1 through integration of the XPS peaks.

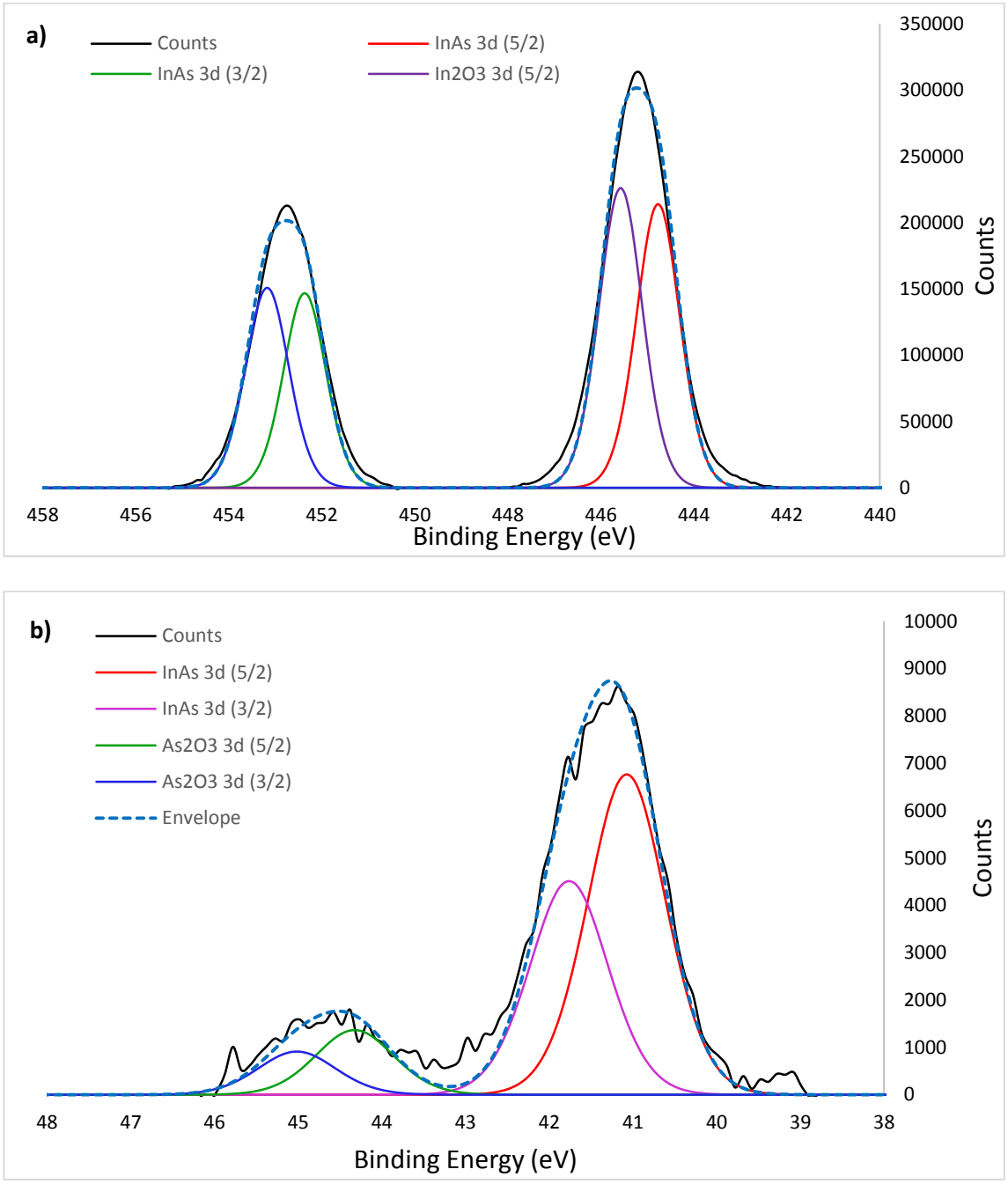

Figure 4.6 - XPS peaks for a) In 3d and b) As 3d at surface of film grown under condition 1.

Similarly, the presence of two sets of As 3d peaks suggested the presence of two As species at the surface of the film. The peak at 40.29 eV confirmed the presence of InAs, matching the literature value of 40.78 eV.[217] The second $3d_{5/2}$ peak at 43.55 eV indicated the formation of As_2O_3 by comparison to literature, though the InAs to As_2O_3 ratio was much higher at 5:1, showing that much less As_2O_3 exists at the surface than In_2O_3. The total In:As ratio at the surface of the film was 2.6:1, as

opposed to 1:1 which would be expected for stoichiometric InAs, which can be attributed to the presence of a significant amount of In_2O_3. Depth profiling was therefore carried out to determine the composition of the film below the surface, with the results being shown in Figure 4.7.

The amount of In_2O_3 within the film is seen to significantly decrease by the disappearance of the shoulder on both the $3d_{5/2}$ (lower binding energy) and $3d_{3/2}$ (higher binding energy) peaks, in addition to the InAs peaks increasing in intensity, thus also showing a greater InAs content below the surface. Similarly, the As_2O_3 3d peaks (*ca.* 43.5 eV) are found to disappear after sputtering for 100 seconds, showing the absence of As_2O_3 below the surface.

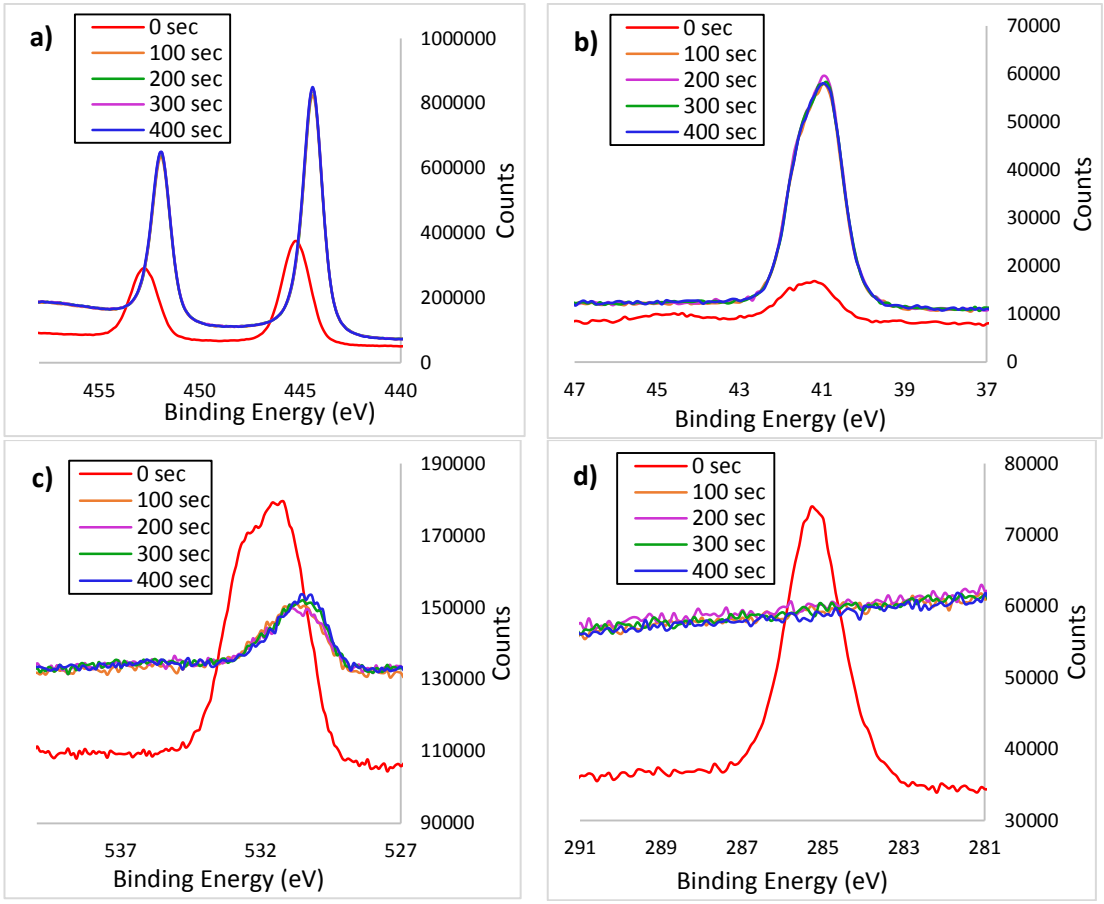

Figure 4.7 - XPS depth profiling of film grown under condition 1. a) In 3d peak; b) As 3d peak; c) O 1s peak; and d) C 1s peak.

Depth profiling of the oxygen 1s peak showed the presence of oxygen at the surface of the film, unsurprisingly given the previous data for In and As 3d showing the formation of their native oxides. However, a small amount of oxygen was found to be present below the surface, even after sputtering for 400 seconds (Figure 4.7(c)), indicating the presence of some oxide species within the bulk. Whilst this implies the

formation of some oxides during the deposition process despite the use of N_2 as a carrier gas and strictly anhydrous, oxygen-free conditions throughout the precursor synthesis and preparation, the oxygen content in the bulk of the film is very low. Carbon was also observed at the surface of the film (Figure 4.7(d)), however none was found within the bulk as shown by the absence of the C 1s peak after sputtering for 100 seconds.

Condition 2

XPS analysis of the InAs film **2** yielded similar results to those found for film **1**, as discussed in the previous section. Surface analysis of the film showed the presence of two indium species, identified by their $3d_{5/2}$ binding energies of 444.00 eV (InAs) and 444.95 eV (In_2O_3), which were in agreement with literature values of 443.99 eV and 444.79 eV, respectively.[216, 217] In this case, the ratio of InAs to In_2O_3 was slightly higher at 1.4:1. The data quality for As 3d peaks at the surface was poor, however it was still possible to observe two different As species, whose binding energies were consistent with the formation of both InAs and As_2O_3.

Depth profiling was again carried out to gain an understanding of the bulk properties of the film, as shown in Figure 4.9. Again, the presence of both In_2O_3 and As_2O_3 were found to be largely limited to the surface of the film, though some oxygen was found within the bulk. Carbon was observed only on the surface.

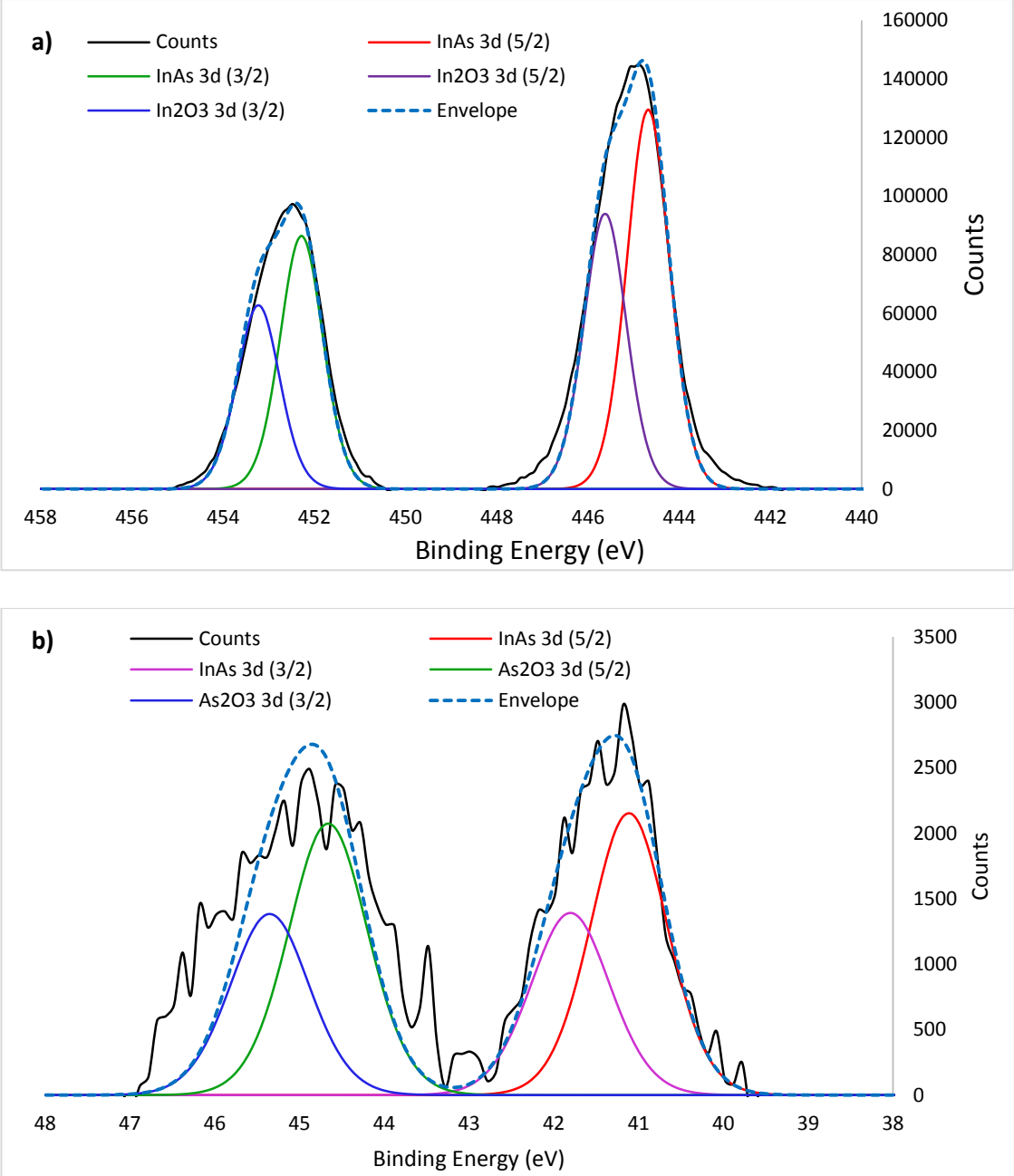

Figure 4.8 - XPS peaks for a) In 3d and b) As 3d at surface of film grown under condition 2.

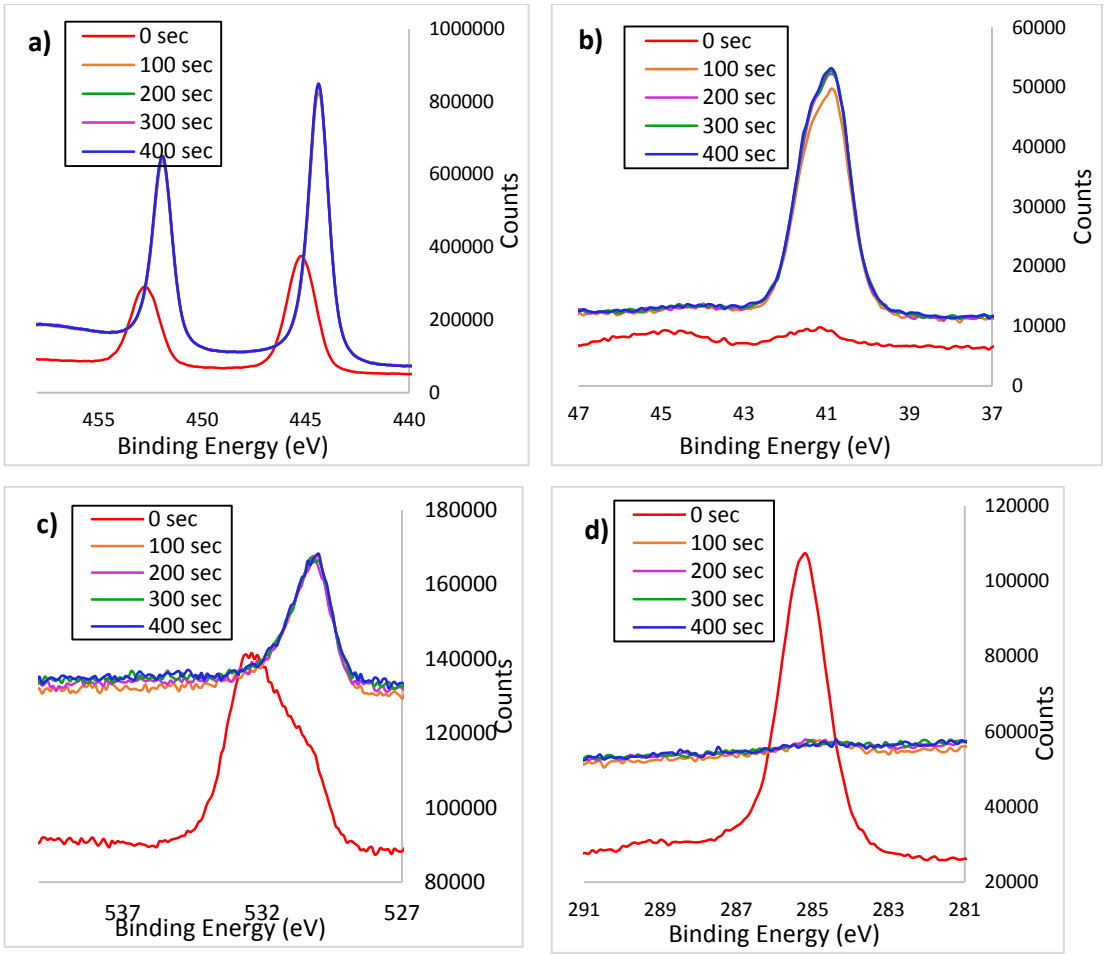

Figure 4.9 - XPS depth profiling of film grown under condition 2. a) In 3d peak; b) As 3d peak; c) O 1s peak; and d) C 1s peak.

Condition 3

Figure 4.10 shows the XPS peaks for In 3d at the surface of the film. Two peaks were observed within the experiment, which were deconvoluted to fit two sets of $3d_{5/2}$ and $3d_{3/2}$ peaks. The two $3d_{5/2}$ peaks were seen at binding energies of 444.75 eV and 445.75 eV, with the former displaying much greater intensity. Though shifted to a slightly higher binding energy, the In $3d_{5/2}$ peaks are at comparable binding energies to literature values for InAs[216, 218] and In_2O_3[217, 219] and by comparison to the observations of the films grown under conditions **1** and **2** it seems likely that the larger set of peaks of lower binding energy correspond to InAs and the smaller set at higher binding energy correspond to the native oxide. Data quality for the As 3d peaks was very poor and no meaningful observations could be drawn.

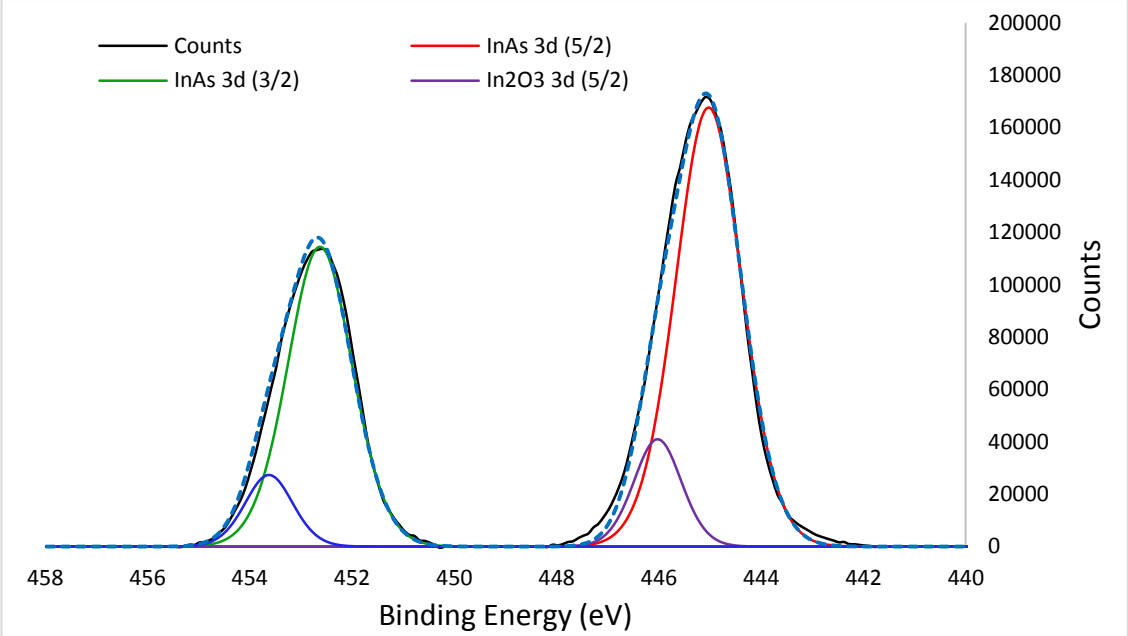

Figure 4.10 - XPS peaks for In 3d at surface of film grown under condition 3.

Depth profiling of the film (Figure 4.11) again showed the significant reduction of the higher binding energy shoulder peak within the In 3d spectrum (a), offering further evidence that this corresponds to In_2O_3, which is present predominantly at the surface of the material. Sputtering for 100 seconds also revealed the presence of an As 3d peak at a binding energy of 40.80 eV, corresponding to the As $3d_{5/2}$ state within InAs.[218] Oxygen was again found to be present within the bulk of the film, however carbon was seen only at the surface (Figure 4.11(c) and (d)).

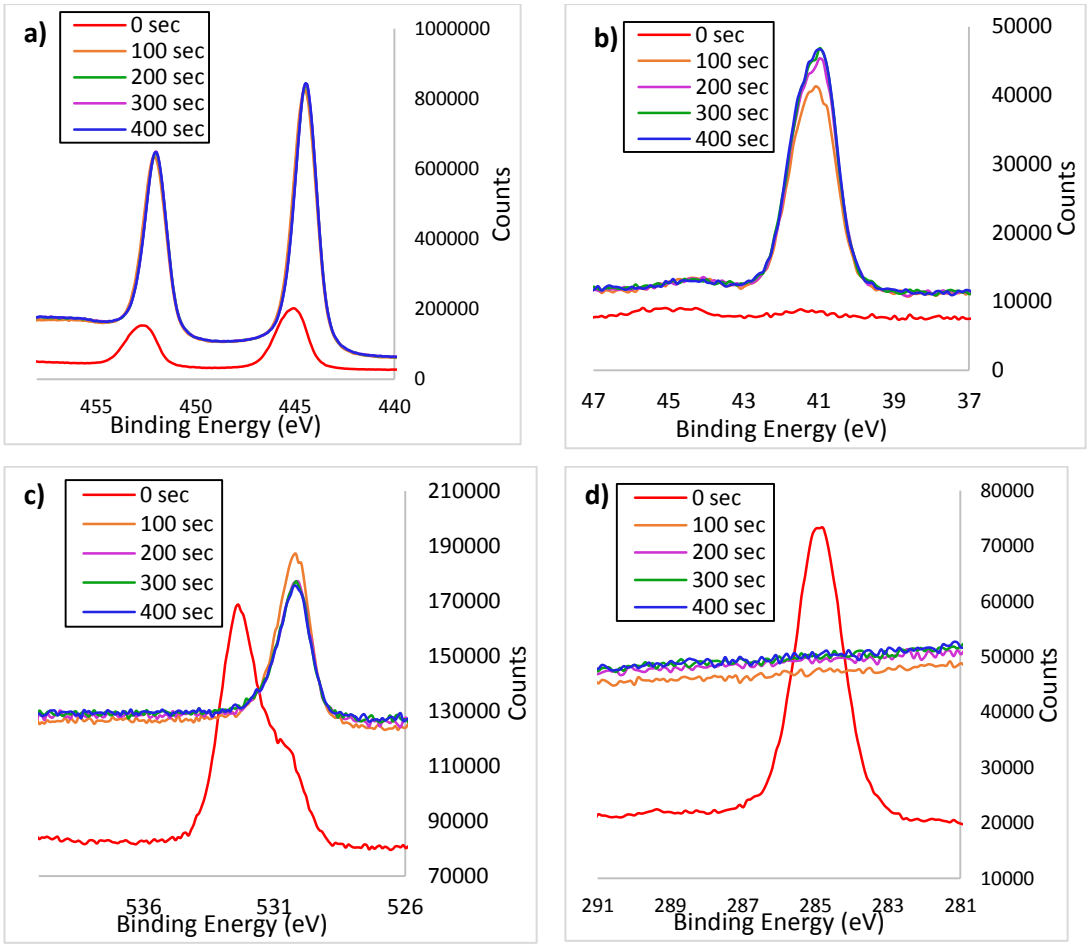

Figure 4.11 - XPS depth profiling of film grown under condition 3. a) In 3d peak; b) As 3d peak; c) O 1s peak; and d) C 1s peak.

Condition 4

Figure 4.12(a) shows the XPS peaks for In 3d at the surface of the film, which were deconvoluted to fit two sets of $3d_{5/2}$ and $3d_{3/2}$ peaks. The two $3d_{5/2}$ peaks correspond to the presence of In^{3+} in the form of In_2O_3 at a binding energy of 445.06 eV and InAs at 444.00 eV, agreeing well with the literature values for the two materials of 444.79 eV and 443.99 eV, respectively.[216, 217]

Similarly, two As species were identified, as shown in Figure 4.12(b). Two peaks at 41.04 eV and 41.73 eV, with a doublet separation of 0.69 eV and an intensity ratio of 3:2, correspond to As $3d_{5/2}$ and $3d_{3/2}$, respectively. These show a reasonable match to the respective literature values of 40.78 eV and 41.79 eV.[217] The second doublet shows peaks at 44.63 eV and 45.32 eV, corresponding to the $3d_{5/2}$ and $3d_{3/2}$ states within the oxide As_2O_3.[220]

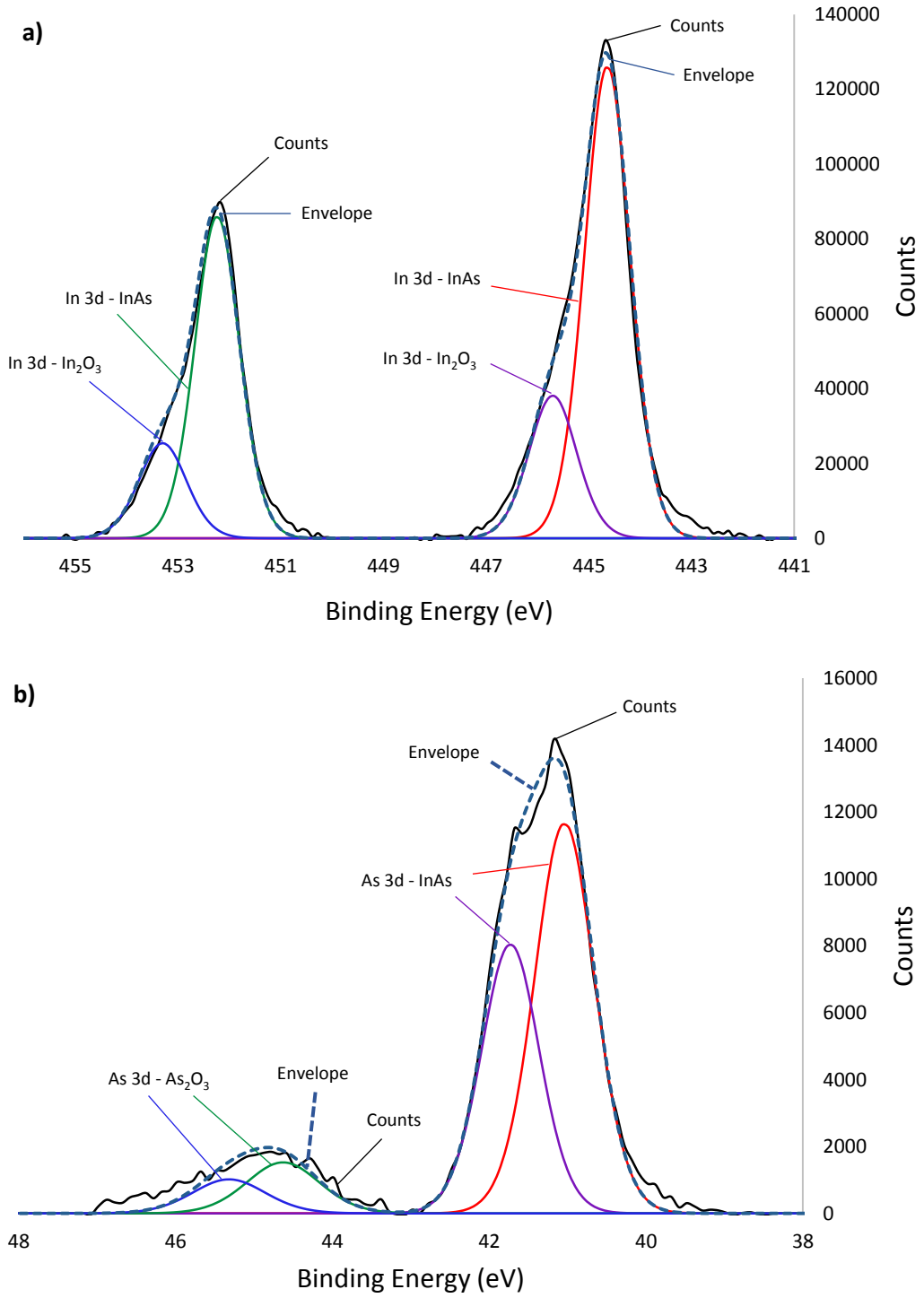

Figure 4.12 - XPS peaks for a) In 3d and b) As 3d at surface of film grown under condition 4.

Depth profiling of the InAs film (Figure 4.13) shows the disappearance of the peaks corresponding to the native oxides after sputtering for 100 seconds, indicating the presence of the oxide species is limited to the surface of the material with no oxidation of the material beyond a certain thickness. It is therefore likely that the oxide formed post-deposition. Depth profiling of the peak for O 1s (Figure 4.13(c)) confirms this observation, with oxygen appearing only at the surface of the material

and becoming absent after sputtering for 100 seconds. XPS also showed the presence of carbon at the surface of the material, however this also becomes absent after sputtering for 100 seconds (Figure 4.13(d)). Since the C 1s peak appears only at the surface it is likely that the presence of carbon is a result of external contaminants picked up post-deposition (e.g. grease dust etc.), rather than through retention of carbon from the precursor.

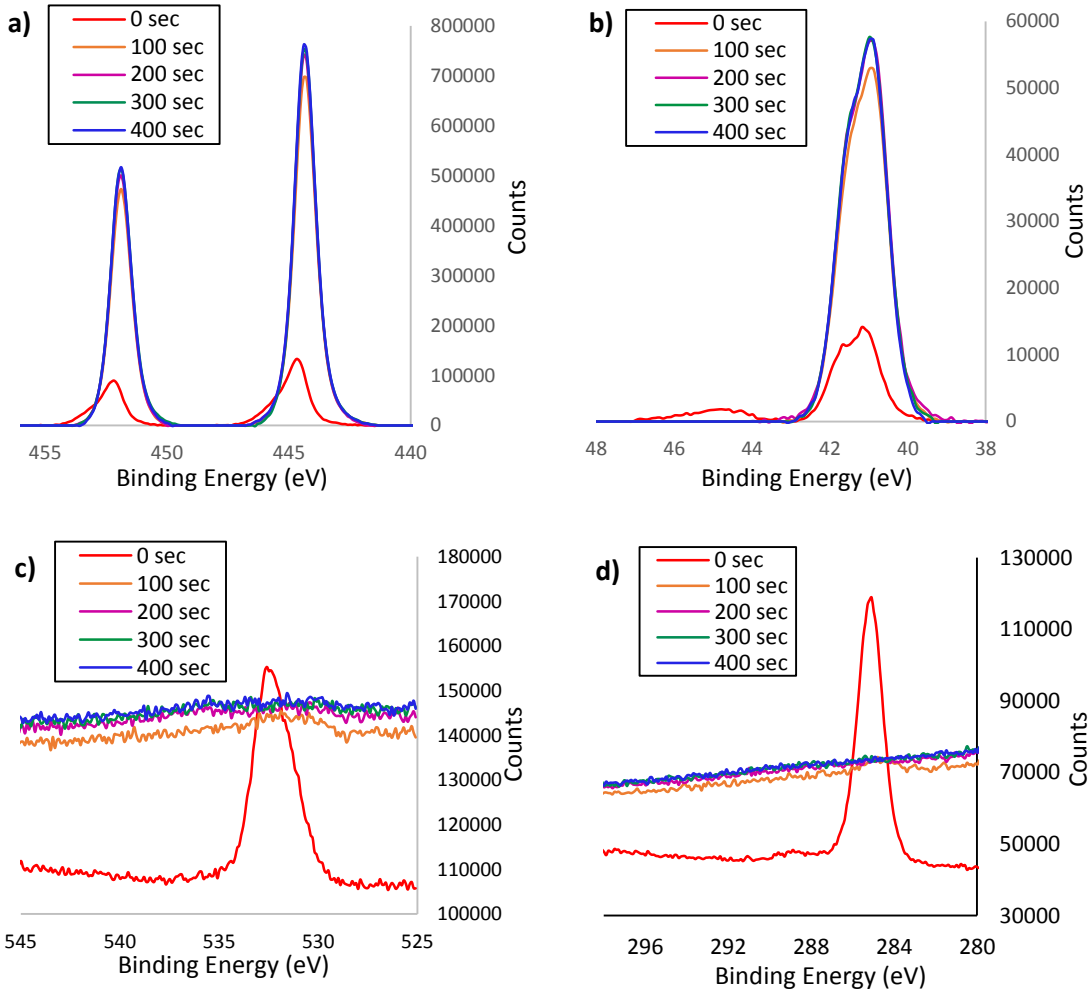

Figure 4.13 - XPS depth profiling of film grown under condition 4. a) In 3d peak; b) As 3d peak; c) O 1s peak; and d) C 1s peak.

Condition 5

XPS analysis of the film grown under condition **5** showed similarities to that of film **4**, where only the reaction conditions used in the preparation of the precursor were altered. Two peaks were observed for In 3d, which were deconvoluted to fit two sets of In 3d peaks with $3d_{5/2}$ binding energies of 444.02 eV and 444.96 eV, corresponding to the literature values of 443.99 eV (InAs) and 444.79 eV (In_2O_3), respectively.[216, 217] However, in contrast to condition **4**, the areas of the In_2O_3 peaks

were much larger than those of InAs, indicating that the oxide is the dominant species at the surface of the film. Indeed, the ratio of InAs to In_2O_3 was calculated as 1:2 by integration of the peaks, in contrast to 3:1 observed under condition **4**. The formation of the surface oxide is an expected observation for III/V materials with the rate of oxide formation of the metal arsenides decreasing in the order In > Al > Ga.[221] This oxide formation is irreversible and has implications for semiconductor device performance, thus optimisation of the reaction conditions to minimise this effect is important.

Data for As 3d at the surface of the film showed unsatisfactory signal to noise ratios preventing any reasonable peak fitting and deconvolution.

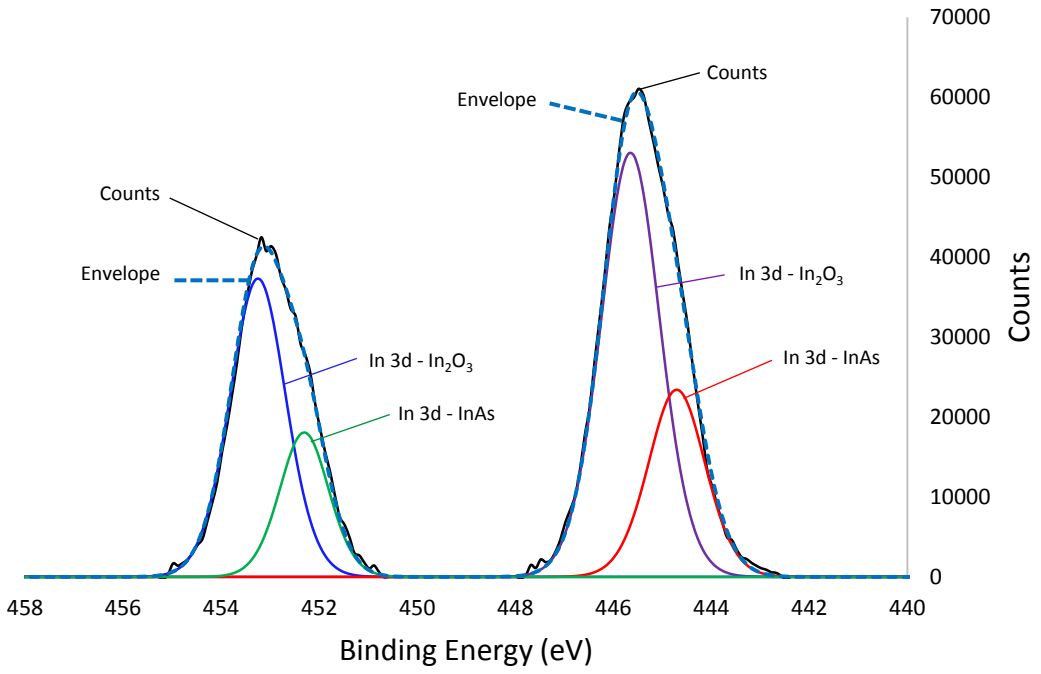

Figure 4.14 - XPS peaks for In 3d at surface of film grown under condition 5 – sample 1.

In spite of the large amount of In_2O_3 observed at the surface of the film, depth profiling again showed that the presence of the oxide is limited largely to the surface of the film (Figure 4.15(a)). After sputtering for 100 seconds, the InAs peak becomes dominant and the intensity of the peak increases with increasing length of sputtering time. Whilst poor data prevented reliable analysis of the As species present at the surface of the film, depth profiling revealed an increasing amount of InAs with increased sputtering time. Similarly to conditions **1** – **3**, though in contrast to condition **4**, a small amount of oxygen was also observed in the bulk, though the

majority remained at the surface. Film **5** was, however, the only film to display any carbon content within the bulk, though the C 1s was almost completely absent after 400 seconds of sputtering.

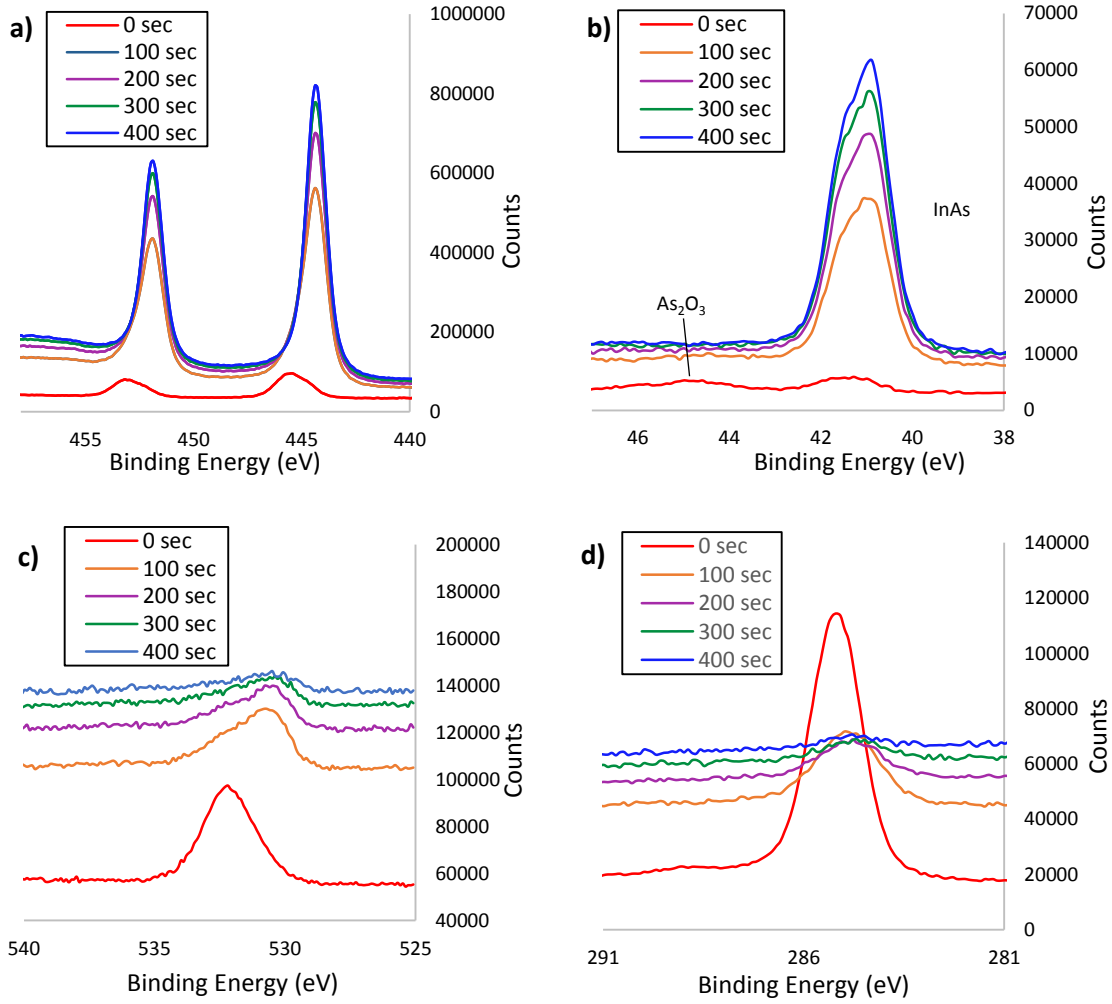

Figure 4.15 - XPS depth profiling of film grown under condition 5. a) In 3d peak; b) As 3d peak; c) O 1s peak; and d) C 1s peak.

In order to determine whether the oxide was formed consistently across the surface of the InAs film, XPS analysis was carried out on the surface of a second sample of film **5** taken from a different part of the substrate. The In 3d and As 3d XPS fitting for this second sample is shown in Figure 4.16. Whilst In_2O_3 is again present at the surface of the film, it is immediately evident from the In 3d fitting that the dominant peaks in this case correspond to In $3d_{5/2}$ and $3d_{3/2}$ of InAs. Data for As 3d were of much better quality that for sample **1**, with $3d_{5/2}$ peaks at binding energies of 41.1 and 44.6 eV corresponding well with literature values for InAs and As_2O_3, respectively.[217, 220] These results suggest that the degree of oxidation is not consistent

across the entire surface of the film, i.e. some regions of the film exhibit a greater amount of In_2O_3 present at the surface than others.

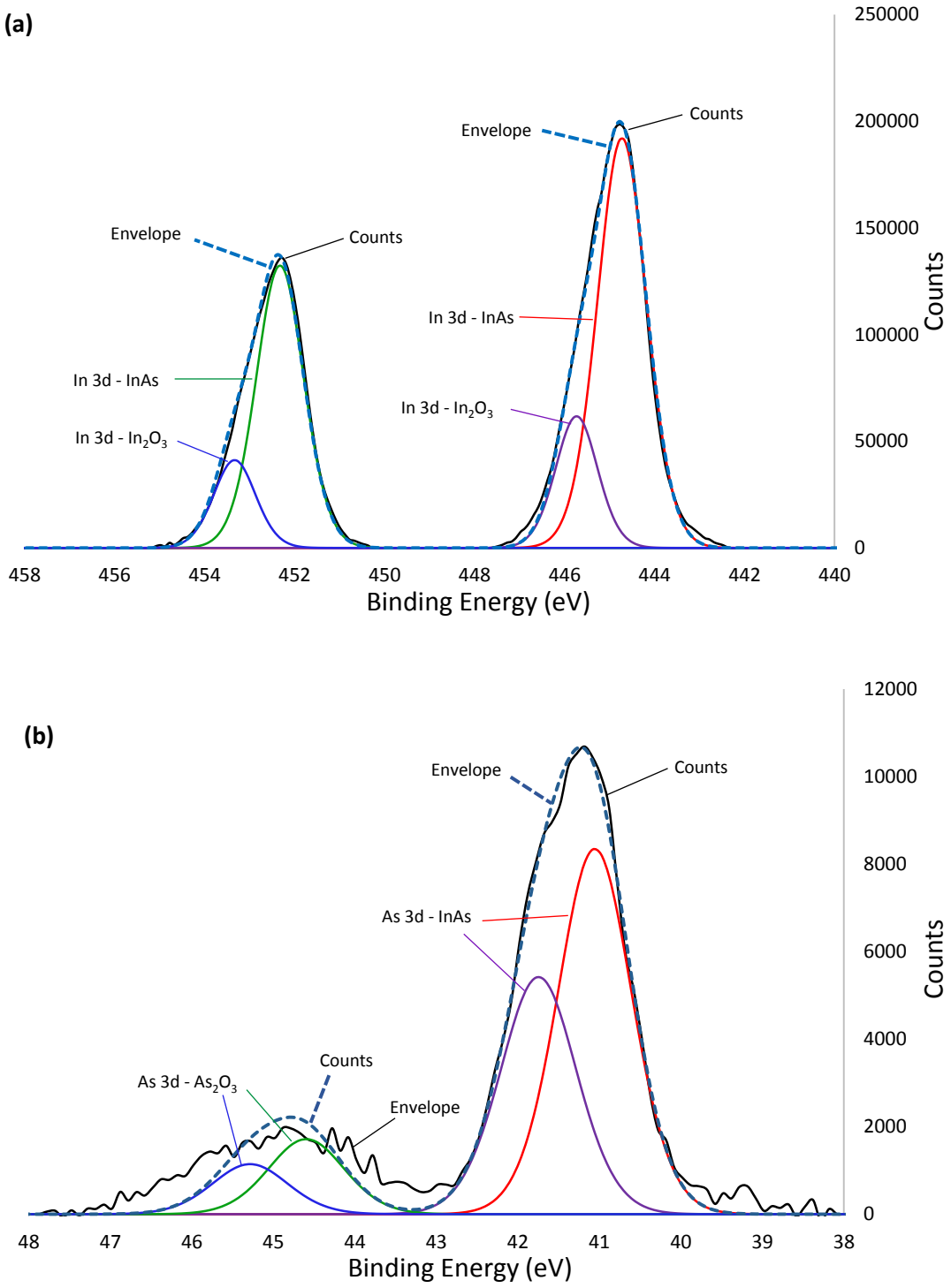

Figure 4.16 - XPS peaks for (a) In 3d and (b) As 3d at surface of film grown under condition 5 – sample 2.

4.2.4.4 Scanning Electron Microscopy (SEM)

SEM imaging on gold coated samples of the films grown under conditions **1** – **4** was carried out in secondary electron mode at 5 kV in order to study their microstructure. Figure 4.17 shows the films grown under conditions **1** – **3**, where the deposition temperature has been varied between 400 and 500 °C with all other variables kept constant.

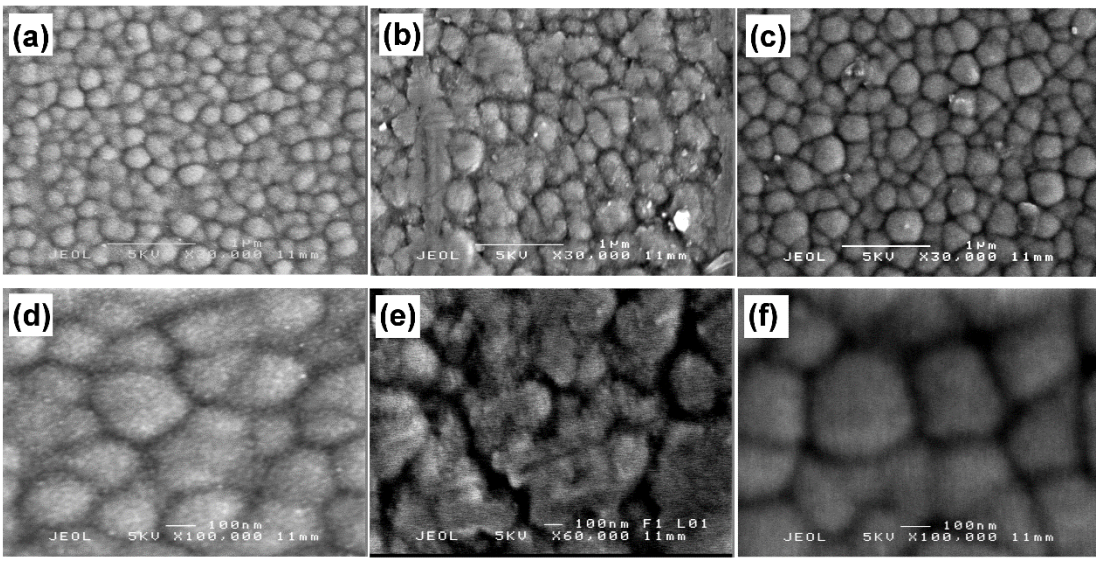

Figure 4.17 - SEM images of InAs films grown under (a) and (d) condition 1; (b) and (e) condition 2; (c) and (f) condition 3.

The films were particulate in nature showing compact, spherical features. At a deposition temperature of 400 °C, the average grain size was roughly 200 to 300 nm and was fairly uniform across the film. Increasing the deposition temperature to 450 and 500 °C afforded films with a slightly greater variation in grain size, with some smaller and some larger spherical grains being formed. However, little overall change was observed in the morphology of the films upon increasing the deposition temperature.

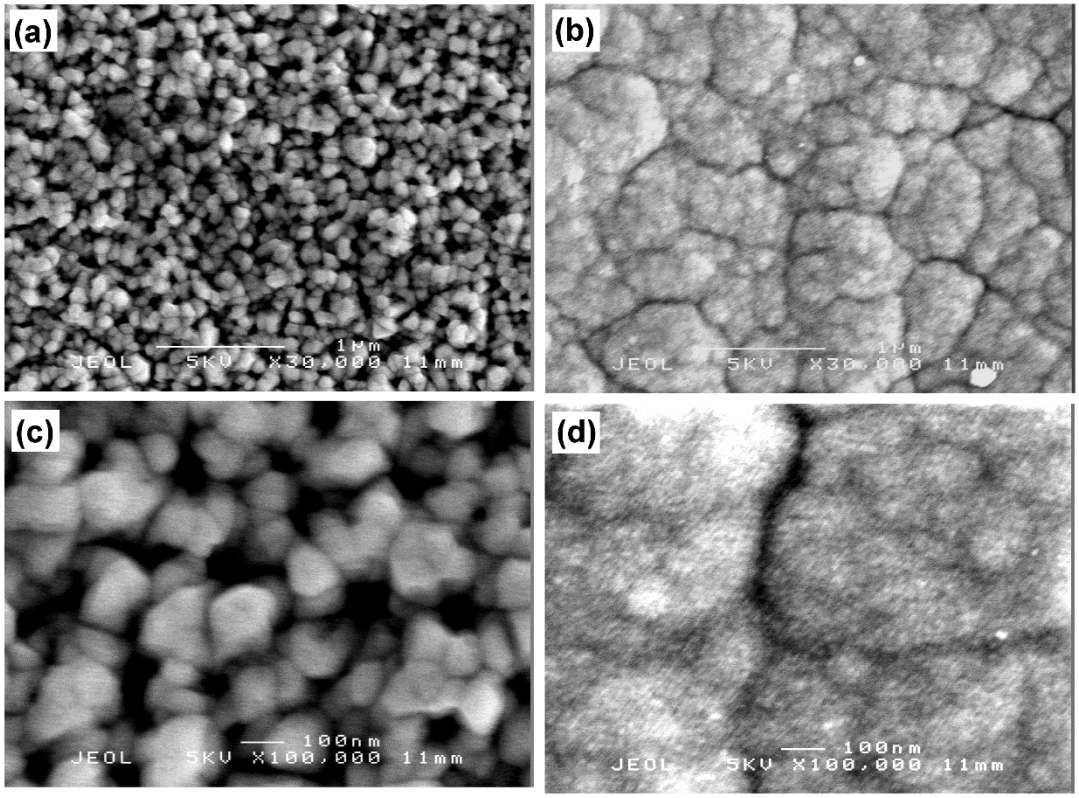

Figure 4.18 - SEM images of InAs films grown under (a) and (c) condition 4; (b) and (d) condition 5.

Under condition **4**, films were grown at a deposition temperature of 450 °C and a greater mass of precursor used (0.5 g *vs.* 0.2 g used in conditions **1** – **3**). However, despite the increase in the amount of precursor used, the volume of solvent was kept the same, thus the precursor solution was at a higher concentration. The resulting film again showed particulate growth, though the grain size was much smaller (*ca.* 100 nm) and the film was not so compact (Figure 4.18(a) and (c)). These two observations are indicative of much faster growing films, presumably as a result of the high concentration of the precursor solution.

Interestingly, the SEM imaging of the film grown under condition **5** showed a flatter and more featureless morphology compared to all the other conditions (Figure 4.18(b) and (d)). As discussed earlier, XPS and EDXA analysis indicated the formation of a large amount of In_2O_3 at the surface of the film and the large discrepancy in surface morphology is attributed to the formation of In_2O_3 at the surface.

In order to gain a measure of the film thicknesses, cross sectional images were obtained through side-on SEM, as shown in Figure 4.19. Film thicknesses are given in Table 4.7.

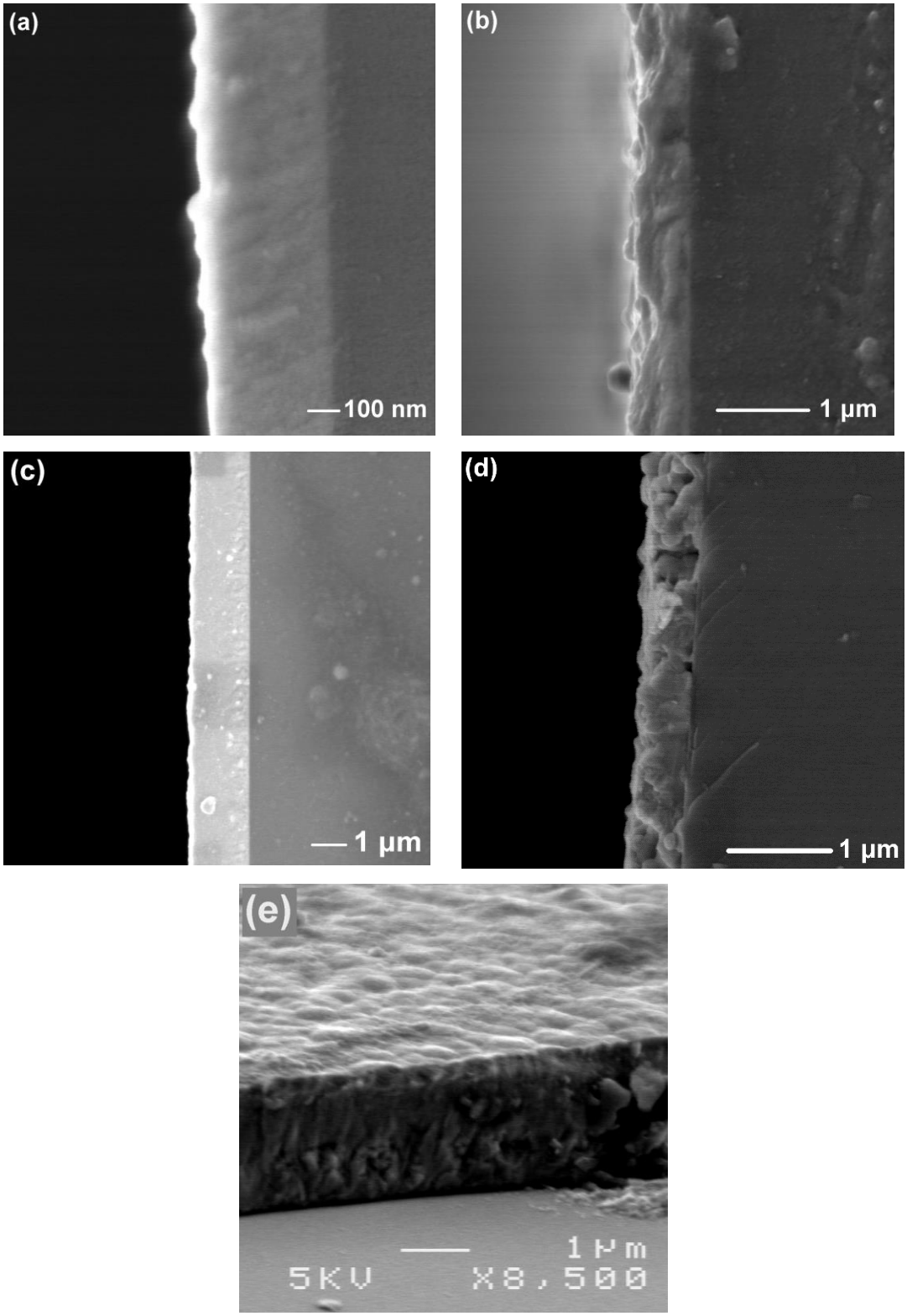

Figure 4.19 - Side on SEM images of films grown under (a) condition 1; (b) condition 2; (c) condition 3; (d) condition 4; and (e) condition 5. (Note: Image (e) shows a tilted-angle SEM image of film 5 for clarity, as the film was offset from the edge of the substrate.)

*Table 4.7 - Film thicknesses for films **1 - 5**, as determined by side on SEM imaging.*

Film no.	1	2	3	4	5
Film Thickness (μm)	0.4	0.7	1.5	0.5	1.7

Films **1** – **3**, represent an increase in deposition temperature from 400 °C to 500 °C. Increasing the deposition temperature from 400 °C to 450 °C (films 1 and 2, respectively) resulted in a slight increase in film thickness, from 0.4 μm to 0.7 μm. Increasing the deposition temperature further to 500 °C (film **3**) resulted in a marked increase in thickness (1.5 μm). Whilst film **4** was grown with a greater amount of precursor, the film thickness was not found to differ significantly from film **2**, which was grown at the same temperature with less precursor. In fact, the thickness of the latter was 0.2 μm less than that of the former, an observation attributed to the formation of larger amounts of In_2O_3. This suggests that substrate temperature is the controlling factor with regards to film thickness. The thickness of film **5** was found to be particularly large (1.7 μm), which is an anomalous result. This could be a result of the formation of a significant amount of In_2O_3, as has been established through XPS analysis.

4.2.4.5 Hall Effect Measurements

In order to briefly assess the electrical properties of the deposited films, Hall effect measurements were carried out on samples of films **1** - **5**. Results showed the formation of conductive, n-type InAs thin films in all cases. However, electron mobilities (as shown in Table 4.8) were found to lie in the range 20 - 410 $cm^2\ V^{-1}\ s^{-1}$, which are 2 - 3 orders of magnitude lower than reported electron mobilities of more than 20,000 $cm^2\ V^{-1}\ s^{-1}$ for InAs.[42, 222]

*Table 4.8 - Hall effect measurements on InAs films **1 - 5**.*

Film no.	Resistivity (Ω cm)	Conductivity (1/Ω cm)	Bulk carrier concentration (cm^{-3})	Carrier Mobility ($cm^2\ V^{-1}\ s^{-1}$)	Average Hall Coefficient ($cm^3\ C^{-1}$)
1	4.7×10^{-2}	21	4.7×10^{18}	28	1.3
2	4.7×10^{-3}	210	1.2×10^{19}	110	0.5
3	1.1×10^{-2}	93	1.2×10^{19}	47	0.5
4	3.6×10^{-3}	280	4.2×10^{18}	410	1.5
5	7.2×10^{-2}	14	4.3×10^{18}	20	1.5

The performance of the films is not of device-quality, which is likely to be due to the presence of In_2O_3 within the films. Indeed, film **4** shows the highest electron mobility and conductivity and lowest resistivity whilst also displaying the lowest levels of In_2O_3 by XPS analysis. Further optimisation of the film deposition should lead to significant improvements in the electrical properties of the films.

4.3 Summary

The development of processes for the fabrication of III/V semiconducting materials remains a significant focus of research efforts across the globe. Indium arsenide is a material of interest due to its particularly high electron mobility at room temperature. Whilst CVD processes offer potentially useful means for the industrial-scale fabrication of thin films of such materials in high quality, difficulties arise in the production of indium phosphide/arsenide materials by traditional dual-source methods due to the need to have a large excess of extremely toxic arsine precursors to achieve film stoichiometry.[214] One way to alleviate the use of large amounts of hazardous precursors is the development of single-source precursors containing preformed In-E bonds in the required stoichiometry, with a choice of alkyl substituents to offer clean decomposition pathways to the binary materials. Recent success in the production of high quality GaAs thin films from single-source precursors by AACVD,[114] coupled with the relative scarcity of literature relating to the single-source CVD of InAs prompted an exploration into the extension of this approach to InAs thin films.

The methane elimination reaction between $InMe_3$ and $^tBuAsH_2$ was investigated with a view to forming a suitable organometallic InAs precursor. The reaction, carried out in toluene and heated to 80 °C, showed the expected evolution of gas and a yellow solid product was isolated. However, ^1H and ^{13}C NMR analysis was not consistent with the formation of the expected dimeric complex but instead pointed towards the formation of a mixture of higher oligomers. Crystallisation followed by single crystal X-ray diffraction analysis revealed the isolation of a large InAs cluster containing eight In and As centres. Whilst this was not the anticipated product and the large size of the cluster limits the applicability of the precursor in traditional thermal CVD processes, the cluster showed good solubility in non-polar solvents, in particular toluene, and thus remained a good candidate for the AACVD of InAs.

A brief investigation into the decomposition properties of the precursor was carried out by TGA, which showed a reasonably clean pathway and full decomposition below 600 °C. AACVD studies were then carried out in toluene at substrate temperatures ranging between 400 and 500 °C, which resulted in the deposition of blue, metallic films with the best coverage over the 4.5 x 19 cm float glass substrate at the intermediate temperature of 450 °C. XRD analysis of the three films confirmed the formation of crystalline InAs with preferential orientation in the (111) plane. XPS analysis of the thin films also confirmed the formation of InAs, however in all three cases a significant amount of In_2O_3 was also found at the surface of the substrate. Since no In_2O_3 reflections were found in the XRD of the films, this can be assumed to be amorphous and can therefore be attributed with the poor observed crystallinity. The post-deposition formation of the native oxide at the surface is not unexpected and XPS depth profiling showed the presence of oxygen in the bulk of the film, albeit at much lower levels. The amount of precursor used in the deposition process was therefore increased, resulting in the formation of thicker films of much improved crystallinity. Whilst In_2O_3 was still detected at the surface of the film by XPS, sputtering for 100 s showed complete disappearance of the O 1s peaks. Finally, the synthetic procedure was altered, to determine whether milder conditions could be used to achieve the same results. Stirring the reaction mixture at room temperature for 2 hours resulted in no deposition at all, whereas stirring at room temperature for 72 hours did afford a thin film of InAs. However, the film quality was poor and In_2O_3 was detected at the surface of the film by XPS. It is expected that these observations are a result of no or incomplete reaction in the precursor synthesis. The first stage in the reaction of $InMe_3$ and $^tBuAsH_2$ is likely to be adduct formation, according to equation 4.7, followed by methane elimination to form the sigma-bonded product.

$$InMe_3 + {}^tBuAsH_2 \rightarrow [Me_3In{\cdot}As({}^tBu)H_2] \qquad (4.7)$$

Without heating the reaction, not enough energy is supplied to overcome the activation energy barrier to the methane elimination reaction and thus only the adduct is formed (or in the case of the longer stir, a mixture of the reaction product and the adduct exists). This then results in the deposition of no material, or a mixture of InAs and In_2O_3, similar to the results observed in the attempted deposition of

titanium and tin arsenide from adducted precursors which yielded only the oxides.[195, 196]

Further characterisation has been carried out by EDXA, confirming the presence of In and As. Results showed a large excess of In within all of the films, attributed to the presence of In_2O_3. Whilst the formation of the native oxide at the surface of the films is likely to occur post-deposition, the presence of oxygen in the bulk of some samples suggests the possibility of oxide formation during the deposition. Probable sources of oxygen include the carrier gas and the solvent, which despite being anhydrous (by passing through molecular sieves and drying over activated alumina, respectively) are still likely to contain trace amounts of O_2 and H_2O. Future optimisation of the deposition should include an investigation into the source of oxide contamination by using freshly dried solvents and carrier gases of ultra-high purity. Hall effect measurements showed the films to be n-type semiconductors, however carrier mobilities were significantly lower than expected for InAs, which characteristically shows high electron mobility. This was attributed to excess In_2O_3 present within the films and further deposition optimisation would be required to yield films with enhanced electrical properties.

4.4 Experimental Methods

4.4.1 General procedures – synthesis

Nitrogen (99.99%) was obtained from BOC and passed through activated molecular sieves to remove moisture. All solvents were dried over activated alumina by the Grubbs method using anhydrous engineering equipment, such that the water concentration was 5 – 10 ppm.[192]

4.4.2 Precursor synthesis

Precursor synthesis was carried out in batch processes, stored as a stock solution in toluene (0.02 g mL^{-1}) and used as required. The following describes a typical synthesis.

$^{t}BuAsH_2$ (1.00 g, 7.46 mmol) was cooled to -78 °C and dissolved in toluene (*ca.* 10 mL) and added dropwise to a stirring solution of $InMe_3$ (1.00 g, 6.25 mmol) in toluene (*ca.* 10 mL) at -78 °C. The mixture was stirred at this temperature for *ca.* 30 mins before being warmed slowly to room temperature, with which the slow evolution of gas was observed. The colourless reaction mixture was slowly warmed to 80 °C in an oil bath (during which time the evolution of gas was seen to increase) and allowed to stir for 16 hours. After this time, the evolution of gas had ceased and a yellow solution had formed, indicating the completion of the reaction. Solvent was removed *in vacuo* to yield a solid yellow product. The product was then redissolved in anhydrous toluene and stored as a stock solution of concentration 0.02 g mL^{-1} in a Youngs flask.

Crystals of the product were grown from a concentrated toluene solution, cooled to -20 °C. Yield = 0.21 g, 13%. **^{1}H NMR δ/ppm (C_6D_6):** 0.42 - 0.86 (30H, InMe), 1.31 - 1.62 (72H, As^{t}Bu), 2.51 - 2.52 (2H, AsH). **^{13}C{^{1}H} NMR δ/ppm (C_6D_6):** -5.2 - -2.0 (InMe), 31.3 – 40.4 (As^{t}Bu). **Anal. Calcd for $C_{21}H_{52}In_4As_4$:** C, 23.71; H, 4.93. **Found:** C, 24.24; H, 5.06. **MS (m/z; found):** 145 [$InMe_2$].

4.4.3 General Procedures - AACVD

Depositions were carried out using the AACVD process, which is described in detail in Chapter 1. A schematic diagram of the AACVD reactor is shown in chapter 3, section 3.4.1. Films were grown on SiCO coated float-glass substrates supplied by Pilkington Group Ltd, of dimensions *ca.* 90 mm x 45 mm x 4 mm. Prior to use the

substrates were cleaned using water and detergent, propan-2-ol and acetone and were dried in air. For each deposition, two substrates were placed within the reactor with the lower surface of the 'top-plate' sitting at a distance of *ca.* 8 mm above the upper surface of the 'bottom-plate'. The reactor was heated to the relevant temperature by a graphite block containing a Whatman cartridge heater and the temperature of the block was monitored by a Pt-Rh thermocouple. All deposition temperatures quoted refer to this temperature. The temperature of the top-plate was generally found to be *ca.* 50 – 70 °C higher than that of the bottom-plate. After reaching the desired temperature, the temperature within the reactor was allowed to equilibrate for 30 mins prior to commencing the deposition.

The precursors were dissolved in anhydrous solvent using standard Schlenk techniques, from which an aerosol was generated at room temperature by use of an ultrasonic humidifier. The aerosol was carried into the reactor using nitrogen through a brass baffle to obtain laminar flow. The total time for each deposition was dependent upon the solvents, volumes and flow rates being used. Depositions were carried out at substrate temperatures ranging between 400 – 600 °C.

4.4.4 Analysis Techniques

Thermogravimetric analysis was carried out on a Netzsch system from 20 °C to 600 °C. Samples of *ca.* 10 – 20 mg were run under an inert atmosphere of helium in sealed aluminium pans.

X-ray diffraction (XRD) was used to analyse the samples in a modified Bruker-Axs D8 diffractometer with parallel beam optics equipped with a PSD LinxEye silicon strip detector to collect diffracted X-ray photons. This instrument uses a Cu source for X-ray generation with $CuK\alpha_1$ and $CuK\alpha_2$ radiation of wavelengths 1.54056 Å and 1.54439 Å respectively, emitted with an intensity ratio of 2:1, a voltage of 40 kV and current of 30 mA. The incident beam angle was kept at 1° and the angular range of the patterns collected was $10° < 2\theta < 66°$ with a step size of 0.05° counted at 0.5s/sep.

Scanning Electron Microscopy (SEM) was performed to determine surface morphology and film thickness using a JEOL JSM-6301F Field Emission SEM at an accelerating voltage of 5 keV. Images were captured using SEMAfore software.

Samples were cut to 10 mm x 10 mm coupons and coated with a fine layer of gold to avoid charging.

X-ray photoemission spectroscopy (XPS) was performed using a Thermo Scientific K-alpha photoelectron spectrometer using monochromatic Al-K_α radiation. Survey scans were collected in the range 0–1100 eV (binding energy) at a pass energy of 160 eV. Higher resolution scans were recorded for the principal peaks of In (3d), As (3d), O (1s) and C (1s) at a pass energy of 50 eV. Peak positions were calibrated to carbon and plotted using the CasaXPS software.

Energy dispersive (EDX) analysis was carried out on a JEOL JSM-6301F Field Emission instrument with acceleration voltage of 20 kV. The As atom% was derived from the As-K_α line (10.530 keV) and the In atom% derived from the In-L_α (3.286 keV).

Chapter 5

Summary & Conclusions

5 Summary & Conclusions

The overarching concept for the research detailed in this thesis has been the single-source precursor approach to the formation of group 13 metal oxide and pnictide thin films. This encompasses the strategic design of molecular precursors, the investigation of their thermal properties, their use in deposition reactions - including the optimisation of those processes - and their characterisation and analysis of functional properties by a range of techniques. Overall, the research acts as a good demonstration of the entire materials development process, from precursor design to thin film deposition.

Chapters 2 and 3 focussed on the development of a new class of single-source precursor for the deposition of group 13 oxide thin films. *β*-ketoimines are a surprisingly under-investigated class of ligand for the stabilisation of group 13 complexes, especially when compared to the literature relating to structurally similar *β*-diketonates, which have been widely used as single-source precursors. Furthermore, to the best of our knowledge only one example of the deposition of main group metal oxide materials using *β*-ketoiminate complexes existed in literature prior to the start of this project.[119] The attraction in *β*-ketoimines as a class of ligand for this purpose was the potential to functionalise at the imino position, either with additional pendant arms containing donor groups (methoxy, amino), or with bulky substituents (aryl, silyl), in order to electronically or sterically fill up the coordination sphere of the metal centre and prevent oligomerisation. This led to the synthesis of a range of bis-*β*-ketoimines from the condensation reaction between two equivalents of acetylacetone with the ethylene-, propylene- and tetramethylene-diamine. The ligands, denoted L^nH_2, where n corresponds to the length of the carbon chain of the diamine, were all synthesised in high purity and high yield by optimisation of the reaction conditions.

The reactivity of the *β*-ketoimines was initially investigated through salt metathesis with MCl_3 (M = Al, Ga, In), *via* intermediate sodium salts formed by deprotonation of the *β*-ketoimines with sodium hydride. These reactions yielded a range of complexes of varying structural types. Geometries of the monomeric, 5-coordinaete species varied between the two geometrical extremes of trigonal bipyramidal and square-based pyramidal, with slight distortion observed in all cases. Due to the larger

size of the indium cation, reaction with L^2H_2 afforded a range of 6-coordinate complexes by coordination of solvent molecules, excess free ligand molecules and by dimerisation through bridges formed by the *β*-ketoiminate oxygen atoms. This was attributed to the small size of the bridging group and the larger size of the indium cation, preventing the ligand from fully wrapping around the cation and leaving the coordination sphere open. Use of ligands with larger bridging groups facilitated the isolation of the expected monomeric species.

Alkane elimination reactions were carried out with MMe_3 (M = Ga, In) and the free ligands L^nH_2 with the aim of isolating complexes of the type $[M(L^n)Me]$. Isolation and structural characterisation of the complex $[Ga(L^2)Me]$ was successful, yielding the expected 5-coordinate, monomeric species. For the propylene and tetramethylene derivative, however, a 2:1 reaction was observed in the formation of the bimetallic species $[L^n(GaMe_2)_2]$ (n = 3, 4), as determined by ^1H and ^{13}C NMR and supported by mass spectrometry and elemental analysis. Analytical data for the indium analogues were consistent with the formation of the mono-metallic products, however attempts at recrystallisation were unsuccessful and thus it is uncertain if monomeric or dimeric species were formed. Mass spectrometry showed no peaks corresponding to the expect parent ion of the dimers, providing an indication that the monomers were indeed formed.

Finally, reaction of the free *β*-ketomines with freshly prepared ethereal solutions of the gallane adduct $[H_3Ga(NMe_3)]$ led to the isolation of two β-ketoimine-stabilised gallium monohydride complexes, $[Ga(L^n)H]$ (n = 2, 3), which were structurally characterised. The isolation of these complexes was of particular significance owing to the general instability of gallium hydrides at ambient temperatures. TGA analysis of the complexes showed the onset of decomposition to occur at *ca.* 210 °C, not only showing the excellent thermal stability of the hydrides but also their potential for application as precursors in CVD processes.

TGA analysis of the precursors showed, in all cases, a good temperature window between melting and the onset of decomposition, suggesting their potential for use in thermal CVD processes where sublimation of the precursor prior to decomposition is necessary for successful transport of the precursor to the reaction chamber in the gas phase. The decomposition profiles indicated the methyl precursor were the most

suitable precursors, showing the lowest decomposition temperatures and the cleanest decomposition pathways.

Despite encouraging TGA data, initial deposition studies using LPCVD of [Ga(L^2)H] showed significant decomposition of the precursor prior to any significant sublimation and attention was therefore turned to AACVD to aid the transport of the precursor as an aerosol. Depositions were carried out at a range of temperatures up to 600 °C on glass substrates. The chloride complexes showed no film growth under any conditions, indicating that higher temperatures would be required in order to achieve this. Film growth was observed using the methyl and hydride complexes, though substrate temperatures up to 600 °C were necessary for good coverage over the substrate. Thin films were analysed by a range of common techniques, such as XPS, EDXA, SEM, and pXRD. The as-deposited films showed varying compositions, with films ranging from oxygen-rich to oxygen-deficient, though XPS analysis was consistent with the formation of Ga_2O_3. Of the as-deposited films, those deposited from the precursor [L^3($GaMe_2$)$_2$] were of the highest quality, showing stoichiometries close to the expected values for Ga_2O_3.

All as-deposited films were found to be amorphous by pXRD, as expected for Ga_2O_3 grown at temperatures < 600 °C. Depositions were repeated on quartz substrates and followed by an annealing step at 1000 °C in an attempt to form crystalline Ga_2O_3. However, in most cases, the films were found to be very thin and were removed from the substrate by the annealing step. Annealing the film grown from [Ga(L^2)H], on the other hand, yielded crystalline Ga_2O_3. Optical analysis of the film revealed the band gap of the material to be 4.65 eV, high transparency in the visible regions (80 – 90% transmission) and low reflectivity (5 – 10%). These values meet the industry requirements for transparent oxide devices.

In addition to exploring the reactivity of *β*-ketoimines towards group 13 metals and the synthesis and characterisation of a range of novel group 13 metal *β*-ketoiminate complexes, the CVD studies show the potential of these precursors towards the deposition of group 13 oxide thin films. Whilst the quality of the Ga_2O_3 thin films was not as high as has been achieved using alternative precursors, optimisation of the precursors and deposition conditions should lead to a significant improvement in

film quality (see below) and the work outlined in this thesis acts as a good proof-of-concept for the deposition of group 13 oxides from *β*-ketoiminate precursors.

Chapter 4 describes the first deposition of InAs *via* AACVD, from a single-source precursor derived from the 1:1 reaction of $InMe_3$ and $^tBuAsH_2$. Analysis of the crude reaction product indicated the formation of a mixture of different oligomers, with recrystallisation from toluene allowing the isolation and structural characterisation of a large InAs cluster complex containing eight In atoms and eight As atoms, all of which were four-coordinate. Dark blue, metallic thin films of InAs were grown from toluene solutions of the precursor, at a range of substrate temperatures and precursor concentrations. Glancing angle pXRD analysis of the films showed the formation of crystalline InAs, whilst EDXA showed the presence of both In and As. Atomic% ratios of the two elements showed the films to be indium-rich at the surface, which is an expected observation caused by the formation of In_2O_3 at the surface. This is a trend commonly observed for III/V materials and was confirmed by XPS analysis. The best quality films by far were deposited using a larger mass of precursor (0.5 g) in 30 mL toluene at a substrate temperature of 450 °C, yielding highly crystalline thin films with minimal oxide formation at the surface, as well as minimal oxygen and carbon contamination in the bulk. Hall effect measurements showed the films to be n-type semiconductors, however carrier mobilities were found to be 2 - 3 orders of magnitude lower than some literature values for InAs. This was attributed to the formation of In_2O_3 both at the surface of the film and in some cases within the bulk.

5.1 Outlook

Results have shown *β*-ketoiminates to be a potentially useful class of compound for the deposition of group 13 metal oxide thin films. In particular, the development of the tetradentate ligand system has facilitated the formation of monomeric species, compare to the dimeric species often formed using donor-functionalised alkoxide ligand systems.[104] This should aid the synthesis of precursors sufficiently volatile for application in LP and APCVD processes, however attempts outlined in chapter 3 showed decomposition of the precursors under these conditions. Further tuning of the ligand system should improve the volatility of the precursors, giving them increase application. One such method for enhancing the volatility of precursors is the use of fluorinated ligands.[119] The synthesis of *β*-ketoimines derived from

1,1,1,5,5,5-hexafluoroacetylacetone is therefore one area of interest for the tuning of the precursor system towards improved volatility.

A number of co-ligands have been used in these studies, namely chlorides, methyls and hydrides. Whilst deposition of Ga_2O_3 was achieved using the latter two, exploration of alternative co-ligands could also lead to improvement in thin film deposition. In particular, simple monodentate alkoxides would offer an additional inherent M-O bond, which would be likely to improve the deposition characteristics. As discussed in chapter 2, attempts were made at the formation of such complexes, however isolation of sufficiently pure products was unsuccessful. Furthermore, the deposition routes outlined as part of this work could be optimised to afford thicker, higher quality films. Use of alternative substrates would also allow the exploration of deposition at temperatures higher than 600 °C, which may enable In_2O_3 film growth or growth of crystalline Ga_2O_3 without the need for a post-deposition annealing step.

The work outlined in chapter 4 represents the first example of InAs films growth *via* AACVD. Similar work recently carried out has also demonstrated the first deposition of GaAs by AACVD, resulting in the production of device-quality materials.[114] The deposition conditions used in both cases would be complementary and thus present the potential for the formation of mixed metal materials of the type $Ga_{1-x}In_xAs$ from either one-pot or two-pot AACVD reactions. Furthermore, the recent demonstration of a combinatorial AACVD technique for the formation of gallium-indium oxide thin films could be extended to explore the effect of the varying composition of $Ga_{1-x}In_xAs$ on the material's electrical properties.

There is also current interest in the formation of InAs quantum dots (QDs) within GaAs matrices for future optoelectronic applications and solar cells with ultra-high efficiency solar conversion.[223, 224] Most methods currently employed involve the self-assembly of the QDs during the deposition process. However, using AACVD it would be possible to achieve the deposition of pre-assembled QDs within the host matrix, allowing the physical properties of the particles to be tuned more easily.

References

1. L. Smart, *Solid state chemistry an introduction / Lesley Smart and Elaine Moore*, Boca Raton : CRC Press, Boca Raton, 2005.
2. I. R. Grant, in *Chemistry of Aluminium, Gallium, Indium and Thallium*, ed. A. J. Downs, Blackie Academic & Professional, Glasgow, 1993, pp. 292 - 320.
3. K. A. Evans, in *Chemistry of Aluminium, Gallium, Indium and Thallium*, ed. A. J. Downs, Blackie Academic & Professional, Glasgow, 1993, pp. 248 - 291.
4. J. Koo, S. Kim, S. Jeon, H. Jeon, Y. Kim and Y. Won, *J. Korean Phys. Soc.*, 2006, **48**, 131-136.
5. B. E. Yoldas, *Appl. Optics*, 1980, **19**, 1425-1429.
6. S. E. Potts, L. Schmalz, M. Fenker, B. Diaz, J. Swiatowska, V. Maurice, A. Seyeux, P. Marcus, G. Radnoczi, L. Toth and W. M. M. Kessels, *J. Electrochem. Soc.*, 2011, **158**, C132-C138.
7. N. Bahlawane, S. Blittersdorf, K. Kohse-Hoinghaus, B. Atakan and J. Muller, *J. Electrochem. Soc.*, 2004, **151**, C182-C186.
8. J. Robertson, *Eur. Phys. J.-Appl. Phys.*, 2004, **28**, 265-291.
9. T. Kobayashi, M. Okamura, E. Yamaguchi, Y. Shinoda and Y. Hirota, *J. Appl. Phys.*, 1981, **52**, 6434-6436.
10. L. M. Foster and H. C. Stumpf, *J. Am. Chem. Soc.*, 1951, **73**, 1590-1595.
11. M. Marezio and J. P. Remeika, *J. Chem. Phys.*, 1967, **46**, 1862-1865.
12. T. Harwig, G. J. Wubs and G. J. Dirksen, *Solid State Commun.*, 1976, **18**, 1223-1225.
13. Z. Hajnal, J. Miro, G. Kiss, F. Reti, P. Deak, R. C. Herndon and J. M. Kuperberg, *J. Appl. Phys.*, 1999, **86**, 3792-3796.
14. M. Fleischer and H. Meixner, *Sens. Actuators B-Chem.*, 1991, **4**, 437-441.
15. M. Fleischer and H. Meixner, *Sens. Actuators B-Chem.*, 1992, **6**, 257-261.
16. M. Fleischer and H. Meixner, *Sens. Actuators B-Chem.*, 1995, **26**, 81-84.
17. Z. F. Liu, T. Yamazaki, Y. Shen, T. Kikuta, N. Nakatani and Y. X. Li, *Sens. Actuators B-Chem.*, 2008, **129**, 666-670.
18. A. C. Tas, P. J. Majewski and F. Aldinger, *J. Am. Ceram. Soc.*, 2000, **83**, 2954-2960.
19. S. C. Vanithakumari and K. K. Nanda, *Adv. Mater.*, 2009, **21**, 3581-+.
20. M. Orita, H. Hiramatsu, H. Ohta, M. Hirano and H. Hosono, *Thin Solid Films*, 2002, **411**, 134-139.
21. P. Meriaudeau and C. Naccache, *J.Mol. Catal.*, 1990, **59**, L31-L36.
22. C. Y. Wang, V. Cimalla, H. Romanus, T. Kups, G. Ecke, T. Stauden, M. Ali, V. Lebedev, J. Pezoldt and O. Ambacher, *Appl. Phys. Lett.*, 2006, **89**, -.
23. P. D. C. King, T. D. Veal, F. Fuchs, C. Y. Wang, D. J. Payne, A. Bourlange, H. Zhang, G. R. Bell, V. Cimalla, O. Ambacher, R. G. Egdell, F. Bechstedt and C. F. McConville, *Phys. Rev. B*, 2009, **79**, 205211.
24. H. K. Müller, *Physica Status Solidi (b)*, 1968, **27**, 723-731.
25. F. Fuchs and F. Bechstedt, *Phys. Rev. B*, 2008, **77**, 155107.

26. A. Walsh, J. L. F. Da Silva, S.-H. Wei, C. Körber, A. Klein, L. F. J. Piper, A. DeMasi, K. E. Smith, G. Panaccione, P. Torelli, D. J. Payne, A. Bourlange and R. G. Egdell, *Phys. Rev. Lett.*, 2008, **100**, 167402.
27. X. Y. Lai, D. Wang, N. Han, J. Du, J. Li, C. J. Xing, Y. F. Chen and X. T. Li, *Chem. Mater.*, 2010, **22**, 3033-3042.
28. J. Frank, A. Fleischer, A. Zimmer and H. Meixner, *Sensors Journal, IEEE*, 2001, **1**, 318-321.
29. R. J. Cava, J. M. Phillips, J. Kwo, G. A. Thomas, R. B. Vandover, S. A. Carter, J. J. Krajewski, W. F. Peck, J. H. Marshall and D. H. Rapkine, *Appl. Phys. Lett.*, 1994, **64**, 2071-2072.
30. J. M. Phillips, J. Kwo, G. A. Thomas, S. A. Carter, R. J. Cava, S. Y. Hou, J. J. Krajewski, J. H. Marshall, W. F. Peck, D. H. Rapkine and R. B. Vandover, *Appl. Phys. Lett.*, 1994, **65**, 115-117.
31. C. G. Granqvist and A. Hultaker, *Thin Solid Films*, 2002, **411**, 1-5.
32. T. Maruyama and K. Fukui, *Japanese J. Appl. Phys. Part 2-Lett.*, 1990, **29**, L1705-L1707.
33. R. Nomura, K. Konishi and H. Matsuda, *J. Electrochem. Soc.*, 1991, **138**, 631-632.
34. C. E. Knapp, G. Hyett, I. P. Parkin and C. J. Carmalt, *Chem. Mater.*, 2011, **23**, 1719-1726.
35. K. R. Reyes-Gil, E. A. Reyes-Garcia and D. Raftery, *J. Phys. Chem. C*, 2007, **111**, 14579-14588.
36. Y. Sakata, Y. Matsuda, T. Yanagida, K. Hirata, H. Imamura and K. Teramura, *Catal. Lett.*, 2008, **125**, 22-26.
37. C. E. Knapp, A. Kafizas, I. P. Parkin and C. J. Carmalt, *J. Mater. Chem.*, 2011, **21**, 12644-12649.
38. D. S. Ginley and C. Bright, *MRS Bull.*, 2000, **25**, 15-18.
39. J.-S. Kim, F. Cacialli and R. Friend, *Thin Solid Films*, 2003, **445**, 358-366.
40. H. H. Wieder, *J. Vac. Sci. Technol.*, 1971, **8**, 210-223.
41. J. L. Pan, J. E. McManis, T. Osadchy, L. Grober, J. M. Woodall and P. J. Kindlmann, *Nat. Mater.*, 2003, **2**, 375-378.
42. A. G. Milnes and A. Y. Polyakov, *Mater. Sci. Eng. B*, 1993, **18**, 237-259.
43. D. L. Partin, L. Green, D. T. Morelli, J. Heremans, B. K. Fuller and C. M. Thrush, *J. of Elec. Mater.*, 1991, **20**, 1109-1115.
44. M. S. Raven, *J. Mater. Sci.: Mater. Electron.*, 1994, **5**, 129-146.
45. E. Klaus, *Journal of Physics D: App. Phys.*, 2000, **33**, R17.
46. Y. Jin, K. Saito, M. Shimada and T. Ono, *J. Vac. Sci. Technol. B*, 2003, **21**, 942-948.
47. F. Shi, S. Zhang and C. Xue, *J. Alloys Compd.*, 2010, **498**, 77-80.
48. N. Joo Hyon, R. Seung Yoon, J. Sung Jin, K. Chang Su, S. Sung-Woo, P. D. Rack, K. Dong-Joo and B. Hong-Koo, *Electron Device Lett., IEEE*, 2010, **31**, 567-569.
49. S. Mishra, S. Daniele, S. Petit, E. Jeanneau and M. Rolland, *Dalton Trans.*, 2009, 2569-2577.
50. M. A. Flores-Mendoza, R. Castanedo-Perez, G. Torres-Delgado, J. Márquez Marín and O. Zelaya-Angel, *Thin Solid Films*, 2008, **517**, 681-685.
51. H. Yang, B. Zhang, X. Wang, X. Wang, T. Li, S. Xie and X. Yao, *J. Cryst. Growth*, 2005, **280**, 521-529.
52. J. B. Mooney and S. B. Radding, *Annu. Rev. Mater. Sci.*, 1982, **12**, 81-101.
53. H. Jianhua and C. Michael, *J. Phys. D: Appl. Phys.*, 2002, **35**, 433.

54. G. Korotcenkov, V. Brinzari, M. Ivanov, A. Cerneavschi, J. Rodriguez, A. Cirera, A. Cornet and J. Morante, *Thin Solid Films*, 2005, **479**, 38-51.
55. A. A. Wernberg, D. J. Lawrence, H. J. Gysling, A. J. Filo and T. N. Blanton, *J. Cryst. Growth*, 1993, **131**, 176-180.
56. J. Will, A. Mitterdorfer, C. Kleinlogel, D. Perednis and L. J. Gauckler, *Solid State Ionics*, 2000, **131**, 79-96.
57. W. F. Chu, *Solid State Ionics*, 1992, **52**, 243-248.
58. R. Binions, C. J. Carmalt and I. P. Parkin, *Meas. Sci. Technol.*, 2007, **18**, 190-200.
59. R. L. Puurunen, *J. Appl. Phys.*, 2005, **97**, 121301-121352.
60. A. C. Jones and M. L. Hitchman, *Chemical Vapour Deposition: Precursors, Processes and Applications*, RSC Publishing, 2009.
61. M. D. Groner, F. H. Fabreguette, J. W. Elam and S. M. George, *Chem. Mater.*, 2004, **16**, 639-645.
62. D. J. Comstock and J. W. Elam, *Chem. Mater.*, 2012, **24**, 4011-4018.
63. O. Nilsen, R. Balasundaraprabhu, E. V. Monakhov, N. Muthukumarasamy, H. Fjellvåg and B. G. Svensson, *Thin Solid Films*, 2009, **517**, 6320-6322.
64. P. D. Ye, G. D. Wilk, B. Yang, J. Kwo, S. N. G. Chu, S. Nakahara, H. J. L. Gossmann, J. P. Mannaerts, M. Hong, K. K. Ng and J. Bude, *Appl. Phys. Lett.*, 2003, **83**, 180-182.
65. S. J. A. Moniz, C. S. Blackman, C. J. Carmalt and G. Hyett, *J. Mater. Chem.*, 2010, **20**, 7881-7886.
66. K. L. Choy, *Prog. Mater. Sci.*, 2003, **48**, 57-170.
67. C. S. Blackman, C. J. Carmalt, I. P. Parkin, L. Apostolico, K. C. Molloy, A. J. P. White and D. J. Williams, *J. Chem. Soc., Dalton Trans.*, 2002, 2702-2709.
68. C. W. Dunnill, Z. A. Aiken, J. Pratten, M. Wilson and I. P. Parkin, *Chem. Vap. Deposition*, 2010, **16**, 50-54.
69. T. Thomas, C. S. Blackman, I. P. Parkin and C. J. Carmalt, *Eur. J. Inorg. Chem.*, 2010, 5629-5634.
70. P. Marchand, I. A. Hassan, I. P. Parkin and C. J. Carmalt, *Dalton Trans.*, 2013, **42**, 9406-9422.
71. X. Hou and K. L. Choy, *Chem. Vap. Deposition*, 2006, **12**, 583-596.
72. P. Marchand and C. J. Carmalt, *Coord. Chem. Rev.*, 2013, **257**, 3202.
73. N. H. Dryden, J. G. Shapter, L. L. Coatsworth, P. R. North and R. J. Puddephatt, *Chem. Mater.* 1992, **4**, 979-981.
74. R. J. Puddephatt and I. Treurnicht, *J. Organomet. Chem.*, 1987, **319**, 129-137.
75. E. Szłyk, P. Piszczek, I. Łakomska, A. Grodzicki, J. Szatkowski and T. Błaszczyk, *Chem. Vap. Deposition*, 2000, **6**, 105-108.
76. A. Grodzicki, I. Łakomska, P. Piszczek, I. Szymańska and E. Szłyk, *Coord. Chem. Rev.*, 2005, **249**, 2232-2258.
77. R. G. Palgrave and I. P. Parkin, *Chem. Mater.*, 2007, **19**, 4639-4647.
78. E. S. Peters, C. J. Carmalt, I. P. Parkin and D. A. Tocher, *Eur. J. Inorg. Chem.*, 2005, 4179-4185.
79. C. Edusi, G. Sankar and I. P. Parkin, *Chem. Vap. Deposition*, 2012, **18**, 126-132.
80. N. Noor and I. P. Parkin, *J. Mater. Chem. C*, 2013, **1**, 984-996.
81. L. Armelao, D. Barreca, G. Bottaro, A. Gasparotto, S. Gross, C. Maragno and E. Tondello, *Coord. Chem. Rev.*, 2006, **250**, 1294-1314.

82. R. G. Palgrave and I. P. Parkin, *J. Am. Chem. Soc.*, 2006, **128**, 1587-1597.
83. M. Saeli, R. Binions, C. Piccirillo, G. Hyett and I. P. Parkin, *Polyhedron*, 2009, **28**, 2233-2239.
84. M. Saeli, R. Binions, C. Piccirillo and I. P. Parkin, *Appl. Surf. Sci.*, 2009, **255**, 7291-7295.
85. A. H. Cowley and R. A. Jones, *Polyhedron*, 1994, **13**, 1149-1157.
86. A. C. Jones, *J. Mater. Chem.*, 2002, **12**, 2576-2590.
87. H. M. Manasevit, *Appl. Phys. Lett.*, 1968, **12**, 156-159.
88. A. H. Cowley, R. A. Jones, M. A. Mardones and C. M. Nunn, *Organometallics*, 1991, **10**, 1635-1637.
89. A. M. Arif, B. L. Benac, A. H. Cowley, R. Geerts, R. A. Jones, K. B. Kidd, J. M. Power and S. T. Schwab, *J. Chem. Soc., Chem. Commun.*, 1986, 1543-1545.
90. A. H. Cowley, B. L. Benac, J. G. Ekerdt, R. A. Jones, K. B. Kidd, J. Y. Lee and J. E. Miller, *J. Am. Chem. Soc.*, 1988, **110**, 6248-6249.
91. J. E. Miller, K. B. Kidd, A. H. Cowley, R. A. Jones, J. G. Ekerdt, H. J. Gysling, A. A. Wernberg and T. N. Blanton, *Chem. Mater.*, 1990, **2**, 589-593.
92. J. E. Miller and J. G. Ekerdt, *Chem. Mater.*, 1992, **4**, 7-9.
93. M. A. Malik, M. Afzaal and P. O'Brien, *Chem. Rev.*, 2010, **110**, 4417-4446.
94. L. G. Bloor, C. J. Carmalt and D. Pugh, *Coord. Chem. Rev.*, 2011, **255**, 1293-1318.
95. C. J. Carmalt and S. J. King, *Coord. Chem. Rev.*, 2006, **250**, 682-709.
96. L. Miinea, S. Suh, S. G. Bott, J.-R. Liu, W.-K. Chu and D. M. Hoffman, *J. Mater. Chem.*, 1999, **9**, 929-935.
97. M. Valet and D. M. Hoffman, *Chem. Mater.*, 2001, **13**, 2135-2143.
98. D. H. Kim, S. H. Yoo, T. M. Chung, K. S. An, H. S. Yoo and Y. Kim, *Bull. Korean Chem. Soc.*, 2002, **23**, 225-228.
99. Y. Kokubun, K. Miura, F. Endo and S. Nakagomi, *Appl. Phys. Lett.*, 2007, **90**, 031912-031913.
100. S. Basharat, W. Betchley, C. J. Carmalt, S. Barnett, D. A. Tocher and H. O. Davies, *Organometallics*, 2007, **26**, 403-407.
101. S. Suh and D. M. Hoffman, *J. Am. Chem. Soc.*, 2000, **122**, 9396-9404.
102. S. Basharat, C. J. Carmalt, S. A. Barnett, D. A. Tocher and H. O. Davies, *Inorg. Chem.*, 2007, **46**, 9473-9480.
103. S. Basharat, C. J. Carmalt, R. Binions, R. Palgrave and I. P. Parkin, *Dalton Trans.*, 2008, 591-595.
104. S. Basharat, C. J. Carmalt, R. Palgrave, S. A. Barnett, D. A. Tocher and H. O. Davies, *J. Organomet. Chem.*, 2008, **693**, 1787-1796.
105. C. E. Knapp, L. Pemberton, C. J. Carmalt, D. Pugh, P. F. McMillan, S. A. Barnett and D. A. Tocher, *Main Group Chem.*, 2010, **9**, 31-40.
106. Y. Chi, T. Y. Chou, Y. J. Wang, S. F. Huang, A. J. Carty, L. Scoles, K. A. Udachin, S. M. Peng and G. H. Lee, *Organometallics*, 2004, **23**, 95-103.
107. L. A. Ryabova and Y. S. Savitskaya, *J. Vac. Sci. Technol.*, 1969, **6**, 934-937.
108. T. Maruyama and K. Fukui, *Journal of Appl. Phys.*, 1991, **70**, 3848-3851.
109. P. Wu, Y. M. Gao, R. Kershaw, K. Dwight and A. Wold, *Mater. Res. Bull.*, 1990, **25**, 357-363.
110. A. Ortiz, J. C. Alonso, E. Andrade and C. Urbiola, *J. Electrochem. Soc.*, 2001, **148**, F26-F29.

111. Q. Peng, D. Hojo, K. J. Park and G. N. Parsons, *Thin Solid Films*, 2008, **516**, 4997-5003.
112. B. Ballarin, G. A. Battiston, F. Benetollo, R. Gerbasi, M. Porchia, D. Favretto and P. Traldi, *Inorg. Chim. Acta*, 1994, **217**, 71-78.
113. G. A. Battiston, R. Gerbasi, M. Porchia, R. Bertoncello and F. Caccavale, *Thin Solid Films*, 1996, **279**, 115-118.
114. S. Sathasivam, PhD Thesis, University College London, 2012.
115. L. A. Lesikar, A. F. Gushwa and A. F. Richards, *J. Organomet. Chem.*, 2008, **693**, 3245-3255.
116. A. F. Lugo and A. F. Richards, *Eur. J. Inorg. Chem.*, 2010, 2025-2035.
117. C. M. Beavers, G. H. Talbo and A. F. Richards, *J. Organomet. Chem.*, 2011, **696**, 2507-2511.
118. F. P. Macedo, C. Gwengo, S. V. Lindeman, M. D. Smith and J. R. Gardinier, *Eur. J. Inorg. Chem.*, 2008, 3200-3211.
119. T. Y. Chou, Y. Chi, S. F. Huang, C. S. Liu, A. J. Carty, L. Scoles and K. A. Uclachin, *Inorg. Chem.*, 2003, **42**, 6041-6049.
120. R. C. Yu, C. H. Hung, J. H. Huang, H. Y. Lee and J. T. Chen, *Inorganic Chemistry*, 2002, **41**, 6450-6455.
121. P. C. Kuo, I. C. Chen, J. C. Chang, M. T. Lee, C. H. Hu, C. H. Hung, H. M. Lee and J. H. Huang, *Eur. J. Inorg. Chem.*, 2004, 4898-4906.
122. P. Shukla, J. C. Gordon, A. H. Cowley and J. N. Jones, *J. Organomet. Chem.*, 2005, **690**, 1366-1371.
123. H. M. Kao, S. M. Ho, I. C. Chen, P. C. Kuo, C. Y. Lin, C. Y. Tu, C. H. Hu, J. H. Huang and G. H. Lee, *Inorg. Chim. Acta*, 2008, **361**, 2792-2798.
124. P. C. Kuo, I. C. Chen, H. M. Lee, C. H. Hung and J. H. Huang, *Inorg. Chim. Acta*, 2005, **358**, 3761-3767.
125. C. H. Huang, L. F. Hsueh, P. C. Kuo, H. M. Lee, C. L. Uno, J. H. Huang, C. Y. Tu, C. H. Hu, G. H. Lee and C. H. Hung, *Eur. J. Inorg. Chem.*, 2008, 3000-3008.
126. J. K. Vohs, D. O. Miller, D. R. Denomme, J. W. Ziller and B. D. Fahlman, *Acta Crystallogr., Sect. C: Cryst. Struct. Commun.*, 2005, **61**, M287-M288.
127. A. T. S. Wee, A. J. Murrell, N. K. Singh, D. O'Hare and J. S. Foord, *J. Chem. Soc., Chem. Commun.*, 1990, 11-13.
128. C. Jones, G. A. Koutsantonis and C. L. Raston, *Polyhedron*, 1993, **12**, 1829-1848.
129. C. R. Pulham, A. J. Downs, M. J. Goode, D. W. H. Rankin and H. E. Robertson, *J. Am. Chem. Soc.*, 1991, **113**, 5149-5162.
130. A. J. Downs, *Coord. Chem. Rev.*, 1999, **189**, 59-100.
131. C. L. Raston, *J. Organomet. Chem.*, 1994, **475**, 15-24.
132. M. G. Gardiner and C. L. Raston, *Coord. Chem. Rev.*, 1997, **166**, 1-34.
133. S. Aldridge and A. J. Downs, *Chem. Rev.*, 2001, **101**, 3305-3366.
134. N. N. Greenwood, A. Storr and M. G. H. Wallbridge, *Inorg. Chem.*, 1963, **2**, 1036-1039.
135. P. C. Andrews, M. G. Gardiner, C. L. Raston and V.-A. Tolhurst, *Inorg. Chim. Acta*, 1997, **259**, 249-255.
136. J. L. Atwood, S. G. Bott, F. M. Elms, C. Jones and C. L. Raston, *Inorg. Chem.*, 1991, **30**, 3792-3793.
137. A. R. Cowley, A. J. Downs, H.-J. Himmel, S. Marchant, S. Parsons and J. A. Yeoman, *Dalton Trans.*, 2005, 1591-1597.

138. D. D. Perrin, *Dissociation constants of inorganic acids and bases in aqueous solution / by D. D. Perrin*, London : Butterworths, London, 1969.
139. W. A. Henderson and C. A. Streuli, *J. Am. Chem. Soc.*, 1960, **82**, 5791-5794.
140. C. D. Abernethy, M. L. Cole and C. Jones, *Organometallics*, 2000, **19**, 4852-4857.
141. T. L. Amyes, S. T. Diver, J. P. Richard, F. M. Rivas and K. Toth, *J. Am. Chem. Soc.*, 2004, **126**, 4366-4374.
142. P. T. Brain, H. E. Brown, A. J. Downs, T. M. Greene, E. Johnsen, S. Parsons, D. W. H. Rankin, B. A. Smart and C. Y. Tang, *J. Chem. Soc., Dalton Trans.*, 1998, 3685-3692.
143. J. Lorberth, R. Dorn, S. Wocadlo, W. Massa, E. O. Göbel, T. Marschner, H. Protzmann, O. Zsebök and W. Stolz, *Adv. Mater.*, 1992, **4**, 576-579.
144. N. N. Greenwood, E. J. F. Ross and A. Storr, *J. Chem. Soc. A*, 1966, 706-711.
145. C. Y. Tang, R. A. Coxall, A. J. Downs, T. M. Greene and S. Parsons, *J. Chem. Soc., Dalton Trans.*, 2001, 2141-2147.
146. J. L. Atwood, F. R. Bennett, F. M. Elms, G. A. Koutsantonis, C. L. Raston, K. D. Robinson and D. J. Young, *Inorg. Chem.*, 1992, **31**, 2673-2674.
147. N. N. Greenwood, E. J. F. Ross and A. Storr, *J. Chem. Soc.*, 1965, 1400-1406.
148. T. J. Clark, C. A. Jaska, A. Turak, A. J. Lough, Z.-H. Lu and I. Manners, *Inorg. Chem.*, 2007, **46**, 7394-7402.
149. F. M. Elms, M. G. Gardiner, G. A. Koutsantonis, C. L. Raston, J. L. Atwood and K. D. Robinson, *J. Organomet. Chem.*, 1993, **449**, 45-52.
150. D. O'Hare, J. S. Foord, T. C. M. Page and T. J. Whitaker, *J. Chem. Soc., Chem. Commun.*, 1991, 1445-1447.
151. M. D. Francis, D. E. Hibbs, M. B. Hursthouse, C. Jones and N. A. Smithies, *J Chem. Soc., Dalton Trans.*, 1998, 3249-3254.
152. R. J. Baker, M. L. Cole, C. Jones and M. F. Mahon, *J Chem. Soc., Dalton Trans.*, 2002, 1992-1996.
153. M. L. Cole, S. K. Furfari and M. Kloth, *J. Organomet. Chem.*, 2009, **694**, 2934-2940.
154. M. Veith, S. Faber, H. Wolfanger and V. Huch, *Ber.*, 1996, **129**, 381-384.
155. G. A. Koutsantonis, F. C. Lee and C. L. Raston, *Main Group Chem.*, 1995, **1**, 21-28.
156. D. Pugh, L. G. Bloor, I. P. Parkin and C. J. Carmalt, *Chem. Eur. J.*, 2012, **18**, 6079-6087.
157. A. W. Addison, T. N. Rao, J. Reedijk, J. Vanrijn and G. C. Verschoor, *J Chem. Soc.-Dalton Trans.*, 1984, 1349-1356.
158. S. Gogoi, R. Bhuyan and N. C. Barua, *Synth. Commun.*, 2005, **35**, 2811-2818.
159. D. H. Lee, S.-E. Park, K. Cho, Y. Kim, T. Athar and I.-M. Lee, *Tetrahedron Lett.*, 2007, **48**, 8281-8284.
160. F. H. Allen, O. Kennard, D. G. Watson, L. Brammer, A. G. Orpen and R. Taylor, *J Chem. Soc.-Perkin Trans. 2*, 1987, S1-S19.
161. S. Bhattacharya, S. Singh and V. D. Gupta, *J. Chem. Crystallogr.*, 2002, **32**, 299-305.
162. L. A. Miinea, S. Suh and D. M. Hoffman, *Inorg. Chem.*, 1999, **38**, 4447-4454.

163. N. Brescianipahor, M. Calligaris, G. Nardin, L. Randaccio and D. Viterbo, *Acta Crystallogr., Sect. B: Struct. Sci*, 1979, **35**, 2776-2778.
164. K. George, C. H. de Groot, C. Gurnani, A. L. Hector, R. Huang, M. Jura, W. Levason and G. Reid, *Chem. Mater.*, 2013, **25**, 1829-1836.
165. S. Basharat, C. J. Carmalt, S. J. King, E. S. Peters and D. A. Tocher, *Dalton Trans.*, 2004, 3475-3480.
166. H. Tang, R. Fabicon and H. G. Richey, *Organometallics*, 1998, **17**, 139-145.
167. E. Johnsen, A. J. Downs, T. M. Greene, P. F. Souter, K. Aarset, E. M. Page, D. A. Rice, A. N. Richardson, P. T. Brain, D. W. H. Rankin and C. R. Pulham, *Inorg. Chem.*, 2000, **39**, 719-727.
168. C. R. Pulham, A. J. Downs, D. W. H. Rankin and H. E. Robertson, *J Chem. Soc., Dalton Trans.*, 1992, 1509-1520.
169. A. J. Downs, L. A. Harman, P. D. P. Thomas and C. R. Pulham, *Polyhedron*, 1995, **14**, 935-945.
170. O. T. Beachley and R. G. Simmons, *Inorg. Chem.*, 1980, **19**, 783-785.
171. J. Lorberth, R. Dorn, W. Massa and S. Wocadlo, *Z.Naturforsch.(B)*, 1993, **48**, 224-226.
172. R. Binions, C. J. Carmalt, I. P. Parkin, K. F. E. Pratt and G. A. Shaw, *Chem. Mater.*, 2004, **16**, 2489-2493.
173. D. L. Schulz, B. J. Hinds, D. A. Neumayer, C. L. Stern and T. J. Marks, *Chem. Mater.*, 1993, **5**, 1605-1617.
174. D. L. Schulz, B. J. Hinds, C. L. Stern and T. J. Marks, *Inorg. Chem.*, 1993, **32**, 249-250.
175. D. B. Studebaker, D. A. Neumayer, B. J. Hinds, C. L. Stern and T. J. Marks, *Inorg. Chem.*, 2000, **39**, 3148-3157.
176. S. Pasko, L. G. Hubert-Pfalzgraf, P. Richard and A. Abrutis, *Inorg. Chem. Commun.*, 2005, **8**, 483-487.
177. J. S. Matthews, O. Just, B. Obi-Johnson and W. S. Rees, *Chem. Vap. Deposition*, 2000, **6**, 129-132.
178. N. L. Edleman, A. Wang, J. A. Belot, A. W. Metz, J. R. Babcock, A. M. Kawaoka, J. Ni, M. V. Metz, C. J. Flaschenriem, C. L. Stern, L. M. Liable-Sands, A. L. Rheingold, P. R. Markworth, R. P. H. Chang, M. P. Chudzik, C. R. Kannewurf and T. J. Marks, *Inorg. Chem.*, 2002, **41**, 5005-5023.
179. S. Lim, B. Choi, Y.-s. Min, D. Kim, I. Yoon, S. S. Lee and I.-M. Lee, *J. Organomet. Chem.*, 2004, **689**, 224-237.
180. Y. S. Min, Y. J. Cho, D. Kim, J. H. Lee, B. M. Kim, S. K. Lim, I. M. Lee and W. I. Lee, *Chem. Vap. Deposition*, 2001, **7**, 146-149.
181. Y.-H. Liu, Y.-C. Cheng, Y.-L. Tung, Y. Chi, Y.-L. Chen, C.-S. Liu, S.-M. Peng and G.-H. Lee, *J. Mater. Chem.*, 2003, **13**.
182. J. S. Matthews, O. O. Onakoya, T. S. Ouattara and R. J. Butcher, *Dalton Trans.*, 2006.
183. D. Bekermann, D. Rogalla, H.-W. Becker, M. Winter, R. A. Fischer and A. Devi, *Eur. J. Inorg. Chem.*, 2010, **2010**, 1366-1372.
184. D. Bekermann, A. Ludwig, T. Toader, C. Maccato, D. Barreca, A. Gasparotto, C. Bock, A. D. Wieck, U. Kunze, E. Tondello, R. A. Fischer and A. Devi, *Chem. Vap. Deposition*, 2011, **17**, 155-161.
185. D. Pirzada and G. J. Cheng, *J. Appl. Phys.*, 2009, **105**, 093114-093117.
186. S. C. Ghosh, M. C. Biesinger, R. R. LaPierre and P. Kruse, *J. Appl. Phys.*, 2007, **101**, 114322-114328.

187. H. A. Budz, M. C. Biesinger and R. R. LaPierre, *J. Vac. Sci. Technol., B*, 2009, **27**, 637-648.
188. A. Trinchi, S. Kaciulis, L. Pandolfi, M. K. Ghantasala, Y. X. Li, W. Wlodarski, S. Viticoli, E. Comini and G. Sberveglieri, *Sens. Actuators, B*, 2004, **103**, 129-135.
189. W. Mi, J. Ma, Z. Zhu, C. Luan, Y. Lv and H. Xiao, *J. Cryst. Growth*, 2012, **354**, 93-97.
190. J. Tauc, *Mater. Res. Bull.*, 1968, **3**, 37-46.
191. H.-G. Kim and W.-T. Kim, *J. Appl. Phys.*, 1987, **62**, 2000-2002.
192. A. B. Pangborn, M. A. Giardello, R. H. Grubbs, R. K. Rosen and F. J. Timmers, *Organometallics*, 1996, **15**, 1518-1520.
193. M. F. Self, A. T. McPhail, L. J. Jones Iii and R. L. Wells, *Polyhedron*, 1994, **13**, 625-634.
194. R. L. Wells, A. T. McPhail, L. J. Jones, M. F. Self and R. J. Butcher, *Organometallics*, 1992, **11**, 2694-2697.
195. T. Thomas, D. Pugh, I. P. Parkin and C. J. Carmalt, *Dalton Trans.*, 2010, **39**, 5325-5331.
196. M. F. Mahon, N. L. Moldovan, K. C. Molloy, A. Muresan, I. Silaghi-Dumitrescu and L. Silaghi-Dumitrescu, *Dalton Trans.*, 2004, 4017-4021.
197. A. Dashti-Mommertz and B. Neumüller, *Z. Anorg. Allg. Chem.*, 1999, **625**, 954-960.
198. F. Thomas, S. Schulz and M. Nieger, *Z. Anorg. Allg. Chem.*, 2002, **628**, 235-242.
199. M. A. Malik, P. O'Brien and M. Helliwell, *J. Mater. Chem.*, 2005, **15**, 1463-1467.
200. R. L. Wells, A. T. McPhail, L. J. Jones and M. F. Self, *Polyhedron*, 1993, **12**, 141-147.
201. L. J. Jones, A. T. McPhail and R. L. Wells, *Organometallics*, 1994, **13**, 3634-3638.
202. R. L. Wells, L. J. Jones, A. T. McPhail and A. Alvanipour, *Organometallics*, 1991, **10**, 2345-2348.
203. R. L. Wells, A. T. McPhail, L. J. Jones and M. F. Self, *J. Organomet. Chem.*, 1993, **449**, 85-94.
204. A. Dashti-Mommertz, B. Werner and B. Neumüller, *Polyhedron*, 1998, **17**, 523-529.
205. C. von Hänisch, *Z. Anorg. Allg. Chem.*, 2001, **627**, 68-72.
206. G. Aksomaityte, F. Cheng, A. L. Hector, J. R. Hyde, W. Levason, G. Reid, D. C. Smith, J. W. Wilson and W. J. Zhang, *Chem. Mater.*, 2010, **22**, 4246-4253.
207. G. E. Coates and J. Graham, *J Chem. Soc. (Resumed)*, 1963, 233-237.
208. O. T. Beachley and G. E. Coates, *J Chem. Soc. (Resumed)*, 1965, 3241-3247.
209. A. H. Cowley, R. A. Jones, K. B. Kidd, C. M. Nunn and D. L. Westmoreland, *J. Organomet. Chem.*, 1988, **341**, C1-C5.
210. B. Neumüller and E. Iravani, *Coord. Chem. Rev.*, 2004, **248**, 817-834.
211. L. J. Jones, III, A. T. McPhail and R. L. Wells, *Organometallics*, 1994, **13**, 2504-2507.
212. A. H. Cowley, S. Corbelin, R. A. Jones, R. J. Lagow and J. W. Nail, *J. Organomet. Chem.*, 1994, **464**, C1-C3.
213. A. H. Cowley and R. A. Jones, *Angew. Chem. Int. Ed. Engl.*, 1989, **28**, 1208-1215.

214. D. A. Andrews, G. J. Davies, D. C. Bradley, M. M. Faktor, D. M. Frigo and E. A. D. White, *Semicond. Sci. Technol.*, 1988, **3**, 1053.
215. A. L. Patterson, *Phys. Rev.*, 1939, **56**, 978-982.
216. G. E. McGuire, G. K. Schweitzer and T. A. Carlson, *Inorg. Chem.*, 1973, **12**, 2450-2453.
217. M. Procop, *J. Electron. Spectrosc. Relat. Phenom.*, 1992, **59**, R1-R10.
218. D. M. Poirier and J. H. Weaver, *Surf. Sci. Spectra*, 1993, **2**, 224-231.
219. W. K. Liu, W. T. Yuen and R. A. Stradling, *J. Vac. Sci. Technol. B*, 1995, **13**, 1539-1545.
220. I. Lindau, P. Pianetta, C. M. Garner, P. W. Chye, P. E. Gregory and W. E. Spicer, *Surf. Sci.*, 1977, **63**, 45-55.
221. A. J. Rosenberg, *J. Phys. Chem. Solids*, 1960, **14**, 175-180.
222. J. P. McCarthy, *Solid-State Electron.*, 1967, **10**, 649-655.
223. X. Yan, X. Zhang, X. Ren, H. Huang, J. Guo, X. Guo, M. Liu, Q. Wang, S. Cai and Y. Huang, *Nano Lett.*, 2011, **11**, 3941-3945.
224. K. Tanabe, D. Guimard, D. Bordel and Y. Arakawa, *Appl. Phys. Lett.*, 2012, **100**, 193905-193903.
225. R. M. Lum, J. K. Klingert, M. G. Lamont, *Appl. Phys. Lett.*, 1987, **50**, 284.
226. C. A. Larsen, N. I. Buchan, S.H. Li, G. B. Stringfellow, *J. Cryst. Growth*, 1989, **94**, 663.
227. M. Boero, Y. Morikawa, K. Terakura, M. Ozeki, *J. Chem. Phys.*, 2000, **112**, 9549.
228. S. Gogoi, R. Bhuyan, N.C. Barua, *Synth. Commun.*, 2005, **35**, 2811.
229. J. X. Chen, X. L. Yang, M. C. Liu, H. Y. Wu, J. C. Ding, W K. Su, *Synth. Commun.*, **39**, 4180.
230. F. Thomas, S. Schulz and M. Nieger, *Eur. J. Inorg. Chem.*, 2001, **1**, 161.

Appendix

Crystallographic Data

The following tables give the crystal data and structure refinements for the complexes outlined in this thesis.

Table 7.1. Crystal data and structure refinement for [Al(L^4)Cl].

Data collected by the National Crystallography Service, Southampton. Structure solution was carried out by the author.

Identification code	shelxl	
Empirical formula	$C_{14}\,H_{22}\,Al\,Cl\,N_2\,O_2$	
Formula weight	312.77	
Temperature	100 K	
Wavelength	0.71073 Å	
Crystal system	Triclinic	
Space group	P-1	
Unit cell dimensions	a = 8.6638(5) Å	α= 80.362(6)°.
	b = 9.2573(5) Å	β= 77.955(6)°.
	c = 10.9227(7) Å	γ = 64.890(5)°.
Volume	772.701(10) $Å^3$	
Z	2	
Density (calculated)	1.344 Mg/m^3	
Absorption coefficient	0.307 mm^{-1}	
F(000)	332	
Crystal size	0.13 x 0.11 x 0.05 mm^3	
Theta range for data collection	3.0 to 27.5°.	
Index ranges	-10<=h<=11, -12<=k<=11, -13<=l<=14	
Reflections collected	10359	
Independent reflections	3520 [R(int) = 0.036]	
Completeness to theta = 27.5°	99.5 %	
Absorption correction	Semi-empirical from equivalents	
Max. and min. transmission	0.9848 and 0.9612	
Refinement method	Full-matrix least-squares on F^2	
Data / restraints / parameters	3520 / 0 / 185	
Goodness-of-fit on F^2	1.028	
Final R indices [I>2sigma(I)]	R1 = 0.0312, wR2 = 0.0794	
R indices (all data)	R1 = 0.0359, wR2 = 0.0820	
Largest diff. peak and hole	0.350 and -0.245 $e.Å^{-3}$	

Table 7.2. Crystal data and structure refinement for [Ga(L^3)Cl].

Data collection and structure solution was carried out by Dr. David Pugh.

Identification code	str0868	
Empirical formula	$C_{13}\,H_{20}\,Cl\,Ga\,N_2\,O_2$	
Formula weight	341.48	
Temperature	150(2) K	
Wavelength	0.71073 Å	
Crystal system	Triclinic	
Space group	P-1	
Unit cell dimensions	a = 7.4177(9) Å	α= 72.534(2)°.
	b = 8.6862(11) Å	β= 75.996(2)°.
	c = 12.4715(15) Å	γ = 77.103(2)°.
Volume	733.82(16) $Å^3$	
Z	2	
Density (calculated)	1.545 Mg/m^3	
Absorption coefficient	2.056 mm^{-1}	
F(000)	352	
Crystal size	0.50 x 0.40 x 0.20 mm^3	
Theta range for data collection	2.64 to 28.29°.	
Index ranges	-9<=h<=9, -11<=k<=11, -15<=l<=16	
Reflections collected	5937	
Independent reflections	3152 [R(int) = 0.0188]	
Completeness to theta = 25.00°	94.7 %	
Absorption correction	Semi-empirical from equivalents	
Max. and min. transmission	0.6839 and 0.4262	
Refinement method	Full-matrix least-squares on F^2	
Data / restraints / parameters	3152 / 0 / 177	
Goodness-of-fit on F^2	1.082	
Final R indices [I>2sigma(I)]	R1 = 0.0219, wR2 = 0.0566	
R indices (all data)	R1 = 0.0235, wR2 = 0.0576	
Largest diff. peak and hole	0.314 and -0.501 $e.Å^{-3}$	

Table 7.3. Crystal data and structure refinement for [Ga(L^4)Cl].

Data collected by the National Crystallography Service, Southampton. Structure solution was carried out by the author.

Identification code	shelxl	
Empirical formula	$C_{14}\,H_{22}\,Cl\,Ga\,N_2\,O_2$	
Formula weight	355.51	
Temperature	120 K	
Wavelength	0.71073 Å	
Crystal system	Triclinic	
Space group	P-1	
Unit cell dimensions	a = 8.64560(10) Å	α= 79.7260(3)°.
	b = 9.21790(10) Å	β= 77.4020(3)°.
	c = 11.0432(2) Å	γ = 65.5730(3)°.
Volume	778.153(19) $Å^3$	
Z	2	
Density (calculated)	1.517 Mg/m^3	
Absorption coefficient	1.942 mm^{-1}	
F(000)	368	
Crystal size	0.52 x 0.42 x 0.18 mm^3	
Theta range for data collection	2.44 to 27.58°.	
Index ranges	-10<=h<=11, -11<=k<=11, -14<=l<=14	
Reflections collected	9747	
Independent reflections	3567 [R(int) = 0.0337]	
Completeness to theta = 27.58°	99.1 %	
Absorption correction	Semi-empirical from equivalents	
Max. and min. transmission	0.7213 and 0.4316	
Refinement method	Full-matrix least-squares on F^2	
Data / restraints / parameters	3567 / 0 / 185	
Goodness-of-fit on F^2	1.194	
Final R indices [I>2sigma(I)]	R1 = 0.0380, wR2 = 0.1490	
R indices (all data)	R1 = 0.0414, wR2 = 0.1709	
Largest diff. peak and hole	0.957 and -1.152 e.$Å^{-3}$	

Table 7.4. Crystal data and structure refinement for [In(L^2)Cl·THF].

Data collection was carried out by the National Crystallography Service, Southampton and structure solution was carried out by Dr. David Pugh.

Identification code	2011src0027	
Empirical formula	C_{16} H_{26} Cl In N_2 O_3	
Formula weight	444.66	
Temperature	120(2) K	
Wavelength	0.71073 Å	
Crystal system	Monoclinic	
Space group	$P2_1/c$	
Unit cell dimensions	a = 8.0171(3) Å	α= 90°.
	b = 14.7596(5) Å	β= 114.806(2)°.
	c = 17.1126(5) Å	γ = 90°.
Volume	1838.09(11) $Å^3$	
Z	4	
Density (calculated)	1.607 Mg/m^3	
Absorption coefficient	1.446 mm^{-1}	
F(000)	904	
Crystal size	0.10 x 0.10 x 0.04 mm^3	
Theta range for data collection	2.92 to 27.51°.	
Index ranges	-8<=h<=10, -19<=k<=19, -22<=l<=19	
Reflections collected	18466	
Independent reflections	4201 [R(int) = 0.0373]	
Completeness to theta = 27.51°	99.3 %	
Absorption correction	Semi-empirical from equivalents	
Max. and min. transmission	0.9444 and 0.8689	
Refinement method	Full-matrix least-squares on F^2	
Data / restraints / parameters	4201 / 0 / 212	
Goodness-of-fit on F^2	1.124	
Final R indices [I>2sigma(I)]	R1 = 0.0320, wR2 = 0.0601	
R indices (all data)	R1 = 0.0421, wR2 = 0.0651	
Largest diff. peak and hole	0.745 and -0.488 e.$Å^{-3}$	

Table 7.5. Crystal data and structure refinement for $[In(L^2)Cl]_2$.

Data collected by the National Crystallography Service, Southampton. Structure solution was carried out by Dr. David Pugh.

Identification code	2011ncs0194	
Empirical formula	$C_{24}\,H_{36}\,Cl_2\,In_2\,N_4\,O_4$	
Formula weight	745.11	
Temperature	100 K	
Wavelength	0.71073 Å	
Crystal system	Monoclinic	
Space group	$P2_1/c$	
Unit cell dimensions	a = 11.276(4) Å	α= 90°.
	b = 11.797(4) Å	β= 120.50(2)°.
	c = 12.513(3) Å	γ = 90°.
Volume	1434.2(8) $Å^3$	
Z	2	
Density (calculated)	1.725 Mg/m^3	
Absorption coefficient	1.830 mm^{-1}	
F(000)	744	
Crystal size	0.12 x 0.06 x 0.06 mm^3	
Theta range for data collection	3.3 to 27.5°.	
Index ranges	-14<=h<=10, -14<=k<=15, -10<=l<=15	
Reflections collected	0	
Independent reflections	3268 [R(int) = 0.023]	
Completeness to theta = 27.5°	99.2 %	
Absorption correction	Semi-empirical from equivalents	
Max. and min. transmission	0.8981 and 0.8103	
Refinement method	Full-matrix least-squares on F^2	
Data / restraints / parameters	3268 / 0 / 167	
Goodness-of-fit on F^2	1.025	
Final R indices [I>2sigma(I)]	R1 = 0.0239, wR2 = 0.0472	
R indices (all data)	R1 = 0.0294, wR2 = 0.0489	
Largest diff. peak and hole	0.694 and -0.435 $e.Å^{-3}$	

Table 7.6. Crystal data and structure refinement for [{In(L^2)Cl}$_2$(L^2H_2)].

Data collected by the National Crystallography Service, Southampton. Structure solution was carried out by Dr. David Pugh.

Identification code	2011ncs0107	
Empirical formula	C_{36} H_{56} Cl_2 In_2 N_6 O_6	
Formula weight	969.41	
Temperature	120(2) K	
Wavelength	0.71073 Å	
Crystal system	Triclinic	
Space group	P-1	
Unit cell dimensions	a = 8.21910(10) Å	α= 73.9820(10)°.
	b = 9.4727(2) Å	β= 75.8890(10)°.
	c = 14.0874(2) Å	γ = 86.4360(10)°.
Volume	1022.39(3) Å^3	
Z	1	
Density (calculated)	1.574 Mg/m^3	
Absorption coefficient	1.308 mm^{-1}	
F(000)	494	
Crystal size	0.35 x 0.20 x 0.20 mm^3	
Theta range for data collection	3.04 to 27.54°.	
Index ranges	-10<=h<=10, -12<=k<=12, -18<=l<=18	
Reflections collected	23101	
Independent reflections	4701 [R(int) = 0.0395]	
Completeness to theta = 27.54°	99.5 %	
Absorption correction	Semi-empirical from equivalents	
Max. and min. transmission	0.7798 and 0.6574	
Refinement method	Full-matrix least-squares on F^2	
Data / restraints / parameters	4701 / 0 / 245	
Goodness-of-fit on F^2	1.055	
Final R indices [I>2sigma(I)]	R1 = 0.0225, wR2 = 0.0516	
R indices (all data)	R1 = 0.0254, wR2 = 0.0530	
Largest diff. peak and hole	0.441 and -0.605 e.Å^{-3}	

Table 7.7. Crystal data and structure refinement for [In(L^3)Cl].

Data collection and structure solution was carried out by Dr. David Pugh.

Identification code	str0869	
Empirical formula	C_{13} H_{20} Cl In N_2 O_2	
Formula weight	386.58	
Temperature	150(2) K	
Wavelength	0.71073 Å	
Crystal system	Triclinic	
Space group	P-1	
Unit cell dimensions	a = 8.8098(8) Å	α= 94.3270(10)°.
	b = 12.6328(11) Å	β= 95.4480(10)°.
	c = 14.7568(13) Å	γ = 110.0580(10)°.
Volume	1525.5(2) $Å^3$	
Z	4	
Density (calculated)	1.683 Mg/m^3	
Absorption coefficient	1.724 mm^{-1}	
F(000)	776	
Crystal size	0.50 x 0.30 x 0.20 mm^3	
Theta range for data collection	3.00 to 25.03°.	
Index ranges	-10<=h<=10, -15<=k<=15, -17<=l<=17	
Reflections collected	10370	
Independent reflections	5135 [R(int) = 0.0166]	
Completeness to theta = 25.03°	95.2 %	
Absorption correction	Semi-empirical from equivalents	
Max. and min. transmission	0.7243 and 0.4794	
Refinement method	Full-matrix least-squares on F^2	
Data / restraints / parameters	5135 / 0 / 351	
Goodness-of-fit on F^2	1.054	
Final R indices [I>2sigma(I)]	R1 = 0.0235, wR2 = 0.0624	
R indices (all data)	R1 = 0.0275, wR2 = 0.0644	
Largest diff. peak and hole	1.016 and -0.758 $e.Å^{-3}$	

Table 7.8. Crystal data and structure refinement for [Ga(L^2)Me].

Data collection and structure solution was carried out by Dr. David Pugh.

Identification code	str0915	
Empirical formula	C_{13} H_{21} Ga N_2 O_2	
Formula weight	307.04	
Temperature	150(2) K	
Wavelength	0.71073 Å	
Crystal system	Monoclinic	
Space group	$P2_1/c$	
Unit cell dimensions	a = 8.148(2) Å	α= 90°.
	b = 13.014(3) Å	β= 110.298(11)°.
	c = 14.885(3) Å	γ = 90°.
Volume	1480.4(6) $Å^3$	
Z	4	
Density (calculated)	1.378 Mg/m^3	
Absorption coefficient	1.855 mm^{-1}	
F(000)	640	
Crystal size	0.15 x 0.08 x 0.05 mm^3	
Theta range for data collection	2.67 to 28.31°.	
Index ranges	-10<=h<=10, -17<=k<=17, -18<=l<=18	
Reflections collected	12073	
Independent reflections	3432 [R(int) = 0.0943]	
Completeness to theta = 28.31°	93.3 %	
Absorption correction	Semi-empirical from equivalents	
Max. and min. transmission	0.9129 and 0.7682	
Refinement method	Full-matrix least-squares on F^2	
Data / restraints / parameters	3432 / 0 / 168	
Goodness-of-fit on F^2	0.892	
Final R indices [I>2sigma(I)]	R1 = 0.0596, wR2 = 0.1375	
R indices (all data)	R1 = 0.1171, wR2 = 0.1598	
Largest diff. peak and hole	0.875 and -1.216 $e.Å^{-3}$	

Table 7.9. Crystal data and structure refinement for [Ga(L^2)H].

Data collected by the National Crystallography Service, Southampton. Structure solution was carried out by the author.

Identification code	shelxl	
Empirical formula	C_{12} H_{19} Ga N_2 O_2	
Formula weight	293.01	
Temperature	120 K	
Wavelength	0.71073 Å	
Crystal system	Monoclinic	
Space group	$P2_1/c$	
Unit cell dimensions	a = 7.9220(2) Å	α= 90°.
	b = 12.0209(3) Å	β= 93.0450(18)°.
	c = 13.5746(5) Å	γ = 90°.
Volume	1290.88(7) $Å^3$	
Z	4	
Density (calculated)	1.508 Mg/m^3	
Absorption coefficient	2.124 mm^{-1}	
F(000)	608	
Crystal size	0.45 x 0.38 x 0.06 mm^3	
Theta range for data collection	2.3 to 27.7°.	
Index ranges	-9<=h<=10, -15<=k<=15, -17<=l<=17	
Reflections collected	13504	
Independent reflections	2961 [R(int) = 0.0406]	
Completeness to theta = 27.7°	99.4 %	
Absorption correction	Semi-empirical from equivalents	
Max. and min. transmission	0.8831 and 0.4483	
Refinement method	Full-matrix least-squares on F^2	
Data / restraints / parameters	2961 / 0 / 162	
Goodness-of-fit on F^2	1.130	
Final R indices [I>2sigma(I)]	R1 = 0.0373, wR2 = 0.0939	
R indices (all data)	R1 = 0.0394, wR2 = 0.0953	
Largest diff. peak and hole	1.084 and -0.810 $e.Å^{-3}$	

Table 7.10. Crystal data and structure refinement for [Ga(L^3)H].

Data collected by the National Crystallography Service, Southampton. Structure solution was carried out by the author.

Identification code	shelxl	
Empirical formula	C_{13} H_{21} Ga N_2 O_2	
Formula weight	307.04	
Temperature	100(2) K	
Wavelength	0.71073 Å	
Crystal system	Monoclinic	
Space group	$P2_1/c$	
Unit cell dimensions	a = 7.4450(5) Å	α= 90°.
	b = 15.1760(9) Å	β= 97.1120(10)°.
	c = 12.4920(8) Å	γ = 90°.
Volume	1400.55(15) $Å^3$	
Z	4	
Density (calculated)	1.456 Mg/m^3	
Absorption coefficient	1.961 mm^{-1}	
F(000)	640	
Crystal size	0.14 x 0.12 x 0.03 mm^3	
Theta range for data collection	2.68 to 30.08°.	
Index ranges	-9<=h<=10, -20<=k<=21, -16<=l<=14	
Reflections collected	9989	
Independent reflections	3354 [R(int) = 0.0329]	
Completeness to theta = 30.08°	81.4 %	
Absorption correction	Semi-empirical from equivalents	
Max. and min. transmission	0.9435 and 0.7708	
Refinement method	Full-matrix least-squares on F^2	
Data / restraints / parameters	3354 / 0 / 171	
Goodness-of-fit on F^2	1.115	
Final R indices [I>2sigma(I)]	R1 = 0.0436, wR2 = 0.1190	
R indices (all data)	R1 = 0.0484, wR2 = 0.1239	
Largest diff. peak and hole	1.031 and -0.734 $e.Å^{-3}$	

Table 7.11. Crystal data and structure refinement for InAs precursor complex.
Data collected by the National Crystallography Service, Southampton. Structure solution was carried out by Dr. David Pugh.

Identification code	shelxl	
Empirical formula	$C_{21} H_{52} As_4 In_4$	
Formula weight	1063.61	
Temperature	100(2) K	
Wavelength	0.71073 Å	
Crystal system	Monoclinic	
Space group	$P2_1/c$	
Unit cell dimensions	a = 14.4602(10) Å	α= 90°.
	b = 12.4339(9) Å	β= 107.5640(10)°.
	c = 23.7507(17) Å	γ = 90°.
Volume	4071.2(5) $Å^3$	
Z	8	
Density (calculated)	1.886 Mg/m^3	
Absorption coefficient	5.478 mm^{-1}	
F(000)	2224	
Crystal size	0.13 x 0.04 x 0.02 mm^3	
Theta range for data collection	2.96 to 27.48°.	
Index ranges	-18<=h<=17, -16<=k<=16, -30<=l<=27	
Reflections collected	43045	
Independent reflections	9286 [R(int) = 0.0515]	
Completeness to theta = 27.48°	99.5 %	
Absorption correction	Semi-empirical from equivalents	
Max. and min. transmission	0.8983 and 0.5361	
Refinement method	Full-matrix least-squares on F^2	
Data / restraints / parameters	9286 / 63 / 458	
Goodness-of-fit on F^2	1.052	
Final R indices [I>2sigma(I)]	R1 = 0.0322, wR2 = 0.0672	
R indices (all data)	R1 = 0.0479, wR2 = 0.0742	
Largest diff. peak and hole	0.870 and -0.715 $e.Å^{-3}$	